Numerical Methods for Electromagnetic Wave Propagation and Scattering in Complex Media

by

Christopher D. Moss

B.S., University of Alberta (June 1997)
S.M., Massachusetts Institute of Technology (May 2000)

Submitted to the Department of Electrical Engineering and Computer Science
in partial fulfillment of the requirements for the degree of

Doctor of Philosophy

at the

MASSACHUSETTS INSTITUTE OF TECHNOLOGY
[February 2004]
January 2004

Author .....
Department of Electrical Engineering and Computer Science
January 23, 2004

Certified by .....
Jin Au Kong
Professor of Electrical Engineering and Computer Science
Thesis Supervisor

Accepted by .....
Arthur C. Smith
Professor of Electrical Engineering and Computer Science
Chairman, Department Committee on Graduate Students

Numerical Methods for Electromagnetic Wave Propagation and Scattering in Complex Media

by

Christopher D. Moss

Submitted to the Department of Electrical Engineering and Computer Science
on January 23, 2004, in partial fulfillment of the
requirements for the degree of
Doctor of Philosophy

Abstract

Numerical methods are developed to study various applications in electromagnetic wave propagation and scattering. Analytical methods are used where possible to enhance the efficiency, accuracy, and applicability of the numerical methods.

Electromagnetic induction (EMI) sensing is a popular technique to detect and discriminate buried unexploded ordnance (UXO). Time domain EMI sensing uses a transient primary magnetic field to induce currents within the UXO. These currents induce a secondary field that is measured and used to determine characteristics of the UXO. It is shown that the EMI response is difficult to calculate in early time when the skin depth is small. A new numerical method is developed to obtain an accurate and fast solution of the early time EMI response. The method is combined with the finite element method to provide the entire time domain response. The results are compared with analytical solutions and experimental data, and excellent agreement is obtained.

A fast Method of Moments is presented to calculate electromagnetic wave scattering from layered one dimensional rough surfaces. To facilitate the solution, the Forward Backward method with Spectral Acceleration is applied. As an example, a dielectric layer on a perfect electric conductor surface is studied. First, the numerical results are compared with the analytical solution for layered flat surfaces to partly validate the formulation. Second, the accuracy, efficiency, and convergence of the method are studied for various rough surfaces and layer permittivities.

The Finite Difference Time Domain (FDTD) method is used to study metamaterials exhibiting both negative permittivity and permeability in certain frequency bands. The structure under study is the well-known periodic arrangement of rods and split-ring resonators, previously used in experimental setups. For the first time, the numerical results of this work show that fields propagating inside the metamaterial with a forward power direction exhibit a backward phase velocity and negative

index of refraction. A new metamaterial design is presented that is less lossy than previous designs.

The effects of numerical dispersion in the FDTD method are investigated for layered, anisotropic media. The numerical dispersion relation is derived for diagonally anisotropic media. The analysis is applied to minimize the numerical dispersion error of Huygens' plane wave sources in layered, uniaxial media. For usual discretization sizes, a typical reduction of the scattered field error on the order of 30 dB is demonstrated.

The new FDTD method is then used to study the Angular Correlation Function (ACF) of the scattered fields from continuous random media with and without a target object present. The ACF is shown to be as much as 10 dB greater when a target object is present for situations where the target is undetectable by examination of the radar cross section only.

Thesis Supervisor: Jin Au Kong
Title: Professor of Electrical Engineering and Computer Science

Acknowledgments

I would like to thank Professor Kong for allowing me the opportunity to join his research group, the Center for Electromagnetic Theory and Applications (CETA). CETA has provided me with a wonderful environment in which to learn and grow, through Professor Kong's guidance and through the excellence of my peers. I have also enjoyed considerable freedom in choosing my research topics, which allowed me to pursue the work and challenges that interested me the most. I am also grateful to Professor Kong for his superb lectures that presented electromagnetic theory with such clarity and spirit.

I would also like to thank Dr. Tomasz Grzegorcyzk, a CETA research scientist from 2001 through to the present. Tomasz has been both a friend and mentor to me, and I have never ceased to be amazed by his breadth of knowledge and his remarkable insights. Tomasz has also served as a good example to me that one can balance an appreciation for the finer things in life (i.e. a personal life) with the often enormous workload of a dedicated scientist. I am also grateful for his help in proofreading this thesis and for serving on my Doctoral Thesis Committee.

From 2002 through to the present, I have worked with Dr. Kevin O'Neill of the Army Cold Regions Research and Engineering Laboratory and of Dartmouth University. I am grateful to Kevin for his support of my project, and for his ideas and brainstorms that formed the foundation of the work in Chapter 2. I have enjoyed working with him and have appreciated the interest he took in my project, the patience he had for the 'Two Month Bug' in my code, his confidence in me, and his general enthusiasm for what we were doing.

Professor Fernando Teixeira (now at the Ohio State University) was a postdoc at CETA from 1999 through 2000, a good friend, and a considerable influence on my graduate work. When my early research led to a dead end, Fernando helped me revise my work into a new project that yielded great results. The research in Chapter 5 and Chapter 6 was carried out with guidance from Fernando, who took my vague ideas

and "what ifs?" and helped me with the mathematics and background to develop original research. I thank him for his help and guidance.

I would like to thank my academic advisor, Professor Cardinal Warde, for providing me with advice over the many years I've been at MIT. I have also appreciated his interest in my research, and his efforts as part of my RQE committee (along with Professor Alan Grodzinsky) and as part of my Doctoral Thesis Committee.

I am indebted to various members of Group 49 at Lincoln Laboratory: Dr. Bob Atkins, Dr. Bob Shin, Dr. Hsiu Han, and Dr. Eliahu Niewood, to name a few. They provided me with research advice (Chapter 3) and the majority of my graduate school funding.

Other research scientists in CETA have also been a great help, such as Dr. Yan Zhang who motivated me to dive into research on Left Handed Metamaterials, and Dr. Eric Yang, who provided me with early advice on my research.

It's been a long time since that day in September of 1998 when I showed up for the first time at my office at 26-440, nervous and unsure of what to expect at MIT. There that day to greet me were Henning Braunisch and Bae-Ian Wu (now both Drs.), who patiently answered all my questions and let me know what the MIT experience was like from a student perspective. Henning helped me with research whenever asked, and I often tapped into Bae-Ian's expertise. Another former student, Chi On Ao, provided me with expert advice on analytical scattering techniques, a 1991 Toyota Corolla, and many great squash games, all of which contributed to my positive graduate school experience.

I would also like to note my contemporary students in CETA, Ben Barrowes and Joe Pacheco, who have been friends and excellent peers for the last five years. I am particularly grateful to Ben for his advice on Linux, Matlab, and Fortran, and for showing me the truth about Macs. For their help and friendship, I would like to thank Ben and Joe as well as all the other students at CETA over the years: Xudong Chen, James Chen, Jie Lu, Madhusudhan Nikku, and Fuwan Gan.

Beyond CETA, I would like to acknowledge my close circle of friends who have jumped over all the hurdles of MIT graduate school with me: Jim Anderson, Tony Briggs, and Vincent Leslie. Always there to celebrate or commiserate, you guys are great friends.

I must also thank the MIT EECS graduate office, particularly Marilyn Pierce, for making the administrative side of graduate school so easy. I got the sense that they really care about their students, and were always there to advise on paperwork and procedure.

I would like to thank anybody who reads this thesis for their patience with typos. I am sure a few have escaped my notice.

Finally, I would like to thank my family. Without my family's love and support, this thesis work could not have been accomplished. My parents have done so much for me, and have been such great role models. My father has always been there with advice on just about anything, and convinced me to apply to MIT in the first place. My mother has provided unwavering enthusiasm and support of my work. My sister has been a voice of reason when faced with the frustrations and uncertainties of graduate school. Rob, Peg, Kiki, and my grandmothers have always been there to provide warm company and great conversation. Most importantly Christine, my better half, has been incredibly patient and caring over these many years of graduate school. Whether she was giving me a bag of apples to hit into the Charles River or planning our escapes to Vermont, she has always been there for me.

Contents

List of Figures

List of Tables

Chapter 1

Introduction

Electromagnetic wave theory is well-established scientific discipline, whose applications include, but are not limited to, remote sensing, digital and analog electronics, power systems, wireless and wired communications, radar systems, optics, and astronomy. Each application involves the creation, manipulation, and/or reception of electric and magnetic fields. The behavior of electromagnetic fields is completely described by Maxwell's Equations, a set of four partial differential equations (PDEs) that relate electric and magnetic fields in time and space. Physical media are accounted for in Maxwell's Equations through a set of two equations known as the constitutive relations. To calculate an electromagnetic field from a set of sources in a given physical geometry, the supporting medium must be characterized through the constitutive relations and the appropriate boundary conditions on the electric and magnetic fields must be enforced. Natural and man-made geometries are often irregular and inhomogeneous (i.e. complex), and the solutions to Maxwell's Equations are almost always nontrivial.

Consider the design of a remote sensing system. Remote sensing has many definitions: in general it is defined as "the acquisition of information about an object without being in physical contact with it" [1], or more specifically it is "the science of acquiring, processing, and interpreting images that record the interaction between

electromagnetic energy and matter" [2]. A remote sensing system must have a sensor that measures electromagnetic waves and, for the case of active remote sensing, must have a source. The source (or sources) creates an electromagnetic field that propagates through a medium, inducing further sources and fields, that are then measured by the sensor. Calculating the field from the initial source and the effects of the medium is necessary to predict what the sensor will measure. For example, ground penetrating radar (GPR) systems are designed to detect landmines. The source and sensor in such systems are transmitter and receiver antennas. The designer of a remote sensing system needs to calculate the wave from the transmitter antenna, the scattered wave from the landmine, and the effect of the ground on the transmitted and scattered waves, all to predict what type of response to expect at the receiver antenna. The sensor, ground, and landmine could be characterized and accounted for through the constitutive relations and by enforcing the correct boundary conditions, thus enabling a solution of Maxwell's Equations. Unfortunately, depending on the complexity of the sensor, ground, and landmine, the problem is difficult if not impossible to solve analytically. The designer then has two options. First, an exact (perhaps analytical) solution should still be sought, but is usually only attainable for specific canonical problems. Therefore, approximations of the sensor, ground, and landmine characteristics must be made to simplify the problem. For example, if the source is approximated as a plane wave, if the ground is assumed to be homogeneous, and if the landmine is approximated as a sphere, then the scattered wave is exactly described by a convergent infinite series (Mie scattering [3]). However, these can be significant approximations that can result in significant error. The second option available to the designer is a numerical, also known as computational, method that searches for a solution to the complete problem. Numerical methods are powerful tools that enable the solution of the differential, integral, or algebraic equations that arise in engineering and physics problems. Depending on the method, irregular geometries and inhomogeneous media can easily be incorporated. However, often such

methods in their basic forms create a large matrix equation (or series of matrix equations) that require excessive computational time and memory to solve. As a result, the evolution of numerical methods toward better efficiency and accuracy is a natural topic of research. While some efficiency gains can be made through improved algorithms that accelerate the solution of the matrix equation, major improvements in speed or accuracy are usually a result of reformulating the numerical method to include analytical techniques based on physical insight into the problem.

This thesis develops numerical methods to solve various problems in electromagnetic wave theory, incorporating analytical techniques where possible to improve the efficiency, accuracy, or applicability of the methods. The methods presented in this work are not specific to the topics studied, and can be applied or expanded to other applications. The following sections introduce the numerical methods that form the foundation of this thesis. The applications of the thesis will then be discussed, addressing their importance and the reasons why improved numerical methods are required.

1.1 Background of Numerical Methods

A popular numerical method used to solve PDEs, such as Maxwell's Equations, is the Finite Element Method (FEM). The FEM is widely used in many scientific areas, particularly in civil and mechanical engineering applications [4, 5]. The FEM uses either the Rayleigh-Ritz method [6] to solve variational problems, or the method of weighted residuals [7] (such as a Galerkin method) to solve problems that are posed with a PDE and associated boundary conditions. For electromagnetic wave problems, the FEM could be used to solve the Helmholtz equation in a finite space with given boundary conditions. The FEM relies on discretizing the solution of the governing equation. The domain of interest is discretized into a mesh, the elements of which give the method its name. The unknown solution is expressed as a summation of

basis functions that each exist over a single element. The Galerkin method reduces the PDE to a system of ordinary differential equations, or to a system of simple algebraic equations. The result is a sparse matrix equation that can be efficiently solved with a suitable linear algebra package. The FEM may be used in the time or frequency domain, and is being continuously improved. In particular, the problem of modeling unbounded media on a finite mesh has been solved with absorbing boundary conditions (ABCs) [8]. Furthermore, spectral methods have been developed [9], new basis functions have been implemented [10], and newer sparse matrix solvers and preconditioners have been applied [11]. Chapter 2 uses the FEM to solve Maxwell's Equations in a potentially inhomogeneous and irregular object.

Another popular numerical method is the Method of Moments (MoM) [12]. The MoM is actually very similar to the FEM, and can be thought of as the weighted residual method applied to integral equations. The starting point for the MoM is usually Green's Theorem or Huygens' Principle [3], both of which express an observation field in terms of the incident field and an integration over a finite surface (such as a scattering body) containing sources. The MoM requires the Green's functions for the domain between the sources and observation points. Hence, the MoM is well-suited for scattering problems where the unknowns are the currents over the scattering body that exists in a medium that may be characterized with a Green's function. The MoM is usually solved in the frequency domain, where numerous theories have been developed to deal with the Green's functions. The method solves for the unknown sources (usually currents) over the surface from a given incident field. As with the FEM, the surface (or volume) is meshed and the unknowns are expressed in terms of basis functions. A weighted residual method can then be applied (also referred to as inner product), reducing the problem to a set of algebraic equations that yield a dense matrix equation. However, because the MoM solves unknowns over a surface and the FEM must solve unknowns everywhere in space, the MoM dense matrix is much smaller than the FEM sparse matrix. Recently, a time do-

main MoM (marching-on-in-time scheme) has been investigated [13] and is a topic of current research. Enhanced MoM techniques are continuously developed, often with efficiency in mind. Avenues of research include Green's function manipulation [14], spectral methods [15] and novel basis functions [16]. Chapter 2 uses an two dimensional MoM coupled with an FEM and a new numerical method. Chapter 3 extends a one dimensional MoM formulation to solve the scattered fields from layered rough surfaces.

Finally, the Finite Difference Time Domain (FDTD) method is perhaps the most popular numerical method used to solve Maxwell's Equations. Introduced by Yee [17] in 1966, the FDTD method was not widely used until the advent of modern computers and the work by Taflove [18] and others [19]. The FDTD method is a PDE method, solving Maxwell's Equations directly using central differencing in space and an explicit Euler method in time. Space is discretized into a regular grid (usually Cartesian, spherical, or cylindrical), with unknowns placed around each node. The unknowns are usually the electric and magnetic field vectors, and the grid discretization is on a sub-wavelength scale. Each unknown is solved using the adjacent field vectors and the method is iterated forward in time. The appeal of the FDTD method lies in its simplicity, elegance, ease of use, and efficiency. While the FEM has more flexibility in its mesh, and hence its ability to solve problems with arbitrary geometries, it is more complex to implement than the FDTD method. Many improvements in the FDTD method have been published in the past 10 years, incorporating advanced ABCs [20, 21, 22, 23] to account for unbounded domains, and implementing higher order schemes [24, 25] to improve accuracy. The FDTD has also been modified to become an implicit time stepping method [26, 27] that is unconditionally stable, allowing for larger time steps and faster solutions (at the expense of accuracy). Recently, spectral methods have been incorporated, and the FDTD method has evolved into newer forms such as the Multi-Resolution Time Domain method [28]. Chapter 4 of this thesis concerns a new application of the FDTD method, while Chapter 5 and

Chapter 6 introduce a new, more accurate FDTD method.

1.2 Thesis Work

This thesis concerns the development of models that predict electromagnetic wave propagation and scattering in complex media. The work in this thesis is based almost entirely on previously published or forthcoming (submitted for publication) material by the author.

Chapter 2 presents a numerical method for time domain electromagnetic induction (EMI) sensing of conducting and permeable targets. Time domain EMI sensing uses a transient primary magnetic field to induce currents within the target. These currents induce a secondary field that is measured and used to determine characteristics of the target. The application in mind is the detection and discrimination of buried unexploded ordnance (UXO) [29]. EMI sensing of UXO lies within the magnetoquasistatic (low frequency) regime, at which soil is transparent. Despite that, due to the enormous amount of scrap (exploded ordnance) that surrounds UXOs, detection and discrimination remains a difficult problem. Hence, the availability of accurate forward EMI models is necessary to develop useful inversion algorithms. However, standard numerical methods that rely on spatial discretization have difficulty solving this problem due to the small penetration (skin depth) of the primary field into the target. In Chapter 2, a standard FEM is used for the interior of the target, coupled with an MoM for the exterior of the target. It is shown that these numerical methods are indeed inaccurate, early in time after the primary field transient, as they cannot resolve the skin depths of typical UXO materials. This work addresses the problem with a technique that replaces the interior FEM with the divergence equation of the magnetic field, which only requires a mesh on the target surface. The new technique requires an expression for the normal derivative of the magnetic field, which is calculated using an approximation based on the analytical solution of the

governing equation. For larger skin depths, however, the FEM method is still used for the interior region. The result is a hybrid technique that can accurately calculate the entire EMI time domain response with greater accuracy and efficiency than was previously possible.

While Chapter 2 examines the EMI sensing technique that uses very low frequency (magnetoquasistatic) fields, most remote sensing systems utilize electromagnetic waves at higher frequencies, such as microwave or millimeter wave radar systems. For buried object detection and discrimination, using higher frequency waves results in scattered fields that yield more information (greater resolution) of the target. However, as opposed to EMI sensing, the ground and surface are no longer transparent at higher frequencies, so reflections and scattering from the surrounding soil must be taken into account. Chapter 3 addresses the problem of electromagnetic wave scattering from an arbitrary number of layered rough surfaces. Specifically, the formulation allows for layers of geophysical media that may represent snow or foliage. The goal of this work is to develop accurate models to study the effects of terrain on the performance of ground based radar and communication systems. However, the method is equally well-suited to studying the effects of a stratified ground on the performance of ground penetrating radar systems (in general, the material properties of soil vary with depth). The MoM is used to calculate electromagnetic wave scattering from stratified regions that are separated by rough surfaces. Compared to the single surface case, the solution of scattering from multiple surfaces requires significantly more memory and computational time. Given the large terrain size of interest, spectral and iterative solution techniques are adapted for a tenable solution. As an example, a dielectric layer on a perfect electric conductor surface is studied. First, the numerical results are compared with the analytical solution for layered flat surfaces to partially validate the formulation. Second, the accuracy, efficiency, and convergence of the method are studied for various rough surfaces and layer permittivities.

The previous cases concern problems that begin with a space containing a complex

(uncontrolled) medium, such as a buried UXO or geophysical medium, and require models that predict the effects of such a medium on electromagnetic waves. In such cases, the complex medium is part of the problem and the scattered electromagnetic waves are the solution. However, there are other problems that begin by specifying a desired electromagnetic wave behavior, and require an engineered medium to create and support that behavior. Obtaining the desired electromagnetic wave behavior is then the problem, and the medium is the solution. Such a case is examined in Chapter 4, which presents an implementation of the FDTD method to model a metamaterial that exhibits a negative index of refraction. Metamaterials are composite structures, engineered to exhibit electromagnetic properties that do not naturally occur. In this case, the metamaterial is a periodic array of metallic wires and split ring resonators (SRRs) designed to yield simultaneously negative permittivity and permeability, and thus a negative index of refraction, at certain frequencies. The simulation is based on a recent experimental setup [30] that was the first to demonstrate that a negative index of refraction is realizable. However, the experiment was controversial and further validation was necessary. The goal of this chapter is to present a numerical demonstration of the negative index of refraction using a well-established FDTD method. Three parameters are studied: the transmission coefficient of a slab, the phase variation of the propagating fields within the metamaterial, and the refraction of a wave through a prism. The work in this thesis is based on a publication [31] that was the first to use a numerical method to simulate the entire metamaterial structure and show the resulting negative index of refraction. Various metamaterial geometries are studied, and a new SRR geometry is introduced.

In Chapter 5, the numerical error of the FDTD method is studied in detail. Like many other numerical techniques, the FDTD method approximates continuous space physics on a finite grid. The error of the method depends on the discretization of the grid, specified by the user to balance accuracy, stability, and speed. The most fundamental error of the method is known as numerical dispersion error, which is the

difference between continuous and discrete space dispersion relations. In this work, Maxwell's equations in discrete space are used to derive the numerical dispersion relation of anisotropic media that are modeled with the FDTD method. Exact expressions are also derived for the reflection and transmission coefficients from planar boundaries in the FDTD grid. With these expressions, a new method is presented that reduces the error of plane wave Huygens' sources that are commonly used in FDTD simulations. Applications of this new method include microstrip circuit simulations and subsurface sensing models. The latter is the focus of Chapter 6, where the new FDTD method is employed in a ground penetrating radar simulation. The application is similar to the EMI sensing of buried UXO in Chapter 2, but in this case a radar in the MHz frequency range is used. At radar frequencies, the soil is no longer transparent, and spatial fluctuations of the soil material significantly perturb the electromagnetic waves. Such soil material fluctuations are not deterministic, and a random medium model is used. A post-processing technique, the Angular Correlation Function (ACF), is applied to the scattered fields from random media with and without embedded targets. The effectiveness of the ACF is studied to determine if it aids in target detection in the presence of volumetric clutter.

The summary of the publications associated with each chapter is shown in Table 1.1.

Chapter	Subject	Publication
2	Time Domain Method for EMI Sensing	[32, 33]
3	EM Wave Scattering From Layered Rough Surfaces	[34]
4	An FDTD Study of Left Handed Metamaterials	[31]
5	Numerical Dispersion Compensation in FDTD	[35]
6	Detection of Targets Using the ACF	[36]

Table 1.1: Publications associated with each chapter of the thesis. Conference abstracts are not included.

Chapter 2

Hybrid Time Domain Method for Electromagnetic Induction Sensing

2.1 Introduction

The detection and removal of buried unexploded ordnance (UXO) is an expensive and challenging task. In the United States, an estimated 11 million acres of land may contain buried UXO [37]. The problem is more widespread in European countries, where millions of buried UXO remain from two world wars. The overwhelming task of finding and removing these UXO is exacerbated by the fact that almost three-quarters of the costs and efforts are expended responding to sensor false-alarms caused by metallic clutter [38]. Hence, accurate detection and discrimination techniques are a popular area of active research. Ground penetrating radar is one area of focus, although it is hampered by significant clutter from the surface and surrounding soil [39]. Another promising technique is electromagnetic induction (EMI) [40] sensing, which uses frequencies at which the natural environment is transparent (generally less than 500 kHz). In time domain EMI sensing, targets are first saturated in a static primary magnetic field that is then shut off. The transient primary field causes currents to flow in the target, inducing a secondary magnetic field that is measured with a receiver

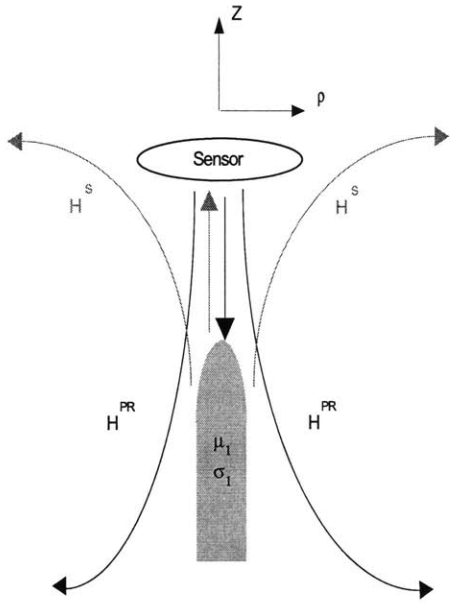

Figure 2-1: A sensor transmits a static primary magnetic field that is turned on and off. The induced magnetic field is measured to infer characteristics of the object.

coil. These currents, and the secondary field, eventually decay to zero due to the finite conductivity of the target. Depending on the instrument, the receiver coil takes sample of the decaying secondary field anywhere between 50 μ s and 0.1 s after the primary field transient. The secondary field is often referred to as the EMI scattered field. Frequency domain EMI sensing measures the induced field from primary fields at discrete frequencies instead of a transient. The time or frequency domain profile of the scattered field reveals characteristics of the target such as dimension, permeability, and conductivity. Figure 2.1 shows the geometry of the problem. As a new detection and discrimination technology, research in EMI sensing is concentrating on developing three areas: forward models, hardware, and inversion algorithms. This work concerns the first area: the development of an efficient and accurate forward model of time domain EMI scattering. Many EMI systems operate in the time domain, which offers more flexibility in receiver and transmitter coil placement. Current models treat the problem at various levels of complexity, often trading off accuracy

for efficiency. For example, UXO can be approximated by canonical geometries, for which analytical solutions exist. Indeed, the EMI response from a conducting and permeable sphere [41] is well established. The EMI response from spheroids has recently been developed [42] and successfully applied to model spheroid-like UXO geometries. Note that this solution for the spheroidal geometries will be referred to as the 'analytical solution' in this work, even though it is actually an infinite series. Other simplified models include approximations of the UXO as multiple dipoles [43], which has shown promise for basic shapes. However, UXO are usually heterogeneous and irregular objects, and in such cases general numerical solutions are required to obtain accurate results.

Common numerical methods for EMI scattering, such as the finite difference or the finite element method (FEM), rely on a meshed discretization of the target to solve for the interior fields (or currents). However, these fields often penetrate only a very shallow depth (skin depth) into the target immediately after the transient primary field. Depending on the material, the skin depth may remain quite small for the entire decay time (and measurement time) of the secondary field. To accurately model the interior fields, the spatial discretization must be fine enough to resolve the skin depth, which is usually much smaller than the dimensions of the target. The same problem applies to frequency domain methods, where the skin depth decreases as frequency increases. For example, a typical non-magnetic UXO has a conductivity of 10^7 S/m, which results in a skin depth of approximately 5 mm at 1 kHz (or 1 ms). For magnetic materials, such as steel ($\mu_r = 100$), the skin depth is on the order of 10^{-4} m. Given that most targets of interest are 0.1 m to 1 m in size, the stringent mesh requirements can become difficult to satisfy, even for a 2D body of revolution (BOR) mesh. Hence, contemporary time domain numerical methods can only accurately model the later time (or low frequency) response, which is particularly unfortunate because the secondary field decays rapidly and often is too weak to be measured in late time. Integral equation approaches also suffer from this problem [44], as the

surface must be discretized finely enough to resolve the interior Green's function. Often frequency domain numerical treatments have simply avoided the problematic high frequency regions [45], neglecting important EMI response characteristics. Other methods treat the target as a perfect conductor and neglect the interior fields, which may work for the very early time (or high frequency) response but leads to incorrect results at all other times [46, 47] where the interior fields are neglected. Various other methods have been tried, such as impedance boundary conditions [48, 49] and special finite element basis functions [50, 51], all with limited success. Even the frequency domain analytical EMI scattering solutions for spheroids cannot be solved at high frequencies, and a Small Penetration Approximation (SPA) [52] or asymptotic methods [14] must be used instead. Recently, a new numerical method called the Thin Skin Approximation (TSA) was developed to model the middle to high frequency EMI response, and accurate results were obtained [53]. However, it is still difficult to obtain an accurate time domain response from a frequency domain model that is only accurate at either low or high frequencies. In this work, a time domain TSA method is developed and combined with standard numerical methods to obtain a solution that is accurate for any skin depth.

In this paper, a method of moments (MoM) is used to solve the boundary integral (BI) for the exterior region [54]. Two separate formulations are used for the interior region, depending on the skin depth. When the skin depth can be resolved on a reasonable mesh, an FEM is used to solve the interior problem for the magnetic vector potential [55, 56, 7]. The technique will be referred to as the FE-BI method. When the skin depth is small, the divergence equation for the magnetic field is implemented in the interior, similar to [53]. A new method is developed in which the normal derivative of the magnetic field is calculated using a type of TSA, so that no interior mesh is required. This second technique will be referred to as the TSA-BI method. The two approaches, FE-BI and TSA-BI, can both be solved separately in their regimes of validity to obtain the entire time domain response. The method's accuracy will be

compared with analytical solutions for spheres and spheroids, as well as experimental results. Various typical target geometries can be studied to identify important characteristics of the time domain response that may be useful for inversion algorithms such as a Support Vector Machine or the Linear Least Squares method. Furthermore, objects with simple material inhomogeneities (such as aluminum and steel parts) can be examined for identifiable characteristics in the time domain response.

2.1.1 Formulation

The geometry under consideration is that of a conducting, permeable axisymmetric target, an example of which is shown in Figure 2.1. The object has a conductivity on the order of $\sigma_1 = 10^7$ S/m, may have a relative permeability μ_{1r} from 1 to 100, and has a relative permittivity $\epsilon_{1r} = 1$. The region outside the object, V_2, is considered weakly conducting, $\sigma_2 < 1$, and nonpermeable, $\mu_{2r} = 1$. Consider the wave equation for the interior magnetic field,

$$\nabla^2 \overline{H} - \mu_1 \epsilon_1 \frac{\partial^2 \overline{H}}{\partial t^2} - \sigma_1 \mu_1 \frac{\partial \overline{H}}{\partial t} = 0 \tag{2.1}$$

For the object of interest, the $\sigma_1 \mu_1$ product is many orders of magnitude larger than the $\epsilon_1 \mu_1$ product, and Equation 2.1 reduces to a diffusion equation. This is equivalent to neglecting the displacement current and applying magnetoquasistatic (MQS) approximations. Hence, inside the object we have

$$\nabla \times \overline{H} = \overline{J} \tag{2.2}$$

which results in

$$\nabla \cdot \overline{J} = 0 \tag{2.3}$$

In the FEM, it is more convenient to work with the magnetic vector potential, $\overline{A}$. Specifically, $\overline{A}$ is continuous across adjacent finite elements with differing permeability

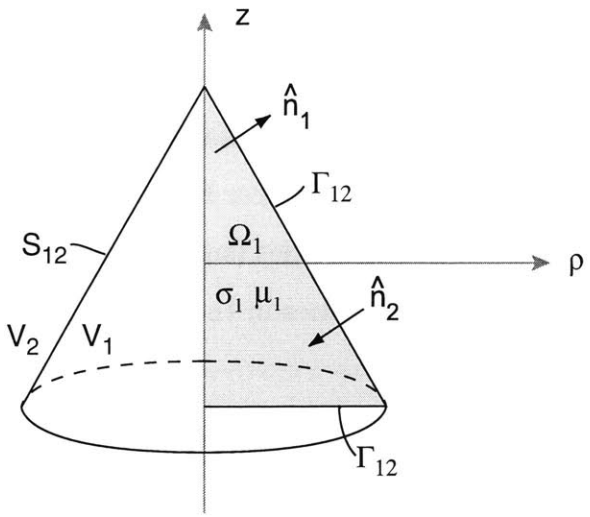

Figure 2-2: An axisymmetric three dimensional object with volume V_1 enclosed by surface S_{12}. The two dimensional generating surface and contour are Ω_1 and Γ_{12}. The normal vector out of the object is $\hat{n}_1$, and the normal vector into the object is $\hat{n}_2$.

or conductivity. As will be shown in the next section, continuity is necessary for nodal based FE methods. The definition of $\overline{A}$ is

$$\overline{B} = \nabla \times \overline{A} = \mu_1 \overline{H} \tag{2.4}$$

which, combined with Faraday's Law, results in

$$\overline{J} = \sigma_1 \overline{E} = -\sigma_1 \frac{\partial \overline{A}}{\partial t} - \sigma_1 \nabla \Phi \tag{2.5}$$

where Φ is the scalar electric potential. Now Equations 2.4 and 2.5 can be substituted into Equation 2.2 to obtain

$$\nabla \times \frac{1}{\mu_1} \nabla \times \overline{A} + \sigma_1 \frac{\partial \overline{A}}{\partial t} + \sigma_1 \nabla \Phi = 0 \tag{2.6}$$

where Equation 2.3 is automatically satisfied by the nondivergence of the curl vectors. The definition of $\overline{A}$ in Equation 2.4 is incomplete, and a gauge must be specified to

guarantee uniqueness. For MQS problems, it is common to use the Coulomb gauge,

$$\nabla \cdot \overline{A} = 0 \tag{2.7}$$

This allows Equation 2.6 to be rewritten as

$$\nabla \times \frac{1}{\mu_1} \nabla \times \overline{A} - \nabla \frac{1}{\mu_1} \nabla \cdot \overline{A} + \sigma \frac{\partial \overline{A}}{\partial t} + \sigma_1 \nabla \Phi = 0 \tag{2.8}$$

The first two terms of Equation 2.8 then reduce to the vector Laplace operator. However, Equation 2.3 is no longer satisfied, and must be separately enforced with

$$\nabla \cdot \sigma_1 \left(\frac{\partial \overline{A}}{\partial t} + \nabla \Phi \right) = 0 \tag{2.9}$$

Thus Equations 2.8 and 2.9 are the governing equations for the object interior. The exterior wave equation can also be reduced to MQS, in this case due to low frequencies of the EMI problem where the wavelengths of the exterior fields are large with respect to the object. Given the insignificant current, the magnetic field is irrotational and can be represented in terms of a scalar potential,

$$\overline{H} = -\nabla \psi \tag{2.10}$$

Combined with $\nabla \cdot \overline{B} = 0$, the equation for the nonmagnetic exterior is simply

$$\nabla^2 \psi = 0 \tag{2.11}$$

With Equations 2.8, 2.9, and 2.11, there are three equations with three unknowns. With a suitable surface gauge for $\overline{A}$, the scalar electric potential and Equation 2.9 can be eliminated to simplify the problem. This is demonstrated in the following section.

2.1.2 Solution Uniqueness

The curl and divergence of $\overline{A}$ have been specified in Equations 2.4 and 2.7, and are sufficient to guarantee uniqueness in free space. However, in a finite region it is also necessary to specify the boundary condition of $\overline{A}$. Consider two vector potentials $\overline{A}_1$ and $\overline{A}_2$ that arise as solutions to the same physical problem. Were the solutions unique, the difference between them, $\overline{A}_0 = \overline{A}_1 - \overline{A}_2$, would be zero. From Equations 2.2 and 2.7,

$$\nabla \times \overline{A}_0 = 0 \tag{2.12}$$

$$\nabla \cdot \overline{A}_0 = 0 \tag{2.13}$$

From Equations 2.12 and 2.13, $\overline{A}_0$ can be expressed as the gradient of any scalar (e.g. χ), resulting in

$$\overline{A}_0 = \nabla\chi \tag{2.14}$$

$$\nabla^2\chi = 0 \tag{2.15}$$

In order to satisfy Equation 2.15 in free space, χ must be a constant. However for a finite region this is not necessarily true and so $\nabla\chi$ can be non-zero. For this problem, a suitable boundary condition for $\overline{A}$ on S_{12} is

$$\hat{n}_1 \cdot \overline{A} = 0 \tag{2.16}$$

which results in

$$\frac{\partial\chi}{\partial n_1} = 0 \tag{2.17}$$

on S_{12}. A constant is only solution to the Laplace equation in a closed domain with a Neumann boundary condition. Thus χ must be a constant within the region, $\overline{A}_0$ is zero, and uniqueness is obtained. Furthermore, Equation 2.16 reduces the boundary

condition Equation 2.22 to

$$\frac{\partial \Phi}{\partial n_1} = 0 \tag{2.18}$$

and, if σ_1 is piecewise continuous, Equation 2.9 becomes

$$\nabla^2 \Phi = 0 \tag{2.19}$$

Hence the interior scalar potential is a constant or zero, and Equations 2.9 and 2.22 are no longer required. The magnetic vector potential $\overline{A}$ is the only variable required in the interior region, solved with Equation 2.8.

2.1.3 Boundary Conditions

Across the boundary, it is necessary to enforce continuity of $\hat{n} \times \overline{H}$ and $\hat{n} \cdot \overline{B}$. This is ensured by

$$\hat{n}_1 \cdot (\nabla \times \overline{A}) - \hat{n}_2 \cdot \mu_0 \nabla \psi = 0 \tag{2.20}$$

$$\frac{1}{\mu_1}(\nabla \times \overline{A}) \times \hat{n}_1 - \nabla \psi \times \hat{n}_2 = 0 \tag{2.21}$$

on S_{12} (see Figure 2-2). Another boundary condition is that no current may flow into the nonconducting regions, hence

$$\hat{n}_1 \cdot \left(\frac{\partial \overline{A}}{\partial t} + \nabla \Phi \right) = 0 \tag{2.22}$$

With Equations 2.8 and 2.11, combined with the gauge of Equation 2.16 and the boundary conditions of Equations 2.20 and 2.21, the problem is reduced to a system of two equations with two unknowns. The interior equation over the finite, possibly inhomogeneous target volume is well-suited to an FEM implementation, while the unbounded exterior problem can be solved with a boundary integral formulation.

2.2 Finite Element - Boundary Integral Method

The FEM is used for the interior region (region 1, Equation 2.8), and a Boundary Integral (BI) formulation is used to handle the infinite exterior region (region 2, Equation 2.11). The two methods are combined using the appropriate boundary conditions.

2.2.1 Interior Problem

Formulation

The FEM requires a restatement of the governing differential equation using an approximation technique, examples of which are the variational method or the weighted residual method. This derivation will focus on the latter, using a Galerkin formulation to obtain

$$\int_{V_1} \left(\overline{W} \cdot \nabla \times \frac{1}{\mu_1} \nabla \times \overline{A} - \overline{W} \cdot \nabla \frac{1}{\mu_1} \left(\nabla \cdot \overline{A} \right) + \overline{W} \cdot \sigma_1 \frac{\partial \overline{A}}{\partial t} \right) dV = 0 \tag{2.23}$$

where V_1 represents the volume of region 1. Integrating by parts:

$$\begin{aligned} \int_{V_1} \frac{1}{\mu} \left(\nabla \times \overline{W} \right) \cdot \left(\nabla \times \overline{A} \right) dV \; &- \; \int_{S_{12}} \frac{1}{\mu} \overline{W} \times \left(\nabla \times \overline{A} \right) \cdot \hat{n}_1 dS \\ + \int_{V_1} \frac{1}{\mu} \left(\nabla \cdot \overline{W} \right) \left(\nabla \cdot \overline{A} \right) dV \; &+ \; \int_{S_{12}} \frac{1}{\mu} \left(\nabla \cdot A \right) \overline{W} \cdot \hat{n}_1 dS \\ &- \; \int_{V_1} \overline{W} \cdot \sigma \frac{\partial \overline{A}}{\partial t} dV = 0 \end{aligned} \tag{2.24}$$

results in the general vector equation for the interior of the object that may be solved by the FE method. The surface integrals are evaluated over S_{12}, and are used to enforce the boundary conditions. The boundary condition of Equation 2.16 for $\overline{A}$ must also apply for the weighting function $\overline{W}$, and may be enforced by setting

the second surface integral of Equation 2.24 to zero. However, Equation 2.16 for $\overline{A}$ must still be enforced as an essential (or Dirichlet) boundary condition, which will be discussed later in this section. For axisymmetric geometries, considerable computational savings can be gained by taking advantage of the symmetry of the problem. Any arbitrary incident field is first decomposed into azimuthal Fourier modes. The three dimensional problem of Equation 2.24 can then be reduced to a two dimensional problem by integrating out the azimuthal dimension and solving over the object cross-section in the (ρ, z) plane. The incident modes decouple in an obvious fashion during the azimuthal integration, leaving a set of two dimensional equations to be solved for each mode. The scattered field is then reconstructed from the sum of the solutions for each incident field mode. This work will begin by considering only axial or transverse primary magnetic fields, such as $\overline{H}^{PR} = \hat{z}H(\rho, z)$ or $H^{PR} = \hat{x}H(\rho, z)$. In such cases, the exterior scalar potential can be described by

$$\psi(\rho, \phi, z) = \sum_{p=0}^{\infty} \psi_p(\rho, z) \cos(p\phi) \tag{2.25}$$

Where $\psi_p(\rho, z)$ is a function describing the scalar potential in the (ρ, z) plane for the p^{th} mode. The interior vector potential and weighting function are represented as

$$\overline{A}(\rho, \phi, z) = \sum_{p=0}^{\infty} \left[\hat{\rho}A_p^{(\rho)}(\rho, z) \sin(p\phi) + \hat{\phi}A_p^{(\phi)}(\rho, z) \cos(p\phi) + \hat{z}A_p^{(z)}(\rho, z) \sin(p\phi)\right] \tag{2.26}$$

$$\overline{W}(\rho, \phi, z) = \sum_{q=0}^{\infty} \left[\hat{\rho}W_q^{(\rho)}(\rho, z) \sin(q\phi) + \hat{\phi}W_q^{(\phi)}(\rho, z) \cos(q\phi) + \hat{z}W_q^{(z)}(\rho, z) \sin(q\phi)\right] \tag{2.27}$$

Using these forms in Equation 2.24 results in ρ^{-1} terms that lead to difficulties in evaluating the integrations near the axis of revolution. To avoid this problem, a

modified vector potential may be used instead:

$$\overline{\mathcal{A}}(\rho,\phi,z) = \frac{\overline{A}(\rho,\phi,z)}{\rho} \tag{2.28}$$

The FEM is then used to solve for $\overline{\mathcal{A}}$ instead of $\overline{A}$, and the ρ term is reintroduced in post-processing. (Henceforth, the relationship of the $\overline{\mathcal{A}}$ and $\overline{W}$ terms on (ρ, z) will be suppressed.) This method eliminates the singularity in the integrand, and results in straightforward analytical expressions for the FE integrations of Equation 2.24, as detailed in the next section. However, this method requires that $\overline{\mathcal{A}}$ itself is a well-behaved function. In general, $\overline{A}$ is a function that has ρ^n dependence, in which case $\overline{\mathcal{A}}$ has ρ^{n-1} dependence. Hence, if $n \geq 1$, which happens to be the case for axial excitation, then $\overline{\mathcal{A}}$ is a suitable unknown and may be used to eliminate the singularity. However, for the transverse case, components of $\overline{A}$ may not depend on ρ at all, and so $\overline{\mathcal{A}}$ may have a ρ^{-1} singularity at the origin. The FEM cannot be used to solve for such a function, as the coefficients of elements on the origin would diverge. In that case, the singularity in the integrand has been exchanged for a singularity in the solution, which is less desirable. As a result, for the transverse case $\overline{A}$ will remain the unknown, and the singularity in the integrand will be dealt with by moving the mesh 1 μm off the axis of symmetry. Extensive numerical testing reveals that this approximation is both stable and accurate. Analytical expressions (to follow in this section) can still be used for the majority of the terms in Equation 2.24, providing fast and accurate solutions. For the ρ^{-1} singular terms, a quadrature numerical integration technique will be used [57].

The simplest case of uniform axial excitation (i.e. $\overline{H}^{PR} = \hat{z}H^{PR}$) is represented with $p = 0$. For that case, the primary magnetic scalar potential is $\psi_0(\rho, z) = z$ (from Equation 2.10). The exterior unknown is ψ and $\mathcal{A}_0^{(\phi)}$ is the only interior unknown. The Coulomb gauge is automatically satisfied in this case, and the second volume integral of Equation 2.24 is no longer required. Furthermore, the boundary condition

Equation 2.16 is also automatically satisfied. Hence, for uniform axial excitation, Equation 2.24 becomes

$$\int\int_{\Omega_1} \frac{1}{\mu_1}\left[\rho^2\left(\nabla\mathcal{A}_0^{(\phi)}\cdot\nabla W_0^{(\phi)}\right)+\rho\left(W_0^{(\phi)}\frac{\partial\mathcal{A}_0^{(\phi)}}{\partial\rho'}+2\mathcal{A}_0^{(\phi)}\frac{\partial W_0^{(\phi)}}{\partial\rho'}\right)+2\mathcal{A}_0^{(\phi)}W_0^{(\phi)}\right]d\rho dz$$
$$-\int_{S_{12}}\frac{1}{\mu_1}\overline{W}_0\times\left(\nabla\times\overline{A}_0\right)\cdot\hat{n}_1 dS+\int\int_{\Omega}\sigma_1 W_0^{(\phi)}\frac{\partial\mathcal{A}_0^{(\phi)}}{\partial t}\rho^2 d\rho dz=0 \qquad (2.29)$$

In Equation 2.29, the $d\phi$ integration has been carried out, yielding 2π terms that have been dropped. The interior volume integration domain has become a surface (cross-section of V_1) domain in the (ρ, z) plane, and is defined as Ω_1. The surface has become a contour at the intersection of S and the (ρ, z) plane, defined as Γ_{12}. Note that $dV = d\rho\rho d\phi dz$ and $dS = \rho d\phi ds$, where s is the tangential variable along Γ_{12}. The ∇ operators now only contain ρ and z components. The surface integral in Equation 2.29 has been left in vector form to implement the boundary conditions.

The case of uniform transverse excitation (i.e. $\overline{H}^{PR} = \hat{x}H^{PR}$) is represented with $p = 1$. For that case, all three vector components of the magnetic vector potential must be kept. The number of terms in the volume integration increases by more than a factor of ten, and will not be included here. Incident field modes above $p = 1$ may be included to represent other incident field cases, such as a linear transverse field (i.e. $\overline{H} = \hat{x}x$). In such cases, each term in the volume and surface integrations is zero for $p \neq q$ (due to the orthogonality of the modes), and hence only the p terms are required.

Finite Element Method

The FEM approximates the unknown function as a set of polynomial basis functions, each of which has local support within a finite element. In this work, the derivations will be limited a nodal FEM with first order interpolative polynomials over triangular elements. The Silvester universal matrices will be used [7], and thus extension to

higher orders is straightforward.

The interior region, Ω, is discretized into a triangular mesh using a Delaunay algorithm. The mesh contains the set of $n = \{1, 2, \ldots N\}$ nodes, located at coordinates $\{(\rho_1, z_1), (\rho_2, z_2), \ldots (\rho_N, z_N)\}$. The magnetic vector potential and weighting function are represented over each triangle by scalar basis functions:

$$\overline{A}_p = \sum_{n=1}^{N} \left[\hat{\rho} A_{np}^{(\rho)} \alpha_n^{(\rho)} + \hat{\phi} A_{np}^{(\phi)} \alpha_n^{(\phi)} + \hat{z} A_{np}^{(z)} \alpha_n^{(z)} \right] \tag{2.30}$$

$$\overline{W}_p = \sum_{m=1}^{N} \left[\hat{\rho} \alpha_m^{(\rho)} + \hat{\phi} \alpha_m^{(\phi)} + \hat{z} \alpha_m^{(z)} \right] \tag{2.31}$$

where, for example, $\alpha_n^{(\rho)}$ represents the basis function at the nth node in the ρ direction. The magnetic vector potential has now been expanded as a summation over modes, basis functions, and vector components, hence $A_{np}^{(\rho)}$ is the unknown ρ coefficient for the pth mode at node n. To demonstrate the FEM implementation, consider the axial case where $p = 0$, for which $\overline{\mathcal{A}}_0^{(\phi)}$ is the only interior unknown vector (over the mesh nodes), Equation 2.29 over each finite element can then be written in matrix form as

$$(\overline{\overline{S}}_{AA}^{(1)} + \overline{\overline{S}}_{AA}^{(2)} + \overline{\overline{S}}_{AA}^{(3)}) \, \overline{\mathcal{A}}_0^{(\phi)} + \overline{\overline{F}}_{AA} \, \frac{\partial \overline{\mathcal{A}}_0^{(\phi)}}{\partial t} + \overline{\overline{S}}_{\psi A} \, \overline{A}_0 = 0 \tag{2.32}$$

where $\overline{\mathcal{A}}_0^{(\phi)} = [\mathcal{A}_{10}^{(\phi)} \mathcal{A}_{20}^{(\phi)} .. \mathcal{A}_{N0}^{(\phi)}]'$ and

$$\overline{\overline{S}}_{AA,mn}^{(1)} = \frac{1}{\mu_1} \int\int \rho^2 \left(\frac{\partial \alpha_m^{(\phi)}}{\partial \rho} \frac{\partial \alpha_n^{(\phi)}}{\partial \rho} + \frac{\partial \alpha_m^{(\phi)}}{\partial z} \frac{\partial \alpha_n^{(\phi)}}{\partial z} \right) d\rho dz \tag{2.33}$$

$$\overline{\overline{S}}_{AA,mn}^{(2)} = \frac{1}{\mu_1} \int\int \rho \left(2\alpha_n^{(\phi)} \frac{\partial \alpha_m^{(\phi)}}{\partial \rho} + \alpha_m^{(\phi)} \frac{\partial \alpha_n^{(\phi)}}{\partial \rho} \right) d\rho dz \tag{2.34}$$

$$\overline{\overline{S}}_{AA,mn}^{(3)} = \frac{2}{\mu_1} \int\int \alpha_m^{(\phi)} \alpha_n^{(\phi)} d\rho dz \tag{2.35}$$

$$\overline{\overline{F}}_{AA,mn} = \sigma_1 \int\int \rho^2 \alpha_m^{(\phi)} \alpha_n^{(\phi)} d\rho dz \tag{2.36}$$

and $\overline{\overline{S}}_{\psi A}$ is the integral over the surface (now contour) of the object. The choice of AA and ψA subscripts notes which which variables the matrices operate on and in which equation they are obtained. For example, the ψA subscript means that the matrix will be operating on the ψ variable but is contained in the equation for A. In Equation 2.32, $\overline{\overline{S}}_{\psi A}$ currently operates on A, and will be related to ψ in Section 2.2.3. The implementation of the FEM will be specifically outlined for Equations 2.33-2.36, and the higher order p cases are easily generalized from these integrals. It is next necessary to choose a suitable set of basis and weighting functions α_i^j to substitute into Equation 2.32.

Simplex Coordinates

For the following sections dealing with the FEM, the subscripts and superscripts will be dropped for generality. In two dimensional space the triangle is known as a simplex shape, which is the minimum possible nontrivial geometric figure. A triangle with indices a, b, and c is defined as triangle $1-2-3$. The area of a triangular simplex, whose coordinates are $(\rho_1, z_1), (\rho_2, z_2)$, and (ρ_3, z_3), is

$$R = \frac{1}{2}\begin{vmatrix} 1 & \rho_1 & z_1 \\ 1 & \rho_2 & z_2 \\ 1 & \rho_3 & z_3 \end{vmatrix} \tag{2.37}$$

Within each triangle can be defined three simplex coordinates, one associated with each vertex. Each simplex coordinate, ζ, is defined to be equal to one at its corresponding vertex and decreases to zero at the opposite edge. The value of each ζ can be expressed in terms of the ratio of two triangles; for example ζ_1 is the ratio of the area of the triangle $\zeta_1 - 2 - 3$ over the area of triangle $1-2-3$. This can be understood given that the ratio of triangle areas is the same as the ratio of triangle

heights. Hence, the simplex coordinate ζ_1 can be written as:

$$\zeta_1 = \frac{\begin{vmatrix} 1 & \rho & z \\ 1 & \rho_2 & z_2 \\ 1 & \rho_3 & z_3 \end{vmatrix}}{\begin{vmatrix} 1 & \rho_1 & z_1 \\ 1 & \rho_2 & z_2 \\ 1 & \rho_3 & z_3 \end{vmatrix}} \tag{2.38}$$

and all the simplex coordinates are:

$$\begin{bmatrix} \zeta_1 \\ \zeta_2 \\ \zeta_3 \end{bmatrix} = \frac{1}{2R} \begin{bmatrix} \rho_2 z_3 - \rho_3 z_2 & z_2 - z_3 & \rho_3 - \rho_2 \\ \rho_3 z_1 - \rho_1 z_3 & z_3 - z_1 & \rho_1 - \rho_3 \\ \rho_1 z_2 - \rho_2 z_1 & z_1 - z_2 & \rho_2 - \rho_1 \end{bmatrix} \begin{bmatrix} 1 \\ \rho \\ z \end{bmatrix} \tag{2.39}$$

The simplex coordinate system is advantageous in that it is strictly local, and as such any formulations can be derived independent of triangle shape.

Basis Functions

The simplex coordinates are the first order basis functions over the triangular finite elements. Higher order basis functions can also be derived in terms of the simplex coordinates using a set of Lagrange polynomials. A set of P^{th} order polynomials $L_u(P, \zeta)$ is defined by

$$L_u(P, \zeta) = \frac{1}{u!} \prod_{k=0}^{u-1} (P\zeta - k), \qquad u > 0 \tag{2.40}$$

$$L_0(P, \zeta) = 1 \tag{2.41}$$

The P^{th} order basis functions over the triangle are

$$\alpha_{ijk}(\zeta_1, \zeta_2, \zeta_3) = L_i(P, \zeta_1) L_j(P, \zeta_2) L_k(P, \zeta_3), \qquad i + j + k = P \tag{2.42}$$

Each triangle of order P contains $X = (P+1)(P+2)/2$ basis functions, which equal unity at point ijk and zero at all other points. Various numbering schemes may be chosen over the triangle [7]. The first order basis functions α_{100}, α_{010}, and α_{001} are simply ζ_1, ζ_2, and ζ_3, respectively.

Universal Matrices

The surface integrals in Equation 2.32 may now be restated in terms of simplex coordinates and solved over a single arbitrary triangle. The $\overline{\overline{S}}$ matrices in the following are *local* element matrices, defined with an 'e' superscript. The previously defined matrices will be referred to as the *global* matrices. $S^{(3)e}_{mn}$ is the product of the basis and weighting functions, and can be expressed in simplex coordinates as

$$S^{(3)e}_{AA,mn} = \frac{2R}{\mu_1} \int\int \alpha_n \alpha_m \frac{d\rho dz}{R} \tag{2.43}$$

where the integration is carried out over the triangle area. Using the identity

$$\int\int \zeta_1^i \zeta_2^j \zeta_3^k \frac{dS}{R} = \frac{i!j!k!2!}{(i+j+k+2)!} \tag{2.44}$$

the integral can be expressed as a constant matrix, multiplied by the area of the triangle. Hence the element matrix is simply

$$\overline{\overline{S}}^{(3)e}_{AA} = \frac{2R}{\mu_1} \overline{\overline{T}} \tag{2.45}$$

The matrix $\overline{\overline{T}}$ is known as a type of universal matrix, named as such because it is the solution to the integration of simplex polynomials over any triangular element. $\overline{\overline{T}}$ for

a first order element is simply:

$$\overline{\overline{T}} = \frac{1}{12}\begin{bmatrix} 2 & 1 & 1 \\ 1 & 2 & 1 \\ 1 & 1 & 2 \end{bmatrix} \tag{2.46}$$

Matrices for higher order polynomials are easily derived. $\overline{\overline{T}}$ is also the simplest universal matrix, and alone is insufficient to characterize any of the other integrands in Equation 2.29, which contain derivatives and powers of ρ.

Universal Matrices: Differentiation Operators

Differential operators may also be expressed as universal matrices. The derivative of any P^{th} order basis function polynomial can be represented in terms of $P-1$ order polynomials. However, for simplicity it is easier to represent the derivative as a polynomial of the same order as the original function. The derivative of $\mathcal{A}$ with respect to ρ can be written as

$$\frac{\partial \mathcal{A}}{\partial \rho} = \sum_{n=1}^{N} \frac{\partial \alpha_n}{\partial \rho} \mathcal{A}_n = \sum_{n=1}^{N} \left(\sum_{i=1}^{3} \frac{\partial \alpha_n}{\partial \zeta_i} \frac{\partial \zeta_i}{\partial \rho} \right) \mathcal{A}_n \tag{2.47}$$

From Equation 2.39 it can be shown that

$$\frac{\partial \zeta_i}{\partial \rho} = \frac{z_{i+1} - z_{i-1}}{2R} = \frac{b_i}{2R} \tag{2.48}$$

and

$$\frac{\partial \zeta_i}{\partial z} = \frac{\rho_{i-1} - \rho_{i+1}}{2R} = \frac{c_i}{2R} \tag{2.49}$$

A differentiation matrix may now be derived to express the derivatives of the simplex

coordinates in terms of the basis polynomials, such that

$$\frac{\partial \alpha_n}{\partial \zeta_i} = \sum_k D_{nk}^{(i)} \alpha_k \tag{2.50}$$

Equation 2.50 may be solved for $D_{nk}^{(i)}$, the values of the differentiation matrix $\overline{\overline{D}}$. This is done by solving Equation 2.50 at each node n on the triangle for each basis function α_k, taking into account that all basis functions vanish at that node except α_n. Hence, the values of $\overline{\overline{D}}^{(i)}$ are found through differentiation of α_n evaluated at node k:

$$D_{nk}^{(i)} = \left. \frac{\partial \alpha_n}{\partial \zeta_i} \right|_k \tag{2.51}$$

Combining the above steps, a derivative may be expressed as

$$\frac{\partial \mathcal{A}}{\partial \rho} = \sum_{n=1}^{N} \left(\sum_{i=1}^{3} \frac{b_i}{2R} \sum_k D_{nk}^{(i)} \alpha_k \right) \mathcal{A}_n \tag{2.52}$$

or, in matrix form relating the nodal values of $\mathcal{A}$ to the nodal values of the derivative of $\mathcal{A}$ ($\overline{\mathcal{A}}_{\partial\rho}$)

$$\overline{\mathcal{A}}_{\partial\rho} = \sum_{i=1}^{3} \left(\frac{b_i}{2R} \overline{\overline{D}}^{(i)T} \right) \overline{\mathcal{A}} \tag{2.53}$$

Once these matrices are obtained, differentiation of basis function polynomials over the triangular elements becomes a simple sum of matrix multiplications.

Universal Matrices: Embedding Operators

The integrals of Equation 2.29 also contain powers of ρ, which cannot be handled with the $\overline{\overline{T}}$ and $\overline{\overline{D}}$ matrices alone. Hence a third universal matrix, $\overline{\overline{C}}$, known as an embedding operator, is introduced.

First, ρ may be written as a linear interpolate of it's three nodal values,

$$\rho = \sum_{i=1}^{3} \rho_i \zeta_i \tag{2.54}$$

$$\rho^2 = \sum_{i=1}^{3} \rho_i \sum_{j=1}^{3} \rho_j (\zeta_i \zeta_j) \tag{2.55}$$

and, to maintain symmetry when only ρ is present, it is necessary to use

$$\rho_i = \rho_i \cdot 1 = \rho_i \sum_{j=1}^{3} \zeta_j \tag{2.56}$$

Integrals with ρ and $\mathcal{A}$ now take the form of

$$\int\int (\zeta_i \alpha_m)(\zeta_j \alpha_n) d\rho dz \tag{2.57}$$

which contain polynomials of a higher order than the basis functions. To deal with these integrals, it is desirable to express each term in the integrand of Equation 2.57 as a higher order polynomial, so that previously derived universal matrices may then be applied. The process of transforming a polynomial of order P to an order $P+1$ representation is referred to as embedding. For example, a polynomial basis function of order P can be expressed in terms of a higher polynomial as follows

$$\alpha_i^{(P)} = 1 \cdot \alpha_i^{(P)} = \sum_{j=1}^{3} \zeta_j \alpha_i^{(P)} = \sum_{j=1}^{3} \sum_{k} C_{ij}^{(j)} \alpha_k^{(P+1)} \tag{2.58}$$

Note that the superscripts of the polynomials α refer to their order. The coefficients $C_{ij}^{(j)}$ can be found in the same manner in which the coefficients of the differentiation matrices were obtained:

$$C_{ik}^{(j)} = \zeta_j \alpha_i^{(P)} \Big|_{k^{(P+1)}} \tag{2.59}$$

The resulting matrix is referred to as the embedding matrix $\overline{\overline{C}}$, with $X^{(P)}$ rows and X^{P+1} columns. Substituting Equation 2.58 into Equation 2.57 results in:

$$\int\int(\zeta_i\alpha_m)(\zeta_j\alpha_n)d\rho dz = \sum_u\sum_v C_{mu}^{(i)}C_{nv}^{(j)}\int\int\alpha_u^{(P+1)}\alpha_v^{(P+1)}d\rho dz = Y_{mn}^{(ij)} \tag{2.60}$$

The new integral has the form of $\overline{\overline{T}}$ for order $P+1$, and the equation can be written in matrix form as

$$\overline{\overline{Y}}^{(ij)} = \overline{\overline{C}}^{(i)}\overline{\overline{T}}^{(P+1)}\overline{\overline{C}}^{(j)T} \tag{2.61}$$

The three universal matrices $\overline{\overline{T}}$, $\overline{\overline{D}}$, and $\overline{\overline{C}}$ are sufficient to form an analytical solution of the integrations in Equation 2.29 over a single triangular element.

Implementation

$S_{mn}^{(1)e}$ can now be written as

$$S_{mn}^{(1)e} = \frac{1}{\mu_1}\int\int\rho^2\left(\frac{\partial\alpha_m}{\partial\rho}\frac{\partial\alpha_n}{\partial\rho}+\frac{\partial\alpha_m}{\partial z}\frac{\partial\alpha_n}{\partial z}\right)d\rho dz$$

$$= \frac{1}{\mu_1}\sum_{i=1}^{3}\rho_i\sum_{j=1}^{3}\rho_j\int\int\zeta_i\zeta_j\left(\frac{\partial\alpha_m}{\partial\rho}\frac{\partial\alpha_n}{\partial\rho}+\frac{\partial\alpha_m}{\partial z}\frac{\partial\alpha_n}{\partial z}\right)d\rho dz$$

$$= \frac{1}{\mu_1}\sum_{i=1}^{3}\rho_i\sum_{j=1}^{3}\rho_j\int\int\zeta_i\zeta_j\left(\sum_{k=1}^{3}\frac{\partial\alpha_m}{\partial\zeta_k}\frac{\partial\zeta_k}{\partial\rho}\sum_{l=1}^{3}\frac{\partial\alpha_n}{\partial\zeta_l}\frac{\partial\zeta_l}{\partial\rho}+\sum_{k=1}^{3}\frac{\partial\alpha_m}{\partial\zeta_k}\frac{\partial\zeta_k}{\partial z}\sum_{l=1}^{3}\frac{\partial\alpha_n}{\partial\zeta_l}\frac{\partial\zeta_l}{\partial z}\right)d\rho dz$$

$$= \frac{1}{\mu_1}\frac{1}{4R^2}\sum_{i=1}^{3}\rho_i\sum_{j=1}^{3}\rho_j\sum_{k=1}^{3}\sum_{l=1}^{3}(b_kb_l+c_kc_l)\int\int\zeta_i\frac{\partial\alpha_m}{\partial\zeta_k}\zeta_j\frac{\partial\alpha_n}{\partial\zeta_l}d\rho dz \tag{2.62}$$

Using the universal differentiation matrix, Equation 2.62 can be written as

$$S_{mn}^{(1)e} = \frac{1}{\mu_1}\frac{1}{4R^2}\sum_{i=1}^{3}\rho_i\sum_{j=1}^{3}\rho_j\sum_{k=1}^{3}\sum_{l=1}^{3}(b_kb_l+c_kc_l)\sum_u\sum_v D_{mv}^{(k)}D_{nu}^{(l)}\int\int\zeta_i\alpha_m\zeta_j\alpha_n d\rho dz \tag{2.63}$$

The integral in Equation 2.63 can be recognized as that of Equation 2.60, and hence

can be replaced by its corresponding universal matrices as follows

$$\begin{aligned}\overline{\overline{S}}^{(1)e} &= \frac{1}{\mu_1}\frac{1}{4R}\sum_{i=1}^{3}\rho_i\sum_{j=1}^{3}\rho_j\sum_{k=1}^{3}\sum_{l=1}^{3}(b_k b_l + c_k c_l)\sum_{u}\sum_{v} D_{mv}^{(k)} Y_{vu}^{(ij)} D_{nu}^{(l)} \\ &= \frac{1}{\mu_1}\frac{1}{4R}\sum_{i=1}^{3}\rho_i\sum_{j=1}^{3}\rho_j\sum_{k=1}^{3}\sum_{l=1}^{3}(b_k b_l + c_k c_l)\,\overline{\overline{D}}^{(k)}\overline{\overline{C}}^{(i)}\overline{\overline{T}}^{(N+1)}\overline{\overline{C}}^{(j)T}\overline{\overline{D}}^{(l)T} \end{aligned} \tag{2.64}$$

The double summation over k and l in Equation 2.62 can be reduced to a single summation by using the identities

$$b_i b_j + c_i c_j = -2R\cot\theta_k \tag{2.65}$$

$$b_i^2 + c_i^2 = 2R(\cot\theta_j + \cot\theta_k) \tag{2.66}$$

where i, j, k are the vertices of the triangle, θ_k is the angle between the sides of the triangle at node k, and R is the area of the triangle defined in Equation 2.37. Substituting the trigonometric identities into Equation 2.62 and manipulating results in

$$S_{mn}^{(1)e} = \frac{1}{\mu_1}\sum_{i=1}^{3}\rho_i\sum_{j=1}^{3}\rho_j\sum_{k=1}^{3}\cot\theta_k\int\int\zeta_i\zeta_j\left(\frac{\partial\alpha_m}{\partial\zeta_{k+1}} - \frac{\partial\alpha_m}{\partial\zeta_{k-1}}\right)\left(\frac{\partial\alpha_n}{\partial\zeta_{l+1}} - \frac{\partial\alpha_n}{\partial\zeta_{l-1}}\right)d\rho dz \tag{2.67}$$

Which in matrix form is

$$\overline{\overline{S}}^{(1)e} = \frac{1}{\mu_1}\sum_{i=1}^{3}\rho_i\sum_{j=1}^{3}\rho_j\sum_{k=1}^{3}\cot\theta_k\overline{\overline{Q}}^{(ijk)} \tag{2.68}$$

where

$$Q^{(ijk)} = \frac{1}{2}\left(\overline{\overline{D}}^{(k+1)} - \overline{\overline{D}}^{(k-1)}\right)\overline{\overline{C}}^{(i)}\overline{\overline{T}}^{(N+1)}\overline{\overline{C}}^{(j)T}\left(\overline{\overline{D}}^{(k+1)} - \overline{\overline{D}}^{(k-1)}\right) \tag{2.69}$$

$S_{mn}^{(2)e}$ is written as

$$\begin{aligned} S_{mn}^{(2)e} &= \frac{1}{\mu_1}\int\int \rho \left(2\alpha_n \frac{\partial \alpha_m}{\partial \rho} + \alpha_m \frac{\partial \alpha_n}{\partial \rho}\right) d\rho dz \\ &= \frac{1}{\mu_1}\sum_{i=1}^{3}\rho_i \sum_{j=1}^{3}\int\int \zeta_i\zeta_j \left(2\alpha_n \frac{\partial}{\partial \rho}\alpha_n + \alpha_m \frac{\partial \alpha_n}{\partial \rho}\right) d\rho dz \\ &= \frac{1}{\mu_1}\sum_{i=1}^{3}\rho_i \sum_{j=1}^{3}\int\int \zeta_i\zeta_j \left(2\sum_{k=1}^{3}\alpha_n \frac{\partial \alpha_m}{\partial \zeta_k} + \sum_{k=1}^{3}\alpha_n \frac{\partial \alpha_n}{\partial \zeta_k}\right) d\rho dz \\ &= \frac{1}{\mu_1}\frac{1}{2R}\sum_{i=1}^{3}\rho_i \sum_{j=1}^{3}\sum_{k=1}^{3} b_k \sum_{l=1}^{3}\left[2D_{ml}^{(k)}\left(\int\int \zeta_i\alpha_l\zeta_j\alpha_n d\rho dz\right)\right. \\ &+ \left.\left(\int\int \zeta_i\alpha_m\zeta_j\alpha_l d\rho dz\right) D_{nl}^{(k)}\right] \end{aligned} \tag{2.70}$$

which in matrix form is

$$\overline{\overline{S}}^{(2)e} = \frac{1}{2\mu_1}\sum_{i=1}^{3}\rho_i \sum_{j=1}^{3}\sum_{k=1}^{3} b_k \left(2\overline{\overline{D}}^{(k)}\overline{\overline{C}}^{(i)}\overline{\overline{T}}^{(P+1)}\overline{\overline{C}}^{(j)T} + \overline{\overline{C}}^{(i)}\overline{\overline{T}}^{(P+1)}\overline{\overline{C}}^{(j)T}\overline{\overline{D}}^{(k)T}\right) \tag{2.71}$$

The final surface integral term in Equation 2.32 is

$$\overline{\overline{F}} = \sigma_1 R \sum_{i=1}^{3}\rho_i \sum_{j=1}^{3}\rho_j \overline{\overline{C}}^{(i)}\overline{\overline{T}}^{(P+1)}\overline{\overline{C}}^{(j)T} \tag{2.72}$$

The element matrices are evaluated for each triangle in the FE mesh and are used to construct the global matrices. The local coordinate of each term in the element matrix is mapped to its corresponding global coordinate and term in the global matrix.

FEM Equation, Axial Case

If we define $\overline{\overline{S}}_{AA} = \overline{\overline{S}}_{AA}^{(1)} + \overline{\overline{S}}_{AA}^{(2)} + \overline{\overline{S}}_{AA}^{(3)}$, the FEM equation can be written as

$$\overline{\overline{S}}_{AA}\ \overline{\mathcal{A}}_0^{(\phi)} + \overline{\overline{F}}_{AA}\ \frac{\partial}{\partial t}\overline{\mathcal{A}}_0^{(\phi)} + \overline{\overline{S}}_{\psi A}\ \overline{A}_0^{(\phi)} = 0 \tag{2.73}$$

Section 2.2.3 will address the derivation of $\overline{\overline{S}}_{\psi A}$, resulting in an equation in terms of $\overline{A}_0^{(\phi)}$ and ψ. The time derivative will be addressed in Section 2.2.4.

FEM Equation, Transverse Case

For the transverse case, all the vector components of $\overline{A}$ must be considered. The unknown vector for $p = 1$ becomes $\overline{A}_1 = [\overline{A}_1^{(\rho)} \overline{A}_1^{(\phi)} \overline{A}_1^{(z)}]'$. As mentioned previously, Equation 2.24 contains many more terms than for the axial case, and the derivation is not included here. However, the analytical forms of Equations 2.33 - 2.36 may still be used, along with similar variations, for the majority of terms that are nonsingular. Singular terms are dealt with using numerical integration, with the entire mesh moved 1 μm off the axis of symmetry. For this case, we define $\overline{\overline{S}}_{AA} = \overline{\overline{S}}_{AA}^{(1)} + \overline{\overline{S}}_{AA}^{(2)} + \cdots + \overline{\overline{S}}_{AA}^{(N)}$, and the finite element equation is

$$\overline{\overline{S}}_{AA}\ \overline{A}_1 + \overline{\overline{F}}_{AA}\ \frac{\partial}{\partial t}\overline{A}_1 + \overline{\overline{S}}_{\psi A}\ \overline{A}_1 = 0 \tag{2.74}$$

The boundary condition $\hat{n} \cdot \overline{A} = 0$ must also be enforced as an essential boundary condition in Equation 2.74. This can be done by redefining the $\overline{A}_1$ on the boundary in terms of a rotated coordinate system,

$$\overline{A}_1^{\mathcal{R}} = \begin{bmatrix} \overline{A}_1^{(n)} \\ \overline{A}_1^{(\phi)} \\ \overline{A}_1^{(s)} \end{bmatrix} \tag{2.75}$$

where $\hat{n}$ and $\hat{s}$ are the normal and tangential vectors to the surface contour in the (ρ, z) plane, respectively, and the $\mathcal{R}$ superscript refers to the rotated unknowns. This is accomplished with the use of rotational matrices [4]. The rotation can be performed on a global level, but will be demonstrated here for a single element e. Each element matrix is 9×9, containing interactions between the three vector components at each of the three nodes. The relationship of the cylindrical and rotated coordinate system

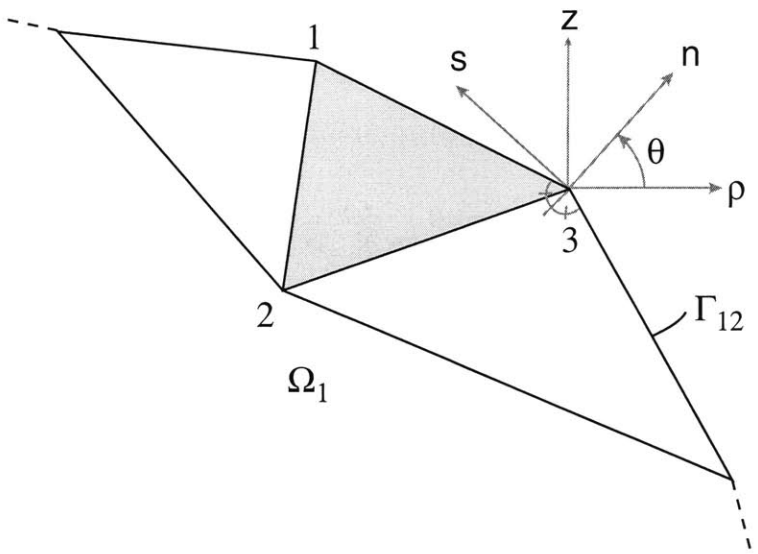

Figure 2-3: Rotation of cylindrical coordinates to tangential and normal coordinates for the surface unknowns. The essential boundary condition of $\hat{n} \cdot \overline{A} = 0$ can then be easily implemented.

is shown in Figure 2-3. For the matrix equation with a given right hand side $\overline{Z}$,

$$\overline{\overline{S}}^{e}\ \overline{A}_1 = \overline{Z} \tag{2.76}$$

the variables are transformed to the rotated coordinate system using a rotation matrix $\overline{\overline{\mathcal{R}}}$

$$\overline{A}_1 = \overline{\overline{\mathcal{R}}}\ \overline{A}_1^{\mathcal{R}} \tag{2.77}$$

$$\overline{Z} = \overline{\overline{\mathcal{R}}}\ \overline{Z}^{\mathcal{R}} \tag{2.78}$$

Substituting Equations 2.77 and 2.78 into Equation 2.76 yields

$$\overline{\overline{S}}^{e}\ \overline{\overline{\mathcal{R}}}\ \overline{A}_1^{\mathcal{R}} = \overline{\overline{\mathcal{R}}}\ \overline{Z}^{\mathcal{R}} \tag{2.79}$$

Using the identity $\overline{\overline{\mathcal{R}}}^{T}\overline{\overline{\mathcal{R}}} = \overline{\overline{I}}$, premultiply Equation 2.79 by $\overline{\overline{\mathcal{R}}}^{T}$ to get

$$\overline{\overline{S}}^{e,\mathcal{R}}\ \overline{A}_1^{\mathcal{R}} = \overline{Z}^{\mathcal{R}} \tag{2.80}$$

where

$$\overline{\overline{S}}^{e,\mathcal{R}} = \overline{\overline{\mathcal{R}}}^{T}\ \overline{\overline{S}}^{e}\ \overline{\overline{\mathcal{R}}} \tag{2.81}$$

$$\overline{Z}^{\mathcal{R}} = \overline{\overline{\mathcal{R}}}^{T}\ \overline{Z} \tag{2.82}$$

For example, given the element shown in Figure 2-3, and organizing the unknown A_1 by node, the rotation is simply

$$\overline{A}_1 = \overline{\overline{\mathcal{R}}}\ \overline{A}_1^{\mathcal{R}} = \begin{bmatrix} \cos\theta & 0 & -\sin\theta & 0 & 0 & 0 & 0 & 0 & 0 \\ 0 & 1 & 0 & 0 & 0 & 0 & 0 & 0 & 0 \\ \sin\theta & 0 & \cos\theta & 0 & 0 & 0 & 0 & 0 & 0 \\ 0 & 0 & 0 & 1 & 0 & 0 & 0 & 0 & 0 \\ 0 & 0 & 0 & 0 & 1 & 0 & 0 & 0 & 0 \\ 0 & 0 & 0 & 0 & 0 & 1 & 0 & 0 & 0 \\ 0 & 0 & 0 & 0 & 0 & 0 & \cos\theta & 0 & -\sin\theta \\ 0 & 0 & 0 & 0 & 0 & 0 & 0 & 1 & 0 \\ 0 & 0 & 0 & 0 & 0 & 0 & \sin\theta & 0 & \cos\theta \end{bmatrix} \begin{bmatrix} A_{11}^{(n)} \\ A_{11}^{(\phi)} \\ A_{11}^{(s)} \\ A_{21}^{(\rho)} \\ A_{21}^{(\phi)} \\ A_{21}^{(z)} \\ A_{31}^{(n)} \\ A_{31}^{(\phi)} \\ A_{31}^{(s)} \end{bmatrix} \tag{2.83}$$

Using a global coordinate rotation, the FEM equation for the transverse case can be written as:

$$\overline{\overline{S}}_{AA}^{\mathcal{R}}\ \overline{A}_1^{\mathcal{R}} + \overline{\overline{F}}_{AA}^{\mathcal{R}}\ \frac{\partial}{\partial t}\overline{A}_1^{\mathcal{R}} + \overline{\overline{S}}_{\psi A}^{\mathcal{R}}\ \overline{A}_1^{\mathcal{R}} = 0 \tag{2.84}$$

2.2.2 Exterior Problem

The interior problem has been implemented in the FEM, and must be coupled with the exterior governing equation (2.11) through the boundary conditions on S_{12}. Although Equation 2.11 may also be solved with an FEM, such an approach is not optimal for the unbounded exterior region. Instead, an integral equation approach is used.

Formulation

The exterior region is governed by the Laplace equation for the scalar magnetic potential ψ. Starting with Green's theorem,

$$\begin{aligned}&\int\int_{V_2} d\overline{r}' \ \left\{\psi(\overline{r}')\nabla^2 g\left(\overline{r},\overline{r}'\right) - g\left(\overline{r},\overline{r}'\right)\nabla^2\psi(\overline{r}')\right\}\\ &= \int_{S_{12}+S_\infty} d\overline{r}' \ \left\{\psi(\overline{r}')\frac{\partial g\left(\overline{r},\overline{r}'\right)}{\partial n_2'} - g\left(\overline{r},\overline{r}'\right)\frac{\partial\psi(\overline{r}')}{\partial n_2'}\right\}\end{aligned} \tag{2.85}$$

where $\psi(\overline{r}') = \psi^{PR}\left(\overline{r}'\right) + \psi^{S}\left(\overline{r}'\right)$, the sum of the primary and secondary potentials. The volume V_2 is the exterior region, bounded at the target by S_{12} and at infinity by S_∞. The normal coordinate n_2 is directed out of V_2 (see Figure 2-2). The field $\psi(\overline{r})$ follows the Laplace equation:

$$\nabla^2\psi = 0 \tag{2.86}$$

The Green's function obeys

$$\nabla^2 g\left(\overline{r},\overline{r}'\right) = -\delta\left(\overline{r}-\overline{r}'\right) \tag{2.87}$$

and for free space is

$$g(\overline{r},\overline{r}') = \frac{1}{4\pi\left|\overline{r}-\overline{r}'\right|} \tag{2.88}$$

Substituting Equations 2.86 and 2.87 into the left side of Equation 2.85 gives:

$$\int\int_{V_2} d\overline{r}\left[\psi(\overline{r}')\nabla^2 g\left(\overline{r},\overline{r}'\right) - g\left(\overline{r},\overline{r}'\right)\nabla^2\psi(\overline{r}')\right] = \begin{cases} -\psi(\overline{r}) & \overline{r}\in V_2 \\ 0 & \overline{r}\notin V_2 \end{cases} \tag{2.89}$$

The surface integral at S_∞ gives the primary field. Taking $\overline{r}$ to the surface requires the removal of singularity of the normal derivative of the Green's function. For a smooth surface, this value is $\pm 1/2$ depending on whether the surface is approached from inside or outside V_2. The difference in sign from the singularity in the Green's

function therefore accounts for the two possible right hand sides of Equation 2.89. When the surface is not smooth, such as on an FE mesh, different values from 1/2 may be obtained, so a general $C(\overline{r})$ is used in the formulation.

$$C(\overline{r})\psi(\overline{r}) + \int_{S_{12}} \left(\psi(\overline{r}') \frac{\partial g(\overline{r}, \overline{r}')}{\partial n'} - g(\overline{r}, \overline{r}') \frac{\partial \psi(\overline{r}')}{\partial n'} \right) dS' = \psi^{PR}(\overline{r}) \tag{2.90}$$

Again, given the axisymmetry of the object, Equation 2.90 only needs to be solved on the (ρ, z) plane. However, both the sources and the Green's function are dependent on ϕ, so that dependence must be dealt with before moving to a two dimensional problem [58].

Having chosen the cosine dependence for the scalar potential (Equation 2.25), the same azimuthal decompositions must be performed for all the terms in Equation 2.90. We can write

$$\psi(\rho, \phi, z) = \sum_{p=0}^{\infty} \psi_p(\rho, z) \cos(p\phi) \tag{2.91}$$

$$\psi^{PR}(\rho, \phi, z) = \sum_{p=0}^{\infty} \psi_p^{PR}(\rho, z) \cos(p\phi) \tag{2.92}$$

$$\psi(\rho', \phi', z') = \sum_{q=0}^{\infty} \psi_q(\rho', z') \cos(q\phi') \tag{2.93}$$

$$g(\rho, \phi, z; \rho', \phi', z') = \sum_{p=0}^{\infty} g_p^*(\rho, z; \rho', \phi', z') \cos(p\phi) \tag{2.94}$$

Substituting Equations 2.91-2.94 into Equation 2.90 results in

$$\sum_{p=0}^{\infty} C(\overline{r})\psi_p(\rho, z) + \int_{S_{12}} \left(\sum_{q=0}^{\infty} \psi_q(\rho', z') \cos(q\phi') \sum_{p=0}^{\infty} \frac{\partial g_p^*(\rho, z; \rho', \phi', z')}{\partial n'} \right.$$
$$\left. - \sum_{p=0}^{\infty} g_p^*(\rho, z; \rho', \phi', z') \sum_{q=0}^{\infty} \frac{\partial \psi_q(\rho', z')}{\partial n'} \cos(q\phi') \right) dS' = \sum_{p=0}^{\infty} \psi_p^{PR}(\rho, z) \tag{2.95}$$

where the linear independence of the $\cos p\phi$ terms has been used. The form of Equa-

tion 2.95 can be rewritten as

$$\sum_{p=0}^{\infty} C(\overline{r})\psi_p(\rho,z) + \int_{S_{12}} \left(\sum_{p=0}^{\infty}\sum_{q=0}^{\infty} \left[\psi_q(\rho',z') \frac{\partial \tilde{g}_{pq}(\rho,z;\rho',z')}{\partial n'} - \tilde{g}_{pq}(\rho,z;\rho',z') \frac{\partial \psi_q(\rho',z')}{\partial n'} \right] \right) dS' = \sum_{p=0}^{\infty} \psi_p^{PR}(\rho,z) \quad (2.96)$$

where

$$\tilde{g}_{pq}(\rho,z;\rho',z') = \int_{-\pi}^{\pi} g_p^*(\rho,z;\rho',\phi',z') \cos(q\phi')\, d\phi' \quad (2.97)$$

$$g_p^*(\rho,z;\rho',\phi',z') = \frac{1}{\pi}\int_{-\pi}^{\pi} g(\rho,\phi,z;\rho',\phi',z') \cos(p\phi)\, d\phi \quad (2.98)$$

Careful examination of Equations 2.97 and 2.98 reveals that $\tilde{g}_{pq}(\rho,z;\rho',z') = 0$ for $p \neq q$. Hence, for each mode p evaluated separately (and dropping the second subscript of the Green's function), the final boundary integral equation becomes

$$C(\overline{r})\psi_p(\overline{r}) + \int_{\Gamma} \left(\left[\psi_p(\overline{r}') \frac{\partial \tilde{g}_p(\overline{r},\overline{r}')}{\partial n'} - \tilde{g}_p(\overline{r},\overline{r}') \frac{\partial \psi_p(r')}{\partial n'} \right] \right) \rho' d\Gamma' = \psi_p^{PR}(\overline{r}) \quad (2.99)$$

evaluated over the contour Γ, the intersection of S_{12} and the (ρ, z) plane. The Green's function of Equation 2.97 is dependent only on ρ and z, and can be interpreted as the Green's function of ring sources. Using the change of variables $\phi^\dagger = \phi - \phi'$, the Green's function may be written as

$$\tilde{g}_p(\overline{r},\overline{r}') = \int_{-\pi}^{\pi} \frac{\cos(p\phi^\dagger) d\phi^\dagger}{4\pi\sqrt{\rho^2 + \rho'^2 - 2\rho\rho'\cos\phi^\dagger + (z-z')^2}} \quad (2.100)$$

With another change of variables $\phi^\ddagger = \phi^\dagger/2$, Equation 2.100 becomes

$$\tilde{g}_p(\overline{r},\overline{r}') = \frac{1}{2\pi\sqrt{a+b}} \int_{-\pi/2}^{\pi/2} \frac{1 - 2\sin^2(p\phi^\ddagger)}{\sqrt{1 - m^2\sin^2\phi^\ddagger}} d\phi^\ddagger \quad (2.101)$$

where

$$a = \rho^2 + \rho'^2 + (z - z')^2$$
$$b = 2\rho\rho'$$
$$m = \sqrt{\frac{2b}{a+b}}$$

The Green's function of Equation 2.101 can be expressed in terms of complete elliptical integrals of the first kind, $K(m)$, and second kind, $E(m)$.

Axial Case, p=0

When $p = 0$, the integral of Equation 2.101 is exactly the complete elliptical integral of the first kind,

$$\tilde{g}_0(\overline{r}, \overline{r}') = \frac{K(m)}{\pi\sqrt{a+b}} \tag{2.102}$$

The normal derivative of the Green's function is treated in the same manner:

$$\frac{\partial \tilde{g}_0(\overline{r}, \overline{r}')}{\partial n'} = \hat{n}' \cdot \hat{z}' \frac{\partial}{\partial z} \frac{K(m)}{\pi\sqrt{a+b}} + \hat{n}' \cdot \hat{\rho}' \frac{\partial}{\partial \rho} \frac{K(m)}{\pi\sqrt{a+b}} \tag{2.103}$$

Using

$$\frac{\partial K(m)}{\partial m} = \frac{1}{m}\left(\frac{E(m)}{1-m^2} - K(m)\right) \tag{2.104}$$

we obtain

$$\frac{\partial \tilde{g}_0(\overline{r}, \overline{r}')}{\partial n'} = \hat{n}' \cdot \hat{z}' \frac{E(m)\,(z - z')}{\pi\,(a-b)\sqrt{a+b}} + \hat{n}' \cdot \hat{\rho}' \frac{\rho}{b\pi\sqrt{a+b}} \left(\frac{\left(a - 2\rho'^2\right) E(m)}{a-b} - K(m)\right) \tag{2.105}$$

Transverse Case, p=1

When $p = 1$, the integral of Equation 2.101 becomes

$$\tilde{g}_1(\overline{r}, \overline{r}') = \frac{-1}{\pi\sqrt{a+b}} \left[\left(1 - \frac{2}{m^2}\right) K(m) + \frac{2}{m^2} E(m)\right] \tag{2.106}$$

and the normal derivative of the Green's function is

$$\frac{\partial \tilde{g}_1(\overline{r},\overline{r}')}{\partial n'} = -\hat{n}'\cdot\hat{z}'\frac{z-z'}{\pi b\sqrt{a+b}}\left[K(m)-\frac{a}{a-b}E(m)\right] + -\hat{n}'\cdot\hat{\rho}'\frac{1}{\pi b\rho'\sqrt{a+b}}\left[(a-\rho'^2)K(m)-\frac{a(a-\rho'^2)-2\rho^2\rho'^2}{a-b}E(m)\right] \tag{2.107}$$

where we have used

$$\frac{\partial E(m)}{\partial m} = \frac{1}{m}\left[E(m)-K(m)\right] \tag{2.108}$$

The Green's functions for higher order modes can be derived in the same fashion.

Boundary Integral Method

An MoM is used to solve the boundary integral of Equation 2.99. On the FEM mesh, the contour Γ contains $N_\Gamma - 1$ flat segments connected by N_Γ nodes. The location of node n is defined by (ρ_n, z_n) and is denoted by Γ_n. We define the nth patch p_n of length Δ_n to lie between node Γ_n and node Γ_{n+1}. The unknowns of ψ and $\frac{\partial\psi}{\partial n}$ are represented with linear basis functions α. First we introduce a local coordinate s on each patch p_n, increasing linearly from 0 to Δ_n. Hence, on patch p_n between node Γ_n and node Γ_{n+1}, the global coordinates may be written in terms of local coordinate as

$$\rho = \rho_n + \frac{\rho_{n+1}-\rho_n}{\Delta_n}s \tag{2.109}$$

$$z = z_n + \frac{z_{n+1}-z_n}{\Delta_n}s \tag{2.110}$$

The unknowns of mode p may be represented as

$$\psi_p(\overline{r}') = \sum_{n=1}^{N_\Gamma}\left[\alpha_l^n(s')+\alpha_r^n(s')\right]\psi_{np} \tag{2.111}$$

$$\frac{\partial\psi_p(\overline{r}')}{\partial n} = \sum_{n=1}^{N_\Gamma}\left[\alpha_l^n(s')+\alpha_r^n(s')\right]\frac{\partial\psi_{np}}{\partial n} \tag{2.112}$$

The linear basis functions are then simply

$$\alpha_l^n(s) = \begin{cases} s/\Delta_{n-1} & s \in p_{n-1} \\ 0 & s \notin p_{n-1} \end{cases} \tag{2.113}$$

$$\alpha_r^n(s) = \begin{cases} 1 - s/\Delta_n & s \in p_n \\ 0 & s \notin p_n \end{cases} \tag{2.114}$$

Note that patches p_0 and p_{N_Γ} do not exist, hence the first and last basis functions are α_r^1 and $\alpha_l^{N_\Gamma}$, respectively. Substituting Equations 2.111 and 2.112 into 2.90 results in

$$\begin{aligned} &\left[C(s)\sum_{n=1}^{N+1}\left[\alpha_l^n(s)+\alpha_r^n(s)\right]+\sum_{n=1}^{N+1}\int_{\Gamma_{n-1}}^{\Gamma_{n+1}}\left[\alpha_l^n(s')+\alpha_r^n(s')\right]\frac{\partial\tilde{g}_p(\overline{r},\overline{r}')}{\partial n'}\rho' ds'\right]\psi_{np} \\ &-\left[\sum_{n=1}^{N+1}\int_{\Gamma_{n-1}}^{\Gamma_{n+1}}\left[\alpha_l^n(s')+\alpha_r^n(s')\right]\tilde{g}_p(\overline{r},\overline{r}')\rho' ds'\right]\frac{\partial\psi_{np}}{\partial n} = \psi_p^{PR}(\overline{r}) \end{aligned} \tag{2.115}$$

A Galerkin scheme using the testing function $[\alpha_l^m(s)+\alpha_r^m(s)]$ then used to obtain:

$$\begin{aligned} &\left[\sum_{n=1}^{N+1}\int_{\Gamma_{m-1}}^{\Gamma_{m+1}}C(s)\left[\alpha_l^m(s)+\alpha_r^m(s)\right]\left[\alpha_l^n(s)+\alpha_r^n(s)\right]ds\right]\psi_{np} \\ &+\left[\sum_{n=1}^{N+1}\int_{\Gamma_{m-1}}^{\Gamma_{m+1}}\int_{\Gamma_{n-1}}^{\Gamma_{n+1}}\left[\alpha_l^m(s)+\alpha_r^m(s)\right]\left[\alpha_l^n(s')+\alpha_r^n(s')\right]\frac{\partial\tilde{g}_p(\overline{r},\overline{r}')}{\partial n'}\rho' ds' ds\right]\psi_{np} \\ &-\left[\sum_{n=1}^{N+1}\int_{\Gamma_{m-1}}^{\Gamma_{m+1}}\int_{\Gamma_{n-1}}^{\Gamma_{n+1}}\left[\alpha_l^m(s)+\alpha_r^m(s)\right]\left[\alpha_l^n(s')+\alpha_r^n(s')\right]\tilde{g}_p(\overline{r},\overline{r}')\rho' ds' ds\right]\frac{\partial\psi_{np}}{\partial n} \\ &=\int_{\Gamma_{m-1}}^{\Gamma_{m+1}}\left[\alpha_l^m(s)+\alpha_r^m(s)\right]\psi_p^P(\overline{r})ds \end{aligned} \tag{2.116}$$

for $m = 1...N$. The integrations in Equation 2.116 can be solved numerically using a quadrature scheme. However, care must be taken when dealing with the singular integrals and when integrating near the axis of symmetry.

Singular Integrals (Self-Term)

When $\overline{r} \rightarrow \overline{r}'$, m approaches 1, and the value $K(m)$ goes to infinity. A singularity then exists along the $s = s'$ line in the domain of integration for the self-terms $C_{m,m}$ and $Z_{m,m}$. To enable the evaluation of these terms, the elliptic integrals can be expressed in terms of Legendre functions of the second kind [59], using

$$Q_{-\frac{1}{2}}(\gamma) = \xi K(\xi) \tag{2.117}$$

$$Q_{\frac{1}{2}}(\gamma) = \frac{1}{\xi}\left[\left(2-\xi^2\right)K(\xi) - 2E(\xi)\right] \tag{2.118}$$

$$\frac{\partial Q_{\frac{1}{2}}(\gamma)}{\partial \gamma} = \frac{\frac{1}{2}Q_{\frac{1}{2}}(\gamma) - \frac{1}{2}Q_{-\frac{1}{2}}(\gamma)}{\gamma^2 - 1} \tag{2.119}$$

$$\xi = \sqrt{\frac{2}{\gamma+1}} \tag{2.120}$$

Substituting Equations 2.117-2.120 into the expressions for $\tilde{g}_0(\overline{r},\overline{r}')$ and $\frac{\partial \tilde{g}_0(\overline{r},\overline{r}')}{\partial n'}$ results in

$$\tilde{g}(\overline{r},\overline{r}') = \frac{Q_{-\frac{1}{2}}(\gamma)}{\sqrt{2b}\pi} \tag{2.121}$$

$$\begin{aligned}\frac{\partial \tilde{g}(\overline{r},\overline{r}')}{\partial n'} = &-\frac{\hat{n}'\cdot\hat{\rho}'}{\sqrt{2b}\pi\rho'}\left(\frac{Q_{-\frac{1}{2}}(\gamma)}{2} + \frac{a-2\rho'^2}{b}\frac{\partial Q_{\frac{1}{2}}(\gamma)}{\partial\gamma}\right)\\ &- \frac{\hat{n}'\cdot\hat{z}'}{\sqrt{2b}\pi\rho'}\frac{z-z'}{\rho}\frac{\partial Q_{\frac{1}{2}}(\gamma)}{\partial\gamma}\end{aligned} \tag{2.122}$$

$$\gamma = 1 + \frac{a-b}{b} \quad , \quad 1 \leq \gamma \leq \infty \tag{2.123}$$

Now as $\overline{r}' \rightarrow \overline{r}$, $\gamma \rightarrow 1$, and the Legendre functions can be expanded as:

$$Q_{-\frac{1}{2}} = -\frac{1}{2}\ln\left(\frac{\gamma-1}{32}\right) \tag{2.124}$$

$$\frac{\partial Q_{\frac{1}{2}}(\gamma)}{\partial\gamma} = -\frac{1}{2(\gamma-1)} \tag{2.125}$$

Substituting Equations 2.124 and 2.125 into Equations 2.121 and 2.122 results in

$$\tilde{g}(\overline{r},\overline{r}') = \frac{-1}{2\sqrt{2b}\pi}\ln\left(\frac{(\rho-\rho')^2+(z-z')^2}{64\rho\rho'}\right) \tag{2.126}$$

$$\frac{\partial\tilde{g}(\overline{r},\overline{r}')}{\partial n'} = -\frac{\hat{n}'\cdot\hat{\rho}'}{\sqrt{\rho}\rho'^{3/2}\pi}\left[\frac{1}{2}\ln\left(\frac{(\rho-\rho')^2+(z-z')^2}{64\rho\rho'}\right)+\frac{\rho^2-\rho'^2+(z-z')^2}{(\rho-\rho')^2+(z-z')^2}\right] - \frac{\hat{n}'\cdot\hat{z}'\,(z-z')}{\sqrt{2b}\pi\left((\rho-\rho')^2+(z-z')^2\right)} \tag{2.127}$$

For the self term, $\rho_2=\rho_2'$, $z_2=z_2'$, and $\Delta=\Delta'$, hence

$$\rho-\rho' = (s-s')\left(\frac{\rho_2-\rho_1}{\Delta}\right) \tag{2.128}$$

$$z-z' = (s-s')\left(\frac{z_2-z_1}{\Delta}\right) \tag{2.129}$$

The singularity of Equation 2.126 then has the form of $\ln\left((s-s')^2\right)$, which is integrable. The logarithmic term in Equation 2.127 has the same form. The two remaining terms contain singularities of the form $1/(s-s')^n$ $(n\geq 1)$, which is not integrable as $s\rightarrow s'$. To handle these integrals, a new variable is introduced $y=s-s'$. The integrals now have the form of

$$\int_{-\Delta}^{-\epsilon}\int_{0}^{\Delta+y}\frac{f(s,y)}{y}dsdy+\int_{\epsilon}^{\Delta}\int_{y}^{\Delta}\frac{f(s,y)}{y}dsdy \tag{2.130}$$

where ϵ is the infinitesimal limit around the singularity, which is now at the $y=0$ axis. These integrals can then be solved numerically using a quadrature scheme.

2.2.3 Boundary Conditions

The separate equations for the interior and exterior domains may be related through the boundary conditions. First we return to $\overline{\overline{S}}_{\psi A}$, from the surface integral of Equation 2.29 that can be used to enforce the continuity of the tangential magnetic fields.

The kernel of the integral may be rewritten as

$$\frac{1}{\mu_1}\overline{W} \times \left(\nabla \times \overline{A}\right) \cdot \hat{n}_1 = \frac{1}{\mu_1}\overline{W} \cdot \left(\nabla \times \overline{A}\right) \times \hat{n}_1 \tag{2.131}$$

Using the continuity of the tangential magnetic fields,

$$\frac{\nabla \times \overline{A}}{\mu_1} \times \hat{n}_1 = \overline{H}_1 \times \hat{n}_1 = -\overline{H}_2 \times \hat{n}_2 = \nabla\psi \times \hat{n}_2 \tag{2.132}$$

Taking into account axisymmetry, the surface integral may then be expressed as:

$$\int_{S_{12}} \frac{1}{\mu_1}\overline{W} \times \left(\nabla \times \overline{A}\right) \cdot \hat{n}_1 \, dS = \int_{S_{12}} \overline{W} \cdot \nabla\psi \times \hat{n}_2 \, dS \tag{2.133}$$

Equations 2.27, 2.28, and 2.111 can now be used to obtain basis and weighting function representations of W and ψ. For the transverse case,

$$\begin{aligned} & S_{\psi A,mn} = \\ & -\pi \sum_{n=1}^{N_\Gamma} \int_{\Gamma_{n-1}}^{\Gamma_{n+1}} \left[(\rho_2 - \rho_1) \left(\rho \frac{\partial}{\partial \rho} \left[\alpha_l^n(s) + \alpha_r^n(s)\right] \alpha_m^{(\phi)} + \left[\alpha_l^n(s) + \alpha_r^n(s)\right] \alpha_m^{(\rho)} \right) \right. \\ & \left. + (z_2 - z_1) \left(\rho \frac{\partial}{\partial z} \left[\alpha_l^n(s) + \alpha_r^n(s)\right] \alpha_m^{(\phi)} + \left[\alpha_l^n(s) + \alpha_r^n(s)\right] \alpha_m^{(z)} \right) \right] \frac{1}{\Delta} ds \end{aligned} \tag{2.134}$$

The weighting function $\overline{\alpha}_m$ is a two-dimensional finite element function that exists over the entire structure, hence the resulting matrix is $N \times N_\Gamma$ in size. However, the kernel of Equation 2.134 is the product of the two types of basis functions over the surface contour, and hence the integral is zero for interior nodes. Only the edges of the weighting functions on the surface contour contribute to the integral, and can be described in the same fashion as the basis functions. For the axial case $\alpha_m^{(z)}$ and $\alpha_m^{(\rho)}$ are both zero.

The second boundary condition is the continuity of $\hat{n} \cdot \overline{B}$, and can be implemented

in the boundary integral equation. The two unknowns in Equation 2.139 are ψ, the scalar potential, and its normal derivative $\frac{\partial\psi}{\partial n}$. Given that $\overline{H} = -\nabla\psi$ in the exterior region, we can show

$$\frac{\partial\psi}{\partial n} = \nabla\psi\cdot\hat{n}_2 = -\frac{\overline{B}_2\cdot\hat{n}_2}{\mu_o} = \frac{\overline{B}_1\cdot\hat{n}_1}{\mu_o} = \frac{(\nabla\times\overline{A})\cdot\hat{n}_1}{\mu_o} = \frac{(\nabla\times\rho\overline{\mathcal{A}})\cdot\hat{n}_1}{\mu_o} \tag{2.135}$$

Substituting the expression for $\mathcal{A}$ into the $\frac{\partial\psi}{\partial n}$ integral of Equation 2.116 for the axial case yields

$$S_{A\psi,mn} = +\frac{1}{\mu_o}\sum_{n=1}^{N+1}\left[\int_{\Gamma_{m-1}}^{\Gamma_{m+1}}\int_{\Gamma_{n-1}}^{\Gamma_{n+1}}\tilde{g}(\overline{r},\overline{r}')\rho'\left[\alpha_l^m(s)+\alpha_r^m(s)\right]\left(2\alpha_n^{(\phi)}n'_{1z}\hat{\phi}\right.\right.$$
$$\left.\left.+\ \rho' n'_z\frac{\partial\alpha_n^{(\phi)}}{\partial\rho'}\hat{\phi} - n'_z\alpha_n^{(\rho)}\hat{\rho} - \rho' n'_\rho\frac{\partial\alpha_n^{(\phi)}}{\partial z'}\hat{\phi} + n'_\rho\alpha_n^{(z)}\hat{z}\right)ds'ds\right] \tag{2.136}$$

Recall the subscript notation $A\psi$ here refers to the matrix operating on the A variable in the equation for ψ. The basis function in Equation 2.136 is the two-dimensional finite element function, hence the resulting matrix is $N_\Gamma \times N$. Again, the integral is zero for basis functions on the interior nodes. For the transverse case the integral is

$$S_{A\psi,mn} = +\frac{1}{\mu_o}\sum_{n=1}^{N+1}\left[\int_{\Gamma_{m-1}}^{\Gamma_{m+1}}\int_{\Gamma_{n-1}}^{\Gamma_{n+1}}\tilde{g}(\overline{r},\overline{r}')\left[\alpha_l^m(s)+\alpha_r^m(s)\right]\left(\alpha_n^{(\phi)}n'_{1z}\hat{\phi}\right.\right.$$
$$\left.\left.+\ \rho' n'_z\frac{\partial\alpha_n^{(\phi)}}{\partial\rho'}\hat{\phi} - n'_z\alpha_n^{(\rho)}\hat{\rho} - \rho' n'_\rho\frac{\partial\alpha_n^{(\phi)}}{\partial z'}\hat{\phi} + n'_\rho\alpha_n^{(z)}\hat{z}\right)ds'ds\right] \tag{2.137}$$

2.2.4 Matrix Equation

The interior and exterior equations may now be combined into a single matrix equation. The interior problem, shown here in terms of $\overline{A}$ without a coordinate rotation, is ultimately defined by the matrix equation

$$\overline{\overline{S}}_{AA}\,\overline{A} + \overline{\overline{F}}_{AA}\,\frac{\partial}{\partial t}\overline{A} + \overline{\overline{S}}_{\psi A}\,\overline{\psi} = 0 \tag{2.138}$$

where $\overline{\overline{S}}_{AA}$ and $\overline{\overline{F}}_{AA}$ are found directly from Equation 2.29, and $\overline{\overline{S}}_{\psi A}$ is found from Equation 2.133. Equation 2.116 has the form

$$\overline{\overline{S}}_{\psi\psi}\ \overline{\psi} - \overline{\overline{S}}_{A\psi}\ \overline{A} = \overline{\Psi}^{PR} \tag{2.139}$$

where $\overline{\Psi}^{PR}$ is the integration of the primary field and weighting functions over the surface contour.

Frequency Domain Solution

For the time harmonic excitation, $H^{PR}(t) = H^{PR}e^{-i\omega t}$, the $\frac{\partial}{\partial t} \rightarrow -i\omega$, and the system of equations to solve becomes

$$\begin{bmatrix} \overline{\overline{S}}_{AA} - i\omega\overline{\overline{F}}_{AA} & -\overline{\overline{S}}_{\psi A} \\ -\overline{\overline{S}}_{A\psi} & S_{\psi\psi} \end{bmatrix} \begin{bmatrix} \overline{A} \\ \overline{\psi} \end{bmatrix} = \begin{bmatrix} 0 \\ \overline{\Psi}^{PR} \end{bmatrix} \tag{2.140}$$

The exterior potential can then be found by integrating $\mathcal{A}$ and ψ over the surface of the BOR with Equation 2.90.

Time Domain Solution

Consider a series of discrete time steps Δt_m, for $m = 1, \ldots, M$. The step size may be increased in time as $\Delta t_m = m^2 \Delta t_0$ [60]. The simplest way to solve Equations 2.138 and 2.139 in the time domain is to use the implicit Euler method [61]. Given time steps m and $m+1$, this method can be expressed in the form of

$$\frac{\overline{x}_{(m+1)} - \overline{x}_{(m)}}{\Delta t_m} = \overline{f}(\overline{x}_{(m+1)}) \equiv \overline{f}_{(m+1)} \tag{2.141}$$

which is unconditionally stable but accumulates error in time on the order of Δt_m. Using the implicit Euler method in Equation 2.138 results in

$$\overline{\overline{S}}_{AA}\ \overline{A}_{(m+1)} + \frac{1}{\Delta t}\overline{\overline{F}}_{AA}\ \overline{A}_{(m+1)} + \overline{\overline{S}}_{\psi A}\ \overline{\psi}_{(m+1)} = \frac{1}{\Delta t}\overline{\overline{F}}_{AA}\ \overline{A}_{(m)} \tag{2.142}$$

Two cases are considered, the response to $H^{PR}(t) = H^{PR}u(t)$ (turn-on) and $H^{PR}(t) = H^{PR}[1 - u(t)]$ (turn-off), where $u(t)$ is the step function. For the turn-on case, the magnetic field is zero everywhere at $t = 0$, and the primary field is imposed through ψ^{PR} for $t > 0$. The turn-off case uses the FE-BI method static solution as the initial condition, with $\psi^{PR} = 0$ for $t > 0$. The two Equations, 2.24 and 2.99, may then be solved for the two unknowns $\overline{A}$ and ψ. For each azimuthal mode, the system may be written in matrix form as

$$\begin{bmatrix} \Delta t_m \overline{\overline{S}}_{AA} + \overline{\overline{F}}_{AA} & -\Delta t_m \overline{\overline{S}}_{\psi A} \\ \overline{\overline{S}}_{A\psi} & \overline{\overline{S}}_{\psi\psi} \end{bmatrix} \begin{bmatrix} \overline{A}_{(m+1)} \\ \overline{\psi}_{(m+1)} \end{bmatrix} = \begin{bmatrix} \overline{\overline{F}}_{AA}\, \overline{A}_{(m)} \\ \overline{\Psi}^{PR}_{(m)} \end{bmatrix} \tag{2.143}$$

where $\overline{\overline{F}}_{AA}$, $\overline{\overline{S}}_{AA}$, and $\overline{\overline{S}}_{\psi A}$ arise from the integrations over the FE-BI mesh in Equation 2.24 ($\overline{\overline{F}}_{AA}$ from the integral with the $\frac{\partial}{\partial t}$ term). The matrices $\overline{\overline{S}}_{A\psi}$, $\overline{\overline{S}}_{\psi\psi}$ and $\overline{\Psi}^{PR}_{(m)}$ arise from the integrations over the patches of Equation 2.99. $\overline{A}_{(m)}$ and $\overline{\psi}_{(m)}$ are the unknowns at time step m. $\overline{A}_{(m)}$ contains the three vector components of $\overline{A}$ for the transverse case. Note that it is not necessary for the primary field to shut off as an ideal step function. Other functions, such as a ramp or exponential decay, can be included in the system in the time dependent $\overline{\Psi}^{PR}$ on the right hand side of Equation 2.143.

The FE-BI method outlined thus far can solve the EMI scattered fields from an axisymmetric target under a uniform axial or transverse primary field. Other uniform excitations can be found from a superposition of these two cases. Non-uniform cases may be studied using higher order modes for which the Green's functions must be derived. For UXO sensing devices, the primary field is a step or ramp function, and is either turned on or off at $t = 0$. As mentioned earlier, and will be shown in the Section 2.3, the FE-BI method cannot resolve the small skin depths that exist in early time. However, for an increasing time step, it is apparent from Equation 2.143 that the FE-BI will always converge to the static ($\frac{\partial}{\partial t} \rightarrow 0$, late time) solution. Hence, it is necessary to develop a new method that will demonstrate early time accuracy.

2.3 Finite Element - Boundary Integral Results

In this section, the numerical solutions are compared with analytical solutions. The limitations of the FE-BI method are first demonstrated by comparison with frequency and time domain solutions for a conducting and permeable sphere. Time domain comparisons are then made between the numerical and analytical solutions for prolate and oblate spheroids. If the numerical result is denoted as $f_{num}(t)$, and the analytical solution is denoted as $f_{ana}(t)$, then we can define a normalized error $e(t)$ to be:

$$e(t) = \frac{|f_{num}(t) - f_{ana}(t)|}{\max(|f_{ana}(t)|)} \tag{2.144}$$

The normalized error is used to demonstrate the accuracy of the FE-BI solution. The numerical method is then compared with time domain experimental results. Finally, the efficiency of the method is investigated.

2.3.1 EMI Scattering from a Sphere

Comparisons can be made to J. R. Wait's solution for a sphere in a uniform magnetic field [41]. The radius of the sphere is 5 cm. A magnetic sphere with $\mu_r = 100$ and a nonmagnetic sphere with $\mu_r = 1$ are investigated. Both spheres have a conductivity of $\sigma = 10^7$ S/m. These properties are representative of metals found in UXOs, such as aluminum and steel. The uniform primary magnetic field is turned on as a step function, and the induced field is calculated 20 cm above the origin. Given that small skin depths are expected, in is natural to use an FE-BI mesh that has a nonuniform discretization that is finest near the surface. Two meshes are used as examples, as shown in Figure 2-4, that each enforce a minimum 1 mm element size near the surface (i.e. subsurface discretization). The meshes are generated by the Matlab command *pdemesh* for the given geometry. The first is referred to as a coarse mesh, containing 400 nodes and 65 boundary nodes. The second is refereed to as a fine mesh, containing 2085 nodes with 129 boundary nodes, and is a single refinement over the coarse mesh

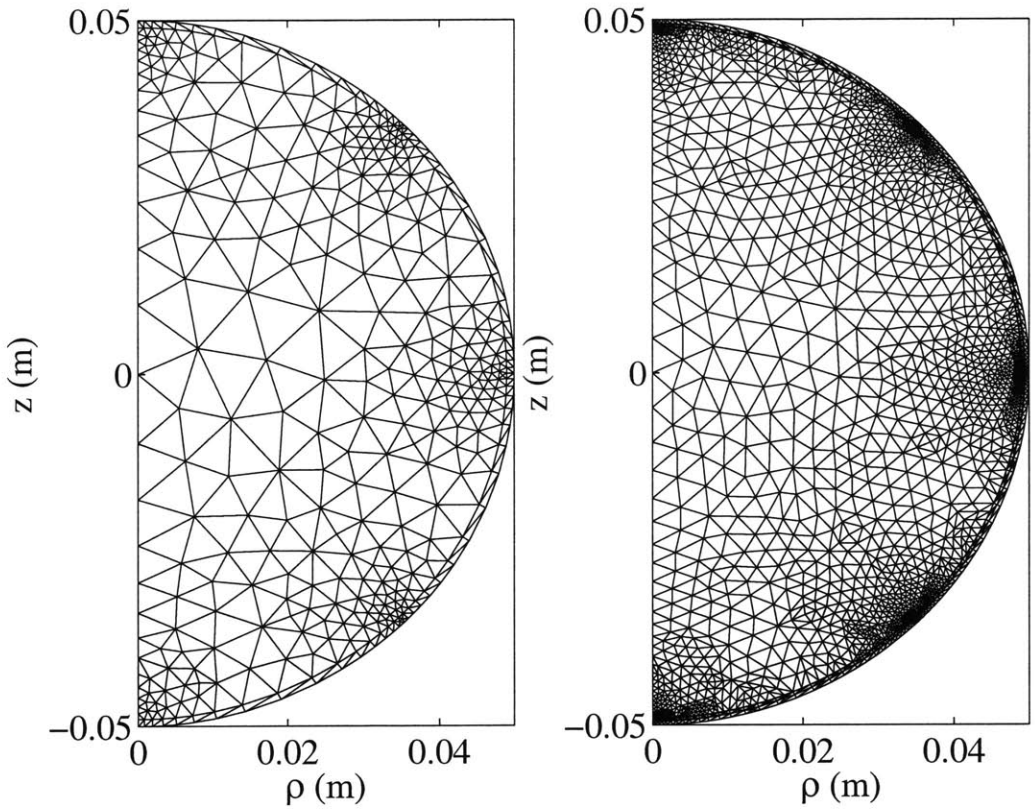

Figure 2-4: Coarse and fine meshes for the sphere, using the Matlab mesh generator. The radius is 5 cm. A 1 mm discretization (normal direction) is enforced at the surface.

(each element is divided into four elements). The fine mesh contains more unknowns should yield greater accuracy at the expense of computational efficiency. The CPU times for the various meshes and methods will be given in a subsequent section. Note that there are many possible mesh options, and these two are simply meant to be representative of typical choices.

Figure 2-5 shows the axial magnetic vector potential, $A^{(\phi)}$, inside the nonmagnetic sphere from an $\overline{H} = \hat{z}\, u(t)$ (axial) primary field. The fine mesh is used. Recall that the current J is the derivative of $A^{(\phi)}$ with respect to time. In very early time at $t = 3.0\ \mu s$, the skin depth appears to be on the order of 1 mm. Physically, currents appear on the surface of the sphere to oppose the changing magnetic field. As time progresses, the skin depth increases as the fields (and currents) penetrate farther

into the sphere. Due to the finite conductivity, the currents decay as they diffuse inward. At $t = 23.8$ ms, the system has reached the static solution; the currents have diffused into the sphere and decayed to zero, hence the field $A^{(\phi)}$ no longer varies in time. Figure 2-6 shows the axial magnetic vector potential, $A^{(\phi)}$, inside the magnetic sphere for the same primary field. In very early time at $t = 3.0$ μs, the skin depth is too small to be resolved on the mesh, and only a few surface nodes are nonzero. At $t = 0.247$ ms, the skin depth has increased and the mesh begins to resolve the fields. As time progresses, the skin depth continues to increase, but by $t = 23.8$ ms the system has not yet reached the static solution. These plots of $A^{(\phi)}$ give a general sense of the μ dependent time scales of the EMI response, as well as the capabilities of the FE-BI method with the fine mesh. Next, the induced fields will be examined to quantify the accuracy of the FE-BI method.

Figure 2-7 shows the axial and transverse responses from the nonmagnetic sphere. In early time (equivalently at high frequencies), currents are set up along the circumference of the sphere to oppose the changing magnetic field. The induced magnetic field from these currents is therefore in the opposite direction as the primary field. As time progresses, these currents diffuse and decay into the sphere, until finally the late time static response becomes zero. In both the axial and transverse cases, the agreement between the analytical solution and the coarse mesh FE-BI solution is excellent. Figure 2-8 and Figure 2-9 show the axial and transverse responses, respectively, from the magnetic sphere with $\mu_r = 100$. The frequency domain solutions are shown for comparison. In these cases, the early time (high frequency) response is similar to the nonmagnetic sphere. In late time the induced field is nonzero in the same direction as the primary field (the static solution). The FE-BI mesh cannot resolve the smaller skin depths that appear in these cases, and significant error is observed over 1 kHz in the frequency domain and before 1 ms in the time domain. However, as predicted in the previous section, the FE-BI method does converge to late time static solution. The FE-BI method also converges in very early time or high frequency,

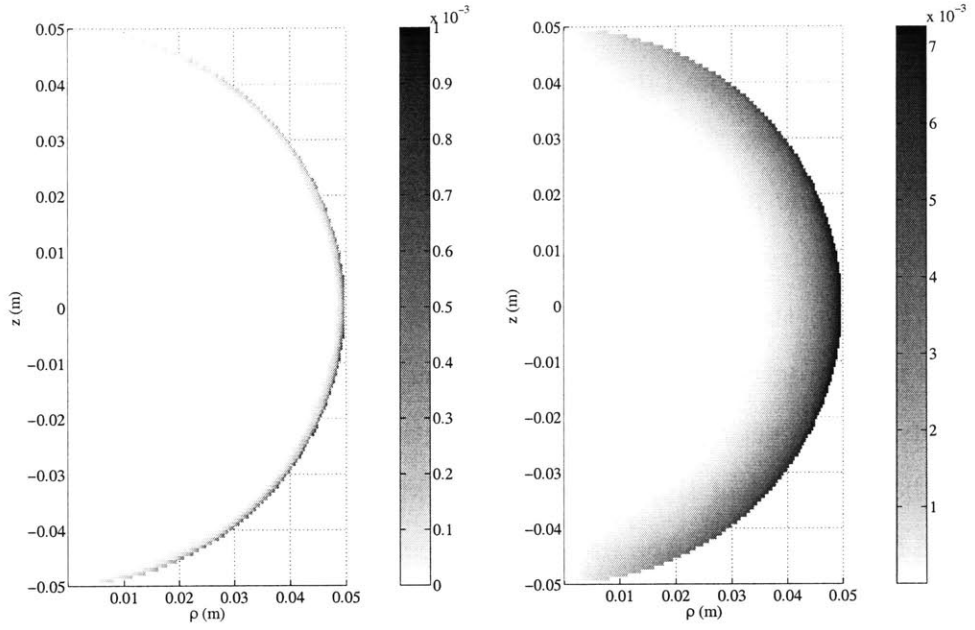

(a) $A^{(\phi)}$ at $t = 3.0\ \mu s$

(b) $A^{(\phi)}$ at $t = 0.247$ ms

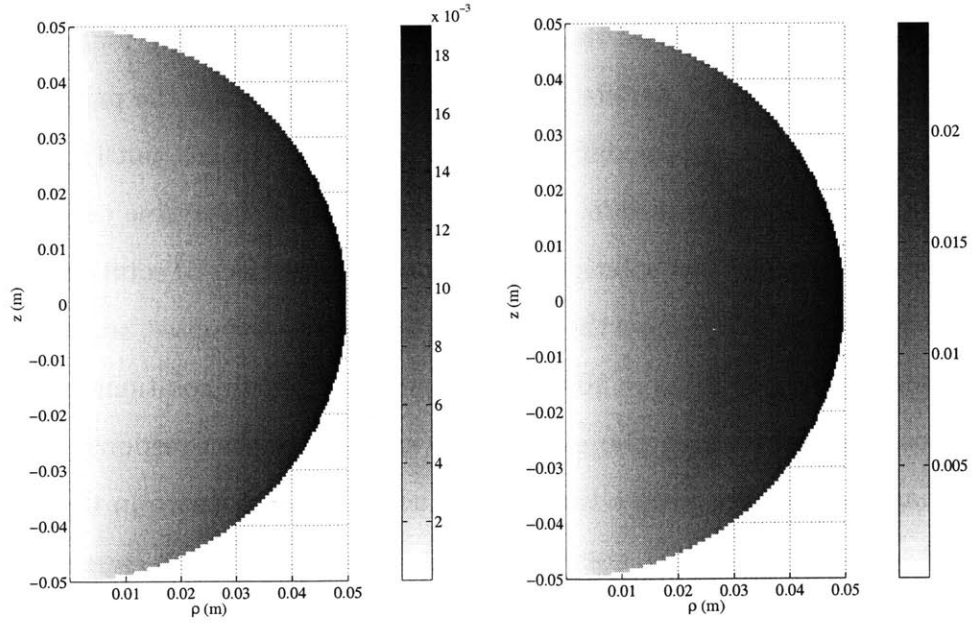

(c) $A^{(\phi)}$ at $t = 2.94$ ms

(d) $A^{(\phi)}$ at $t = 23.8$ ms

Figure 2-5: Magnetic vector potential inside a sphere with $r = 0.05$ m, $\mu_r = 1$, $\sigma = 10^7$ S/m. Uniform primary field turned on at $t = 0$. $\overline{H}^{PR} = \hat{z}$ excitation.

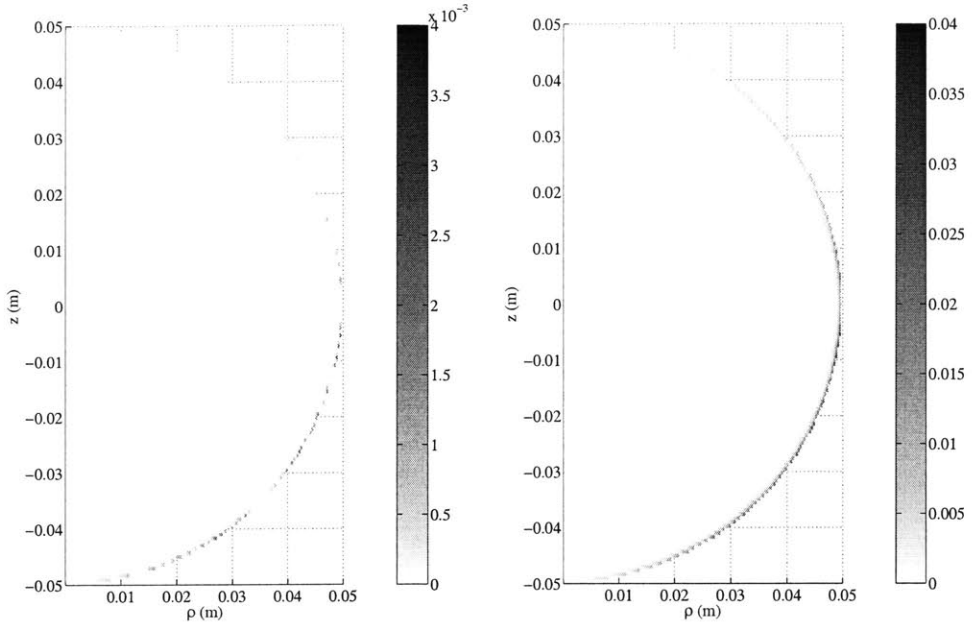

(a) $A^{(\phi)}$ at $t = 3.0\ \mu s$

(b) $A^{(\phi)}$ at $t = 0.247$ ms

(c) $A^{(\phi)}$ at $t = 2.94$ ms

(d) $A^{(\phi)}$ at $t = 23.8$ ms

Figure 2-6: Magnetic vector potential inside a sphere with $r = 0.05$ m, $\mu_r = 100$, $\sigma = 10^7$ S/m. Uniform primary field turned on at $t = 0$. $\overline{H}^{PR} = \hat{z}$ excitation.

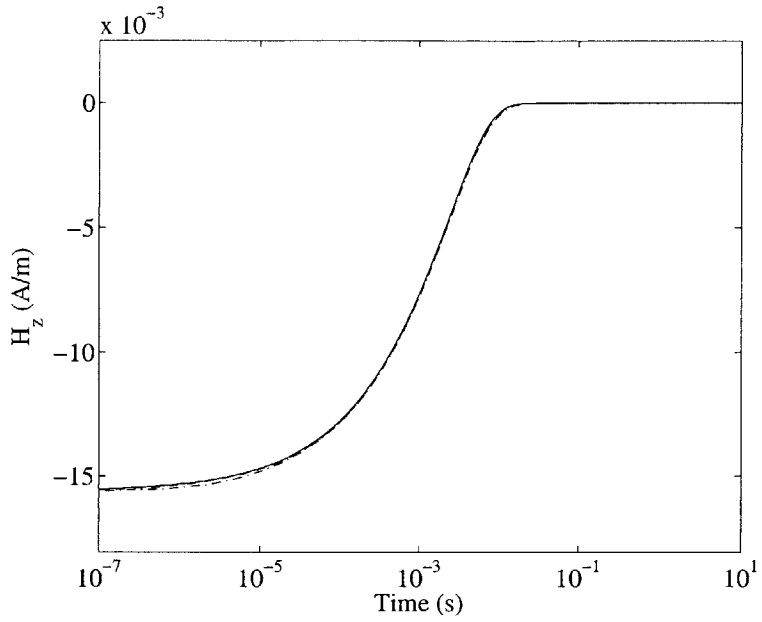

(a) Induced field from $\overline{H}^{PR} = \hat{z}\ u(t)$ excitation

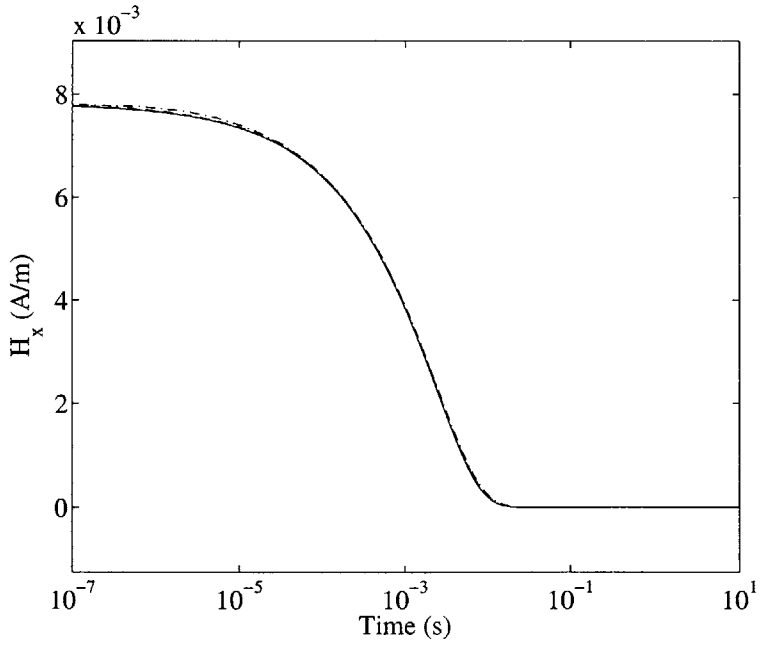

(b) Induced field from $\overline{H}^{PR} = \hat{x}\ u(t)$ excitation

Figure 2-7: Induced magnetic field at $z = 0.2$ m, from a sphere with $r = 0.05$ m, $\mu_r = 1$, $\sigma = 10^7$ S/m. Uniform primary field turned on at $t = 0$. Solid line is the analytical solution, dashed line is the fine mesh, dash-dot line is the coarse mesh.

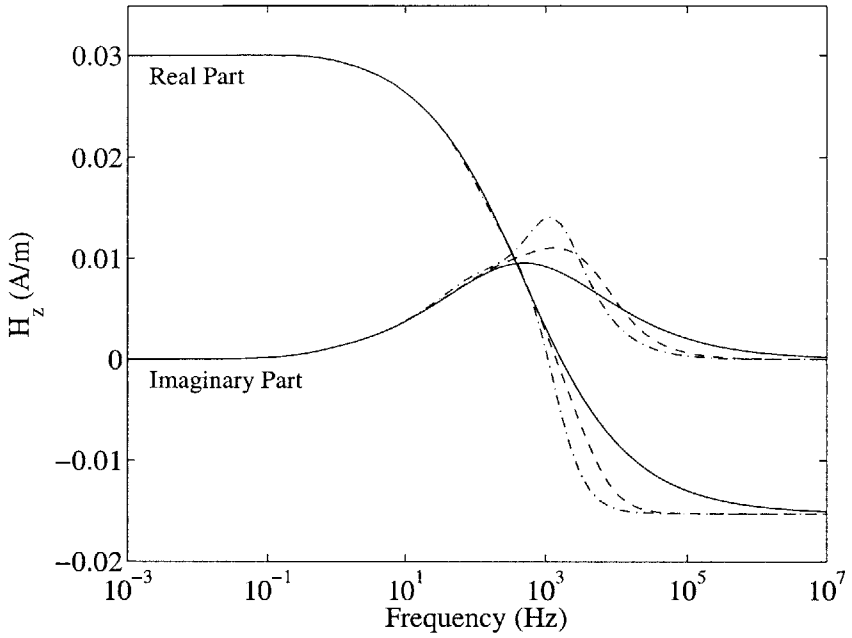

(a) Frequency domain response from $\overline{H}^{PR} = \hat{z}\, e^{i\omega t}$ excitation

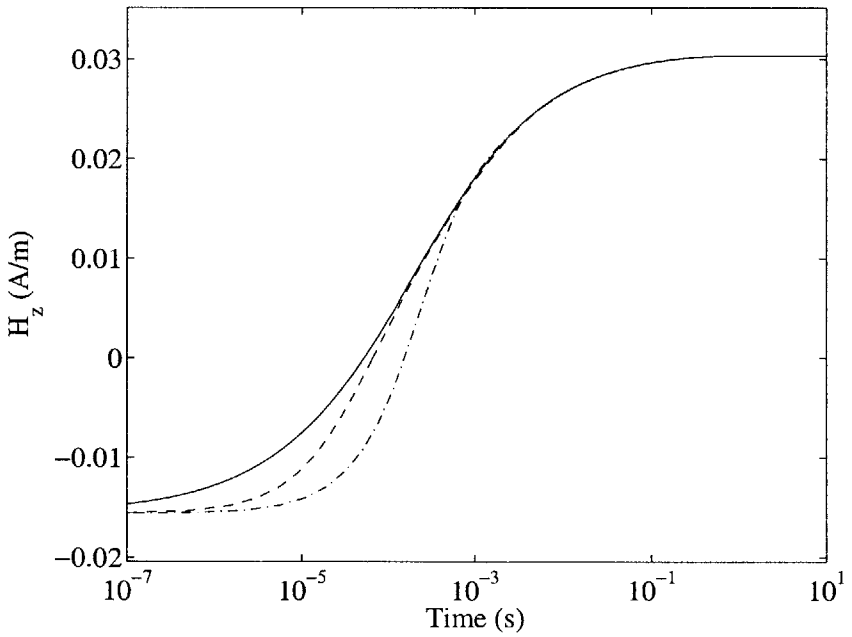

(b) Time domain response from $\overline{H}^{PR} = \hat{z}\, u(t)$ excitation

Figure 2-8: Induced magnetic field at $z = 0.2$ m, from a sphere with $r = 0.05$ m, $\mu_r = 100$, $\sigma = 10^7$ S/m. Uniform primary field turned on at $t = 0$. Solid line is the analytical solution, dashed line is the fine mesh, dash-dot line is the coarse mesh.

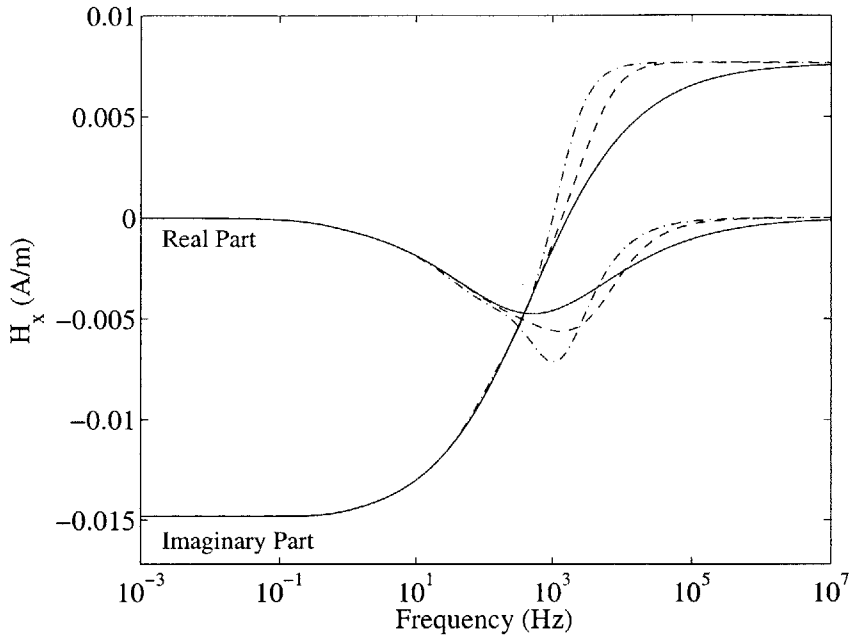

(a) Frequency domain response from $\overline{H}^{PR} = \hat{x}\ e^{i\omega t}$ excitation

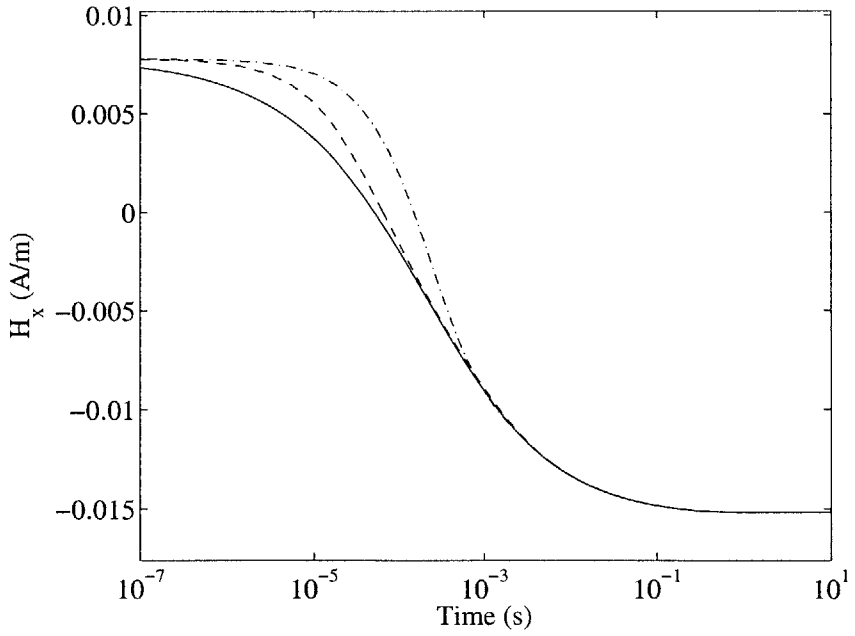

(b) Time domain response from $\overline{H}^{PR} = \hat{x}\ u(t)$ excitation

Figure 2-9: Induced magnetic field at $z = 0.2$ m, from a sphere with $r = 0.05$ m, $\mu_r = 100$, $\sigma = 10^7$ S/m. Uniform primary field turned on at $t = 0$. Solid line is the analytical solution, dashed line is the fine mesh, dash-dot line is the coarse mesh.

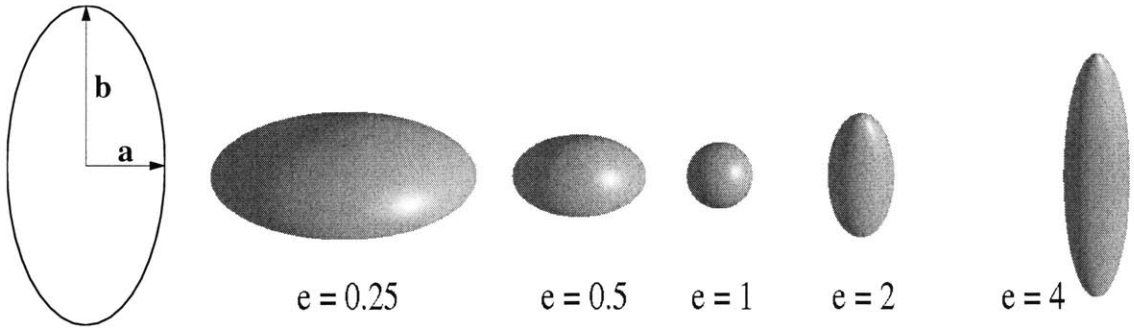

Figure 2-10: Spheroid shapes whose EMI response is used to compare the FE-BI results with exact solutions. Elongation e is the ratio of b (on the z axis) to a (on the ρ axis).

at which time the fields are zero within the object and the integral equation alone provides an accurate solution. Note that the FE-BI method is converging slowly to the analytical solution; increasing the mesh resolution from 400 nodes to 2085 nodes has only approximately halved the error. Section 2.4 will introduce the new method that eliminates the early time error.

2.3.2 EMI Scattering from Spheroids

Using Equation 2.144, the accuracy of the FE-BI solution can be compared with the analytical solution [14, 62, 63]. In addition to the sphere, the EMI scattered field will be calculated from spheroidal geometries. The spheroid radius on the ρ axis is referred to as a, and the length on the z axis is referred to as b. Five different spheroids will be used for this comparison, with elongations ($e = b/a$) between 0.25 and 4, relative permeability $\mu_r = 100$, and conductivity $\sigma = 10^7$ S/m S/m. The spheroid geometry is shown in Figure 2-10, along with examples of the various elongations. The minor axis (a for prolate spheroids, b for oblate spheroids) is kept constant at 0.05 m. Figure 2-11 shows the error of the FE-BI solution using the coarse and fine meshes similar to the sphere case. The maximum error in the FE-BI solution occurs in early time from 10^{-5} s to 10^{-4} s. The maximum error for the fine mesh varies from 0.02 for the $e = 4$ (prolate) spheroid to 0.12 for the sphere. Despite enforcing

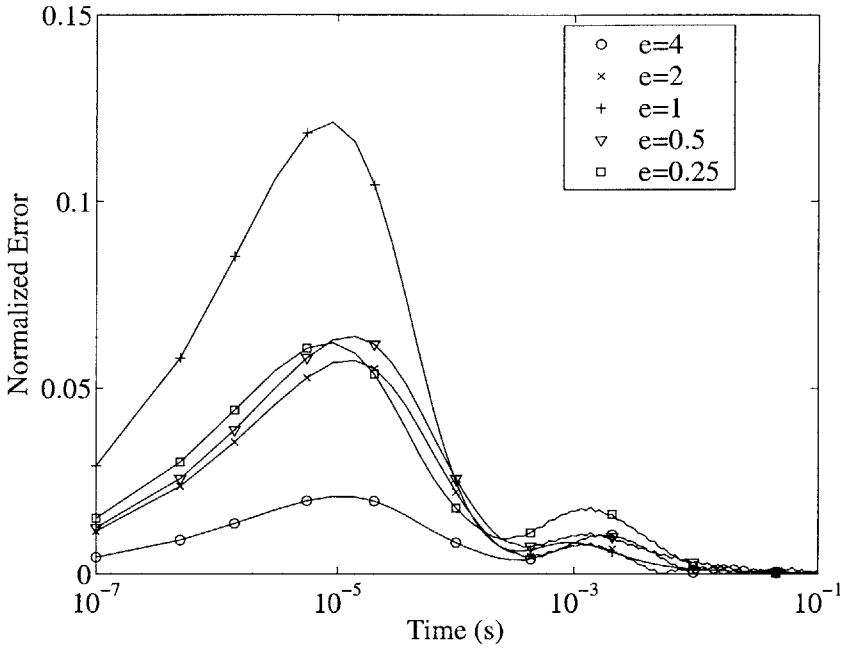

(a) Fine mesh

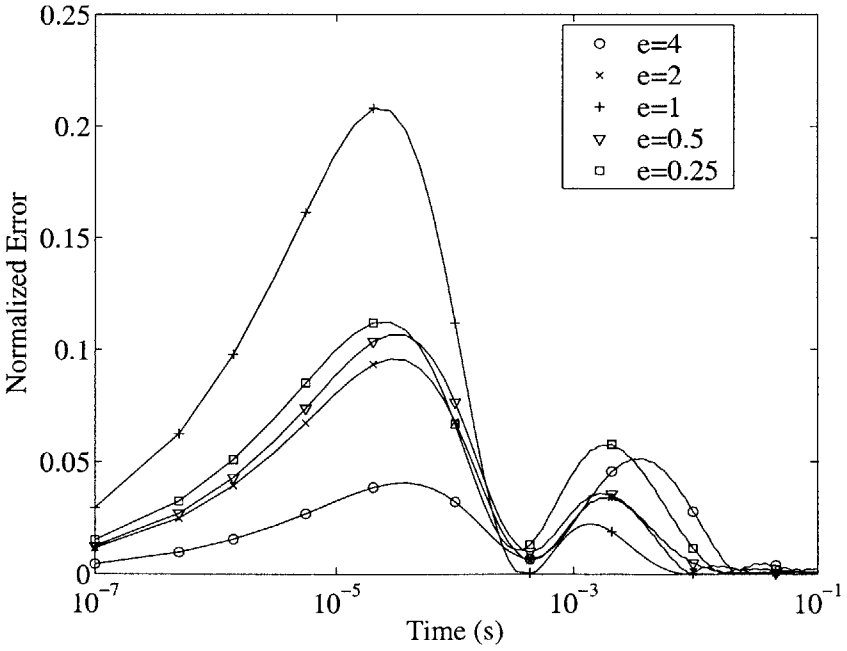

(b) Coarse mesh

Figure 2-11: FE-BI Result. Normalized error of the induced magnetic field at $z = 4b$ m, from spheroids with minor axis 0.05 m, $\sigma = 10^7$ S/m, $\mu_r = 100$. Uniform primary field $\overline{H}^{PR} = \hat{z}\, u(t)$.

the 1 mm subsurface discretization for all geometries, the meshes may still have inhomogeneities and regions of coarse discretization that contribute to the solution error. In addition, the FE-BI method may be more accurate for certain geometries and excitations. For example, with axial excitation the induced currents circle the equator of the spheroid and diffuse inward. The currents have a tangential profile that varies with the surface profile. For the prolate spheroid, the radius of curvature is larger at the equator and the currents have a relatively smooth tangential profile. For the oblate spheroid, the opposite is true. Hence the FE-BI mesh is better able to resolve the currents (in the form of $A^{(\phi)}$) for the prolate cases, and the error is lower. In general, the fine mesh offers a significant improvement in early time error for all spheroid geometries. Furthermore, the coarse mesh solutions exhibit further error of up to 0.05 in intermediate time (10^{-3} s to 10^{-2} s).

Figure 2-12 shows the FE-BI error for the transverse excitation case. In this case the currents circle the spheroid between the poles, where the prolate spheroids have the smaller radius of curvature. Hence the prolate spheroid solutions have a higher error than the oblate spheroid solutions. The errors are generally higher for the transverse excitation case compared to the axial excitation case, approaching 0.15 on the fine mesh and exceeding 0.25 on the coarse mesh. The intermediate time error is again present for the coarse mesh. Figure 2-13 shows the FE-BI normalized error for the induced field from the 5 cm radius sphere with various permeabilities. As the permeability increases, the skin depth decreases, and the FE-BI method accuracy gets worse. The maximum error is approximately 0.35 for the $\mu_r = 500$ case. Both the axial and transverse excitations show similar results. The error for the coarse mesh (not shown here) is worse as expected, with a maximum error of 0.5 for the $\mu_r = 500$ case. Tables 2.1 and 2.2 show the mesh sizes and solution CPU times on the fine and coarse meshes, respectively. A 2 GHz Pentium 4 with 512 MB of RAM is used. The size of the spheroid increases as the elongation increases, so the number of elements also increases to maintain the mesh constraint of a 1 mm resolution at the

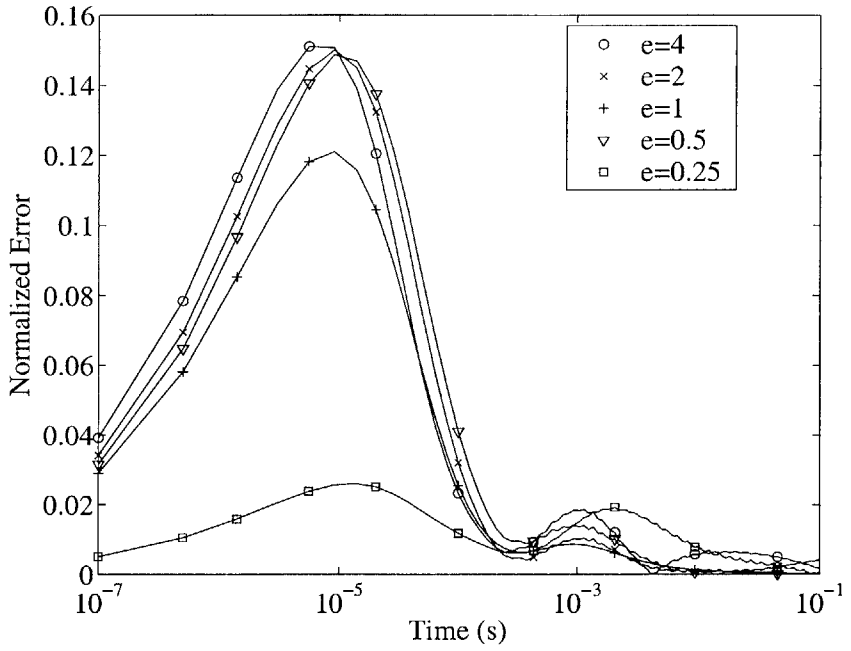

(a) Fine mesh

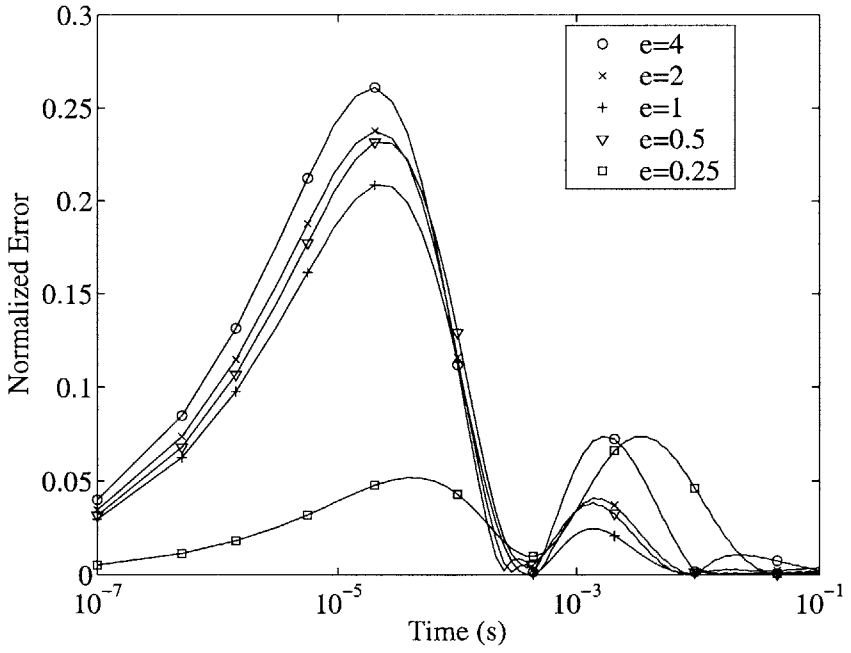

(b) Coarse mesh

Figure 2-12: FE-BI Result. Normalized error of the induced magnetic field at $z = 4b$ m, from spheroids with minor axis 0.05 m, $\sigma = 10^7$ S/m, $\mu_r = 100$. Uniform primary field $\overline{H}^{PR} = \hat{x}\, u(t)$.

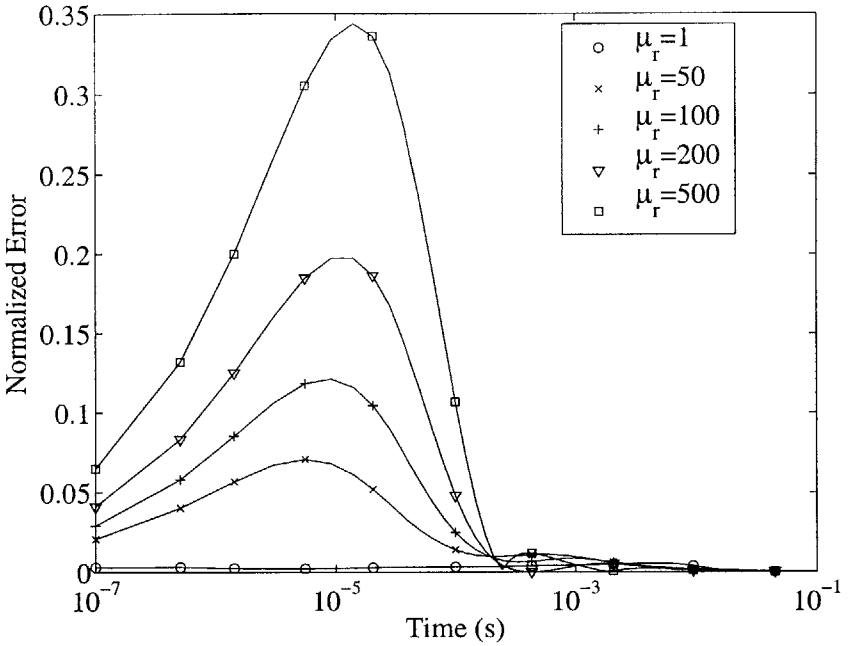

(a) Response from $\overline{H}^{PR} = \hat{z}\ u(t)$ excitation, fine mesh

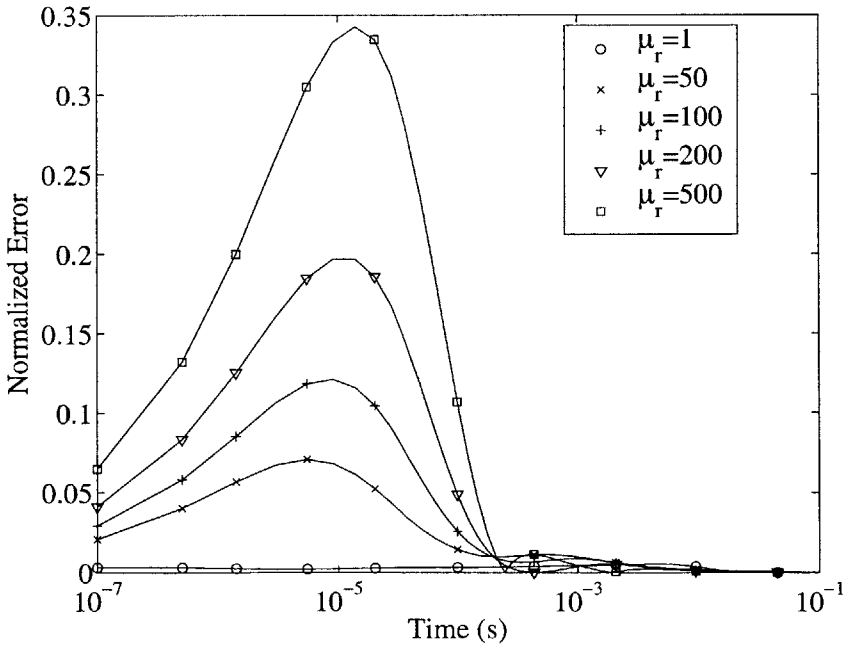

(b) Response from $\overline{H}^{PR} = \hat{x}\ u(t)$ excitation, fine mesh

Figure 2-13: FE-BI Result. Normalized error of the induced magnetic field at $z = 0.2$ m, from a sphere with $r = 0.05$ m, $\sigma = 10^7$ S/m, various μ_r. Uniform primary field turned on at $t = 0$.

e	Total Nodes	Surface Nodes	Axial Solve (s)	Transverse Solve (s)
4	3287	177	104.0	703.7
2	2611	149	78.5	490.9
1	2085	129	62.2	346.9
0.5	2745	145	81.7	557.6
0.25	3645	185	121.6	892.5

Table 2.1: CPU times and mesh sizes for the fine mesh. Matlab mesh generator used, enforcing a 1 mm discretization at the surface. A 2 GHz Pentium 4 with 512 MB of RAM is used.

e	Total Nodes	Surface Nodes	Axial Solve (s)	Transverse Solve (s)
4	596	89	27.0	80.3
2	491	73	22.1	61.1
1	400	65	20.3	51.6
0.5	524	73	23.2	69.2
0.25	634	93	29.4	89.3

Table 2.2: CPU times and mesh sizes for the coarse mesh. Matlab mesh generator used, enforcing a 1 mm discretization at the surface. A 2 GHz Pentium 4 with 512 MB of RAM is used.

surface. The number of unknowns increases between 50-75% for the oblate or prolate spheroid cases. The axial case is solved up to eight times faster than the transverse case. This is due to both the requirement of numerical integrations (as outlined in Section 2.2.1), as well as the increased number of unknowns. For the coarse mesh, the transverse case takes up to three times longer to solve than the axial case. Finally, the solution on the coarse mesh is up to ten times faster than the fine mesh.

The results in this section indicate that the FE-BI method is very inaccurate in early time for objects with $\mu_r = 100$. Furthermore, as the FE-BI method's mesh discretization is increased, the accuracy increases slowly while the solution time increases rapidly. The next section will present a method to improve accuracy and efficiency in early time.

2.4 Thin Skin Approximation - Boundary Integral Method

For the high frequency case, or for the early time response to a step change in the primary field, the previous section showed that the FEM has difficulty resolving the skin depth in early time. An alternative to the FEM is required. One possibility is the TSA method, developed in an earlier work to solve the three dimensional high frequency EMI scattering case [53]. In this section, the method will be extended to the time domain axisymmetric case. The TSA method can then be combined with the BI method of Section 2.2.2, replacing the FEM. The new method will be referred to as the TSA-BI method.

2.4.1 Interior Equation

The TSA method begins by enforcing $\nabla \cdot \overline{B} = 0$ inside the target, or equivalently a divergence free magnetic field for a piecewise continuous permeability. A diffusion

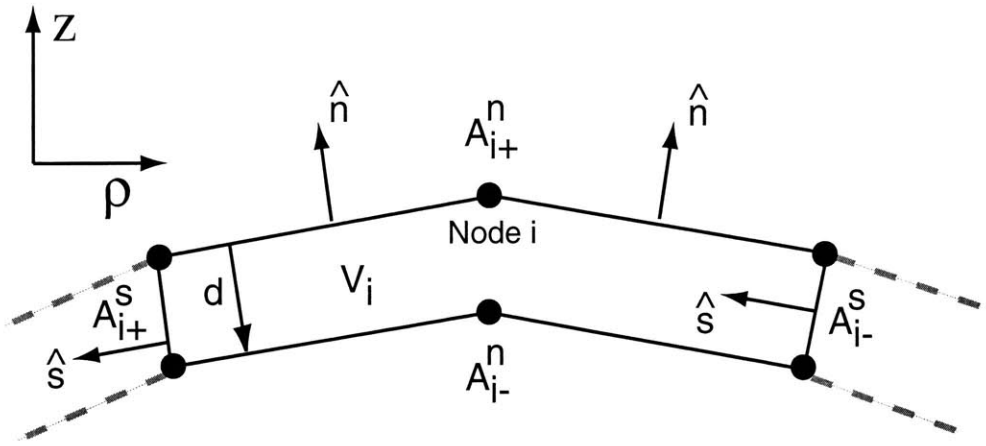

Figure 2-14: The interior control volume used in the divergence equation for the TSA approximation, shown in the $(\hat{\rho}, \hat{z})$ plane. The volume is a ring in three dimensions.

equation (such as Equation 2.8) is no longer used inside the target. A volume V_i is first defined as an interior control volume directly beneath node i on the target surface, as shown in Figure 2-14. Note that the problem is still in three dimensions at this point, such that V_i is a three dimensional ring-like volume, and node i is on a circular contour L_i around the axis of symmetry. A^n_{i+} and A^n_{i-} are the inner and outer areas, joined by surfaces A^s_{i+} and A^s_{i-}. The fields are expressed in the local coordinate system that was introduced in Section 2.2.1. A weighted integral expression of the divergence equation for the magnetic field in the control volume is then

$$\int_{V_i} dV_i \; \alpha_i' \nabla \cdot \overline{H} = \int_{V_i} dV_i \; \{\nabla \cdot (\alpha_i' \overline{H}) - \overline{H} \cdot \nabla \alpha_i'\} = 0 \tag{2.145}$$

where α_i' is a weighting function. The magnetic field in the local coordinate system is $\overline{H} = \hat{n} H^{(n)} + \hat{\phi} H^{(\phi)} + \hat{s} H^{(s)}$. Applying the divergence theorem to Equation 2.145 and dividing through by the volume depth d yields [53]

$$\frac{1}{d}\int_{A_{i+}^{n}} dA\,\alpha_i' H^{(n)} - \frac{1}{d}\int_{A_{i-}^{n}} dA\,\alpha_i' H^{(n)} + \frac{1}{d}\int_{A_{i+}^{s}} dA\,\alpha_i' H^{(s)} - \frac{1}{d}\int_{A_{i-}^{s}} dA\,\alpha_i' H^{(s)}$$
$$- \frac{1}{d}\int_{V_i} dV\,\overline{H}\cdot\nabla\alpha_i' = 0 \tag{2.146}$$

As d is reduced, the first two integrals merge to a normal derivative of the integral over A_n^+. The integrals over A_s^+ and A_s^- reduce to line integrals over L_{i+1} and L_{i-1}, which are the paths created by nodes $(i+1)$ and $(i-1)$ around the axis of symmetry. At this point the weighting function, α_i', can be defined. A Galerkin formulation is used, so that the basis and weighting functions are the same. As a result, an α_i' must be chosen that can approximate the magnetic field and be compatible with the BI formulation. (Note that the BI formulation applied the weighting and basis functions *after* the problem was reduced to two dimensions; here, they are applied immediately to the three dimensional problem.) Hence, in the $(\hat{\rho},\hat{z})$ plane, α_i' must also be a linear (rooftop) function, defined as α_i in Section 2.2.2 (Equations 2.113 and 2.114). Using this function in Equation 2.146, both line integrals are zero, because α_i' is zero at L_{i+1} or L_{i-1} (regardless of the azimuthal variation). The magnetic field in the final integral of Equation 2.146 may be expressed in terms of ψ using Equation 2.10 to obtain

$$\frac{\partial}{\partial n_1}\int_{A_i^n} dA\,\alpha_i' H^{(n)} + \int_{A_i^n} dA\,\nabla\psi\cdot\nabla\alpha_i' = 0 \tag{2.147}$$

The two remaining unknowns in Equation 2.147 are $H^{(n)}$ and ψ, which need to be expanded in terms of α_i'. Recall that ψ has a cosine azimuthal variation (Equation 2.25), and by taking its gradient the magnetic field may be expressed as

$$\overline{H} = \sum_{p=0}^{\infty}\left[\hat{\rho}H_p^{(\rho)}(\rho,z)\cos(p\phi) + \hat{\phi}H_p^{(\phi)}(\rho,z)\sin(p\phi) + \hat{z}H_p^{(z)}(\rho,z)\cos(p\phi)\right] \tag{2.148}$$

For an axisymmetric target, $\hat{n}$ has only $\hat{\rho}$ and $\hat{z}$ dependence, and therefore $H^{(n)}$ has only $\cos(p\phi)$ azimuthal variation. As a result, the weighting function for Equa-

tion 2.147 can now be written as

$$\alpha_i'(\rho,\phi,z) = \sum_{q=0}^{\infty} \alpha_i(\rho,z)\cos(q\phi) \tag{2.149}$$

The normal component of the magnetic field can be written as a summation of basis functions over the contour:

$$H^{(n)} = \sum_{j=1}^{N_\Gamma} H_j^{(n)}\alpha_j' = \sum_{j=1}^{N_\Gamma}\sum_{p=0}^{\infty} H_{pj}^{(n)}\ \alpha_j\cos(p\phi) \tag{2.150}$$

The weighting and basis functions are defined such that $\hat{n}_1\cdot\nabla\alpha_i' = 0$, so the first term of Equation 2.147 can be expressed as

$$\begin{aligned}&\sum_{j=1}^{N_\Gamma}\sum_{p=0}^{\infty}\frac{\partial}{\partial n_1}\int_{A_i^n} dA\,\alpha_i'\ H_{pj}^{(n)}\ \alpha_j\cos(p\phi)\\ &= \sum_{j=1}^{N_\Gamma}\sum_{p=0}^{\infty}\left(\frac{1}{A_i^n}\frac{\partial A_i^n}{\partial n_1}H_{pj}^{(n)} + \frac{\partial H_{pj}^{(n)}}{\partial n_1}\right)\int_{A_i^n} dA\ \ \alpha_i'\ \alpha_j\cos(p\phi)\end{aligned} \tag{2.151}$$

Equation 2.151 can be substituted into Equation 2.147. The azimuthal part is integrated out, for which the terms where $p \neq q$ yield zero. The result is a two dimensional integral over the entire surface contour:

$$\begin{aligned}&\sum_{j=1}^{N_\Gamma}\sum_{p=0}^{\infty}\left(\frac{1}{A_i^n}\frac{\partial A_i^n}{\partial n_1}H_{pj}^{(n)} + \frac{\partial H_{pj}^{(n)}}{\partial n_1}\right)\int_{\Gamma_{i-1}}^{\Gamma_{i+1}} ds\ \rho\ \alpha_i\ \alpha_j\\ &+\sum_{j=1}^{N_\Gamma}\sum_{p=0}^{\infty}\psi_{pj}\int_{\Gamma_{i-1}}^{\Gamma_{i+1}} ds\ \left(\rho\nabla\alpha_i\cdot\nabla\alpha_j + \frac{p^2}{\rho}\ \alpha_i\ \alpha_j\right)\end{aligned} \tag{2.152}$$

for $i = 1,\ldots,N_\Gamma$. Hence, we have an equation in terms of ψ, $H^{(n)}$, and $\frac{\partial H^{(n)}}{\partial n_1}$ along the surface. The problem remains to find an expression for $\frac{\partial H^{(n)}}{\partial n_1}$ in terms of $H^{(n)}$, which would yield an equation with two unknowns that can be solved with Equation 2.143.

2.4.2 Thin Skin Approximation

The TSA was shown in [53] to be successful in the frequency domain using $\frac{\partial H^{(n)}}{\partial n_1} = -ik\xi_n H^{(n)}$, where ξ_n is a correction factor. For a time domain TSA, we begin by considering that the interior magnetic field is governed by the diffusion equation, similar to Equation 2.8. One dimensional solutions of the diffusion equation for a step change at a boundary is the complementary error function [60], denoted as 'erfc'. A time domain TSA can be implemented by assuming that the normal component of the magnetic field at each node can be approximated by the one dimensional solution in the normal direction. Hence, the magnetic field will be defined as a function of time and the normal direction, $H^{(n)}(n,t)$. For a given discrete time t_m, the normal component of the magnetic field on the contour at $n = 0$ is denoted as $H^{(n)}(0,t_m) = H^{(n)}_{(m)}$. The initial condition for the magnetic field on the contour is $H^{(n)}_{(0)}$, and is either equal to zero when $H^{PR}(t) = u(t)$, or is the static solution when $H^{PR}(t) = 1 - u(t)$. The FE-BI method can be used to find static solution very efficiently, as no time stepping is required and a coarse mesh can be used. If the normal component of the magnetic field on the contour at t_1 is to change to $H^{(n)}_{(1)}$, we can approximate the normal dependence of the solutions as

$$H^{(n)}(n,t_1) = H^{(n)}_{(0)} + (H^{(n)}_{(1)} - H^{(n)}_{(0)}) f(t_1 - t_0, n) \tag{2.153}$$

where

$$f(n,t) = \text{erfc}\left(\frac{n}{2\sqrt{\Lambda(t)}}\right) \tag{2.154}$$

where $\Lambda = 1/\sqrt{\sigma\mu}$. Equation 2.153 can be found directly from the one dimensional diffusion equation for the given parameters and appropriate boundary conditions. At time $t = t_2$, the magnetic field would again change, this time to $H^{(n)}_{(2)}$, and the solution of the interior magnetic field would be

$$H^{(n)}(n,t_2) = H^{(n)}_{(0)} + (H^{(n)}_{(1)} - H^{(n)}_{(0)}) f(n,t_2 - t_0) + (H^{(n)}_{(2)} - H^{(n)}_{(1)}) f(n,t_2 - t_1) \tag{2.155}$$

and so on, such that the solution for any $t = t_M$ would be

$$H^{(n)}(n, t_M) = H^{(n)}_{(0)} + \sum_{m=1}^{M} (H^{(n)}_{(m)} - H^{(n)}_{(m-1)}) f(n, t_M - t_{m-1}) \tag{2.156}$$

which can be cast in integral form as

$$H^{(n)}(n, t_M) = H^{(n)}_{(0)} + \int_0^{t_M} d\tau \frac{\partial H^{(n)}(\tau)}{\partial \tau} f(n, t_M - \tau) \tag{2.157}$$

The normal derivative of $H^{(n)}$ for mode p at node i in Equation 2.152 can then be written as a recursion

$$\frac{\partial H^{(n)}_{pj,(M)}}{\partial n_1} = \frac{2}{\sqrt{\Lambda \pi}} \sum_{m=1}^{M} \left(\frac{H^{(n)}_{pj,(m)} - H^{(n)}_{pj,(m-1)}}{\Delta t_m} \right) R(t_M, t_m) \tag{2.158}$$

where $R(t_M, t_m) = \left[\sqrt{(t_M - t_m)} - \sqrt{(t_M - t_{m-1})} \right]$ and $\Delta t_m = t_m - t_{m-1}$. The normal derivative may then be substituted into Equation 2.152, resulting in an equation with two unknowns on the surface: $H^{(n)}_{(M)}$ and $\psi_{(M)}$. The final form of the interior equation is

$$\begin{aligned}
&\sum_{j=1}^{N_\Gamma} \sum_{p=0}^{\infty} H^{(n)}_{pj,(M)} \left[\frac{-2}{\sqrt{\Delta t_M \Lambda \pi}} + \frac{1}{A^n_i} \frac{\partial A^n_i}{\partial n_1} \right] \int_{\Gamma_{i-1}}^{\Gamma_{i+1}} ds\, \rho\, \alpha_i \alpha_j \\
&- \sum_{j=1}^{N_\Gamma} \sum_{p=0}^{\infty} \psi_{pj,(M)} \int_{\Gamma_{i-1}}^{\Gamma_{i+1}} ds \left(\rho \nabla \alpha_i \cdot \nabla \alpha_j + \frac{p^2}{\rho}\, \alpha_i\, \alpha_j \right) = \sum_{j=1}^{N_\Gamma} \sum_{p=0}^{\infty} \frac{2}{\sqrt{\Lambda \pi}} \\
&\times \left[-\frac{H^{(n)}_{pj,(M-1)}}{\sqrt{\Delta t_M}} - \sum_{m=1}^{M-1} \left(\frac{H^{(n)}_{pj,(m)} - H^{(n)}_{pj,(m-1)}}{\Delta t_M} \right) R(t_M, t_m) \right] \int_{\Gamma_{i-1}}^{\Gamma_{i+1}} ds\, \rho\, \alpha_i \alpha_j
\end{aligned} \tag{2.159}$$

Equations 2.159 and 2.99 can then be used to solve for the unknowns on the surface, $H^{(n)}_{(M)}$ and $\psi_{(M)}$. An interior mesh is not required, and hence the TSA-BI method is much more efficient than the FE-BI method. Furthermore, there is no restriction the

skin depth in early time. However at some later time, when the fields have significant penetration into the object, the semi-analytical form of $H^{(n)}$ will no longer be valid and the method will fail. The regime of validity of TSA-BI method is investigated in the following section.

2.5 Thin Skin Approximation - Boundary Integral Results

The TSA-BI solution can also be compared with the analytical solution for a sphere. Figure 2-15 shows the nonmagnetic sphere's induced magnetic field at $z = 0.2$ m for the axial and transverse excitation cases. In both cases, the TSA-BI method is very accurate in early time but begins to diverge from the analytical solution at approximately $t = 10^{-4}$s. At that time the skin depth begins to depend on the geometry and the 1D semi-analytical approximation of Equation 2.154 is no longer accurate. Figure 2-16 shows the induced field from the $\mu_r = 100$ sphere. The accuracy is excellent in this case, with the TSA-BI method solution diverging slightly from the analytical solution at approximately 10^{-2} s. As shown in Figure 2-6, the skin depth appears to be small through intermediate time. Hence, the semi-analytical approximation and the TSA-BI method remains accurate for most of the time history.

The normalized error analysis can be performed for the TSA-BI method, shown in Figure 2-17 for the axial case. For the nonmagnetic case the TSA-BI method begins is very accurate in early time, and begins to diverge from the analytical solution at approximately 10^{-4} s for each spheroid. At 0.1 s, the error ranges from 0.1 to greater than 0.6, and will continue to diverge in time. For the $\mu_r = 100$ case, the error is very low over the entire time history, with a maximum of between 0.01 and 0.05 at 0.1 s. Figure 2-18 shows the TSA-BI method's error for the transverse excitation case. The trends are similar to the axial excitation case, although the oblate spheroid with $e = 0.25$ exhibits larger error for both the $\mu_r = 1$ and $\mu_r = 100$ cases. Figure 2-19

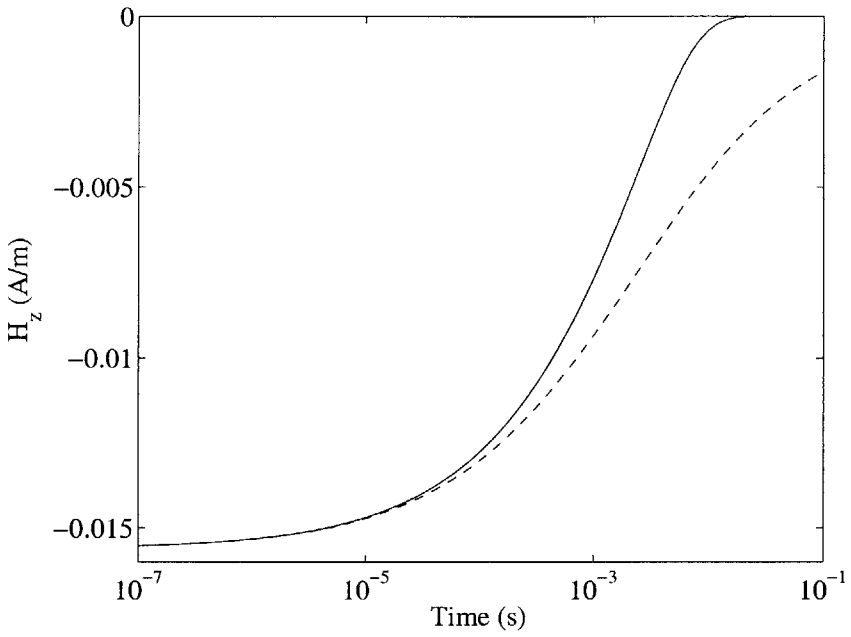

(a) Induced field from $\overline{H}^{PR} = \hat{z}\, u(t)$ excitation

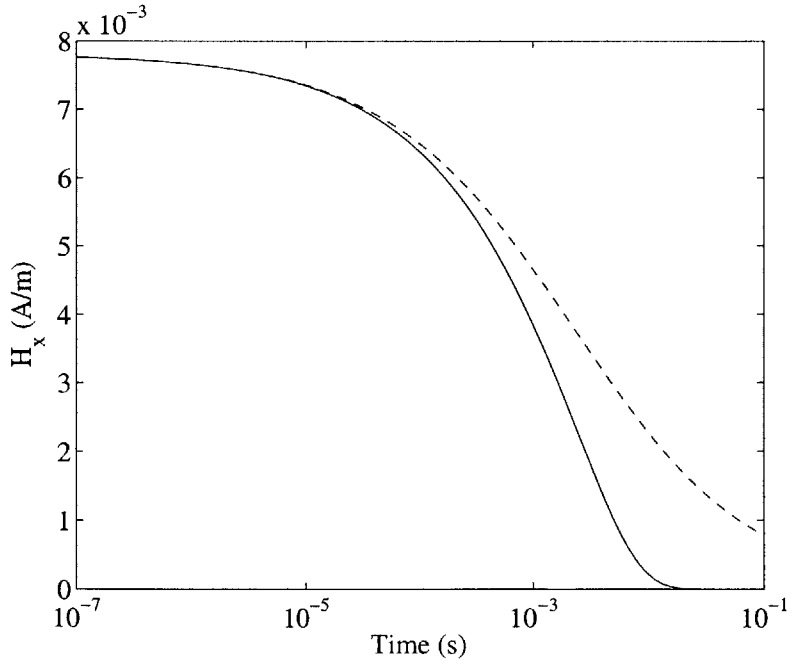

(b) Induced field from $\overline{H}^{PR} = \hat{x}\, u(t)$ excitation

Figure 2-15: Induced magnetic field at $z = 0.2$ m, from a sphere with $r = 0.05$ m, $\mu_r = 1$, $\sigma = 10^7$ S/m. Uniform primary field turned on at $t = 0$. Solid line is the analytical solution, dash line is the TSA-BI method.

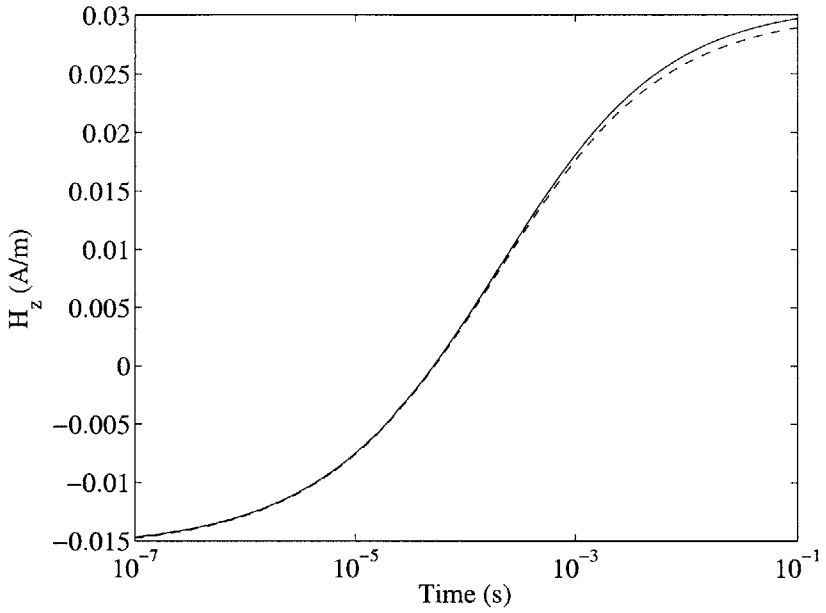

(a) Induced field from $\overline{H}^{PR} = \hat{z}\, u(t)$ excitation

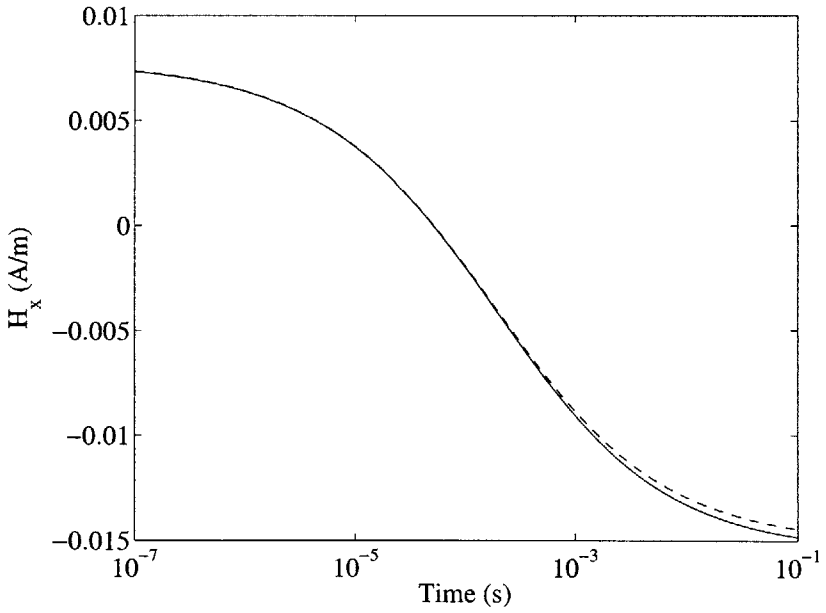

(b) Induced field from $\overline{H}^{PR} = \hat{x}\, u(t)$ excitation

Figure 2-16: Induced magnetic field at $z = 0.2$ m, from a sphere with $r = 0.05$ m, $\mu_r = 100$, $\sigma = 10^7$ S/m. Uniform primary field turned on at $t = 0$. Solid line is the analytical solution, dash line is the TSA-BI method.

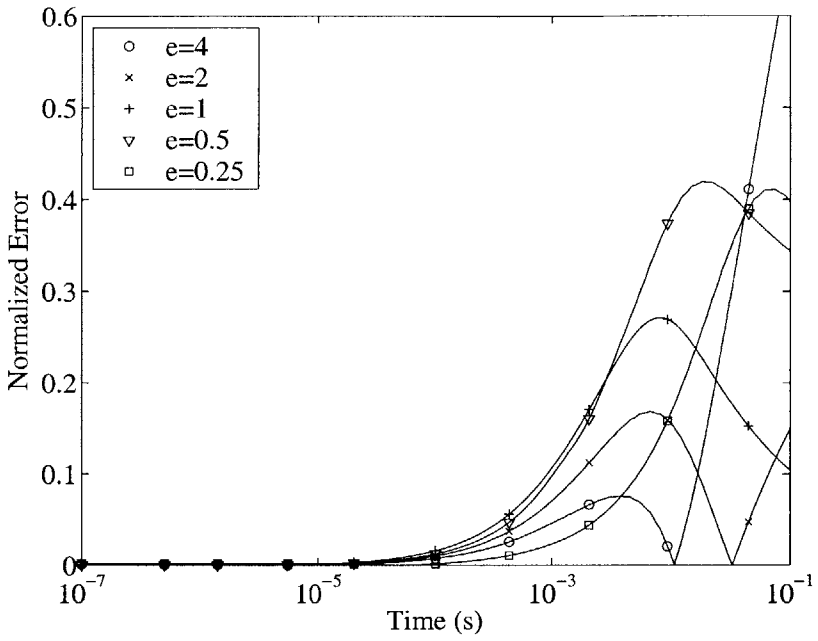

(a) Response from $\overline{H}^{PR} = \hat{z}\, u(t)$ excitation, $\mu_r = 1$

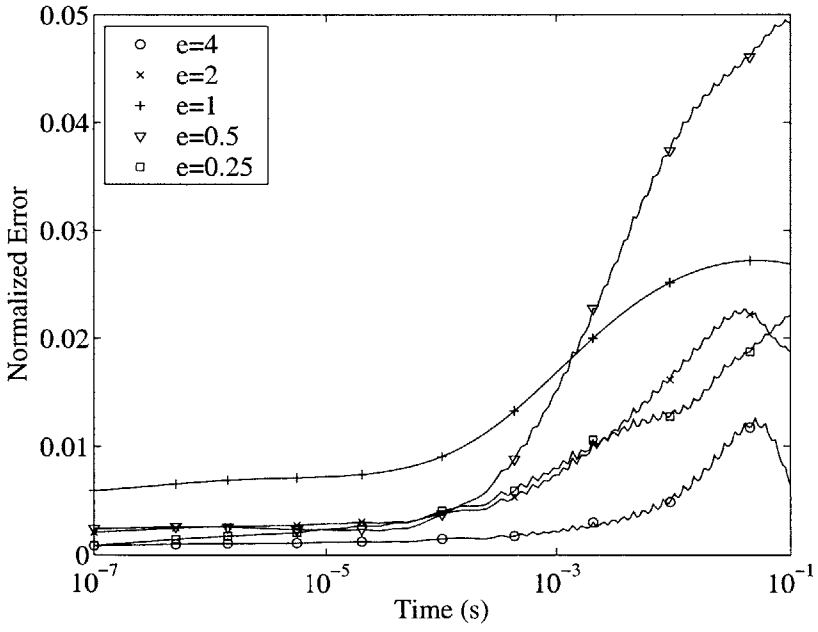

(b) Response from $\overline{H}^{PR} = \hat{z}\, u(t)$ excitation, $\mu_r = 100$

Figure 2-17: TSA-BI Result. Normalized error of the induced magnetic field at $z = 4b$ m from various spheroids. Minor axis a or $b = 0.05$ m $\sigma = 10^7$ S/m. Uniform primary field turned on at $t = 0$.

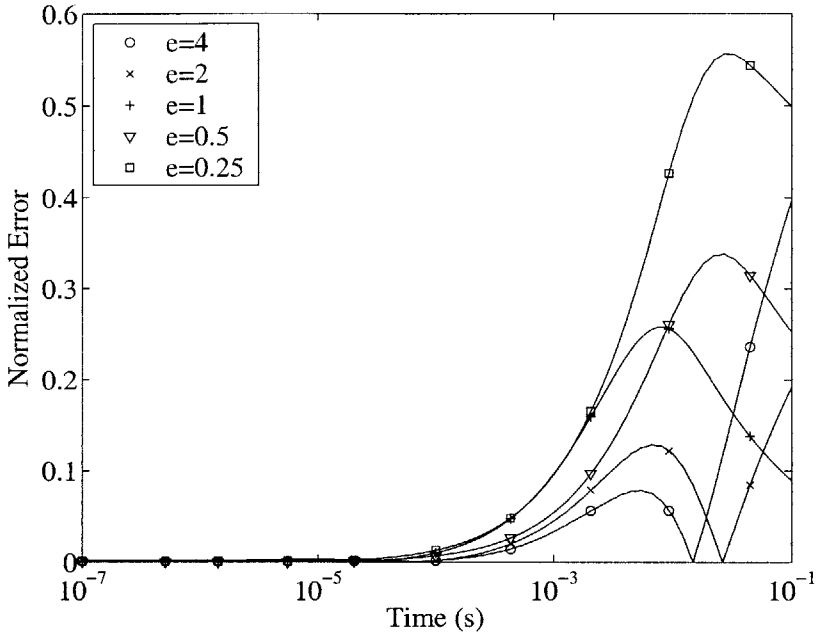

(a) Response from $\overline{H}^{PR} = \hat{x}\ u(t)$ excitation, $\mu_r = 1$

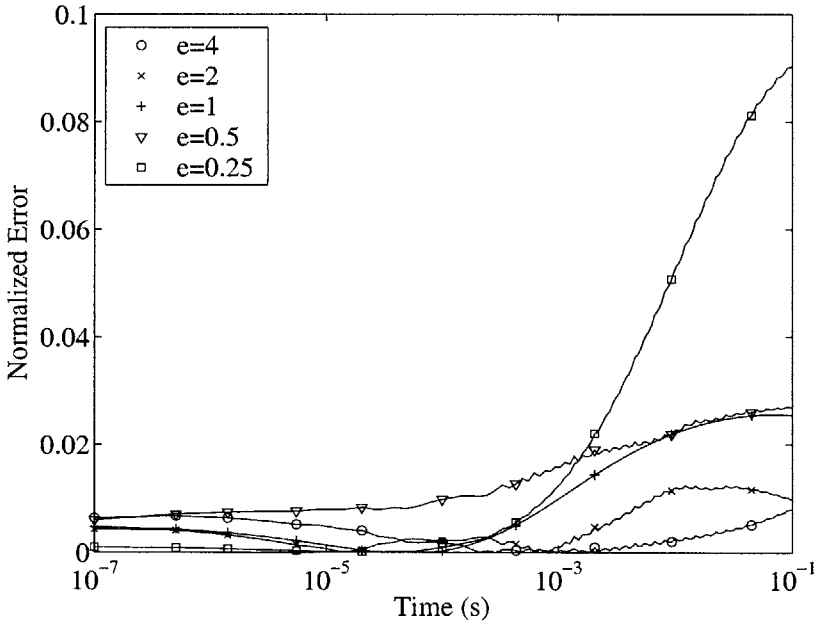

(b) Response from $\overline{H}^{PR} = \hat{x}\ u(t)$ excitation, $\mu_r = 100$

Figure 2-18: TSA-BI Result. Normalized error of the induced magnetic field at $z = 4b$ m from various spheroids. Minor axis a or $b = 0.05$ m $\sigma = 10^7$ S/m. Uniform primary field turned on at $t = 0$.

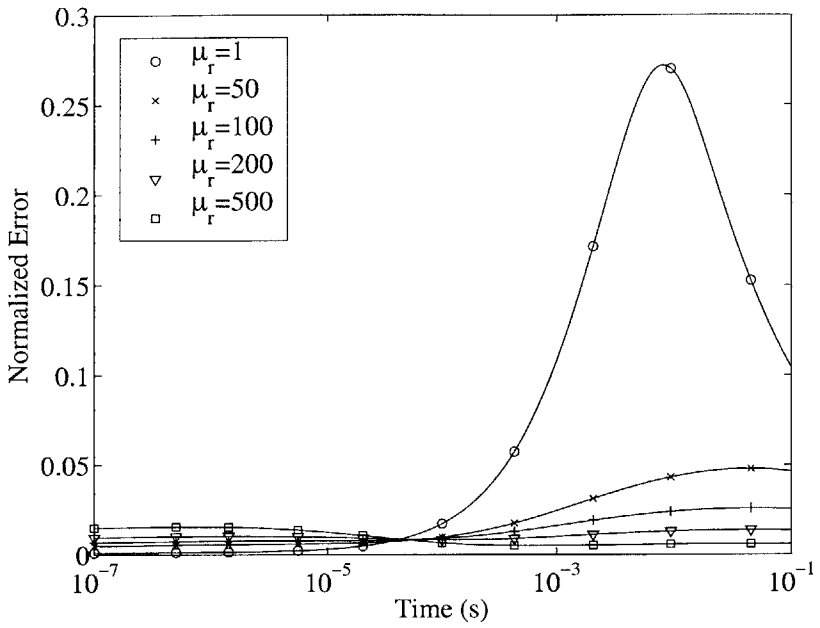

(a) Response from $\overline{H}^{PR} = \hat{z}\, u(t)$ excitation

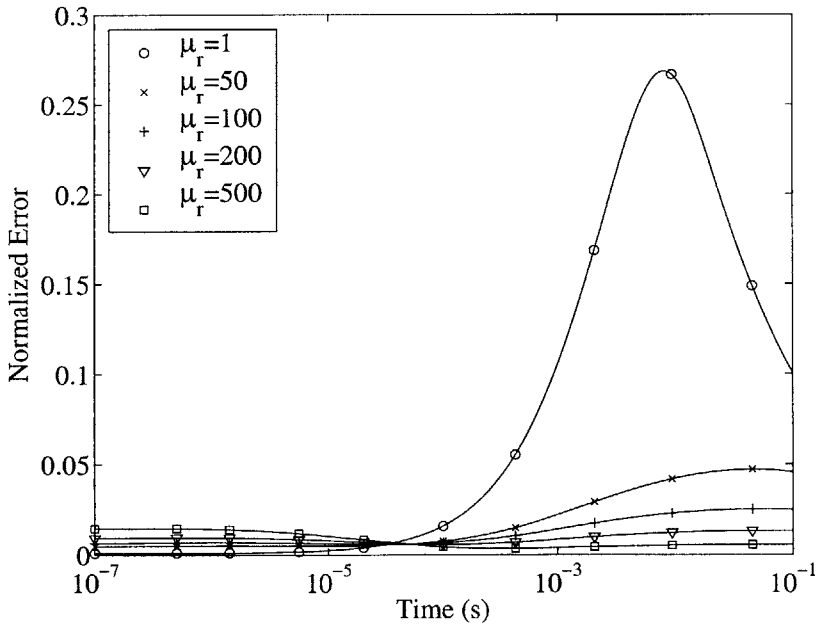

(b) Response from $\overline{H}^{PR} = \hat{x}\, u(t)$ excitation

Figure 2-19: TSA-BI Result. Normalized error of the induced magnetic field at $z = 0.2$ m, from a sphere with $r = 0.05$ m, $\sigma = 10^7$ S/m. Uniform primary field turned on at $t = 0$.

shows the TSA-BI normalized error for the induced field from the 5 cm radius sphere with various permeabilities. As the permeability increases, the skin depth decreases, and the TSA-BI method accuracy gets better. The maximum error is approximately 0.275 for the $\mu_r = 1$ case. Both the axial and transverse excitations show similar results.

Given that the TSA-BI method is accurate in early to intermediate time, and the FE-BI method is accurate in intermediate to late time, it is natural to combine them. The FE-BI method can be run efficiently on a relatively coarse mesh, and the TSA-BI method is run separately. The two results may be combined at the point in time where they converge the closest. Figure 2-20 shows the results for the axial and transverse excitation cases when $\mu_r = 100$. For the combined method, the maximum error occurs in intermediate time when the two methods converge. For the axial excitation case, the maximum error is 0.035 which occurs in the solution for the $e = 0.5$ oblate spheroid (see Figure 2-17). For the transverse excitation case, the maximum error is 0.05, which occurs for the $e = 0.25$ oblate spheroid case (see Figure 2-18). In both cases, and for other spheroids, the error is small and certainly sufficient for inversion techniques. Figure 2-21 shows the normalized error using the combined method for a sphere with various permeabilities. The maximum error is 0.025, which occurs for the $\mu_r = 50$ case. The error of the combined method is very low regardless of the permeability.

Finally, for efficiency concerns it is useful to study the error of the combined method for larger time steps. In general, the FE-BI and TSA-BI methods may be adjusted to march in time as $t = n^\gamma \Delta t_0$ (where $\Delta t_0 = 10^{-7}$ s). The implicit Euler method used for both methods (Equation 2.141) accumulates error on order of Δt. For the previous results, $\gamma = 2$ was chosen due to the $\sqrt{t}$ evolution of diffusion equations. For that time step, the TSA-BI and FE-BI methods are very accurate in their respective regions of validity, so the time stepping error must be small. Hence, γ can be increased to achieve faster solution times while still maintaining reasonable

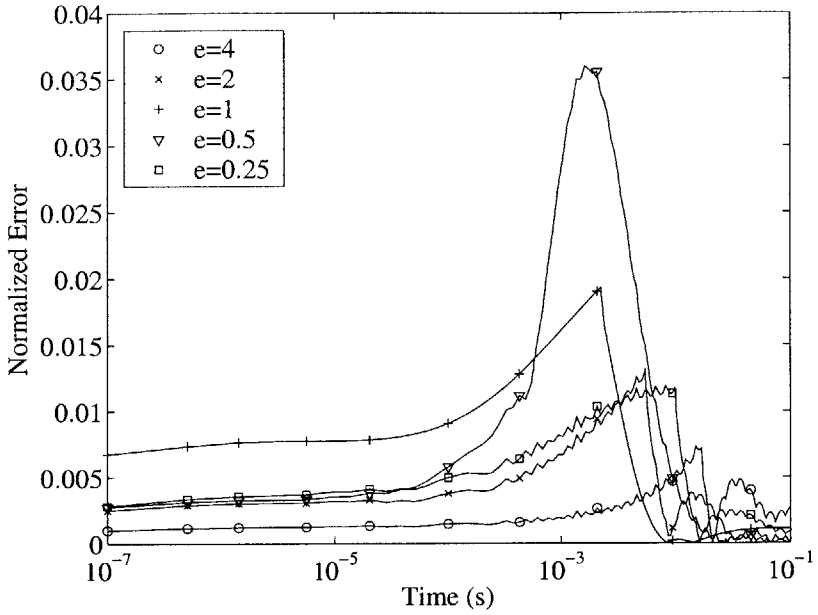

(a) Response from $\overline{H}^{PR} = \hat{z}\, u(t)$ excitation, $\mu_r = 1$

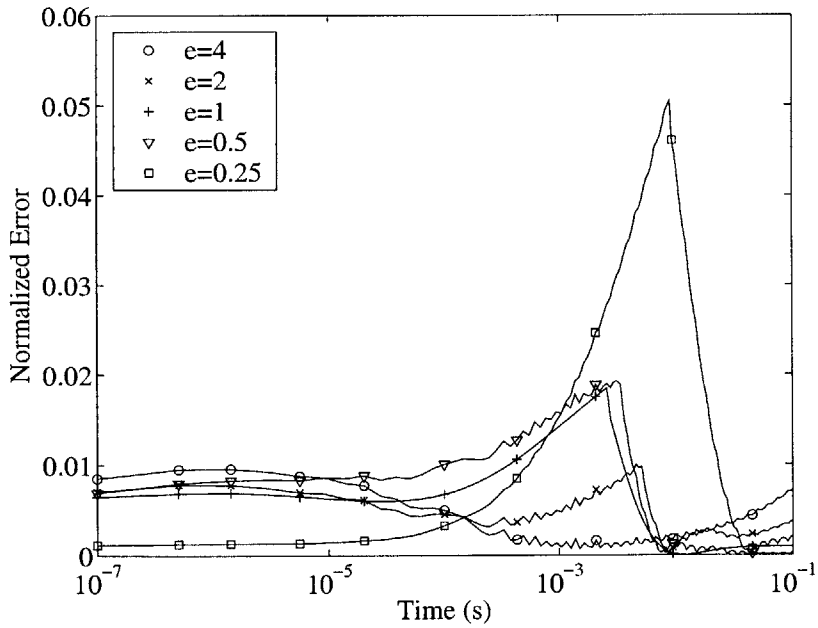

(b) Response from $\overline{H}^{PR} = \hat{z}\, u(t)$ excitation, $\mu_r = 100$

Figure 2-20: FE-BI and TSA-BI Combined result. Normalized error of the induced magnetic field at $z = 4b$ m from various spheroids. Minor axis a or $b = 0.05$ m $\sigma = 10^7$ S/m. Uniform primary field turned on at $t = 0$.

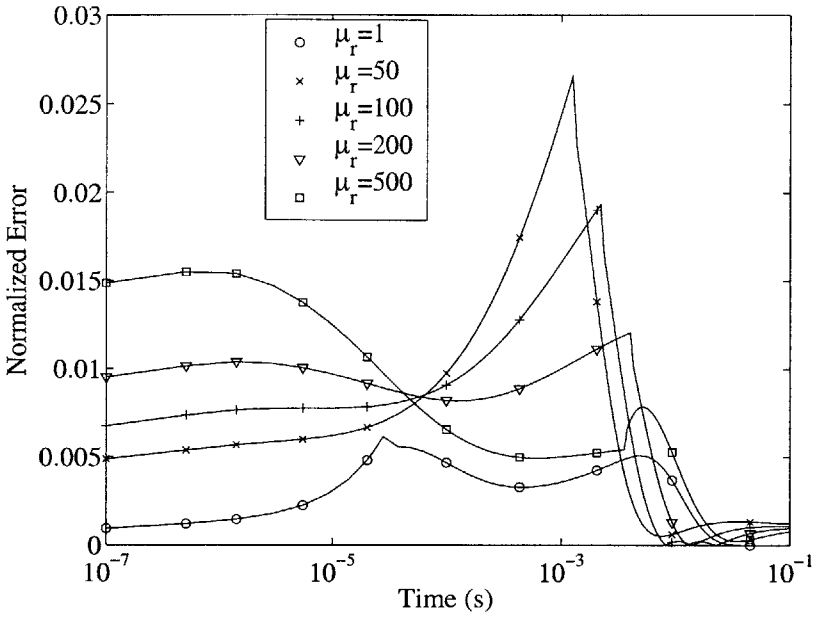

(a) Response from $\overline{H}^{PR} = \hat{z}\ u(t)$ excitation

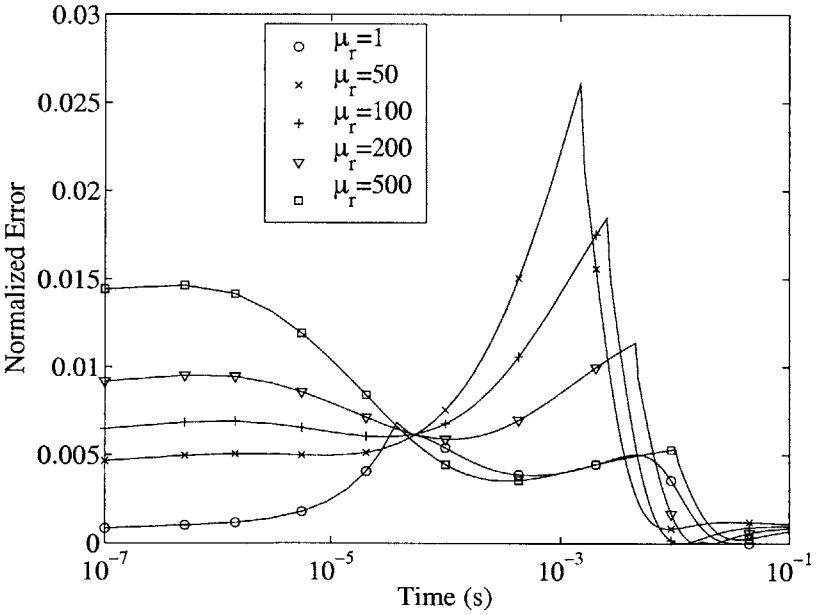

(b) Response from $\overline{H}^{PR} = \hat{x}\ u(t)$ excitation

Figure 2-21: FE-BI and TSA-BI Combined result. Normalized error of the induced magnetic field at $z = 0.2$ m, from a sphere with $r = 0.05$ m, $\sigma = 10^7$ S/m. Uniform primary field turned on at $t = 0$.

	Solution Time (s)			
Case	$\gamma = 2$	$\gamma = 2.5$	$\gamma = 3$	$\gamma = 4$
$e = 4$, Axial	38.6804	18.8927	12.2039	7.5153
$e = 4$, Transverse	92.5527	47.1724	30.9015	19.5674
$e = 2$, Axial	33.1828	16.1154	9.7389	5.8130
$e = 2$, Transverse	73.3687	37.5907	23.7468	14.7628
$e = 1$, Axial	31.7138	14.7736	9.0409	5.2574
$e = 1$, Transverse	63.0937	30.9593	19.9475	12.2008
$e = 0.5$, Axial	45.6018	21.4460	13.1201	7.3437
$e = 0.5$, Transverse	91.0218	45.2780	29.0230	17.3571
$e = 0.25$, Axial	49.2875	24.2587	15.2836	9.0718
$e = 0.25$, Transverse	111.3347	55.9075	36.2661	22.5182

Table 2.3: CPU times of the combined method for different time steps - $t = n^{\gamma}\Delta_t$ where $\Delta_t = 10^{-7}s$. A 2 GHz Pentium 4 with 512 MB of RAM is used.

accuracy. Tables 2.3 and 2.4 provide the CPU times and normalized error as γ is increased. All the cases dealt with earlier are presented in the tables. Generally, the $\gamma = 4$ solution is calculated five times faster than the $\gamma = 2$ solution. The maximum error increases slightly as γ increases, and the user can ultimately decide what compromise to make between accuracy and efficiency.

2.6 Comparison With Experiments

As discussed earlier, EMI scattering sensors operate in both the frequency domain and the time domain. An advantage of time domain instruments is that the primary field is off when the measurements are taken. Hence, more sensitive measurements can be taken and the receiver coils may be set in any configuration. Figure 2-22(a) shows an experimental setup of a chrome-steel sphere placed within a Helmholtz coil. The primary coils are 1.57 m on a side and are separated by 0.89 m. The primary

Case	$\gamma = 2$	$\gamma = 2.5$	$\gamma = 3$	$\gamma = 4$
$e = 4$, Axial, $\mu = 1$	0.0149	0.0157	0.0169	0.0298
$e = 4$, Axial, $\mu = 100$	0.0073	0.0148	0.0101	0.0152
$e = 4$, Transverse, $\mu = 1$	0.0150	0.0158	0.0170	0.0296
$e = 4$, Transverse, $\mu = 100$	0.0096	0.0135	0.0192	0.0369
$e = 2$, Axial, $\mu = 1$	0.0080	0.0090	0.0145	0.0304
$e = 2$, Axial, $\mu = 100$	0.0130	0.0139	0.0153	0.0236
$e = 2$, Transverse, $\mu = 1$	0.0078	0.0087	0.0141	0.0298
$e = 2$, Transverse, $\mu = 100$	0.0100	0.0432	0.0163	0.0323
$e = 1$, Axial, $\mu = 1$	0.0280	0.0282	0.0282	0.0350
$e = 1$, Axial, $\mu = 100$	0.0174	0.0188	0.0216	0.0333
$e = 1$, Transverse, $\mu = 1$	0.0219	0.0221	0.0228	0.0329
$e = 1$, Transverse, $\mu = 100$	0.0276	0.0276	0.0278	0.0293
$e = 0.5$, Axial, $\mu = 1$	0.0036	0.0073	0.0132	0.0279
$e = 0.5$, Axial, $\mu = 100$	0.0192	0.0200	0.0216	0.0392
$e = 0.5$, Transverse, $\mu = 1$	0.0065	0.0092	0.0140	0.0299
$e = 0.5$, Transverse, $\mu = 100$	0.0360	0.0313	0.0338	0.0394
$e = 0.25$, Axial, $\mu = 1$	0.0037	0.0067	0.0118	0.0270
$e = 0.25$, Axial, $\mu = 100$	0.0118	0.0122	0.0133	0.0235
$e = 0.25$, Transverse, $\mu = 1$	0.0165	0.0171	0.0180	0.0317
$e = 0.25$, Transverse, $\mu = 100$	0.0504	0.0541	0.0553	0.0622

Table 2.4: Maximum normalized error of the combined method for different time steps $t = n^{\gamma}\Delta_t$ where $\Delta_t = 10^{-7}s$.

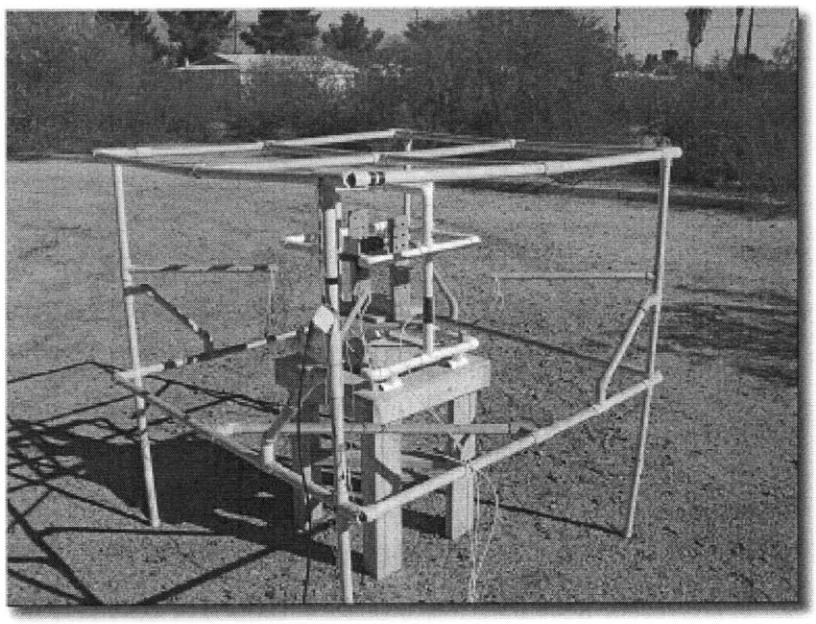

(a) Helmholtz coil, courtesy of: Zonge Engineering, 3322 East Fort Lowell Road, Tucson, AZ 85716.

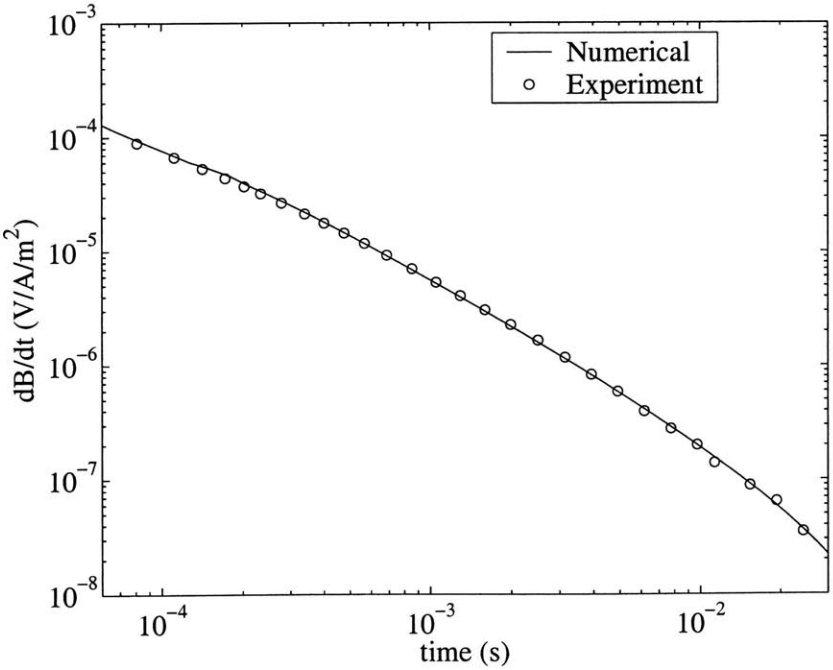

(b) Comparison with experimental data

Figure 2-22: Comparison of the combined method with experimental data from a Helmholtz coil. Parameters extracted are $\sigma = 2.2 \times 10^6$ S/m and $\mu_r = 31$.

field is turned off and the induced field ($\partial B/\partial t$) from the sphere is measured in the receiver coil. The transmitter coil is modeled with the Biot-Savart law to calculate the primary field incident on the sphere. The primary field is used as the input to the FE-BI and TSA-BI methods, and incorporates the 50 μ s linear ramp of the instrument. The induced field is calculated over the area of the receiver coil, and a quadrature integration is used to calculate the effective $\partial B/\partial t$. The parameters of the sphere are unknown, so a Nelder-Mead simplex (direct search) method is used to match the FE-BI and TSA-BI combined method to the data. The best match occurs when $\sigma = 2.2 \times 10^6$ S/m and $\mu_r = 32$. There is some ambiguity in this result, as another reasonable match is $\sigma = 4.2 \times 10^6$ and $\mu_r = 78$. Previous results have indicated that the response depends on the μ_r/σ ratio as much as the parameters themselves [64]. Figure 2-23 shows the Zonge TEM field instrument that is used by Zonge Engineering to detect and discriminate UXO. The chrome steel sphere is buried 17 cm below the instrument. The transmitter is a large octagonal coil, surrounding the three smaller receiver coils. The entire instrument is again modeled with the Biot-Savart law to obtain the primary field, which in this case is not uniform but must be approximated as such. Transverse excitation is obtained by tilting the instrument on its side. Using the parameters determined from the Helmholtz coil, the FE-BI and TSA-BI combined method yields results shown in Figure 2-24 that are very close to the experimental data. As is common practice, a magnitude correction factor of 2.3 is applied to both results, which likely accounts for unknown factors in the receiver circuitry.

2.7 Conclusions

This chapter presented a hybrid time domain numerical method that can calculate the EMI response from a UXO target with greater accuracy and speed than previous available. In response to a transient primary field, a conducting and permeable UXO

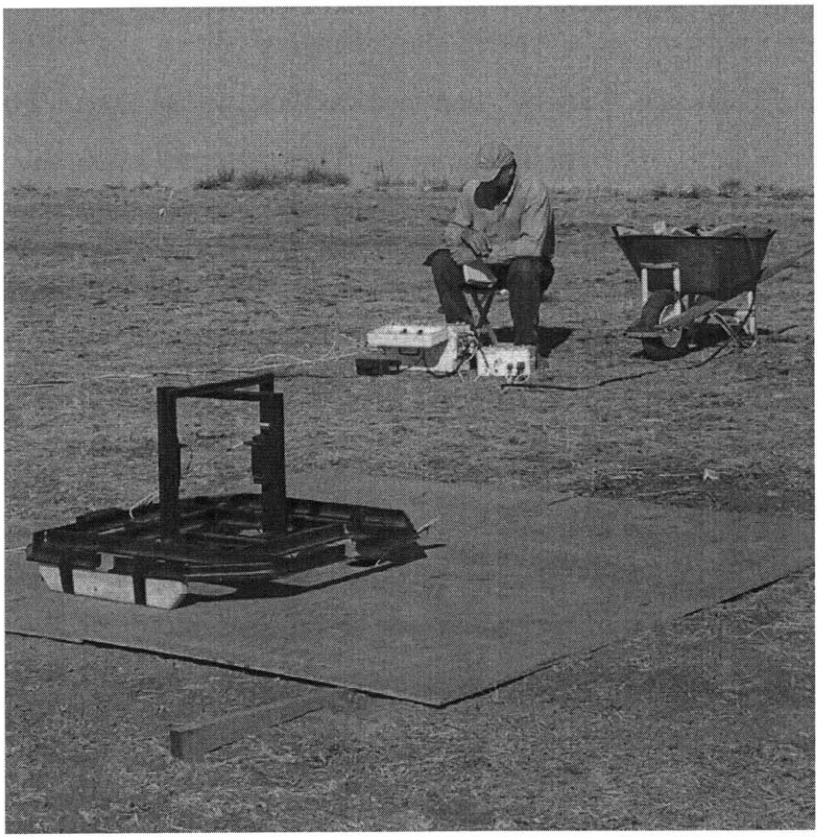

Figure 2-23: TEM instrument, courtesy of: Zonge Engineering, 3322 East Fort Lowell Road, Tucson, AZ 85716.

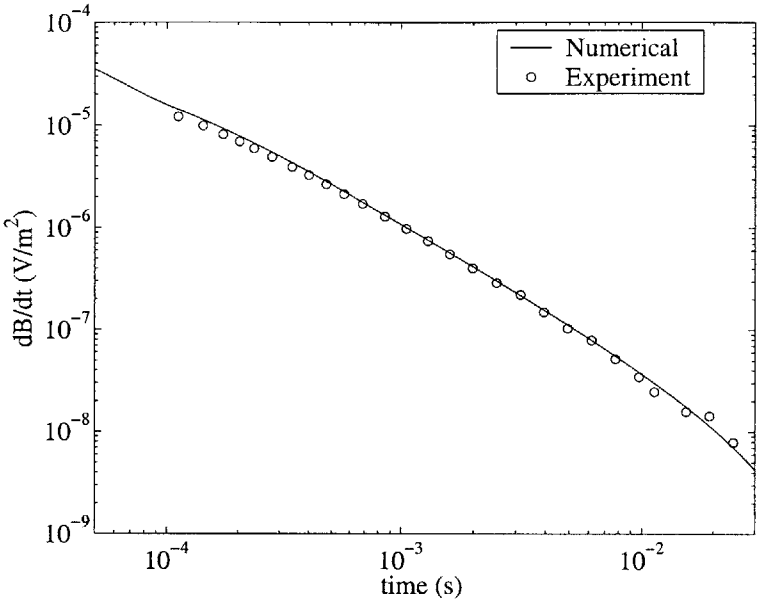

(a) Comparison with experimental data, axial excitation.

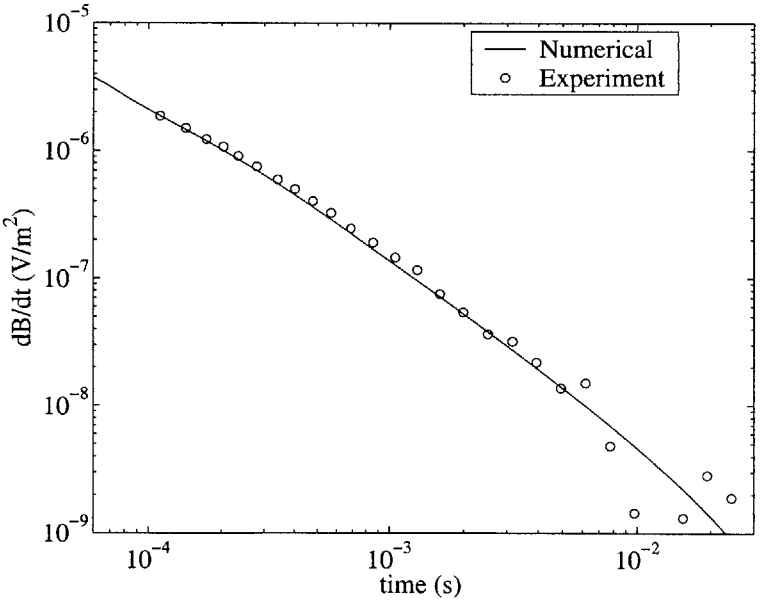

(b) Comparison with experimental data, transverse excitation.

Figure 2-24: Comparison of the combined method with experimental data from the Zonge TEM instrument. Parameters used are $\sigma = 2.2 \times 10^6$ S/m and $\mu_r = 31$, previously extracted from the Helmholtz coil data. Magnitude correction of 2.3 applied to both cases.

target produces a transient secondary field. In early time, the field within the target has a small skin depth that is difficult to model with conventional numerical methods like the FEM. To demonstrate this, an FE-BI method was implemented and shown to be inaccurate in early time. The ability to resolve very small skin depths in early time (or high frequency) was enabled by the TSA method that replaces the interior FEM and does not require an interior mesh. The TSA-BI method produced a faster and more accurate solution to the EMI problem for early to intermediate time scales, compared to the FE-BI method. For certain materials, such as steel, the TSA-BI method was shown to be accurate throughout the entire time of interest. Furthermore, the methods were combined, so that the TSA-BI solution was used for early time and the FE-BI method was used (on an efficient mesh) for late time. Compared to the standard FE-BI method, the new method is much more accurate and at least ten times faster. The results were compared with experimental results, and the agreement was excellent.

Chapter 3

Fast Calculation of Electromagnetic Wave Scattering from Layered Rough Surfaces

3.1 Introduction

Electromagnetic wave scattering from rough surfaces is a popular topic of research, with applications in remote sensing, communications, optics, and radar system modeling. Approximate analytical techniques have been developed to solve the scattering from a single surface, but those solutions are usually based on limiting cases such as small roughness [65, 66, 67]. Numerical techniques have more general applicability, albeit at the expense of computational complexity. A common solution method involves a 1D approximation of the rough surface that is then solved with the Method of Moments (MoM) [68, 69]. The 1D approximation is widely used because full 2D surface simulations are computationally limited to small domains, even with advanced solution techniques [70, 71]. Current research is focusing on increasing the applicability and, in particular, the efficiency of both 1D and 2D surface scattering simulations [72].

Less attention has been paid to the general case of scattering from stratified rough surfaces, such as scattering and propagation over terrain, where the layers may represent a geophysical medium such as snow or foliage. Most work has either focused on a single penetrable rough surface, or has relied on analytical techniques for scattering from layered media with flat interfaces. For some cases, modeling a layered medium with a single rough surface is sufficient, especially if the surface is nonpenetrable, while for other cases an analytical approach may be sufficient if the interface roughness is small. However, many other cases do not fall into either category, and require a model that can account for stratified rough surfaces. For example, recent work [73] has calculated the effective permittivity of a flat layer of foam on the ocean surface, with remote sensing applications in mind. A model of scattering from stratified rough surfaces could be combined with those studies to account for the rough ocean surface and irregular distributions of foam, with few restrictions on the surface profiles. Other applications include scattering from sea ice, soil, and even propagation in waveguide geometries. This chapter concerns the development of a precise model that can completely model the scattering from stratified rough surfaces. Without incorporating the effects of such layers for propagation, over forest or sea ice for example [74, 75], the results may be very inaccurate.

The MoM solution for a single large scale 1D surface is generally solved with pulse basis functions and point matching, although some solution techniques use specialized basis functions for specific incident fields [76]. The unknowns in the MoM are the surface currents, which must be sampled with typically ten pulse basis functions per wavelength. For large surfaces the number of samples, N, can be prohibitively large. The MoM matrix equation requires $\mathcal{O}(N^2)$ memory and up to $\mathcal{O}(N^3)$ operations to solve, a computational complexity that can render the problem intractable. Recent effort has focused on efficient solution techniques for the 1D MoM problem. A complete survey of current numerical techniques for rough surface scattering may be found in [72]. One of these techniques is the Forward Backward (FB) iterative

method [77, 78], that reduces the memory requirements to $\mathcal{O}(N)$ and the computational requirements to $\mathcal{O}(N^2)$. The FB method is based on the physics of the problem, splitting the scattering contributions into forward and backward traveling components, often converging much faster than an $\mathcal{O}(N^2)$ conjugate gradient solution technique. The efficiency of the FB method has been greatly increased with the recently developed Spectral Acceleration (SA) algorithm [79, 80, 15], which further reduces the computational complexity to $\mathcal{O}(N)$. The combined method will be referred to as FBSA throughout this chapter.

This work focuses on scattering from layered rough surfaces, using integral equations derived for M stratified regions separated by $M-1$ rough interfaces and solved with the MoM. Each rough interface may be unique, and each region may have a unique permittivity (the formulation can be easily extended to permeable layers). Fast techniques become important as the number of unknowns increases to $2(M-1)N$, and therefore the FBSA algorithm is applied. Scattering from a single penetrable rough surface has been solved with canonical grid methods [81, 82], and recently with the FB method [83]. The formulation presented in this chapter applies the FBSA method to an arbitrary number of layered rough surfaces. For the sake of illustration, scattering from a dielectric layer on a Perfect Electric Conductor (PEC) is investigated. The accuracy and efficiency of the method are compared to analytical methods for flat surfaces and the exact MoM. Furthermore, convergence of the method is studied for various surface roughness and layer permittivities.

3.2 Formulation

We consider a layered medium as shown in Figure 3-1, containing M regions and $M-1$ rough surface interfaces. An incident field $\psi^{inc}(\overline{r})$ impinges on surface S_1, and we wish to calculate the scattered field $\psi^{s}(\overline{r})$ in region V_1. Note, however, that the formulation can be used to calculate the scattered field in any region from a source

in any region. For TE and TM incident fields, ψ represents the electric field and the magnetic field, respectively. In any region l, the total field is denoted by ψ_l and the scattered field is denoted by ψ_l^s. The notation in this work follows that of [69].

3.2.1 Integral Equations

Using Green's Theorem, for any region V_l, we write:

$$\int\int_{V_l} d\overline{r}' \left[\psi_l(\overline{r}')\ \nabla^2 g_l(\overline{r},\overline{r}') - g_l(\overline{r},\overline{r}')\ \nabla^2\psi_l(\overline{r}')\right]$$
$$= \left[\int_{S_\infty} d\overline{r}' + \int_{S_{l-1}} d\overline{r}' + \int_{S_l} d\overline{r}'\right] \left[\psi_l(\overline{r}')\ \hat{n}_l^* \cdot \nabla g_l(\overline{r},\overline{r}') - g_l(\overline{r},\overline{r}')\ \hat{n}_l^* \cdot \nabla\psi_l(\overline{r}')\right] \quad (3.1)$$

where $\psi_1(\overline{r}) = \psi^{inc}(\overline{r}) + \psi_1^s(\overline{r})$ in region V_1, $\psi_l(\overline{r}) = \psi_l^s(\overline{r})$ elsewhere, and the integral over S_∞ refers to the integral over all surfaces at infinity. The normal vector $\hat{n}_l^*$ to the surface S_l is directed outward from the region V_l, such that in Figure 3-1 the normal vectors are related by $\hat{n}_l^* = \hat{n}_{l-1}$ on S_{l-1} and $\hat{n}_l^* = -\hat{n}_l$ on S_l. The Green's function in two dimensions is the Hankel function:

$$g_l(\overline{r},\overline{r}') = \frac{i}{4} H_0^{(1)}(k_l|\overline{r}-\overline{r}'|) \quad (3.2)$$

An integral in region V_l, where $l = 2, 3, ..., M$, contains four surfaces, $S_\infty = S_{\infty-} + S_{\infty+}$, S_{l-1}, and S_l. The integrals in regions V_1 and V_M contain the surfaces at infinity and S_1 or S_M, respectively. For the cases considered in this work, the incident and scattered fields vanish at the edges of the surfaces and guided modes in the layers generally decay due to the interface roughness, such that the integrals at $S_{\infty-}$ and $S_{\infty+}$ contribute zero. The integral at infinity in the lower halfspace also vanishes by the Sommerfeld's radiation condition and the integral in the upper halfspace gives rise to the incident field [84]. The source and observation points, $\overline{r}'$ and $\overline{r}$, are both on the surface, requiring the analytic extraction of the singularity from the normal

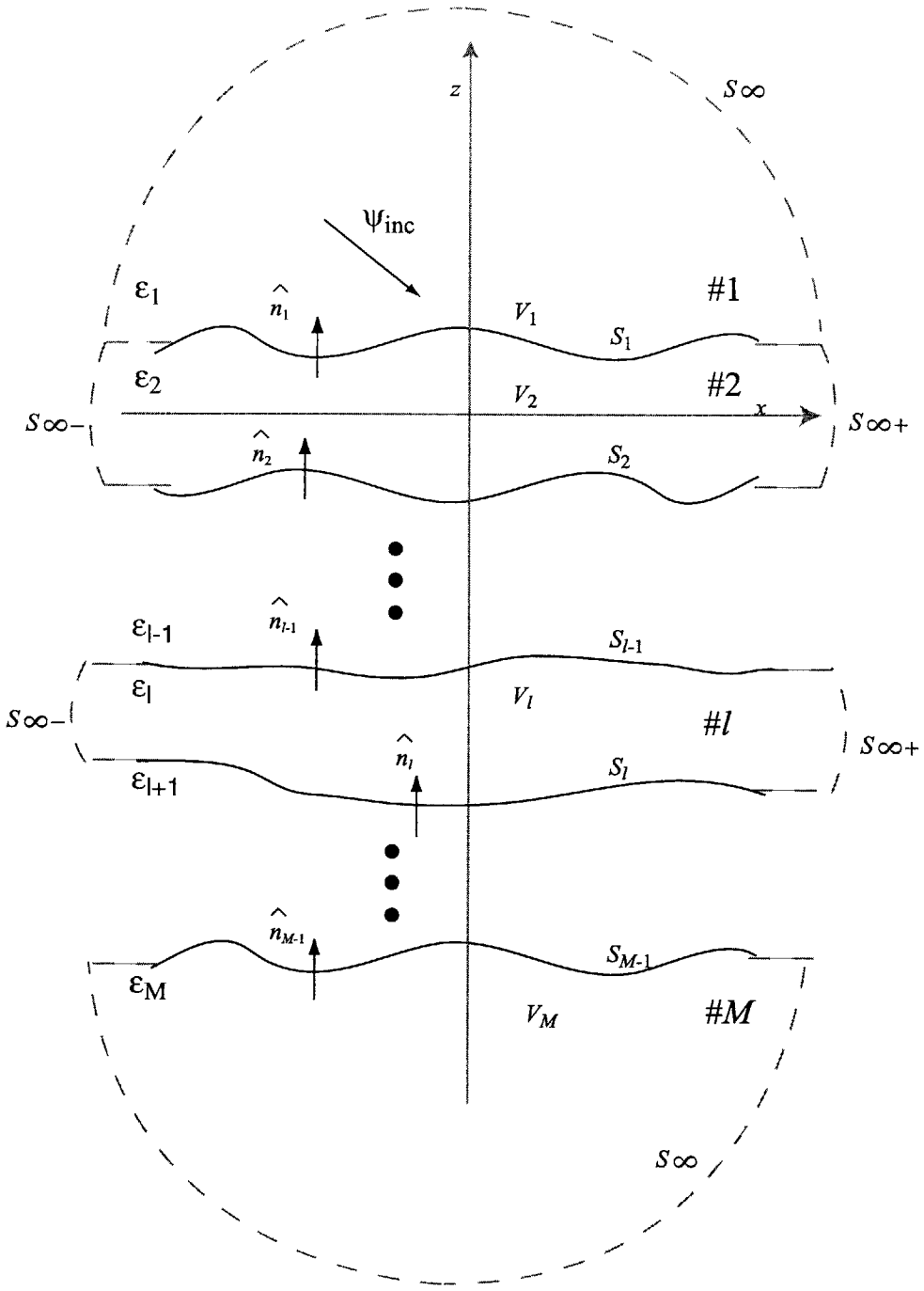

Figure 3-1: Geometry of the 2D problem. The incident field ψ_{inc} impinges on a layered medium with M regions separated by $M-1$ rough surfaces. Green's theorem is applied to obtain a system of equations in terms of ψ and $\partial\psi/\partial n$ on the surfaces.

derivative of the Green's function [69]. On S_1, from the integral equation for region V_1, we have

$$\frac{\psi_1(\overline{r})}{2} - \int_{S_1} ds' \psi_1(\overline{r}')\ \hat{n}_1 \cdot \nabla g_1(\overline{r}, \overline{r}') + \int_{S_1} ds' g_1(\overline{r}, \overline{r}')\ \hat{n}_1 \cdot \nabla \psi_1(\overline{r}') = \psi^{inc}(\overline{r}) \tag{3.3}$$

The general integral equation for region V_l contains both S_l and S_{l+1}:

$$\frac{\psi_l(\overline{r})}{2} + \int_{S_l} ds' \psi_l(\overline{r}')\ \hat{n}_l \cdot \nabla g_l(\overline{r}, \overline{r}') - \int_{S_l} ds' g_l(\overline{r}, \overline{r}')\ \hat{n}_l \cdot \nabla \psi_l(\overline{r}') - \int_{S_{l+1}} ds' \psi_l(\overline{r}')\ \hat{n}_{l+1} \cdot \nabla g_l(\overline{r}, \overline{r}') + \int_{S_{l+1}} ds' g_l(\overline{r}, \overline{r}')\ \hat{n}_{l+1} \cdot \nabla \psi_l(\overline{r}') = 0 \tag{3.4}$$

Finally on S_{M-1}, from the integral equation for region V_M, we have

$$\frac{\psi_M(\overline{r})}{2} + \int_{S_{M-1}} ds' \psi_M(\overline{r}')\, \hat{n}_{M-1} \cdot \nabla g_M(\overline{r}, \overline{r}') - \int_{S_{M-1}} ds' g_M(\overline{r}, \overline{r}')\ \hat{n}_{M-1} \cdot \nabla \psi_M(\overline{r}') = 0 \tag{3.5}$$

Each region V_l has two unknowns that must be solved, $\psi_l(\overline{r})$ and $\hat{n}_l \cdot \nabla \psi_l(\overline{r})$, on each bounding surface. Each surface S_l then has four unknowns, two from region V_l above and two from region V_{l+1} below. The four unknowns can be reduced to two through the boundary conditions. In the TE case, ψ_l represents the electric field, hence

$$\overline{E}_l(\overline{r}) = \hat{y}\psi_l(\overline{r}) \tag{3.6}$$

$$\overline{H}_l(\overline{r}) = -\frac{1}{i\omega\mu}\hat{y} \times \nabla\psi_l(\overline{r}) \tag{3.7}$$

$$\hat{n}_l \times \overline{H}_l(\overline{r}) = -\frac{\hat{y}}{i\omega\mu}\left(\hat{n}_l \cdot \nabla\psi_l(\overline{r})\right) \tag{3.8}$$

The boundary condition of continuous tangential magnetic and electric fields yields

$$\psi_l(\overline{r}) = \psi_{l+1}(\overline{r}) \ , \ \overline{r} \in S_l \tag{3.9}$$

$$\hat{n}_l \cdot \nabla\psi_l(\overline{r}) = -\hat{n}_{l+1} \cdot \nabla\psi_{l+1}(\overline{r}) \ , \ \overline{r} \in S_l \tag{3.10}$$

on S_l. For the TM case, where ψ represents the magnetic field,

$$\overline{H}_l(\overline{r}) = \hat{y}\psi_l(\overline{r}) \tag{3.11}$$

$$\overline{E}_l(\overline{r}) = \frac{1}{i\omega\epsilon_l}\hat{y} \times \nabla\psi_l(\overline{r}) \tag{3.12}$$

$$\overline{E}_l(\overline{r}) \times \hat{n}_l = -\frac{\hat{y}}{i\omega\epsilon_l}\left(\hat{n}_l \cdot \nabla\psi_l(\overline{r})\right) \tag{3.13}$$

The boundary conditions are then

$$\psi_l(\overline{r}) = \psi_{l+1}(\overline{r}) \ , \ \overline{r} \in S_l \tag{3.14}$$

$$\hat{n}_l \cdot \nabla\psi_l(\overline{r}) = -\frac{\epsilon_l}{\epsilon_{1+1}}\hat{n}_{l+1} \cdot \nabla\psi_{l+1}(\overline{r}) \ , \ \overline{r} \in S_l \tag{3.15}$$

on S_l. Applying the boundary conditions to Equation 3.1 may now yield integral equations in terms of the unknowns ψ_l and $\hat{n}_l \cdot \nabla\psi_l$ on surface S_l. Hence the subscripts on the unknowns refers to both the region and the surface on which they exist. For ease of notation, the unknown $\hat{n}_l \cdot \nabla\psi_l(\overline{r}')$ is denoted as U_l.

3.2.2 Method of Moments (MoM) Implementation

The MoM may now be applied to the integral equations. Point matching with pulse basis functions is used in this work. All the surfaces are assumed to be of equal length L, divided up into N segments of width $\Delta_x = L/N$. The z coordinate is denoted by $f_l(x)$ for surface S_l, and the center of the m^{th} surface segment is $(x_m, f_l(x_m))$. The unknowns on surface S_l at segment x_m are denoted as $\psi_{m,l}$ and $U_{m,l}$. At each position x_m, there are $M-1$ segments and $2(M-1)$ unknowns. The differential surface length

at x_m is expressed as $ds_{m,l} = dx_{m,l}\sqrt{1+\left(\frac{df_{m,l}}{dx_{m,l}}\right)^2} = \Delta_x \Delta l_{m,l}$. Equation 3.3 may be written as

$$\overline{\overline{A}}^{(1,1,1)}\overline{U}_1 + \overline{\overline{B}}^{(1,1,1)}\overline{\psi}_1 = \overline{\psi}^{inc} \tag{3.16}$$

Note that the A and B coefficients each have three superscripts, the first referring to the Green's function subscript, the second to the surface of observation, and the third to the surface containing the source. Equation 3.4 splits into two sets of MoM equations; first

$$\rho_l \overline{\overline{A}}^{(l,l-1,l-1)}\overline{U}_{l-1} + \overline{\overline{B}}^{(l,l-1,l-1)}\overline{\psi}_{l-1} + \overline{\overline{A}}^{(l,l-1,l)}\overline{U}_l + \overline{\overline{B}}^{(l,l-1,l)}\overline{\psi}_l = 0 \tag{3.17}$$

for observation points on S_{l-1}, and second

$$\rho_l \overline{\overline{A}}^{(l,l,l-1)}\overline{U}_{l-1} + \overline{\overline{B}}^{(l,l,l-1)}\overline{\psi}_{l-1} + \overline{\overline{A}}^{(l,l,l)}\overline{U}_l + \overline{\overline{B}}^{(l,l,l)}\overline{\psi}_l = 0 \tag{3.18}$$

for observation points on S_l. For the TM case, we define $\rho_l = \epsilon_l/\epsilon_{l-1}$, and for the TE case $\rho_l = \mu_l/\mu_{l-1} = 1.0$. Finally, from Equation 3.4, we obtain

$$\rho_{M-1}\overline{\overline{A}}^{(M,M-1,M-1)}\overline{U}_{M-1} + \overline{\overline{B}}^{(M,M-1,M-1)}\overline{\psi}_{M-1} = 0 \tag{3.19}$$

For a region V_a, given observation at x_m on S_b and source at x_n on S_c, the coefficients may be written as

$$A_{mn}^{(a,b,c)} = \begin{cases} w^{(a,c)}\frac{i\Delta_x}{4}H_0^{(1)}\left(k_a\left|\overline{r}_{m,b}-\overline{r}_{n,c}\right|\right)\Delta l_{m,b} & \text{for } (b=c, m\neq n) \text{ or } b\neq c \\ w^{(a,c)}\frac{i\Delta_x}{4}\left[1+\frac{i2}{\pi}\ln\left(\frac{\gamma k_a \Delta_x \Delta l_{m,b}}{4e^1}\right)\right] & \text{for } (b=c, m=n) \end{cases} \tag{3.20}$$

$$B_{mn}^{(a,b,c)} = \begin{cases} -w^{(a,c)}\frac{ik\Delta_x}{4}\frac{H_1^{(1)}\left(k_a\left|\overline{r}_{m,b}-\overline{r}_{n,c}\right|\right)}{\left|\overline{r}_{m,b}-\overline{r}_{n,c}\right|}\Delta_{f,mn} & \text{for } (b=c, m\neq n) \text{ or } b\neq c \\ \frac{1}{2} - w^{(a,c)}\frac{f_b''(x_m)}{4\pi}\frac{\Delta_x}{1+f_b'(x_m)^2} & \text{for } (b=c, m=n) \end{cases} \tag{3.21}$$

where $w^{(a,c)} = 1$ if $a = c$ and -1 otherwise, γ is the Euler constant, and $\Delta_{f,mn} = (f_c'(x_n)(x_n - x_m) - (f_c(x_n) - f_b(x_m)))$. Furthermore,

$$|\overline{r}_{m,b} - \overline{r}_{n,c}| = \sqrt{(x_m - x_n)^2 + (f_b(x_m) - f_c(x_n))^2}$$

The solutions for the scattered fields in any region may then be obtained using the appropriate integral equation and boundary conditions. A medium with M regions and $M-1$ surfaces will produce $2(M-1)N$ unknowns that can be solved with the resulting $2(M-1)N$ equations, significantly increasing the computational cost and memory requirements over a single surface problem. For brevity, the formulation is continued for a three region geometry, containing four unknowns ψ_1, U_1, ψ_2, and U_2 on two surfaces S_1 and S_2. Equations 3.17-3.19 can be written as

$$\overline{\overline{Z}}\,\overline{I} = \overline{V} \tag{3.22}$$

where

$$\overline{\overline{Z}} = \begin{bmatrix} \overline{\overline{A}}^{(1,1,1)} & \overline{\overline{B}}^{(1,1,1)} & 0 & 0 \\ \rho_2\overline{\overline{A}}^{(2,1,1)} & \overline{\overline{B}}^{(2,1,1)} & \overline{\overline{A}}^{(2,1,2)} & \overline{\overline{B}}^{(2,1,2)} \\ \rho_2\overline{\overline{A}}^{(2,2,1)} & \overline{\overline{B}}^{(2,2,1)} & \overline{\overline{A}}^{(2,2,2)} & \overline{\overline{B}}^{(2,2,2)} \\ 0 & 0 & \rho_3\overline{\overline{A}}^{(3,2,2)} & \overline{\overline{B}}^{(3,2,2)} \end{bmatrix}$$

and

$$\overline{I} = \begin{bmatrix} \overline{U}_1 \\ \overline{\psi}_1 \\ \overline{U}_2 \\ \overline{\psi}_2 \end{bmatrix} \qquad \overline{V} = \begin{bmatrix} \overline{\psi}^{inc} \\ 0 \\ 0 \\ 0 \end{bmatrix}$$

3.2.3 Forward Backward (FB) Method

In this section, the FB method is applied to the three region geometry. The formulation can be extended to the M region geometry in a straightforward way.

Begin by splitting each of the submatrices in $\overline{\overline{Z}}$ into upper, lower, and diagonal parts, denoted with superscripts U, L, and D, respectively. For example, the submatrices for region (l,l,l) are split as

$$\overline{\overline{A}}^{(l,l,l)} = \overline{\overline{A}}^{U,(l,l,l)} + \overline{\overline{A}}^{L,(l,l,l)} + \overline{\overline{A}}^{D,(l,l,l)} \tag{3.23}$$

$$\overline{\overline{B}}^{(l,l,l)} = \overline{\overline{B}}^{U,(l,l,l)} + \overline{\overline{B}}^{L,(l,l,l)} + \overline{\overline{B}}^{D,(l,l,l)} \tag{3.24}$$

The unknown vector is split into forward and backward components, denoted with superscripts f and b, respectively,

$$\overline{I} = \overline{I}^f + \overline{I}^b \tag{3.25}$$

The matrix $\overline{\overline{Z}}$ can also be split up, each component containing all the corresponding components of the submatrices. For example, $\overline{\overline{Z}}^D$ is a block diagonal matrix containing all the diagonal submatrices. With the matrices split, Equation 3.22 can be rewritten as

$$\overline{\overline{Z}}^D \overline{I}^f = \overline{V} - \overline{\overline{Z}}^L (\overline{I}^f + \overline{I}^b) \tag{3.26}$$

$$\overline{\overline{Z}}^D \overline{I}^b = -\overline{\overline{Z}}^U (\overline{I}^f + \overline{I}^b) \tag{3.27}$$

This system of equations is solved with forward and backward substitution. To solve the system, the iterative method 'sweeps' forward and backward across the surfaces, similar to the single surface case. The group of unknown quantities on each surface at position x_m are solved with all the previously calculated values at x_n where $n < m$ in the forward sweep and $n > m$ for the backward sweep. The system may be written

as

$$\overline{\overline{L}}_{mm}\overline{d}_m^f = \overline{s}_m - \sum_{n<m} \overline{\overline{L}}_{mn}(\overline{d}_n^f + \overline{d}_n^b) \tag{3.28}$$

$$\overline{\overline{L}}_{mm}\overline{d}_m^b = -\sum_{n>m} \overline{\overline{L}}_{mn}(\overline{d}_n^f + \overline{d}_n^b) \tag{3.29}$$

where $\overline{\overline{L}}$ is defined as

$$\overline{\overline{L}}_{mn} = \begin{bmatrix} A_{mn}^{(1,1,1)} & B_{mn}^{(1,1,1)} & 0 & 0 \\ \rho_2 A_{mn}^{(2,1,1)} & B_{mn}^{(2,1,1)} & A_{mn}^{(2,1,2)} & B_{mn}^{(2,1,2)} \\ \rho_2 A_{mn}^{(2,2,1)} & B_{mn}^{(2,2,1)} & A_{mn}^{(2,2,2)} & B_{mn}^{(2,2,2)} \\ 0 & 0 & \rho_3 A_{mn}^{(3,2,2)} & B_{mn}^{(3,2,2)} \end{bmatrix}$$

and the vectors contain the unknowns at x_m, for example $\overline{d}_m^f = [U_{1,m}^f \ \psi_{1,m}^f \ U_{2,m}^f \ \psi_{2,m}^f]'$, and $\overline{s}_m = [\psi_m^{inc} \ 0 \ 0 \ 0]$. Each step of the FB method is now a set of $2(M-1)$ (in this case 4) equations containing all the interactions of ψ and U. Thus each forward/backward sweep requires $N(N-1)$ number of 4×4 matrix vector products and $2N$ inversions of 4×4 matrices. As a result, the overall algorithm remains $\mathcal{O}(N^2)$, although N has increased by a factor of four over the case of a simple single PEC surface. The FB method converges at a rate that depends on the roughness of the surface, as each step in the iterative process takes into account another change of direction of the scattered waves. For most rough surfaces the incident wave does not scatter forward and backward on the surface more than a few times, and so the FB method converges in a few iterations as will be shown in subsequent sections.

3.2.4 Spectral Acceleration (SA) Method

The next step is to incorporate the SA algorithm into the FB method to achieve further efficiency gains. The SA algorithm is demonstrated here for the forward

scattering case. The first step splits the integration domains into strong and weak regions, written as

$$\overline{\overline{L}}_{mm}\overline{d}_m^f = \overline{s}_m - \sum_{n=1}^{m-M_s-1} \overline{\overline{L}}_{mn}\overline{d}_n^f - \sum_{n=m-M_s}^{m-1} \overline{\overline{L}}_{mn}\overline{d}_n^f = \overline{s}_m - \overline{W}_m - \overline{S}_m \tag{3.30}$$

so that $\overline{W}$ is the summation of matrix vector products $\overline{\overline{L}}_{mn}\overline{d}_n^f$ for $n < m - M_s - 1$, where $M_s\Delta_x$ is the strong region. The SA algorithm is used for the summations in the weak region, and the standard FB method is used for summations in the strong region. The SA algorithm uses the spectral definition of the Hankel function for two points on the surface, $\overline{r}_m$ and $\overline{r}_n$,

$$H_0^{(1)}(k|\overline{r}_m - \overline{r}_n|) = \frac{1}{\pi}\int_{\Gamma_1} e^{ik[|x_m - x_n|\cos\alpha + (f(x_m) - f(x_n))\sin\alpha]} d\alpha \tag{3.31}$$

where the contour of integration Γ_1 is shown in Figure 3-2. The spectral representation of the Hankel function is next substituted into $\overline{W}$, and the integration and summation are interchanged. The resulting expression for $\overline{W}_m$ is

$$\overline{W}_m = \sum_{n=1}^{m-M_s-1} \overline{\overline{L}}_{mn}\overline{d}_n^f = \frac{i\Delta_x}{4\pi}\int_{\Gamma_1} \overline{g}_m \cdot \sum_{n=1}^{m-M_s-1} \overline{\overline{\mathcal{L}}}_{mn}\overline{d}_n^f \, d\alpha = \frac{i\Delta_x}{4\pi}\int_{\Gamma_1} \overline{g}_m \cdot \overline{F}_m \, d\alpha \tag{3.32}$$

where
$$\overline{g}_m = \begin{bmatrix} e^{ik_1 f_1(x_m)\sin\alpha} \\ e^{ik_2 f_1(x_m)\sin\alpha} \\ e^{ik_2 f_2(x_m)\sin\alpha} \\ e^{ik_3 f_2(x_m)\sin\alpha} \end{bmatrix} \qquad \overline{\overline{\mathcal{L}}}_{mn} = \begin{bmatrix} \mathcal{A}_{mn}^{(1,1)} & \mathcal{B}_{mn}^{(1,1)} & 0 & 0 \\ \rho_2\mathcal{A}_{mn}^{(2,1)} & \mathcal{B}_{mn}^{(2,1)} & \mathcal{A}_{mn}^{(2,2)} & \mathcal{B}_{mn}^{(2,2)} \\ \rho_2\mathcal{A}_{mn}^{(2,1)} & \mathcal{B}_{mn}^{(2,1)} & \mathcal{A}_{mn}^{(2,2)} & \mathcal{B}_{mn}^{(2,2)} \\ 0 & 0 & \rho_3\mathcal{A}_{mn}^{(3,2)} & \mathcal{B}_{mn}^{(3,2)} \end{bmatrix}$$

where $\mathcal{A}$ and $\mathcal{B}$ are the spectral versions of A and B, respectively, and do not depend on the vertical location of the observation (which has been extracted to $\overline{g}_m$). The two superscripts refer to the Green's function (region) and source surface location.

Specifically,

$$\mathcal{A}_{mn}^{(a,c)} = \sqrt{1 + f_c'(x_m)} e^{ik_a[(x_m - x_n)\cos\alpha - f_c(x_n)\sin\alpha]} \tag{3.33}$$

$$\mathcal{B}_{mn}^{(a,c)} = \mathcal{A}_{mn}^{(a,c)} k_a \left[\sqrt{1 + f_c'(x_m)}\cos\alpha + \sin\alpha\right] \tag{3.34}$$

The computational benefit of the SA method is that the expressions for $\overline{F}_m(\alpha)$ can be updated recursively as

$$\overline{F}_m = \overline{F}_{m-1} \cdot \overline{h} + \overline{\overline{\mathcal{L}}}_{mn}\, \overline{d}_n^f, \quad \text{where } n = m - 1 - M_s \tag{3.35}$$

where $\overline{h} = [e^{ik_1\Delta_x\cos\alpha}\ e^{ik_2\Delta_x\cos\alpha}\ e^{ik_2\Delta_x\cos\alpha}\ e^{ik_3\Delta_x\cos\alpha}]'$. The set of unknowns at x_m are calculated by exactly integrating (summing the matrix-vector products in Equation 3.28) the preceding surface currents in the strong region, and using the SA method for the surface currents in the weak region. The contribution of the weak region to the unknowns at x_m are calculated by updating $F_m(\alpha)$ and integrating over Γ_1. Hence, the computationally demanding summation of matrix-vector products over the entire surface preceding x_m is replaced by the integration over Γ_1.

In Equation 3.31, when evaluating the Hankel function in the spectral domain given source ($\overline{r}_n$) and observation ($\overline{r}_m$) points, Γ is usually replaced by the steepest descent path, Γ_{SDP}, passing through the saddle point. Along Γ_{SDP} the integrand does not oscillate and decays exponentially away from the saddle point, and the integration requires fewer sampling points. The saddle point is located along the real α axis at $\tan^{-1}[(z_m - z_n)/(x_m - x_n)]$. For the SA method, the integration for a given observation at $\overline{r}_m$ is taken over a summation of all sources in the weak region, whose saddle points are spread out along the real α axis. There is no longer a unique Γ_{SDP} path, so a new linear integration path Γ_δ is chosen tilted at angle δ, as shown in Figure 3-2. The choice of an optimal contour path is not trivial, and has been addressed in detail [79, 80, 70, 15]. For the layered media case it is efficient to choose more than one integration path, depending on which surfaces the source and observation points lie.

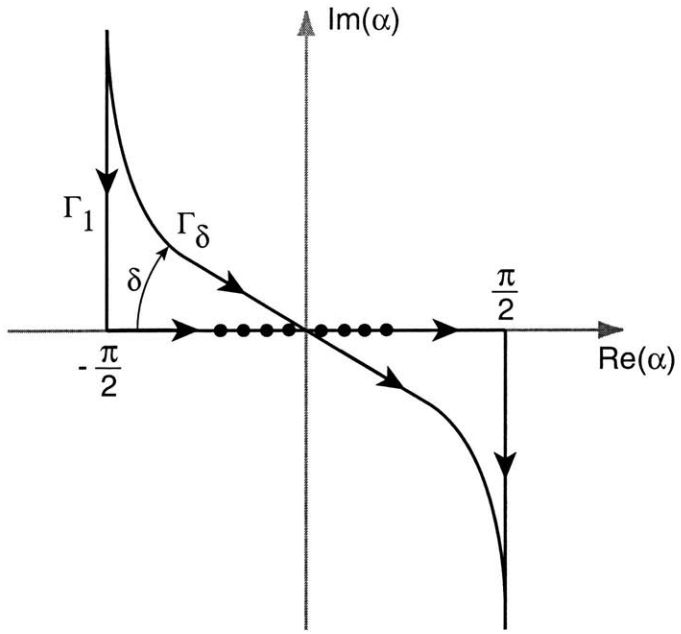

Figure 3-2: Spectral integration path for the Hankel function. The integration path Γ_δ with $\delta = \pi/4$ is the steepest descent path for saddle points on the origin. With multiple saddle points spread out on the Re(α) axis, a new integration path must be chosen with angle δ.

The choice of Γ_δ in this work follows that of [15], which chooses the integration path based on the largest saddle point, α_{SPmax}. For the $M = 3$ case, three saddle points may be chosen as:

$$\alpha_{SPmax1} = \tan^{-1}\left(\frac{f_1(x)_{max} - f_1(x)_{min}}{M_s \Delta x}\right)$$
$$\alpha_{SPmax2} = \tan^{-1}\left(\frac{f_1(x)_{max} - f_2(x)_{min}}{M_s \Delta x}\right)$$
$$\alpha_{SPmax3} = \tan^{-1}\left(\frac{f_2(x)_{max} - f_2(x)_{min}}{M_s \Delta x}\right)$$

where α_{SPmax1} and α_{SPmax3} are used to find the integration path when both source and observation are on S_1 or both are on S_2, respectively, and α_{SPmax2} is used when source and observation are each on different surfaces.

Finally, with the appropriate parameters, the integrations in the spectral domain

may be carried out. For example, we obtain for $\overline{W}_m$:

$$\overline{W}_m = \frac{i\Delta_x\Delta_\alpha e^{-i\delta}}{4\pi} \sum_{p=-Q}^{Q} \overline{g}_m(\alpha_p) \cdot \overline{F}_m(\alpha_p) \tag{3.36}$$

where α has been mapped to the real axis using

$$d\alpha \rightarrow \Delta_\alpha e^{-i\delta} \tag{3.37}$$

$$\alpha \rightarrow \alpha_p = p\Delta_\alpha e^{-i\delta} \tag{3.38}$$

The number of integration points Q is chosen based on the behavior of the integrand, as described in [15]. As with the integration path, the number of integration points may be different for each W_m.

3.2.5 Incident Field

Any source currents for MoM rough surface scattering needs to vanish at the ends of the domain to avoid unwanted edge diffraction. In our case, we construct a tapered wave from a spectrum of plane waves [66],

$$\psi_{inc}(x,z) = \frac{g}{2\pi}\int_{-\infty}^{\infty} dk_x e^{ik_x x - ik_{0z} z} \exp\left[-\frac{(k_x - k_{ix})^2 g^2}{4}\right] \tag{3.39}$$

The footprint of the beam can be chosen with g, such that the magnitude is $1/e$ down at $|g|$ wavelengths from the center. Care must be taken to avoid evanescent modes, which have a form $e^{ik_x x}$ (with exponential decay in z) and travel along the surface. The formulation in this work assumes that the incident field is zero along $S_{\infty-}$, and inclusion of incident waves traveling along $\theta = \pm\pi/2$ violates this assumption, resulting in considerable error. Grazing incidence can still be examined using the tapered wave, but an appropriate g must be chosen such that the spectrum does not exceed k_0 on the k_x axis. Other types of incident fields may also be used, such as the field

from an antenna. In such a case, care must still be taken to ensure the incident field vanishes at the edges of the domain. Generally, the antenna may be placed near the edge of the surface, such that the field at that edge ('behind' the antenna) is weak.

3.3 Results

For the sake of illustration, consider a three-region medium, where the bottom region is a perfect electrical conductor, such that $\psi_2 = 0$ for TE incidence and $U_2 = 0$ for TM incidence.

Note that the same sampling rate of the surface currents is used for both surfaces. Any ϵ_1 may be considered as long as the subwavelength sampling constraint of the MoM is enforced in both regions.

3.3.1 MoM Comparison with Analytic Expressions

The results obtained by the numerical method can be compared to simple analytical solutions for limited cases. The exact analytical solution is easily obtained for the three-region medium under consideration when the interfaces are flat. Although it is not a complete check of the rough surface formulation, this comparison is a useful validation of the layered medium MoM formulation. The total field in region 1 is

$$\psi(x,z) = \frac{g}{2\pi}\int_{-\infty}^{\infty} dk_x (e^{-ik_{1z}z} + Re^{ik_{1z}z})e^{ik_x x}\exp\left[-\frac{(k_x - k_{ix})^2 g^2}{4}\right] \tag{3.40}$$

Considering the first and second interfaces are located at $z = d_0$ and $z = d_1$, we have

$$R = \frac{R_{12} + R_{23}e^{i2k_{1z}(d_2 - d_1)}}{1 + R_{12}R_{23}e^{i2k_{2z}(d_2 - d_1)}} e^{i2k_{1z}d_1} \tag{3.41}$$

where, for the TE case, $R_{12} = (\mu_1 k_{1z} - \mu_1 k_{2z})/(\mu_2 k_{1z} + \mu_1 k_{2z})$ and $R_{23} = -1$, and for the TM case, $R_{12} = (\epsilon_2 k_{1z} - \epsilon_1 k_{2z})/(\epsilon_2 k_{1z} + \epsilon_1 k_{2z})$, and $R_{23} = 1$. For the analytical

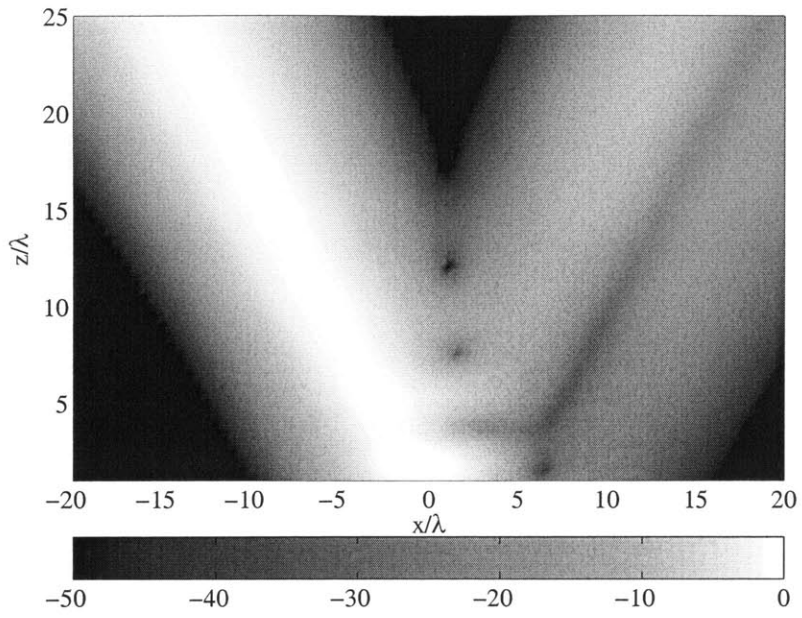

Figure 3-3: TE Incident and scattered fields from dielectric layer on a PEC. The depth of the dielectric layer is $d = 10\lambda$, and the relative permittivity is $\epsilon = 2.0 + i0.05$. Incident field is a tapered wave at $\theta = 30^o$, $g = 4\lambda$. The surface of the dielectric is at $z = 0$. Units are dB.

comparison, a relative permittivity of $\epsilon_{1r} = 2.0 + i0.05$ is considered, and the dielectric layer has a depth of 10λ.

A tapered wave at an angle of $\theta = 30^o$ with $g = 4\lambda$ is considered incident on a surface of length $L = 40\lambda$. The magnitude of the total field is shown in Figure 3-3. Two reflected tapered waves can be seen, the first a reflection from S_1, and the second is a reflection from S_2. Further reflected components are attenuated by the lossy layer. To calculate the error of the MoM solution, the difference between the numerical and analytical solutions are calculated and normalized with respect to the incident field. Figures 3-4(a) and (b) show the error in the TE and TM scattered fields, respectively. The full MoM solution compares well to the analytical solution, with a maximum error of 0.5%. Other incident angles and surface depths produce similar results, and the solutions converge as the sampling rate is increased.

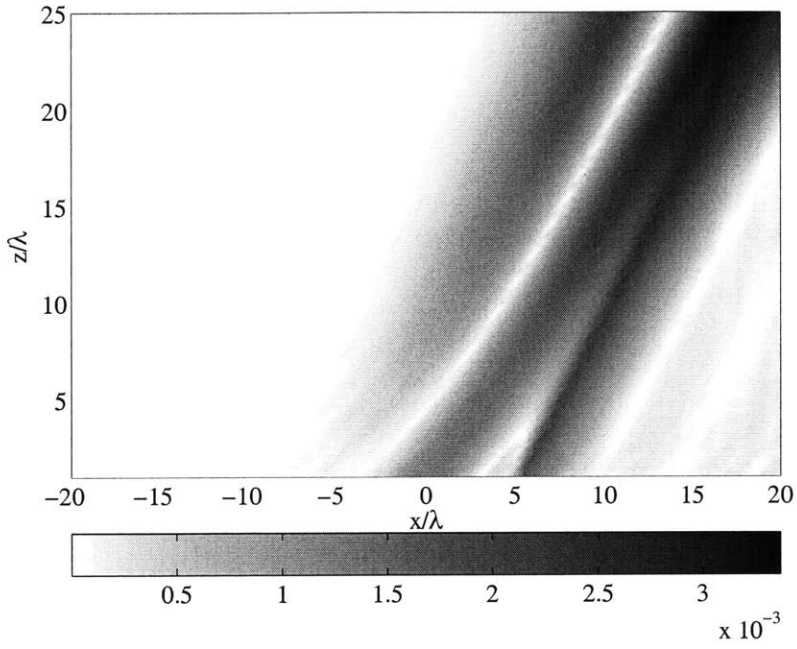

(a) TE Case.

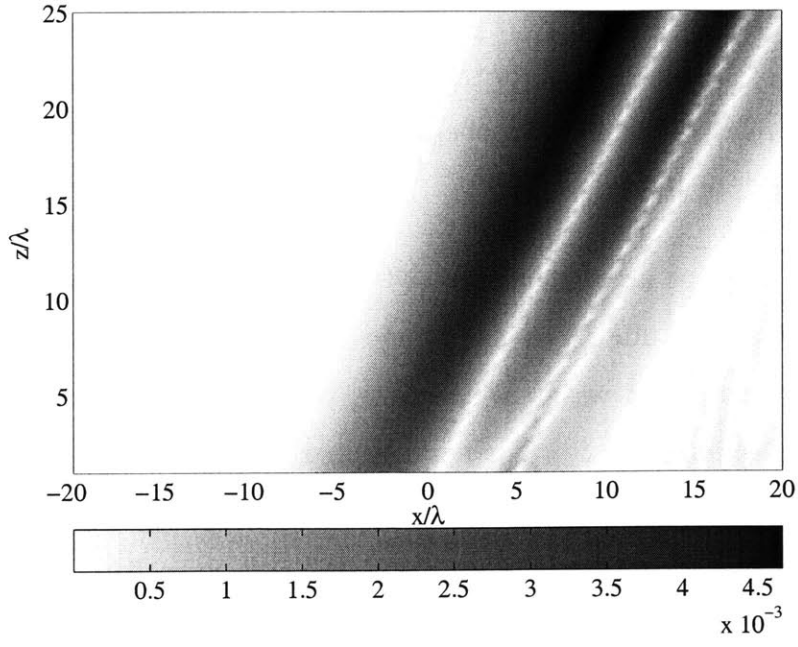

(b) TM Case.

Figure 3-4: Scattered field error. Scattering from a dielectric layer on a PEC with $d = 10\lambda$, $\epsilon = 2.0 + i0.05$, $\theta = 30^o$, $g = 4\lambda$. The surface of the dielectric is at $z = 0$.

3.3.2 FBSA comparison with MoM

Rough surfaces are now considered to compare the standard MoM with the FBSA method for the three-region medium under consideration. A Gaussian rough surface is considered in this comparison, with correlation length l and rms height h. Similar to the analysis carried out in [83], three types of rough surfaces are considered. The first is a slightly rough surface with $l = 1\lambda$ and $h = \lambda/6$ (rms slope = 13^o), the second is a moderately rough surface with $l = 1\lambda$ and $h = \lambda/\sqrt{2}$ (rms slope = 45^o), and the third is a very rough surface with $l = 1.1\lambda$ and $h = 1.33\lambda$ (rms slope = 60^o). The same profile is used for the upper and lower surfaces for convenience, although the formulation does not require that restriction. The depth of the layer is $d = 10\lambda$, and the permittivity is again $\epsilon = 2.0 + i0.05$. The FBSA method uses a strong region of 5λ. Increasing the strong region yields more accurate results at the expense of CPU time. The convergence of the FBSA method at iteration j can be studied with the residual error or the absolute error [85]. The residual error , $r(j)$ is defined as

$$r(j) = \frac{|| \overline{V} - \overline{\overline{Z}}\, \overline{I} ||}{|| \overline{V} ||} = \frac{|| \overline{\overline{Z}}^{L} (\overline{I}^{b,j-1} - \overline{I}^{b,j}) ||}{|| \overline{V} ||} \tag{3.42}$$

The absolute error is calculated by comparing the FBSA solution to the MoM solution at each iteration, and is defined as

$$a(j) = \frac{|| \overline{I}^{j} - \overline{I}^{MoM} ||}{|| \overline{I}^{MoM} ||} \tag{3.43}$$

Figure 3-5(a) shows the residual error convergence of the FBSA method for the TE case. The method converges to $r(j) = 10^{-4}$ in $j = 12$ iterations for the slightly rough surface, increasing to $j = 15$ iterations for the moderately rough surface. The roughest surface has not yet reached $r(j) = 10^{-3}$ after $j = 15$ iterations. Figure 3-5(b) plots the residual error convergence for the TM case, showing slightly faster convergence than the TE case and the same result of slower convergence for rougher

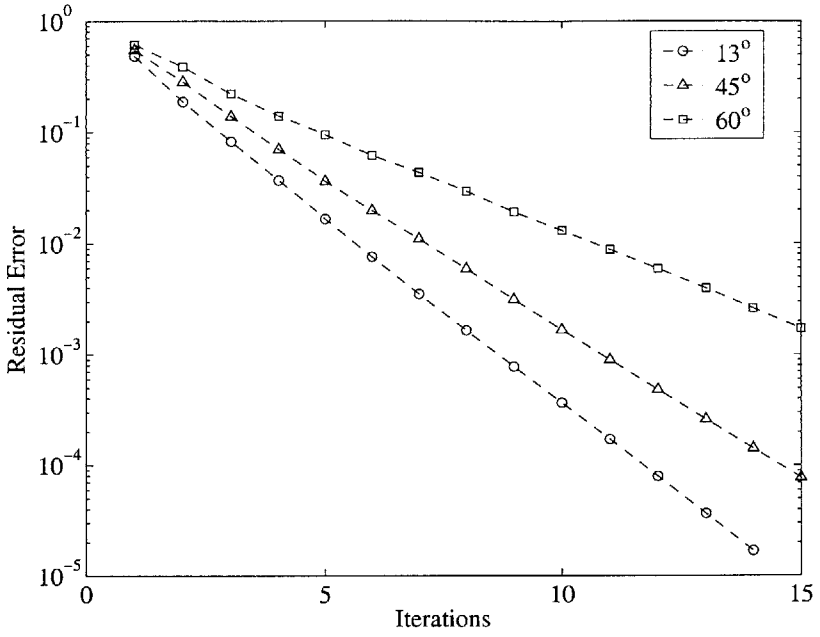

(a) TE case.

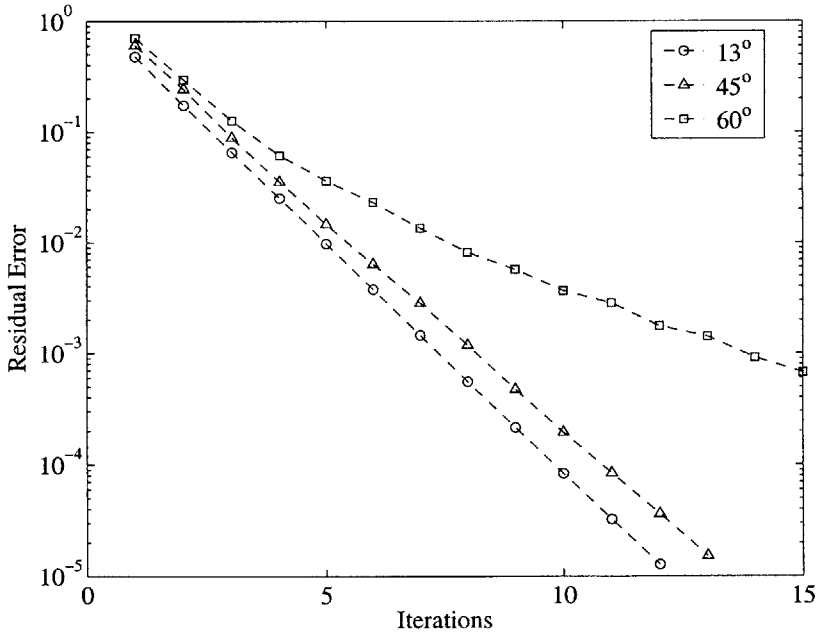

(b) TM case.

Figure 3-5: Residual convergence of FBSA method for different rough surface rms slopes. Incident field with $g = 10\lambda$, $\theta = 30^o$, impinging on a rough surface with $L = 51.2\lambda$, $d = 10\lambda$, $\epsilon_1 = 2.0 + i0.05$.

surfaces. These trends are consistent with the FB method for single rough surfaces [83].

Figure 3-6(a) shows the absolute convergence for the TE case. The absolute error decreases at a similar rate to the residual error, but reaches a minimum level at around $a(j) = 10^{-3}$. This behavior is characteristic of FB iterative methods [86], and the minimum error depends partly on the numerical precision of the computer (for the FB method) and mostly on the accuracy of the SA technique. Increasing the size of the strong region lowers the minimum error. Figure 3-6(b) plots the absolute error convergence for the TM case. The TM case again converges faster than the TE case, but reaches similar minimum error levels. The roughest surface has a minimum error of 10^{-3} after 15 iterations. In practice, the absolute error is not available, and the convergence of the FBSA method must be measured on the residual error, as well as the accuracy of the final solution based on the size of the strong region. These results indicate that the FBSA method does not achieve any further accuracy after it has reached $r(j) < 10^{-3}$, despite the continuing decrease in the residual error.

Results of the FBSA method thus far have been presented only for $\epsilon_r = 2.0 + i0.05$, and it is worthwhile to examine the performance for different permittivities. Table 1 summarizes the results of the FBSA method for twelve different permittivities, averaged over ten rough surface realizations. Each rough surface is 51.2λ in length, with $l = 1\lambda$ and $h = 0.707$, and the incident wave has $\theta = 30^o$ and $g = 10\lambda$. The strong region is 5λ. The method is terminated when the residual error $r(j) < 10^{-2}$, however the final absolute error $a(j)$ is shown in Table 1 as an indication of the solution accuracy. If the method does not converge within 75 iterations for any one of the ten rough surfaces, 'NC' is entered in the table. A number of conclusions may be drawn from the convergence data. First, the FBSA method converges faster as the imaginary part of the permittivity increases. This is expected as a layer with greater loss will attenuate the scattered waves and result in fewer forward and backward changes in direction. Indeed, the FBSA method is not always successful in

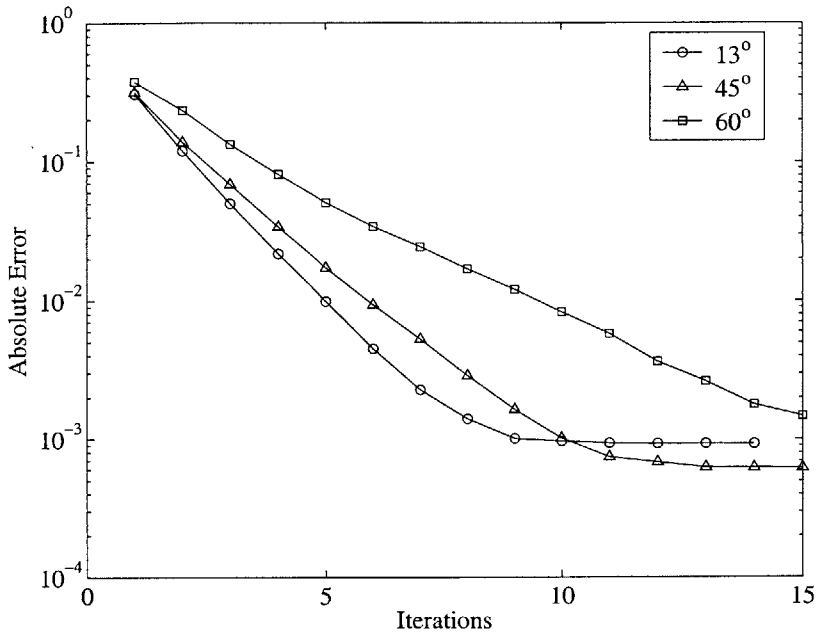

(a) TE case.

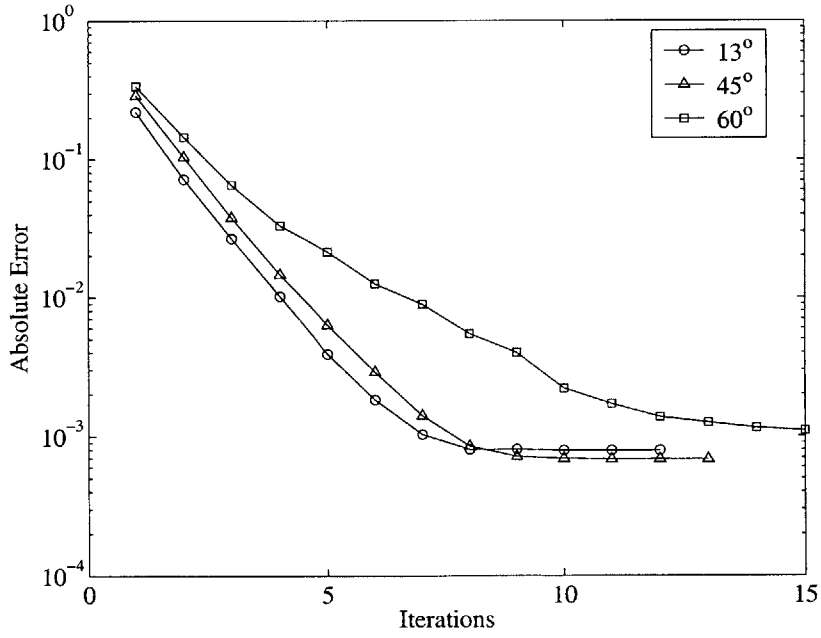

(b) TM case.

Figure 3-6: Absolute convergence of FBSA method for different rough surface rms slopes. Incident field with $g = 10\lambda$, $\theta = 30^o$, impinging on a rough surface with $L = 51.2\lambda$, $d = 10\lambda$, $\epsilon_1 = 2.0 + i0.05$.

the lossless cases. Only the TM case converges for $\epsilon_r = 2.0$, and neither the TE nor TM cases converge for $\epsilon_r = 3.0$. Second, increasing the real part of the permittivity generally increases the number of iterations required for convergence. This is likely due again to the multiple scattering, which increases as the reflection coefficient from the layer increases.

The convergence of the FB method for a single penetrable surface has been studied in great detail in [83], where it was shown that the method converges slowly or not at all for large values of permittivity such as $15 + i4$ and $80 + i66$. Such values are not well suited to the formulation presented in this work either, due to the requirement of subwavelength (at least $\lambda/10$) sampling on the layers. A single interface can yield accurate results with a $\lambda/10$ free space sampling, regardless of the lower halfspace permittivity, due to phase matching. The accuracy will depend on the angle of incidence and roughness, see for example [82]. Note that large permittivities could be included in this formulation at the lowest region, ϵ_M.

Finally, Table 2 presents the results of the FBSA method for four different surface separations and the three rough surfaces when the relative permittivity is $\epsilon_r = 2.0 + i0.05$. For each case, the upper and lower surfaces are identical, which is necessary to avoid overlap. Both the average number of realizations (for ten rough surfaces) and the average absolute error are shown. For certain parameters, the FBSA method does not converge for at least one of the ten rough surfaces, and 'NC' is indicated. Figure 3-7 plots the three different rough surfaces with $d = 1\lambda$. Note that the TE case for the moderate rough surface separated by $d = 1\lambda$ was very slow to converge, in one case requiring more than 75 iterations, but always reached an acceptable absolute error. Hence the number of iterations is 'nc' yet the absolute error is provided. The FBSA method converges the fastest for the least rough surfaces, as was shown before, as well as those that have the largest separation. These cases result in the least amount of multiple scattering. The FBSA method does not work for the rougher surfaces with small separations. The TE and TM cases both diverge for at least one

	$\epsilon_r' = 1.1$		$\epsilon_r' = 2.0$		$\epsilon_r' = 3.0$	
	TE , $min\, a(j)$	TM , $min\, a(j)$	TE , $min\, a(j)$	TM , $min\, a(j)$	TE , $min\, a(j)$	TM , $min\, a(j)$
$\epsilon_r'' = 0.0$	28, 0.004	16, 0.004	NC, NC	31, 0.003	NC, NC	NC, NC
$\epsilon_r'' = 0.01$	16, 0.004	10, 0.003	23, 0.005	12, 0.003	NC, 0.004	12, 0.003
$\epsilon_r'' = 0.05$	7, 0.004	6, 0.003	8, 0.004	6, 0.003	7, 0.004	7, 0.003
$\epsilon_r'' = 0.1$	6, 0.002	6, 0.002	6, 0.003	5, 0.003	6, 0.003	5, 0.002

Table 3.1: Average number of iterations to achieve $r(j) < 10^{-2}$ and average absolute error, versus relative permittivity $(\epsilon_r' + i\epsilon_r'')$ for TE and TM incidence. Layer separation is $d = 5\lambda$, Gaussian rough surface with $h = 0.707\lambda$ and $l = 1.0\lambda$.

	$l = 1\lambda, h = 0.167\lambda$ $(s = 13^o)$		$l = 1\lambda, h = 0.707\lambda$ $(s = 45^o)$		$l = 1.1\lambda, h = 1.33\lambda$ $(s = 60^o)$	
	TE , $min\, a(j)$	TM , $min\, a(j)$	TE , $min\, a(j)$	TM , $min\, a(j)$	TE , $min\, a(j)$	TM , $min\, a(j)$
$d = 1\lambda$	9, 0.006	6, 0.002	NC, 0.005	23, 0.004	NC, NC	NC, NC
$d = 2\lambda$	8, 0.004	7, 0.003	13, 0.005	10, 0.003	NC, NC	NC, NC
$d = 5\lambda$	6, 0.004	5, 0.003	8, 0.004	6, 0.003	14, 0.007	10, 0.005
$d = 10\lambda$	5, 0.003	5, 0.002	6, 0.003	5, 0.003	11, 0.003	7, 0.004

Table 3.2: Average number of iterations to achieve $r(j) < 10^{-2}$ and corresponding absolute error, versus layer separation and rough surface parameters. Relative permittivity is $\epsilon_r = 2.0 + i0.05$.

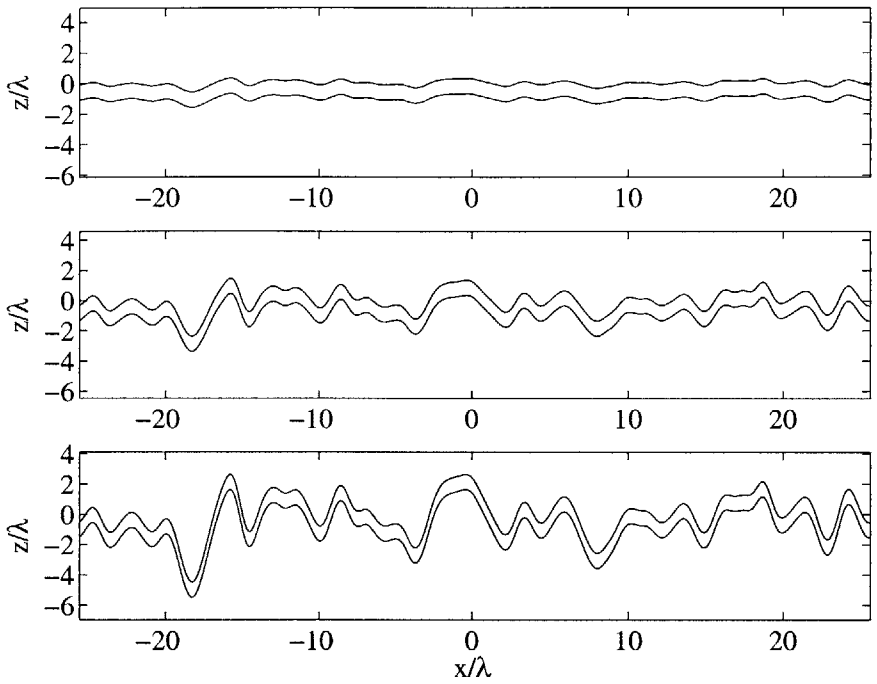

Figure 3-7: Example surface with $d = 1\lambda$ for the three different levels of roughness. Top plot is for $h = 0.167\lambda$ and $l = 1\lambda$ ($s = 13^o$), middle plot is for $h = 0.707\lambda$ and $l = 1\lambda$ ($s = 45^o$), bottom plot is for $h = 1.33\lambda$ and $l = 1.1\lambda$ ($s = 60^o$).

of the ten very rough surface realizations in both the $d = 1\lambda$ and $d = 2\lambda$ separations. The FBSA method is obviously not well suited for the very rough layered surfaces that are closely spaced.

Residual errors of 10^{-2} are considered sufficient for accurate calculation of scattered fields. Figure 3-8(a) shows the bistatic scattered field for the TE case calculated with MoM and FBSA for the moderately rough surface. The FBSA method is terminated with a residual error of 10^{-2}. The FBSA result is very close to the MoM result, and indeed the absolute error is 1.2×10^{-7}. Figure 3-8(b) shows the bistatic scattered fields for the TM case, and the absolute error is 6.7×10^{-7}.

Finally, Figure 3-9 shows the CPU times necessary to solve the system of equations using the MoM and FBSA methods. Four surfaces of lengths 25.6, 51.2, 102.4, and 204.8 wavelengths are considered, which when sampled at $\lambda/10$ result in 768, 1536,

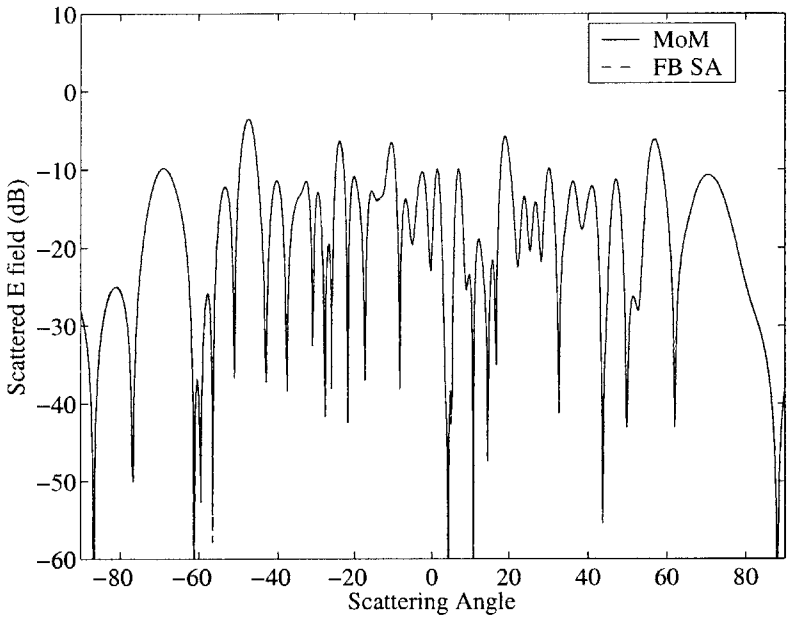

(a) TE incident field.

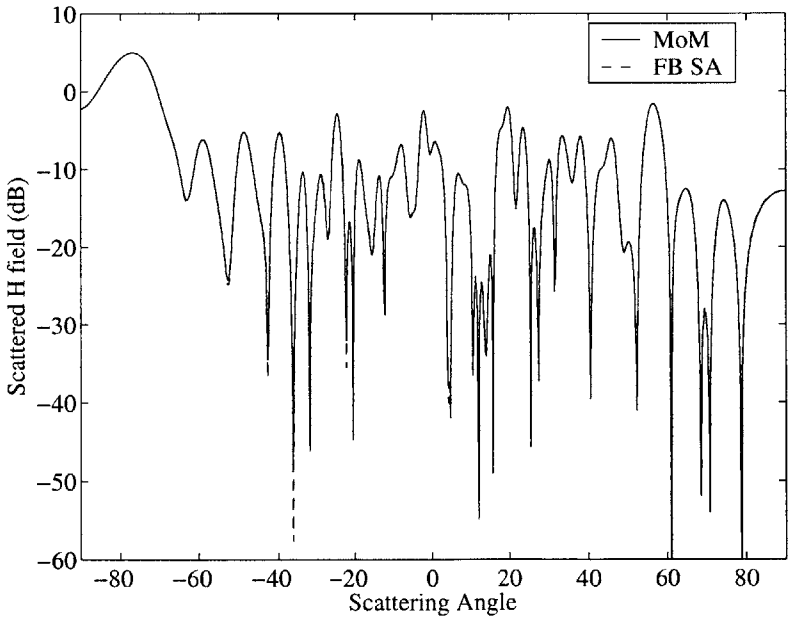

(b) TM incident field.

Figure 3-8: Bistatic scattered field. Incident field with $g = 10\lambda$, $\theta = 30^o$, impinging on a rough surface with $L = 51.2\lambda$, $d = 5\lambda$, $\epsilon_1 = 2.0 + i0.05$, $h = \lambda/\sqrt{2}$, and $l_p = 1\lambda$ ($s = 45^o$). FBSA uses a strong region of 10λ and is terminated with $r(i) = 10^-3$.

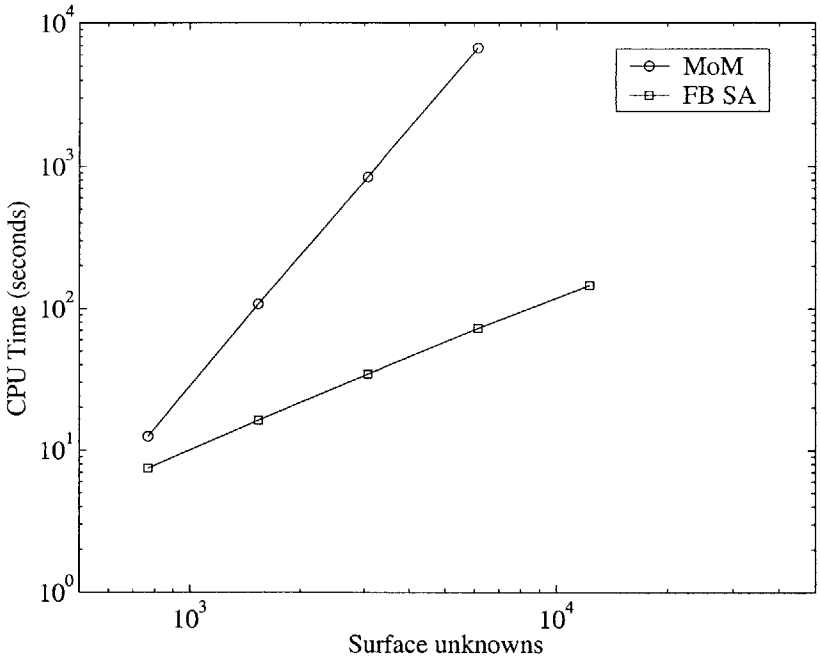

Figure 3-9: CPU times of the MoM and FBSA methods. Rough surface with $h = \lambda/\sqrt{2}$ and $l_p = 1\lambda$ (45^o rms slope), $\epsilon_1 = 2.0 + i0.05$, $d = 5\lambda$. FBSA method takes 8 iterations to reach $r(i) < 10^{-3}$

3072, and 6144 unknowns, respectively. An additional result for a 409.6 wavelength surface is included for the FBSA method. The FBSA method is obviously more efficient, scaling as $\mathcal{O}(N)$ while the MoM method scales as $\mathcal{O}(N^3)$. A 667 MHz DEC Alpha with 4 GB of RAM is used in this work. The 6144×6144 matrix storage for the MoM solution of the largest surface requires 1.8 GB of RAM. The FBSA method calculates the matrix elements 'on-the-fly', as the full matrix storage would be unfeasible given the very large surface sizes for which the method is best suited.

3.4 Conclusions

This chapter has presented an MoM formulation for scattering from 1-D layered rough surfaces. Comparison with analytical solutions validated the MoM formulation for flat surfaces. Given the linear increase in the number of unknowns for each layer, the

FBSA method has been adapted and $\mathcal{O}(\mathcal{N})$ efficiency was demonstrated. The standard MoM and FBSA formulations were compared for scattering from a three-region medium, and excellent agreement was obtained. Finally, numerical experiments were performed to establish the wide applicability of the method.

Chapter 4

An FDTD Study of Left Handed Metamaterials

4.1 Introduction

Materials exhibiting negative permittivity and permeability are a popular topic of current research due to their recent physical realization as metamaterials [87]. Recent research has focused both on the behavior of these metamaterials as well as on the incorporation of negative permittivity and permeability into electromagnetic theory [88]. Currently, the metamaterials under study are composed of a periodic arrangement of metallic printed lines (or rods) that exhibit a negative permittivity, and split-ring resonators (SRRs) that exhibit a negative permeability.

To understand how these metamaterials function, it is best to follow the historical steps that lead to the current geometry. First, it was shown that a 3D array of thin, continuous (infinite) metal wires exhibit a frequency response similar to that of a plasma medium [89, 90]. This type of response is well described by the Drude model:

$$\epsilon(\omega) = \epsilon_0 \left(1 - \frac{\omega_{ep}^2}{\omega(\omega + i\gamma_e)}\right) \tag{4.1}$$

where ω_{ep} is the plasma frequency and γ_e is the damping frequency (or loss factor) [91]. At frequencies below ω_{ep} (for $\gamma_e \simeq 0$), the permittivity becomes negative, the wave vector is imaginary, and there is no transmission. Above ω_{ep}, the permittivity is real and transmission occurs. Second, it was demonstrated that negative permeability could be achieved using an array of SRRs [92]. The SRRs act like magnetic dipoles, with a resonant response resulting from internal inductance and capacitance. This type of frequency response can be approximated with a resonant model [30]:

$$\mu(\omega) = \mu_0 \left(1 - \frac{\omega_{mp}^2 - \omega_{mo}^2}{\omega^2 - \omega_{mo}^2 + i\gamma_m \omega}\right) \tag{4.2}$$

where ω_{mo} is the resonant frequency, ω_{mp} is the plasma frequency, and γ_m is the damping frequency. Close to resonance, the SRRs produce strong magnetic fields whose directions oppose the incident magnetic field, resulting in a negative effective permeability. Once the negative permeability structures had been discovered, finding ways of combining them with negative permittivity structures was the next step in research, leading to the well known geometry shown in [87].

The key theoretical aspects and some applications were first investigated by Veselago in 1968 [93]. In his pioneering work, Veselago introduced the nomenclature 'left-handed (LH) materials', to refer to the left-handed tryad formed by the electric field ($\overline{E}$), magnetic field ($\overline{H}$), and wave vector ($\overline{k}$), as shown in Figure 4-1. As a simple example, the LH nature can be demonstrated by considering Maxwell's Equations for plane waves in source free, unbounded media:

$$\overline{k} \times \overline{E}(\overline{r}) = \omega\mu(\omega)\overline{H}(\overline{r}) \tag{4.3}$$

$$\overline{k} \times \overline{H}(\overline{r}) = -\omega\epsilon(\omega)\overline{E}(\overline{r}) \tag{4.4}$$

When both μ and ϵ are negative, the E, H, and k vectors form a left-handed tryad. It is then straightforward to show that the Poynting vector is in the opposite direction of the wave vector. Veselago predicted LH properties such as a reversed Doppler effect,

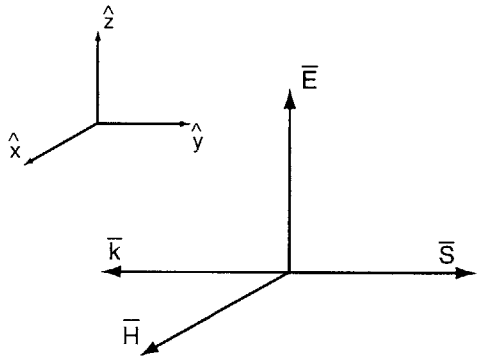

Figure 4-1: Electric field, magnetic field, wave vector, and Poynting vector for left handed media.

reversed Čerenkov radiation, and a negative index of refraction. For example, consider the index of refraction calculated for a passive medium with negative permittivity, $\epsilon_r = -\epsilon_r' + i\epsilon_r''$, and permeability, $\mu_r = -\mu_r' + i\mu_r''$,

$$n = \sqrt{(-\epsilon_r' + i\epsilon_r'')(-\mu_r' + i\mu_r'')} \tag{4.5}$$

Defining $\delta_e = \tan^{-1}(\epsilon_r''/\epsilon_r')$ and $\delta_m = \tan^{-1}(\mu_r''/\mu_r')$, Equation 4.5 becomes

$$n = \sqrt{|\epsilon_r|e^{i\pi - i\delta_e}|\mu_r|e^{i\pi - i\delta_m}} = e^{i\pi - i\delta_e/2 - i\delta_m/2}\sqrt{|\epsilon_r||\mu_r|} = -n' + in'' \tag{4.6}$$

To date, the range of imaginable applications extends to the field of antenna design, vehicle coatings for altering radar cross section properties, and lenses [94].

The demonstration of the LH properties of a metamaterial is not as straightforward as it seems, and showing that permittivity and permeability are separately negative over a similar frequency band does not imply that they remain so when the rods and SRRs are combined into a unique geometry. One of the first observations of the LH nature of these metamaterial structures was inferred by observing transmission and reflection coefficients over a wide frequency band. For the separate geometries (rods only or SRRs only), no transmission occurs because of an imaginary

wave number. In the frequency band where the two parameters are simultaneously negative, transmission occurs when the combined geometry is considered. This pass-band phenomenon was indeed observed in these metamaterials [87]. However, as mentioned before, this transmission is not sufficient to conclude that the material is exhibiting LH behavior, since the interaction between the SRRs and rods could result in a positive permittivity and permeability, which would also yield transmission. A more rigorous test to demonstrate the LH nature of a material is therefore to either directly measure the phase inside the material (this can be done numerically, as will be shown later, but is very difficult to realize practically), or to measure the index of refraction of a prism. Snell's law dictates that the angle of transmission into or out of any right-handed (RH, with positive permittivity and permeability) material must be on the opposite side of the surface normal with respect to the incident angle. For LH materials, however, the angle of transmission is on the same side of the normal, which has been theoretically demonstrated and experimentally verified [93, 30]. Note that recent work has suggested another rigorous way of calculating the index of refraction of a LH slab by measuring the lateral shift of an incident Gaussian beam [95].

Previous numerical modeling has been carried out to study the fields inside homogeneous LH materials in waveguides [96], as well as stratified LH media [88]. Numerical modeling of the metamaterials has been restricted to transmission and reflection coefficient measurements [97], or fields around a single SRR or periodic array of SRRs [98]. To date, little work has been done to investigate and verify the LH behavior of fields propagating within these metamaterials. Furthermore, only experimental work has been carried out to show the refraction from a prism with a negative index of refraction.

The first part of this chapter will use the three dimensional FDTD method to study the transmission characteristics, phase propagation, and index of refraction of metamaterials to unambiguously determine their LH or RH property. Two macroscopic configurations of metamaterials are used toward this purpose: a slab to calculate

the transmission coefficient and phase propagation, and a prism to study the index of refraction. The microscopic configurations of the metamaterials are based on the periodic arrangement of rods and SRRs [87], embedded in a parallel plate waveguide. The results of this work show that fields propagating inside the metamaterial with a forward power direction exhibit a backward phase velocity and negative index of refraction [31]. A brief discussion of the phenomena will follow. Finally, this chapter will investigate a new SRR that has been suggested for infrared frequencies [99]. The SRR is scaled to microwave frequencies and compared to the original SRR design.

4.2 FDTD Model

The numerical model is based on the experimental setup published in [30]. The FDTD computational domain is shown in Figure 4-2, modeling a metamaterial in a parallel plate waveguide. The structure can be either a slab or a prism (Figure 4-2), depending on the type of study performed. The parallel plates are Perfect Electric Conductor (PEC) sheets. Surrounding the structure is a Perfectly Matched Layer (PML) [98] that models microwave absorber, and ensures that reflections are small. In the model, the source is a current sheet that approximates a TE_{10} horn antenna, shown in Figure 4-2 as the wide dashed line. The current sheet radiates both forward and backward, but the wave traveling away from the structure is absorbed by the PML. In Section 4.3.3, the transmitted power in the far-field is calculated using a Huygens' transformation surface, shown in Figure 4-2 by the narrow dashed line. The model chosen for the SRRs is shown in Figure 4-3(a), with a discretization size of 0.25 mm. For an FDTD grid with a uniform cell size, an exact model of the geometry used in the experiment [30] requires a finer discretization and thus many more unknowns (and much longer computation time). For the sake of comparison, a more accurate model of the experimental SRR is shown in Figure 4-3(b), attained through a finer discretization of 0.125 mm. However, due to limited computational

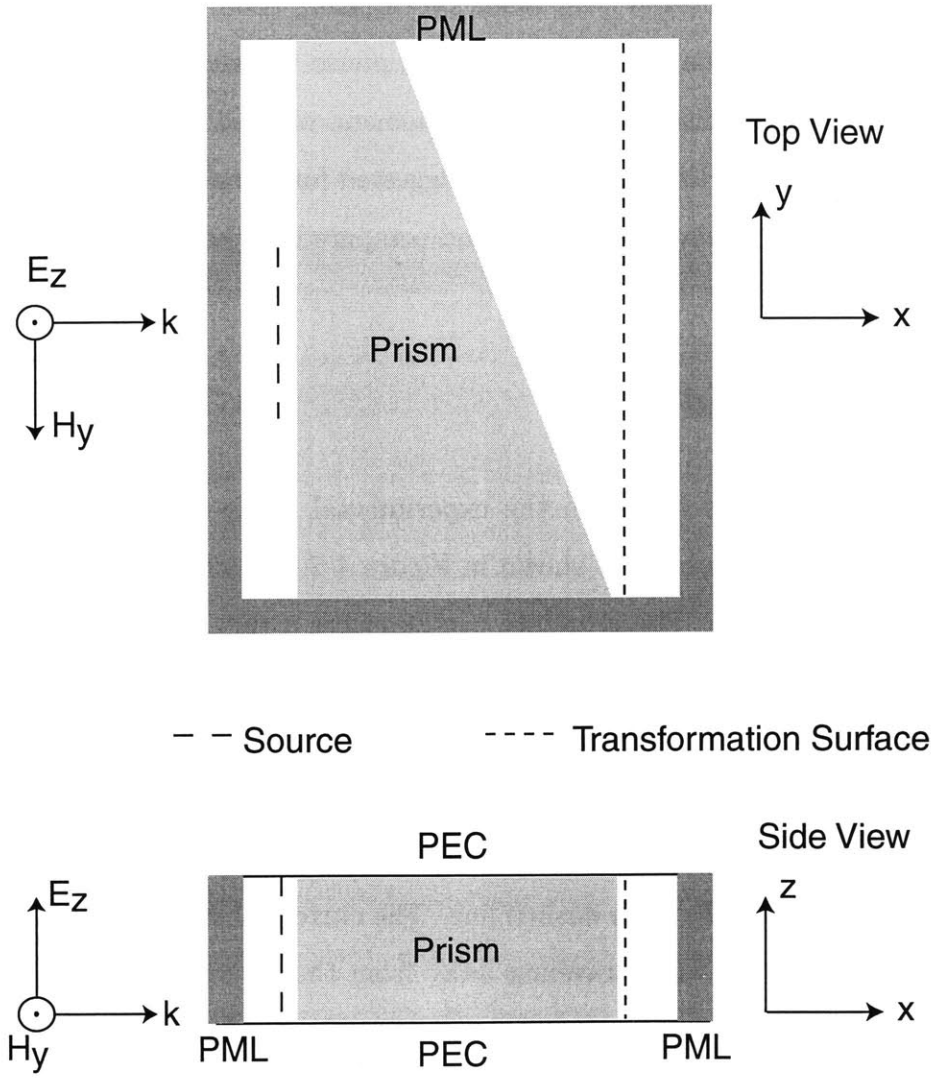

Figure 4-2: FDTD computational domain: a metamaterial structure (prism in this case) is included in a PEC parallel plate waveguide with PML lateral boundaries. Source is a current sheet approximating a horn antenna.

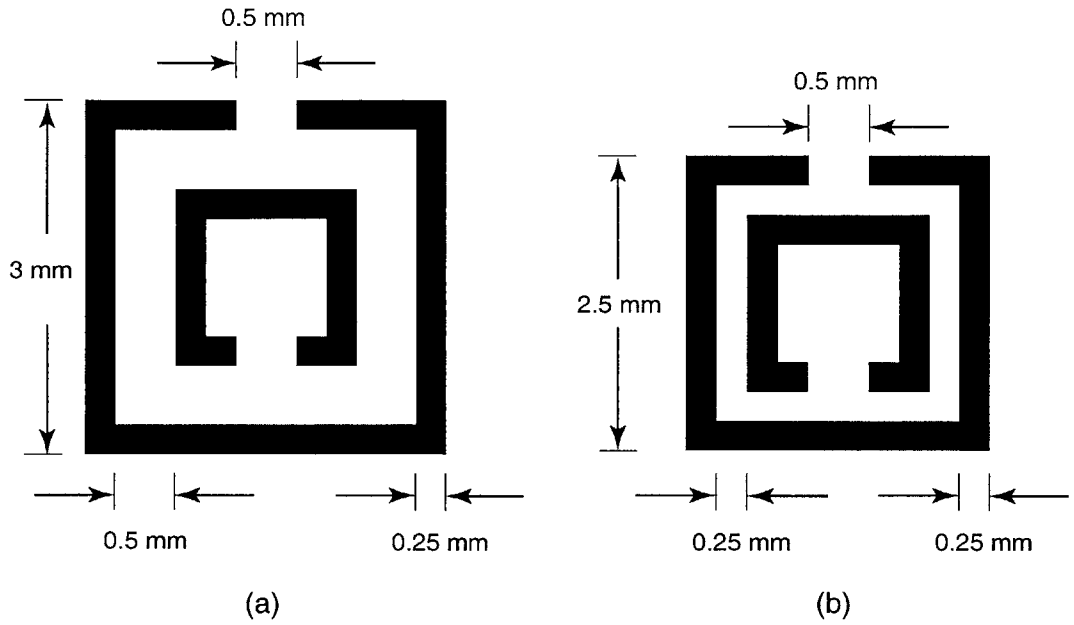

Figure 4-3: Geometry of the split ring resonators, used in FDTD with discretizations of (a) 0.25 mm, (b) 0.125 mm.

resources, most of the results presented in this chapter will be for the SRR geometry of Figure 4-3(a). The new geometry of Figure 4-3(a) will likely exhibit a different resonant frequency and, due to the lack of analytical models, it is not known a priori if it will exhibit a negative permeability and thus create an LH metamaterial.

The SRRs and rods are modeled as PEC materials in the standard fashion by setting the tangential electric fields to zero. The metamaterial consists of a periodic array of unit cells. A unit cell of the structure, in one plane, is shown in Figure 4-4(a). As in the experimental setup, three SRRs are stacked vertically between the PEC waveguide plates, printed on one side of a dielectric substrate (ϵ_r). On the other side of the substrate is printed a metallic rod 0.5 mm wide. A unit cell measures 5 mm $\times$ 5 mm $\times$ 13 mm. Using many unit cells in a single plane alone would create an anisotropic metamaterial, coupling with only one magnetic field component. Following [30], in order to create a more isotropic metamaterial, a structure in two planes is created as shown in Figure 4-4(b), where the unit cell is repeated in the

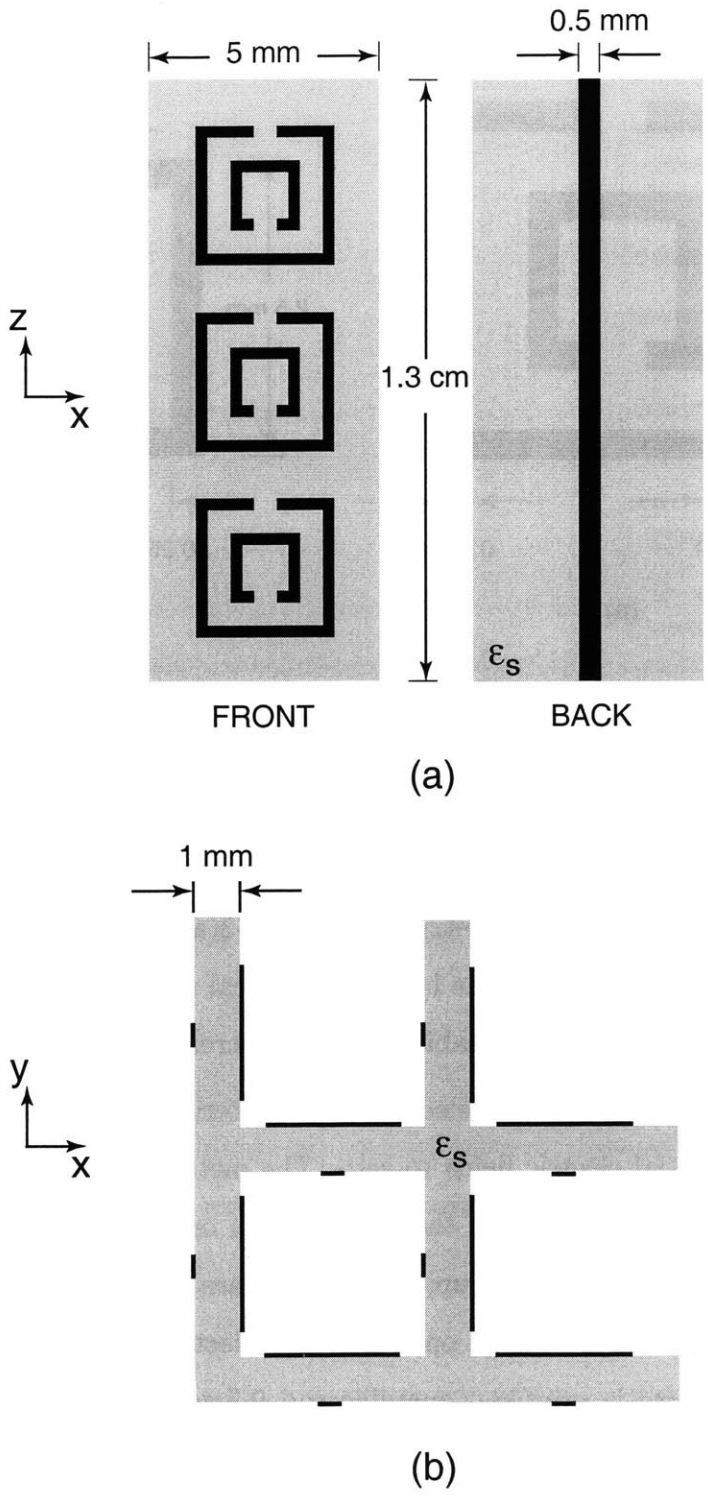

Figure 4-4: (a). Front and back of a single set of split ring resonators and rod. (b) 2×2 array of SRRs and rods.

($\hat{x}$,$\hat{z}$) and ($\hat{y}$,$\hat{z}$) planes. In this case, the SRRs interact with both the $\hat{x}$ and $\hat{y}$ magnetic fields, while the rods still couple with the $\hat{z}$ electric field. The structure shown in Figure 4-4(b) is a 2 $\times$ 2 array of SRRs, and is a typical example of the types of structures that are examined in the following sections.

The following results are from a metamaterial structure containing 9 $\times$ 12 unit cells. The computational domain measures 4.75 cm $\times$ 6.25 cm $\times$ 1.3 cm, or 190 $\times$ 250 $\times$ 52 cells, not including the PML. For the discretization of 0.25 mm, the corresponding time step is 4.77×10^{-4} ns. One simulation requires approximately 14 million unknowns to be solved, and it takes about 1.5 hours to complete 4000 time steps on a 667 MHz DEC Alpha Server with 4 GB of RAM.

4.3 Results

The FDTD model described in the previous section is used to perform three types of simulations. First, it is necessary to determine frequencies at which negative permittivity and permeability might exist. This is done by calculating the transmission coefficient of the metamaterial, and looking for pass-band regions. Once these frequencies are found, a continuous wave is used to examine the phase advance through the structure. Finally, at the same frequencies, a prism is used to calculate the index of refraction of the structure.

Four types of metamaterial are studied:

- Type 1: the structure shown in Figure 4-4(b) with the substrate $\epsilon_r = 1.0$; SRR geometry shown in Figure 4-3(a).
- Type 2: Figure 4-4(b) with $\epsilon_r = 3.4$; SRR geometry shown in Figure 4-3(a).
- Type 3: Figure 4-4(b) with SRRs and rods in the ($\hat{x}$,$\hat{z}$) plane only, $\epsilon_r = 1.0$; SRR geometry shown in Figure 4-3(a).
- Type 4: Figure 4-4(b), with $\epsilon_r = 1.0$; SRR geometry shown in Figure 4-3(b).

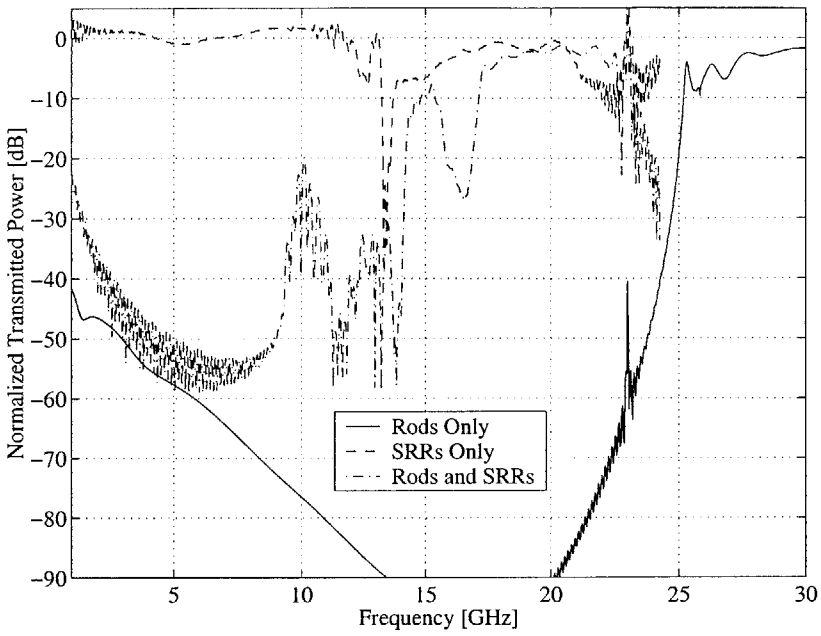

Figure 4-5: Normalized transmitted power through a metamaterial slab without dielectric (Type 1).

4.3.1 Determining Frequencies of LH Behavior

Determining the transmission coefficient of the metamaterial can be done in the FDTD model by using a wideband pulse incident on a metamaterial slab. These simulations use the first derivative of a Blackmann-Harris pulse [100] that vanishes completely after time period $T = 1.55/f_c$ ($f_c = 12$ GHz). Figure 4-5 shows the transmission coefficient of the Type 1 structure. Three cases are shown, for a periodic arrangement of rods alone (without SRRs), for the SRRs alone (without rods), and for the entire structure containing both the rods and SRRs.

The permittivity of the rods (using the plasma model of Equation 4.1) is expected to be negative below the plasma frequency. As shown in Figure 4-5, the structure with the rods alone has a high-pass filter behavior, consistent with the plasma model. Hence transmission only occurs above the plasma frequency for which the permittivity is positive and the wave number is real. For this geometry of rods, the plasma frequency is calculated to be 26 GHz [90], which matches well with the FDTD result.

According to [90] and the model of Equation 4.2, the SRRs are expected to have a resonant frequency, above which there is a small region of negative permeability. In Figure 4-5, the transmission through the structure of SRRs (without rods) has a stop-band, 30 dB down at approximately 13 GHz. The result is consistent with the resonant model, where transmission is not possible in the small region of negative permeability. Note that outside of resonance, the SRRs have little effect on the propagating field, their size being much less than one wavelength.

Now consider the Type 1 structure containing both the rods and SRRs. Below approximately 26 GHz, the rods yield a negative permittivity and no transmission is expected, unless the SRRs are yielding a simultaneously negative permeability that results in an LH pass-band. In Figure 4-5, for both rods and SRRs together, it is found that a pass-band exists between 14 GHz and 16 GHz. These frequencies are near the resonance of the SRRs and may be the LH pass-band. Note that there are other frequency ranges that are pass-bands, but these are not near the resonance of the rings, so they are identified as other phenomena of the metamaterial structure. There is also noise in the data due to the finite time of the FDTD simulation, since the structure is still 'ringing' slightly when the simulation is terminated at 16384 time steps. Longer simulations have been investigated, and it has been determined that this truncation error does not affect the general characteristics of the transmission curves. In addition, the higher frequency portions of the transmitted fields have noise due to both the truncated data and also the beginning of numerical dispersion. For these reasons, the high frequency portions of the transmission data for the SRRs and the complete structure have been truncated at 24 GHz. Figure 4-6 shows the transmitted power for the Type 2 structure. The presence of the dielectric shifts the resonant frequencies down, as is expected from simple physical arguments. The stop-band due to the SRR resonance occurs at 9 GHz and the transmitted signal is attenuated by 20 dB. A pass-band for the metamaterial structure is between 10 GHz and 11 GHz, and is 7 dB down. Figure 4-7 shows the transmitted power for the

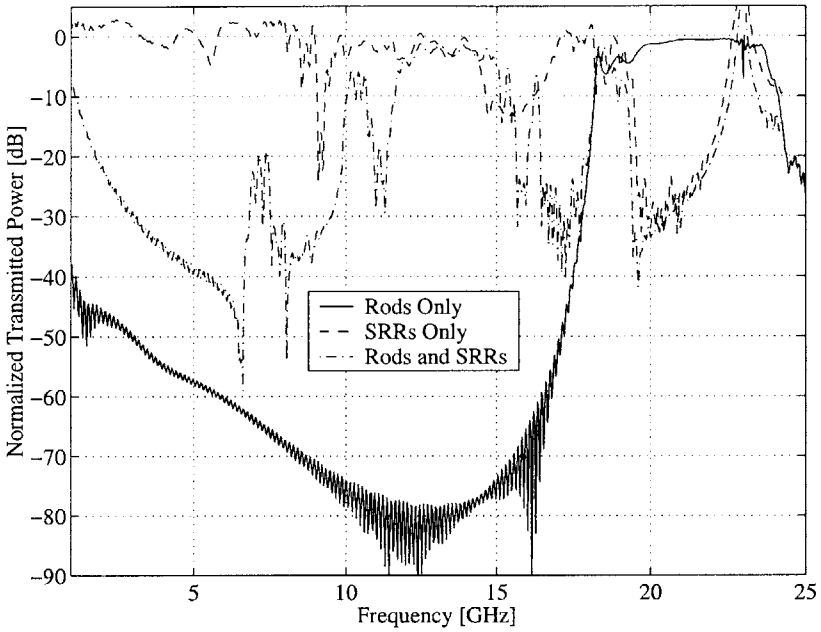

Figure 4-6: Normalized transmitted power through a metamaterial slab with dielectric (Type 2).

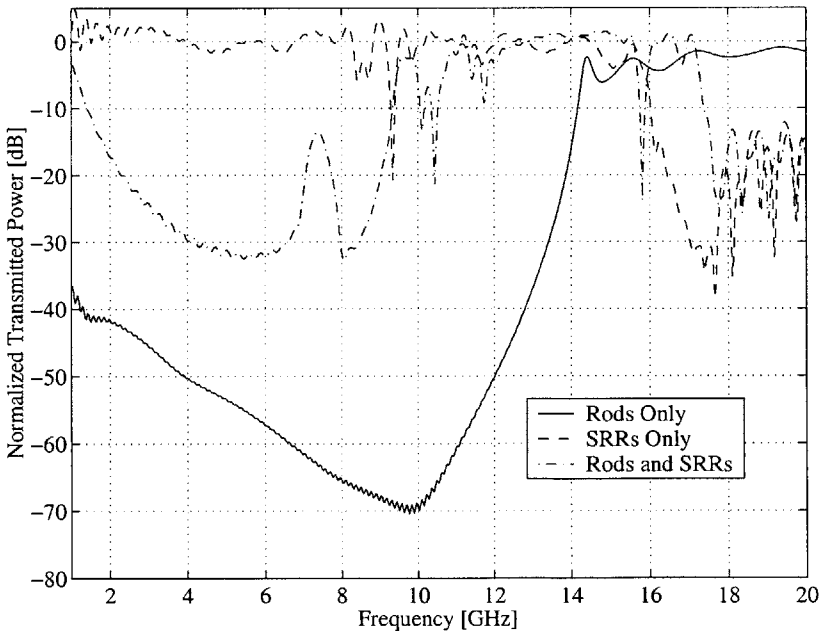

Figure 4-7: Normalized transmitted power through a metamaterial slab containing only SRRs in the $(\hat{z},\hat{y})$ plane with dielectric (Type 3).

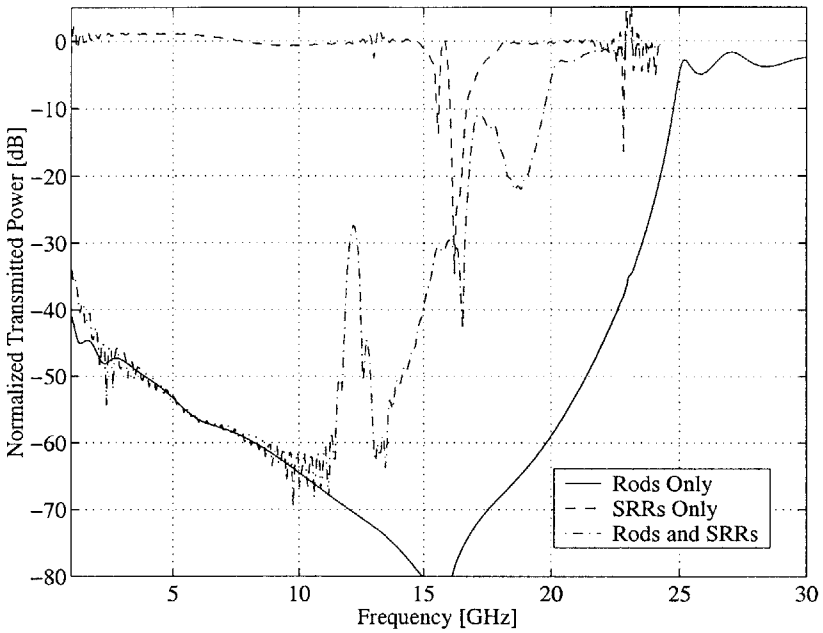

Figure 4-8: Normalized transmitted power through a metamaterial slab without dielectric (Type 4).

Type 3 structure. The resonance of the SRRs is still at 9 GHz, resulting in a 20 dB stop-band. The pass-band is between 9 GHz and 10 GHz, and is approximately 3 dB down from full transmission. From these results, it appears that the SRRs and rods in the $(\hat{y}, \hat{z})$ plane are not strictly required, which is expected given that incident field is almost a TEM wave and has a much stronger H_y field than an H_x field. Finally, in Figure 4-8, the transmission data for the Type 4 structure are shown. The Type 4 structure has very similar transmission characteristics to the previous three types of structures, indicating that the SRR model of Figure 4-3(b) is valid. For that case, the resonance of the SRRs is located around 16 GHz, attenuating the transmitted field by 30 dB. The pass-band occurs between 17 GHz and 18 GHz, and is 10 dB down.

These results demonstrate that wideband examination of the metamaterial's transmission coefficients reveals separate characteristics of negative permittivity and permeability predicted by theoretical models and previous experimental studies. Given that the SRRs create an effective negative permeability near resonance, the next sec-

tion will focus on the nearby pass-bands in the combined SRR and rod structure to determine if left-handed properties exist.

4.3.2 Phase Data in an LH Metamaterial Slab

One way of determining the LH property of a metamaterial is to calculate the phase of a propagating wave inside the structure and determine if the phase velocity is negative. Although a phase measurement is difficult to perform in experimental settings (as the probe could couple with the structure), it is simple to calculate in numerical simulations.

In the frequency regime of negative permeability, an SRR produces a strong internal magnetic field that is in the same direction as the incident field. It is the external, or return field, that opposes the incident magnetic field and thus produces an effective negative permeability. The SRRs are in an array so that they approximate the effect of longer, continuous structures like cylinders (to produce a solenoid magnetic field) [90]. Hence the structure likely exhibits negative permeability external to the SRR rows, where the following phase data is obtained.

Figure 4-9 shows the absolute value of the electric field plotted along the center of the Type 1 structure. The vertical axis of the plot corresponds to the distance through the structure, which begins at $x = 6.75\,\text{mm}$ and ends at $x = 42\,\text{mm}$, and the horizontal axis of the plot is time, in nanoseconds. The field is a continuous waves (CW), ramped up with a Gaussian modulation and shown here in late time where the structure has reached steady state. The electric field can then be expressed as $E_z = \cos(kx - \omega t)$ for which a point of constant phase C results in $x = \frac{\omega}{k}t + \frac{C}{k}$. The visually identifiable constant phase in Figure 4-9 is the null, which can be tracked through the structure. The slope of this phase is the phase velocity, $v_p = \omega/k$. The results shows that v_p is generally negative within the structure, but with positive slopes in regions close to the SRRs. As the wave exits the structure and enters free space, the phase velocity becomes $+c$. The field in the region of $x < 0.00675\,\text{m}$ contains both the incident field

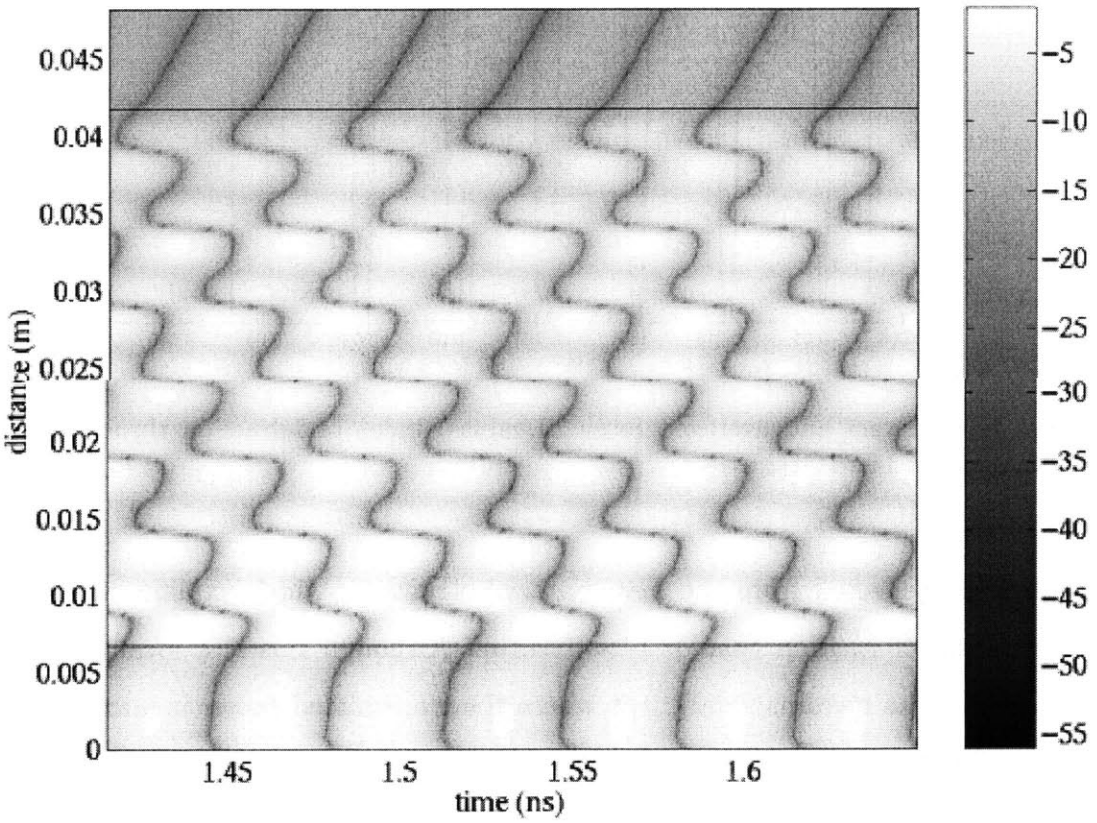

Figure 4-9: Absolute value of the electric field through the center of the Type 1 metamaterial, at 14.75 GHz (dB scale).

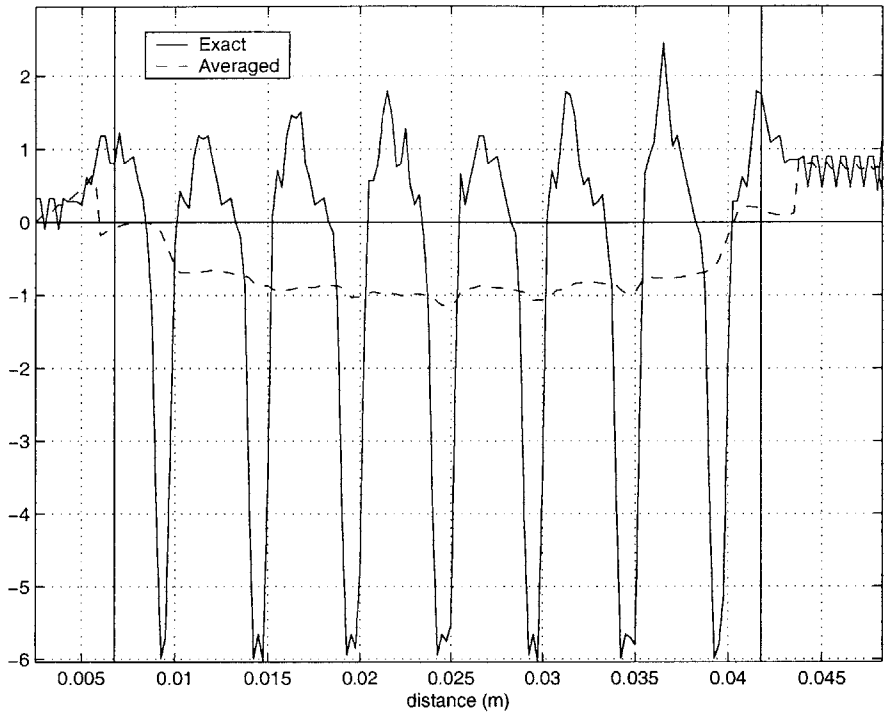

Figure 4-10: Exact and averaged (over 20 values) index of refraction through Type 1 metamaterial, at 14.75 GHz.

and the field reflected from the metamaterial structure, which explains the weaker positive slope of v_p than that of $x > 0.042\,\mathrm{m}$. Although this is a local effect (one path through the metamaterial), it is where the transmitted power is maximum and is demonstrative of the overall phase velocity.

The actual phase velocity of the propagating field can be determined simply by extracting the slope of constant phase on any space-time plot similar to Figure 4-9. Although the null is visually obvious, it is numerically easier to calculate the slope from a maximum or minimum. Once the slope is found, one can determine a normalized v_p of the field and, given the assumption that the phase has the form $kx - \omega t$, also determine the index of refraction as $n = c/v_p$. Figure 4-10 shows the calculated index of refraction, n_1, through the Type 1 structure for the electric field at 14.75 GHz. The phase fluctuates as the field passes near an SRR, and n_1 briefly becomes positive. To achieve a better representation of the overall phase, an

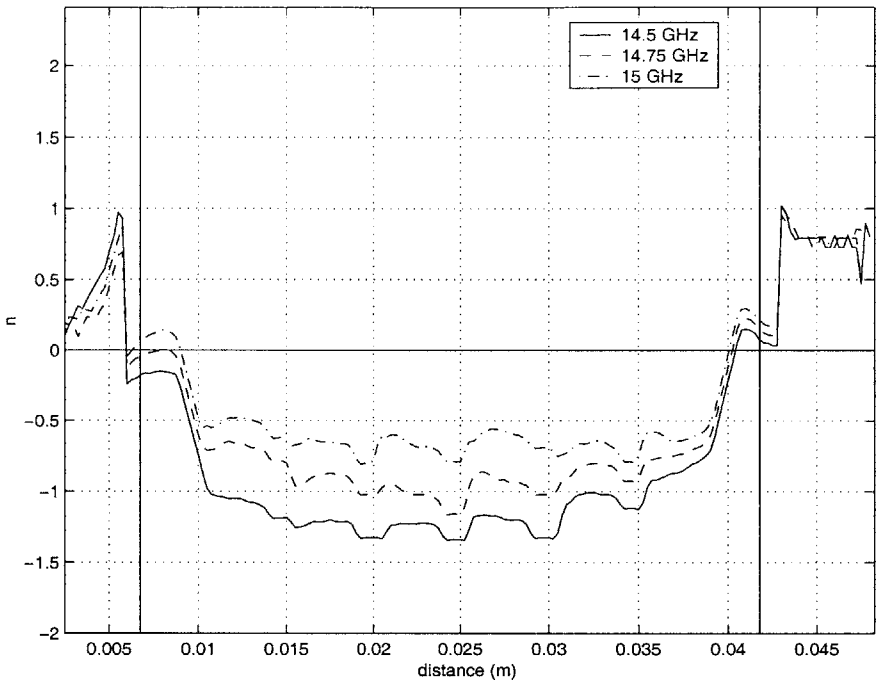

Figure 4-11: Index of refraction through Type 1 metamaterial for different frequencies.

effective n_1 is calculated with an averaging window around each data point (in this case 20 values). The effective normalized n_1 in this structure is fairly constant, around $n_1 = -1$. There are edge effects at the beginning and the end of the metamaterial structure, where n_1 makes a transition from positive to negative ($x = 0.00675\,\text{m}$) and back again ($x = 0.042\,\text{m}$). Note that the imaginary part of n_1 is nonzero, given that the metamaterial was shown to be lossy in the transmission figures. Figure 4-11 shows the averaged n_1 for different frequencies in the Type 1 structure. The metamaterial is very dispersive and inhomogeneous. In Figure 4-11, n_1 can be seen to become less negative as the frequency is increased from 14.5 GHz to 15 GHz, which is due to the narrow frequency band over which the material exhibits LH properties. Outside of that frequency band, n_1 becomes very irregular and eventually the structure no longer allows a propagating field (as the permeability becomes positive).

The averaged data of n_1 is dependent on the averaging window, and assumes the form of $kx - \omega t$ for the phase. To obtain another measure of the phase behavior, the

Type 1		Type 2		Type 3	
Freq. [GHz]	$\Delta\psi$	Freq. [GHz]	$\Delta\psi$	Freq. [GHz]	$\Delta\psi$
14.5	-3.7π	10	-3.3π	9.5	-4.0π
14.75	-2.9π	10.25	-3.5π	9.75	-2.8π
15	-2.2π	10.5	-2.0π	10	-2.2π
15.25	-1.5π	10.75	-1.4π	10.25	-1.5π
15.5	-0.9π	11	-0.5π	10.5	-0.3π

Table 4.1: Total phase shift $\Delta\psi$ through the three types of LH metamaterials.

cumulative phase shift, $\Delta\psi$, for a continuous wave propagating through the structure can also be calculated. Table 4.1 shows the cumulative phase shift for various frequencies in the three types of metamaterial. The phase shift is calculated for 14.5 GHz to 15.5 GHz in the Type 1 structure, with a maximum shift of -3.7π at 14.5 GHz. At smaller frequencies, the phase could not me determined as the transmission through the structure became irregular. At 15 GHz, the phase shift through the Type 1 structure is approaching zero, and the transmitted power is decreasing toward the upper limit of the LH pass-band behavior. In the absence of the metamaterial, the free space phase shift (kd) would be 3.5π for 15 GHz. The same behavior can be seen in $\Delta\psi$ for the Type 2 structure, for frequencies from 10 GHz to 11 GHz, and for the Type 3 structure, for frequencies from 9.25 GHz to 10.25 GHz.

Figure 4-12 shows the power through the Type 1 structure at 14.75 GHz (above the middle SRR). The small regions of backward power are blacked out, and the system has a forward time average power propagation.

The results in this section show that the phase velocity and power are in opposite directions near the center of the metamaterial. However, the fields within the metamaterials are spatially inhomogeneous in the plane transverse to the direction of propagation, and the LH behavior is not uniform over that plane. Edge effects are apparent near the microwave absorber and particularly strong near the waveg-

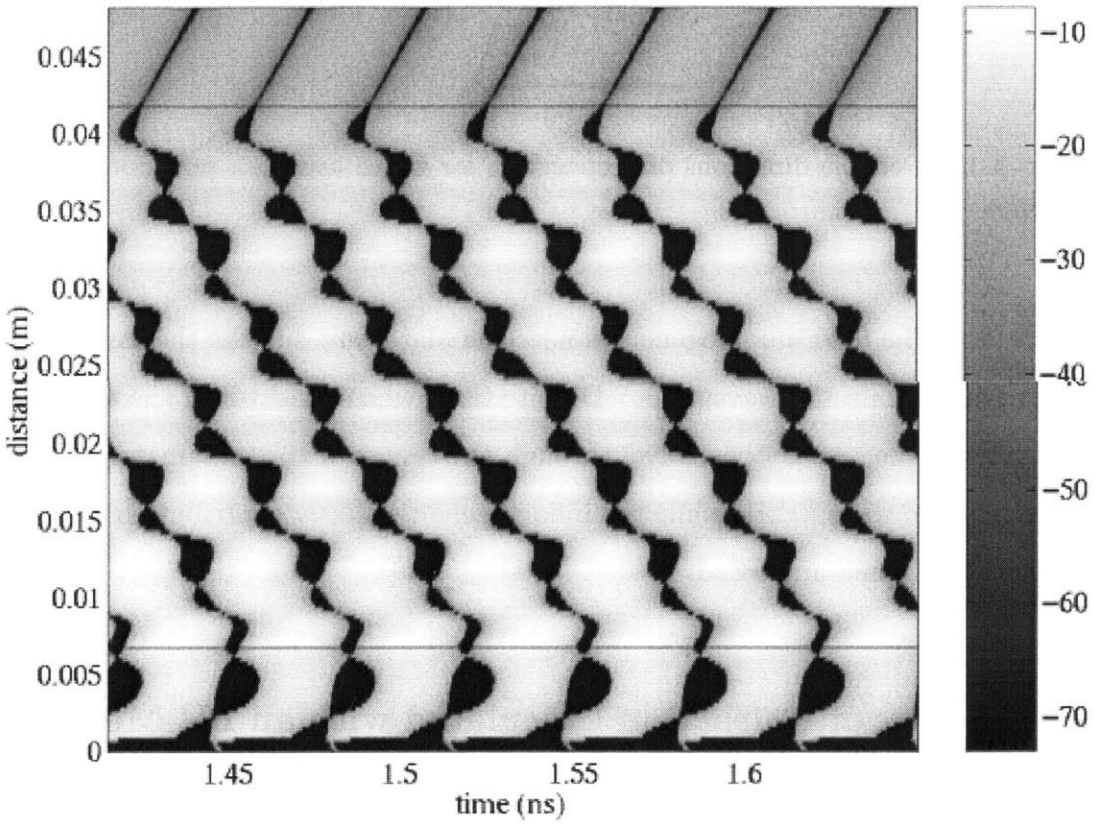

Figure 4-12: Power through the center of the Type 1 metamaterial, at 14.75 GHz (dB scale). Regions of backward (negative) power are blacked out.

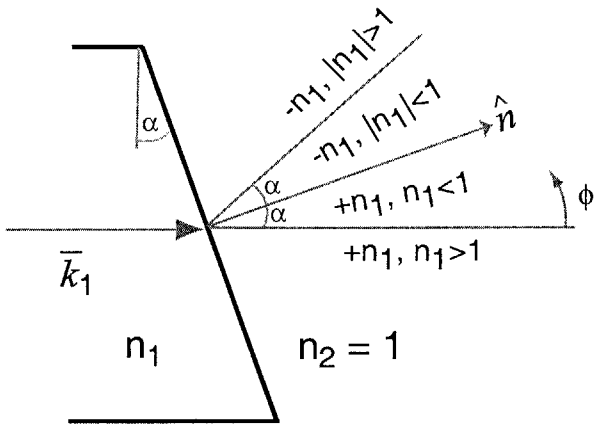

Figure 4-13: Possible directions of propagation for waves leaving a prism of material ϵ_1 into free space.

uide plates. (The field inhomogeneities near the plates are due the the asymmetry of the structure within the waveguide.) Despite that, when considering the transmitted wave, most of the power does travel through the center of the metamaterial. Hence, the transmitted wave is LH, while the inhomogeneities likely contribute to reflections and losses in the metamaterial.

4.3.3 Index of Refraction Calculated with an LH Metamaterial Prism

Another method of demonstrating LH behavior of a material is to construct a prism and calculate the direction of power leaving the structure. This has been carried out experimentally [30], and was first rigorously verified with a numerical approach by this work. Figure 4-13 shows the possibilities of Poynting vectors for power leaving a prism of various values of n_1. Upon measuring the direction of the power ($\overline{S}$) leaving the prism, it is possible to calculate the index of refraction using Snell's law. First consider the direction of $\bar{S}$ leaving a prism of homogeneous dielectric ($\epsilon_r = 3.4$). A staircased approximation of $\alpha = 18.4°$ interface is used to model the prism. To

determine the direction of the fields leaving the prism, the electric and magnetic fields are integrated over the aperture of the waveguide and calculate the far fields using Huygens' principle [3]. In this case $\overline{S} = \overline{E} \times \overline{H} = E_\theta \hat{\theta} \times H_\phi \hat{\phi} = S_r \hat{r}$. A pulse is used as the excitation, and the far fields are calculated at the frequencies determined in the previous section. The quantity $S_r \hat{r}$ models the measurements that would be taken with a horn antenna moved along a radial axis, varying ϕ and keeping $\theta = \pi/2$. Note that the direction of the transmitted wave yields only an effective real index of refraction for the prism. The results for $S_r \hat{r}$ in Figure 4-14 show the fields propagating in the $\phi = -14.5°$ direction, which corresponds to a $\epsilon_r = 2.96$, or $n_1 = 1.72$ in the prism. The reason for this inaccuracy is the slightly non uniform (curved) phase front of the propagating field. Hence, this technique does not provide an exact way to determine n_1 of the prism, but is instead an approximation. The result can be an under-prediction of n_1, as one side of the curved phase front is almost parallel to the prism interface, whereas the other side may reach cut-off. Larger arrays of unit cells would alleviate this problem. In order to build a metamaterial prism, a coarse staircasing approximation is used, now with the metamaterial unit cells (Figure 4-4). To build the $\alpha = 18.4°$ interface, we use three SRRs in $\hat{y}$ for every single SRR in $\hat{x}$. The far field plots are also shown in Figure 4-14 for the Type 1 and Type 2 metamaterials. The Type 1 metamaterial refracts the 14.75 GHz component of the pulse at an angle of $\phi = 35°$, which corresponds to $n_1 = -0.91$. The Type 2 metamaterial refracts the 10.25 GHz component of the pulse at $\phi = 41°$, which corresponds to $n_1 = -1.2$. The metamaterials refract smaller amounts of power around 0°, which is likely due to non-uniform phase front of the incident wave as well as edge effects (apparent in Figure 4-15). The results in this section are consistent with the results in the previous section, where the index of refraction was calculated directly from the phase velocity within a metamaterial slab. In both sections, the Type 1 metamaterial index of refraction is approximately -1, and the Type 2 metamaterial's index of refraction is approximately -1 to -1.5. The main source of error is likely due to the effects of

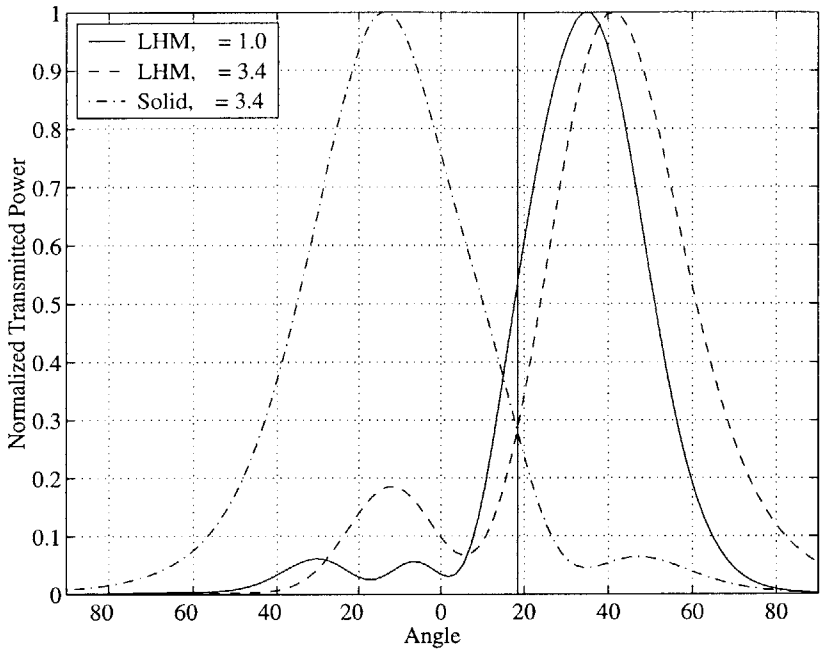

Figure 4-14: Far field power from prism (of various materials) vs azimuthal angle, $\alpha = 18.4^o$.

the curved phase front in the prism calculation.

For visualization purposes, Figure 4-15 shows the electric field of a continuous wave leaving a prism of larger angle ($\alpha = 26.6°$), and one can see the phase fronts indicative of a field refracted from a negative medium into a positive one (free space in this case). The metalization of the metamaterial is indicated in white on the plot, as is the approximate prism boundary (for illustration).

4.4 Discussion

The results of the previous section demonstrate that fields within the metamaterial have phase velocities and Poynting vectors in opposite directions (for an equivalent homogeneous material), and that the metamaterial has a negative index of refraction. As discussed in the introduction, his LH behavior can be accounted for assuming that the metamaterial has a negative permittivity and a negative permeability, predicted

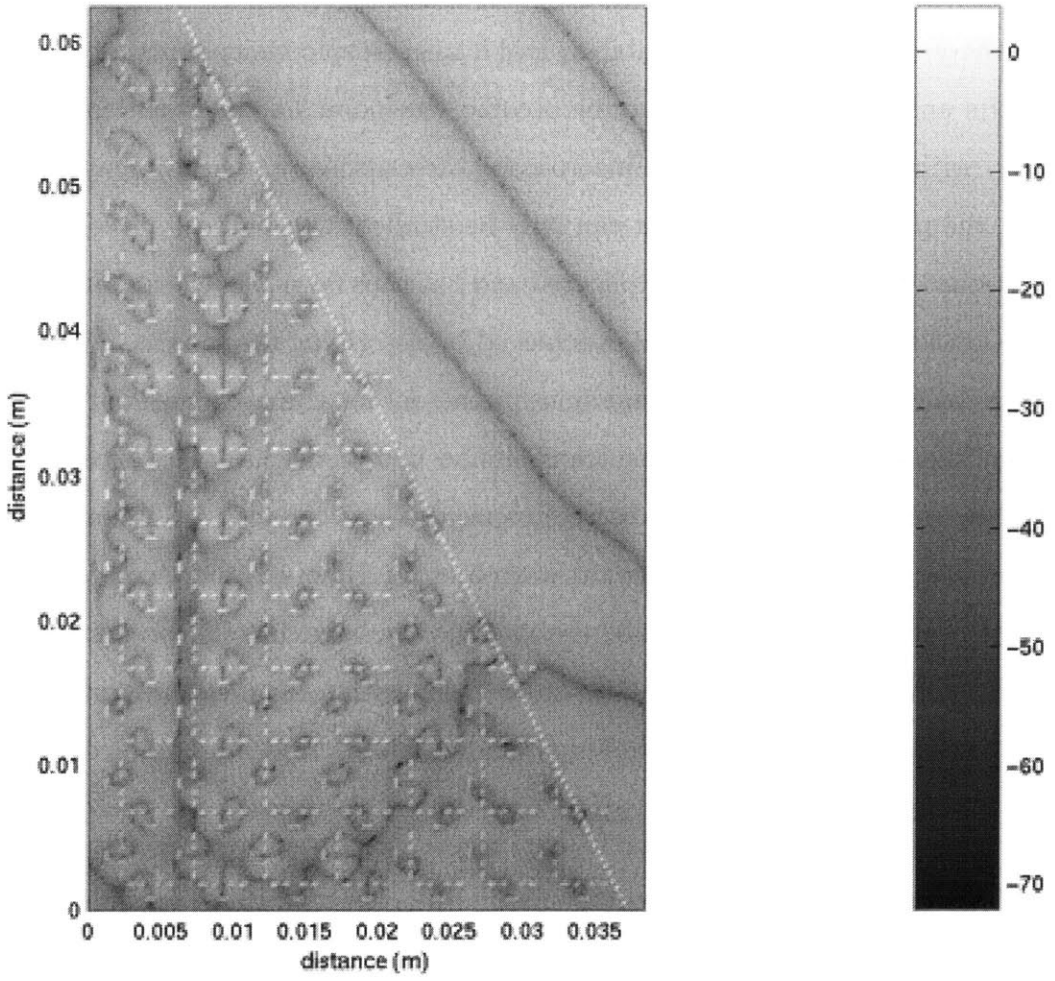

Figure 4-15: Absolute value of the electric field inside a metamaterial prism structure (dB scale), $\alpha = 26.6^o$.

in studies of the rods and SRRs separately [89, 90]. Mathematically, it is easy to show that a negative permittivity and a negative permeability give rise to an LH medium with $n < 0$, but it is less obvious why such a phenomenon would exist for the combined rod and SRRs metamaterial. In fact, there are generally two ways of studying LH materials [101]: a macroscopic viewpoint that deals with the assumed negative permittivity and negative permeability, and a microscopic viewpoint that deals with the SRRs and rods directly. The microscopic viewpoint has been the focus of this chapter, with an aim to develop macroscopic descriptions of the LH metamaterial. Indeed, the microscopic viewpoint can only be studied with numerical techniques, as the metamaterial geometry is complicated and has thus far not been explained analytically. Considerable success has been achieved by describing the rods as inductors and the rings as capacitors in a transmission line model for the metamaterial [102, 103]. The equivalent LH behavior of the transmission line model has been experimentally verified in two dimensions using discrete capacitors and inductors. In one dimension it reduces to the well-known backward wave line [3]. However, more complex models have not been developed to describe the microscopic behavior. This section will provide a brief discussion on the behavior of the fields within the metamaterial, based on calculated FDTD fields, in an attempt to understand the results obtained thus far.

Figure 4-16 is a diagram of the four unit cells, separated by approximately $kx = \pi/2$, of the metamaterial at three different time steps: $\omega t = 0$, $\omega t = \pi/2$, and $\omega t = \pi$. An incident wave, $\overline{E}_i = \hat{y}\cos(kx - \omega t)$, impinges from the left. The electric fields are in the plane of the page, and are illustrated with arrows, while the magnetic fields are perpendicular to the page and illustrated with circles. Again, note that all illustrations are based on calculated FDTD fields, analytical considerations (for example [90]), and physical arguments. At $\omega t = 0$, the incident field excites currents on the rods and on the SRRs. The induced magnetic field from the SRRs and the rod are opposite between the first and second set of SRRs, and the rods stop the incident field from entering the metamaterial. At $\omega t = \pi/2$, the incident field and

induced SRR currents go to zero. The result is that the magnetic field inside the SRRs decays, and new currents are set up to oppose the changing magnetic field (by Lenz's law). These new currents give rise to new electric fields that couple with and induce currents on the second set of SRRs. The combined field between the first and second set of SRRs is shown in Figure 4-16, with the magnetic field in the $-\hat{z}$ direction and the electric field in the $-\hat{y}$ direction. Between the second and third set of SRRs, the magnetic fields are opposite in direction and the electric field from the first ring cannot propagate past the rod. The last time step shown in Figure 4-16 is $\omega t = \pi$. At this time the incident electric and magnetic fields are in opposite directions to the $\omega t = 0$ time, and again induce currents on the first ring. The magnetic fields between the first and second set of SRRs are opposite in sign, and no propagating field exists there. The magnetic field within the second ring is decaying, again setting up new currents and electric fields. These electric fields now couple with the third ring, creating the magnetic fields as shown. The combined fields between the second and third set of SRRs are shown in the figure, with the electric field in the $\hat{y}$ direction and the magnetic field in the $\hat{z}$ direction. Figure 4-17 shows the process continuing through $\omega t = 3\pi/2$, 2π, and $5\pi/2$ in a periodic fashion. The SRRs are resonating in time, coupling electric and magnetic fields to the adjacent SRRs and rods. In these three timesteps, the backward wave can be seen. At $\omega t = 3\pi/2$, between the third and fourth sets of SRRs, the electric field is in the $-\hat{y}$ direction, the magnetic field is in the $-\hat{z}$ direction, and so the Poynting vector is in the $\hat{x}$ direction. As the time steps progress, this point of constant phase moves in the $-\hat{x}$ direction through the structure: to between the second and third sets of SRRs at $\omega t = 2\pi$, to between the first and second sets of SRRs at $\omega t = 5\pi/2$, and so on.

Given the SRR resonance described above, the final row of SRRs in the structure radiate into free space. The propagating field leaving the structure is then similar to the radiated field from an array of magnetic dipoles (each SRR). To show this, we create a dipole array with a similar geometry as the final row of rings in Figure 4-

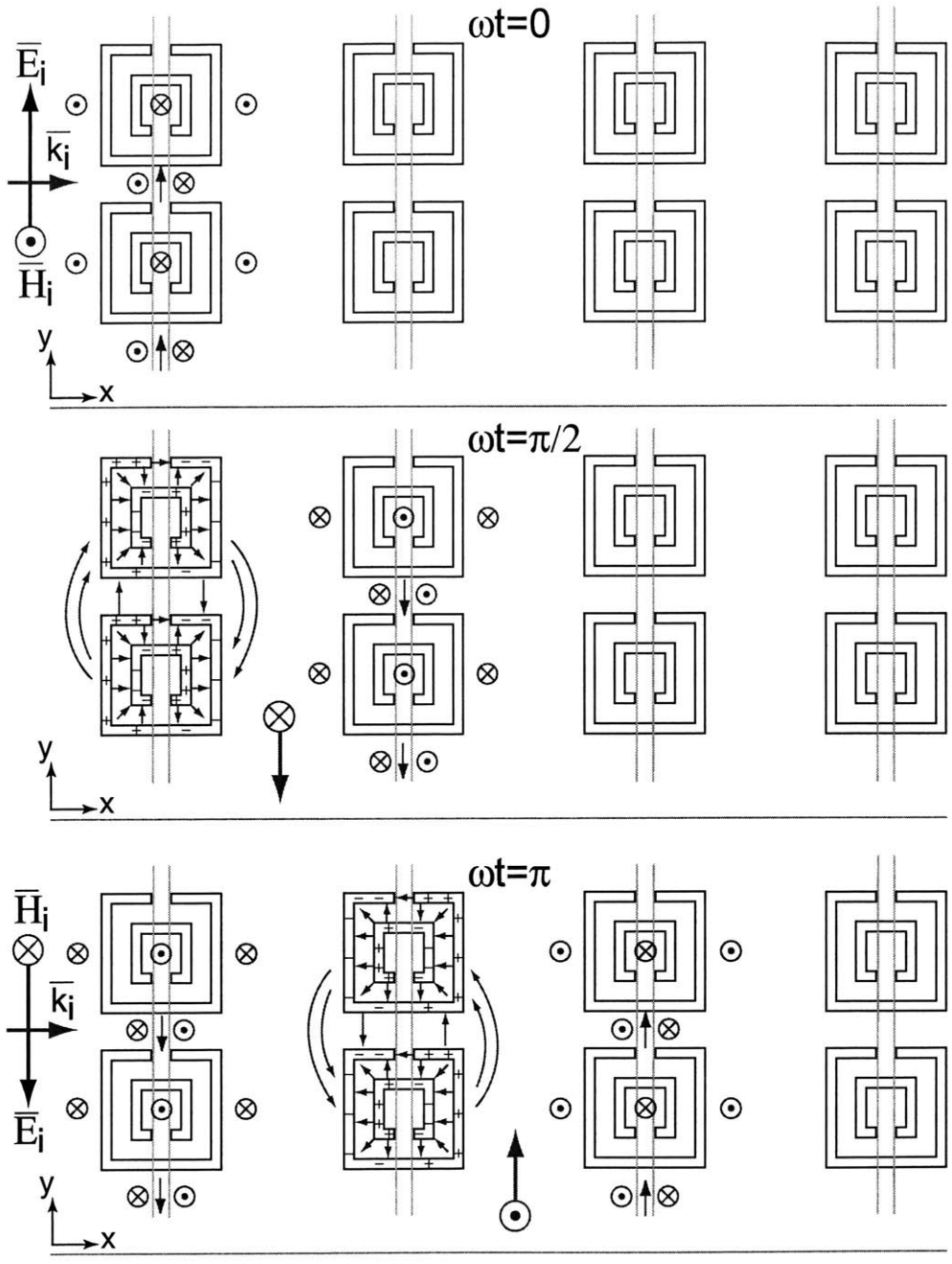

Figure 4-16: Diagram of the electric and magnetic fields within the metamaterial, based on calculated FDTD fields. The electric fields are the arrows in the $(\hat{x}, \hat{y})$ plane, and the magnetic fields are the circles perpendicular to the page. A plane wave is incident from the left and sets up a backward wave within the metamaterial. Initial times $\omega t = 0$, $\pi/4$, and $\pi/2$ are shown. The separation between rings is less than $kx = \pi/2$. Two rings are shown here for illustration purposes, but the same analysis applies to any number of rings.

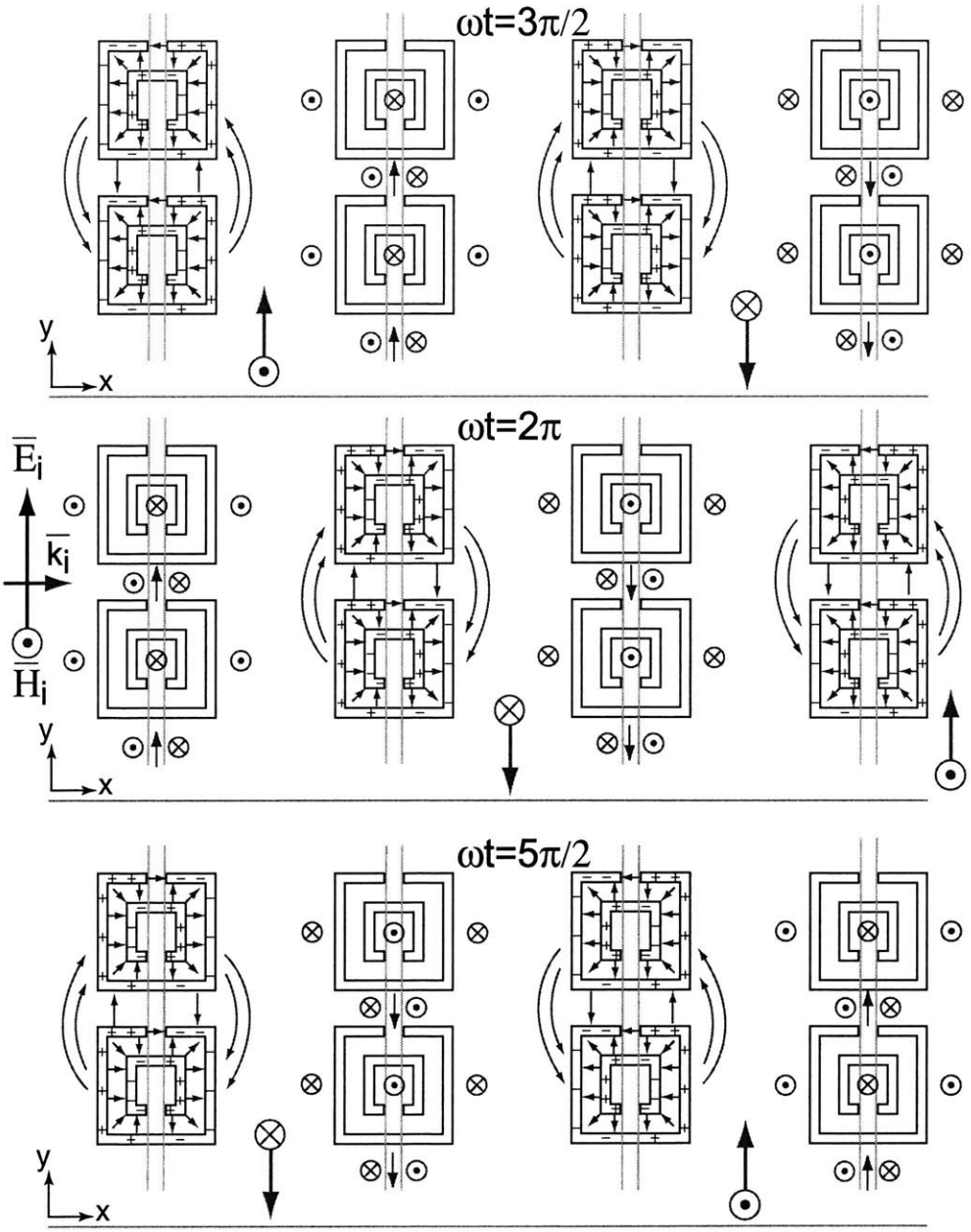

Figure 4-17: Diagram of the electric and magnetic fields within the metamaterial, based on calculated FDTD fields. The electric fields are the arrows in the $(\hat{x}, \hat{y})$ plane, and the magnetic fields are the circles perpendicular to the page. A plane wave is incident from the left and sets up a backward wave within the metamaterial. Initial times $\omega t = 3\pi/4$, π, and $5\pi/4$ are shown. The separation between rings is less than $kx = \pi/2$. Two rings are shown here for illustration purposes, but the same analysis applies to any number of rings.

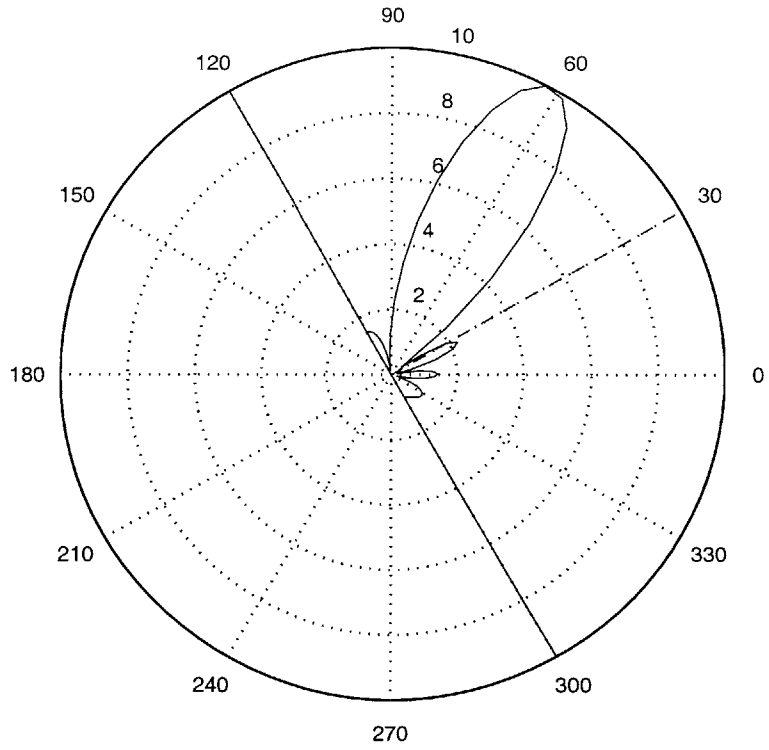

Figure 4-18: Far field pattern of an array of dipoles with backward phase.

15, using 10 dipoles at an exact 30^o angle instead of 12 SRRs at 26.6^o. The phase difference between the dipoles is taken from the FDTD calculations ($kx \simeq -\pi/2$). The far field array pattern from this structure can be easily calculated [3], and is shown in Figure 4-18. The far field pattern consists of one main lobe at 30 degrees above normal, which indicates a negative metamaterial with $n \simeq -1$. For the SRRs to have that phase difference ($-\overline{k}_x$), and for the structure to radiate in the $\hat{x}$ direction ($+\overline{S}_x$), there must be a LH wave within the metamaterial.

4.5 A New SRR geometry

The previous sections contain an analysis on specific SRR geometries to compare with experimental work. However, recent research has yielded other SRR designs that also may provide a negative permeability. One drawback of the original SRR geometry

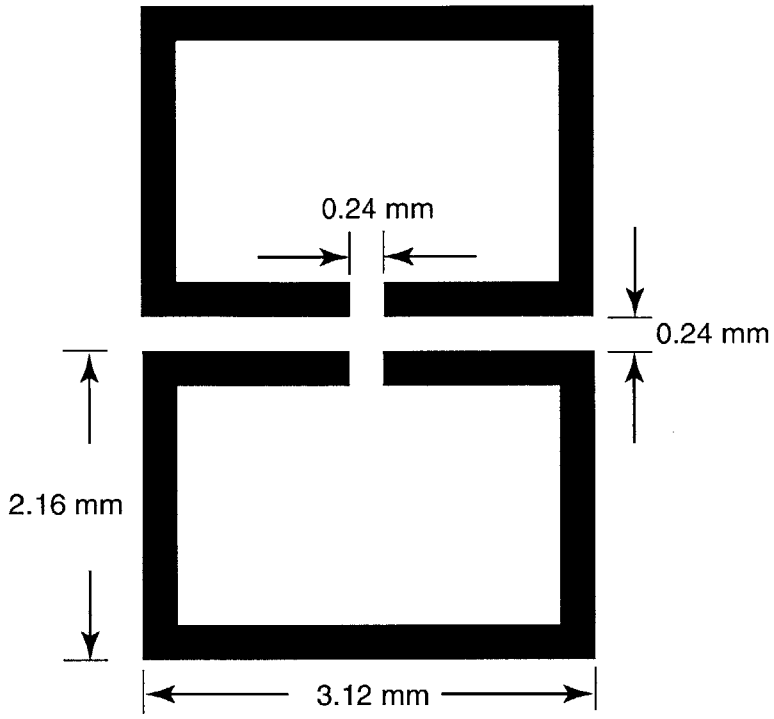

Figure 4-19: New SRR geometry

is its anisotropy, which limits its potential applications, so researchers are working toward isotropic designs [104, 105]. New SRR designs have also been created to reduce the original SRR's bianisotropy [106, 107]. Other researchers have focused on combining the SRRs and rods into one structure, and have been successful with the so called Omega medium [108, 109]. With the FDTD method and analysis techniques developed in this work, other geometries may be studied also. Consider the SRR shown in Figure 4-19, first introduced for infrared frequencies [99] and scaled here for microwave frequencies. A new FDTD discretization of 0.12 mm is used for this SRR. The new unit cell in the $(\hat{x}, \hat{z})$ plane is shown in Figure 4-20(a), composed of two SRRs and a rod that is in contact with the parallel plates. The lattice constant 5.04 mm, and the parallel plate separation is 1.2 cm. Figure 4-20(b) is the view in the $(\hat{x}, \hat{y})$ plane of a 2×2 array of the SRRs and rods. The dielectric constant, ϵ_s, is set to free space for the following results.

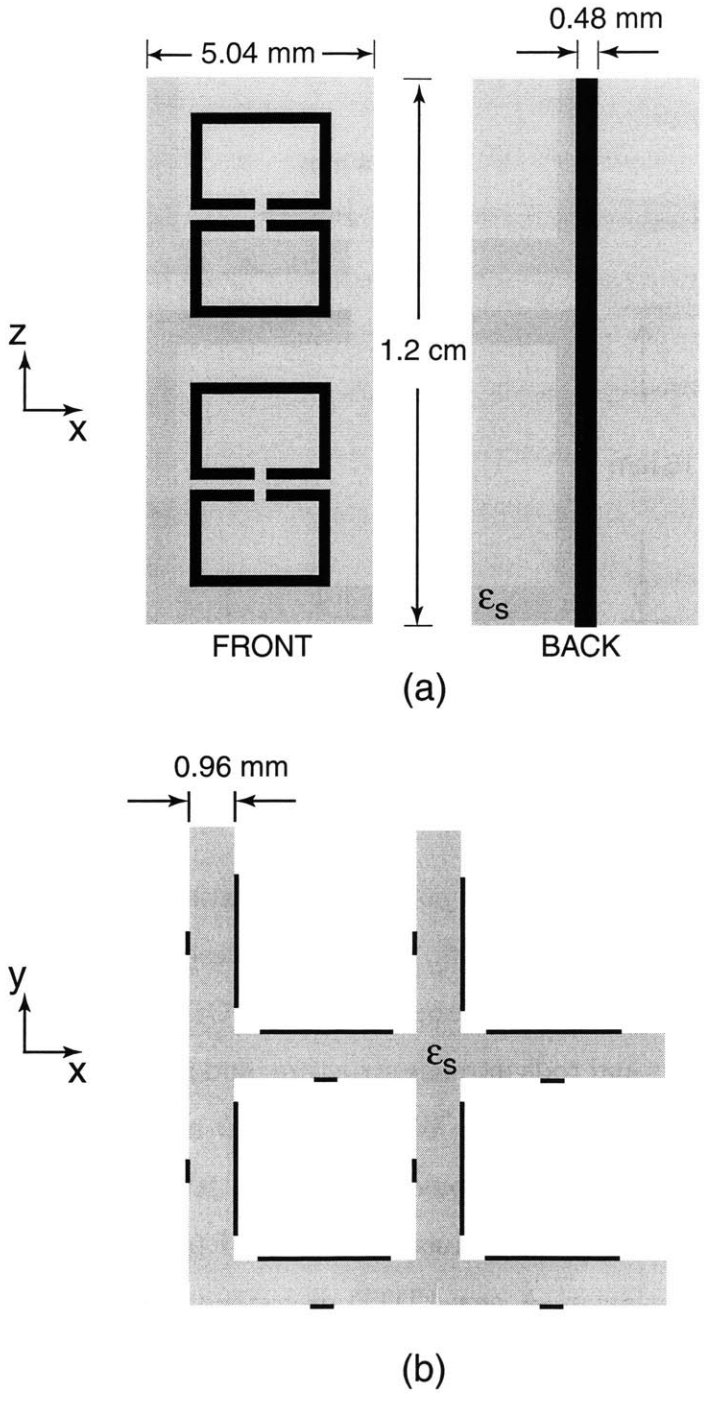

Figure 4-20: (a). Front and back of a single set of split ring resonators and rod. (b) 2 × 2 array of SRRs and rods.

We first consider the transmission through a metamaterial slab to obtain the frequencies of LH behavior. The wideband pulse is used to obtain S21 for a slab of 6×9 unit cells. Metamaterials containing both the new SRR, referred to as Ring A (metamaterial A), and the original SRR, referred to as Ring B (metamaterial B), are considered. Figure 4-21 shows S21 for both types of metamaterial. A possible LH band for metamaterial A appears at approximately 13 - 13.5 GHz, indicating that Ring A has a lower resonant frequency than Ring B (LH band 14.25 - 15 GHz). In the following section, the LH behavior of this pass-band will be verified. The maximum S21 in the LH band of metamaterial A is close to 0 dB, indicating that the structure is almost lossless at that frequency. Note that the SRR is PEC and the substrate is not present, so this is an idealized structure. However, the maximum transmitted power at LH frequencies is 10 dB greater in metamaterial A than in metamaterial B (which has the same idealized conditions). The reason for the larger transmission is the inherent symmetry of the Ring A in the waveguide. Ring B's lack of symmetry results in field inhomogeneities that are detrimental to transmission. Finally, the S21 of the Ring A metamaterial is closer to that predicted by theory: a high pass transmission characteristic (from the rods) with a single pass-band appearing near the SRR resonance.

Now we may calculate n using a prism of metamaterial A. The longest dimension of the prism is 6 x 9 unit cells, staircased 3 to 1 to achieve an 18.4 degree angle. As demonstrated in the previous section, the direction of the far-field power is calculated to determine n. Figure 4-22 shows n over the LH band obtained from Figure 4-21. The normalized far field power is also shown. The LH band is between 12.9 GHz and 13.5 GHz, with a minimum $n = -1.25$. The peak transmitted power occurs at 13.2 GHz where $n = -1$. Finally, we consider time domain plots of a 13.1 GHz CW wave traveling through the metamaterial prism. For the sake of visualization, a 2 to 1 staircased (26.6 degree) prism of 7 x 12 unit cells is used. Figure 4-23 shows the absolute value of the electric field at $\omega t = 0$, $\omega t = \pi/2$, $\omega t = pi$, and $\omega t = 3 * pi/2$,

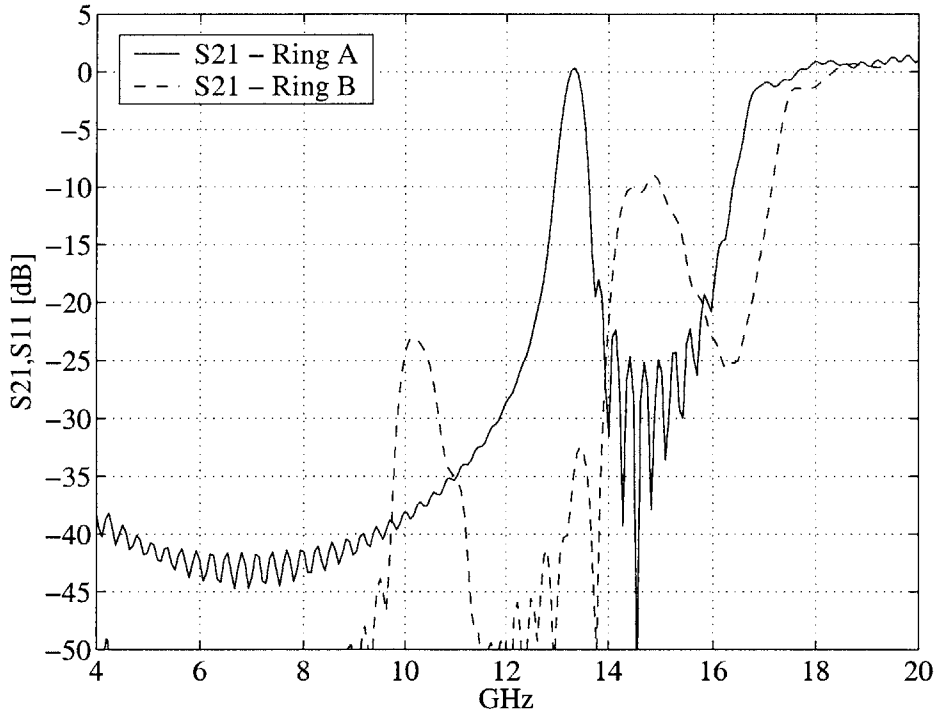

Figure 4-21: S21 of two metamaterial slabs, each 6×9 unit cells. 'Ring A' is the metamaterial composed of the new SRR, 'Ring B' is the metamaterial composed of the original SRR (Type 1).

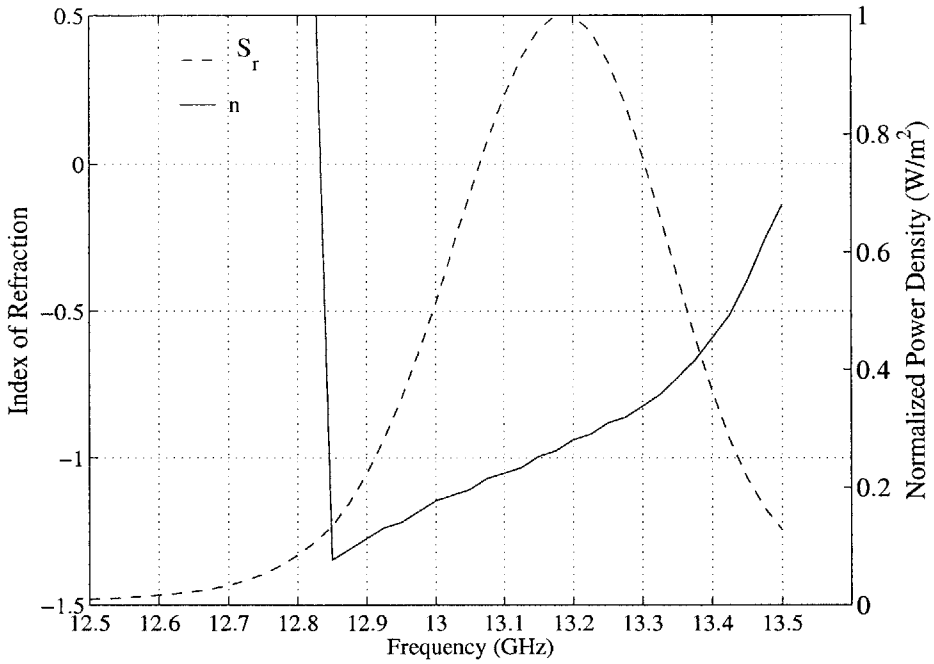

Figure 4-22: Normalized power and index of refraction for the Ring A metamaterial.

relative to $t = 1.8$ ps. The viewpoint is the same as the top view in Figure 4-2. From these plots, it is seen that the phase inside the prism is moving toward the source, and the phase outside the prism is moving away from the source (and prism). Furthermore, given the direction of power is perpendicular to the phase fronts for a single frequency CW, the field leaving the prism in Figure 4-23 is above the normal, indicating that n is negative.

4.6 Conclusions

This chapter examined three techniques to localize and demonstrate the LH behavior of a metamaterial. First, the possible frequency band of LH behavior was determined by calculating the transmitted power of a wideband pulse through the metamaterial. In that frequency band, the backward phase velocity in a slab of metamaterial was

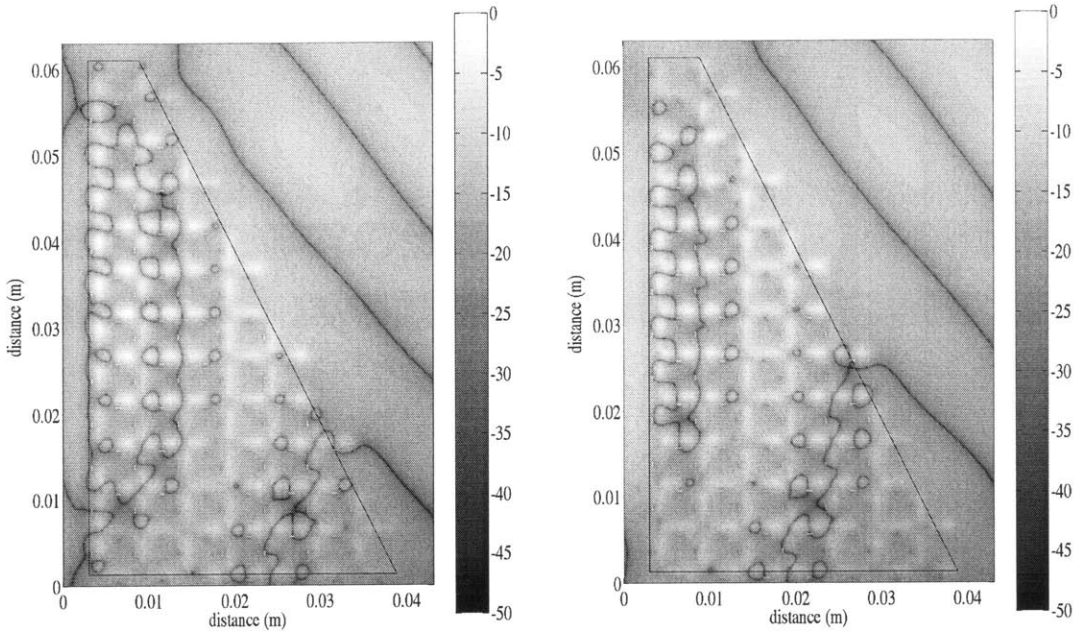

(a) $\omega t = 0$ **(b)** $\omega t = \pi/4$

(c) $\omega t = \pi/2$ **(d)** $\omega t = 3\pi/4$

Figure 4-23: Instantaneous absolute value of the electric field within the Ring A metamaterial, for a 13.2 GHz CW. Initial time $\omega t = 0$ is 1.8 ps into the simulation (the 8000th time step with $\Delta_t = 0.226$ fs).

then verified, and the index of refraction was calculated. At the same frequencies, a negative index of refraction was demonstrated by calculating the direction of power leaving a metamaterial prism. The two methods of calculating the index of refraction of the metamaterials gave consistent results. The FDTD model in this work uses two different SRR geometries, one that is optimal for the uniform Cartesian grid (i.e. realized with less computational requirements), and the other that is a model of geometries used in previous experiments [30]. A new SRR was introduced and shown to be less lossy than previous designs. This numerical study has enabled a greater understanding of the phenomena that leads to LH behavior in metamaterials, and can be easily changed to examine new metamaterial geometries in the future. To our knowledge, this is the first time that the LH properties of metamaterials have been verified and studied using a full wave numerical model of an entire experimental geometry.

Chapter 5

Numerical Dispersion Compensation of the FDTD Technique

5.1 Introduction

One of the main advantages of PDE based methods for computational electromagnetics, such as the FDTD method, against integral equation (IE) based methods is their flexibility to model complex media (e.g., dispersive, inhomogeneous, anisotropic, nonlinear) with less additional effort. However, contrary to IE based methods, PDE based methods are prone to phase dispersion and dissipation error, which accumulate for large problems. It is important to study numerical dispersion in various media to better understand the capabilities and limitations of lower order PDE methods. If necessary, higher order PDE discretization schemes [110] or hybridization can be used to alleviate phase dispersion (both at the cost of loss of sparsity). To better design such higher order PDE methods for complex media, it is again important to characterize the numerical dispersion effects of those media [111, 112]. Numerical dispersion analysis is a classic topic in finite-difference time-domain literature. However,

the conventional analysis is mostly restricted to isotropic, homogeneous domains and regular grids. More recently, studies of temporal dispersion analysis extended to frequency dispersive media and spatial dispersion analysis of irregular grids have been presented [113]. In this Chapter, the numerical dispersion effects in anisotropic (biaxial) and layered media modeled on a regular lattice (i.e., Yee's FDTD lattice) are studied.

As an interesting example of the application of such analysis, the exact implementation of Huygens' sources in the FDTD lattice will be derived. Usually, Huygens' sources are used to introduce and remove a field excitation from the FDTD computational domain using the analytical expression for the incident field. Classically, this method does not account for the numerical dispersion of the incident field, and small errors are introduced into the simulation. Work has been done on dispersion compensated Huygens' sources, considering 1-D phase velocity adjustments (Chapter 6, [18]) and, more recently, broad-band approximate solutions for isotropic homogeneous media [114]. The dispersion compensation method introduced here is exact and can be applied to broadband simulations and is tailored for layered and anisotropic media. This is very useful for instance in ground-penetrating radar (GPR) simulations where a large dynamic range is required due to the small scattering of the buried target (either because of large depth or low contrast). Huygens' sources in layered, lossy media are usually handled in the frequency domain, where analysis is greatly simplified [115]. One can treat the problem as a system response to an arbitrary time domain impulse, where the solution is easily obtained by multiplication in the frequency domain as opposed to convolution in the time domain. The time-domain field incident on the layered media is first specified, and Fourier transformed to the frequency domain. There, for each frequency component, the fields are specified as a sum of upward and downward traveling transmitted and reflected waves, using classic closed form expressions in Chapter 3 of [3]. The final results are then transformed back to the time domain. The processing time of these operations are very small com-

pared to the total FDTD time (much less than 1%) when Fast Fourier Transforms are used. The disadvantage is the requirement that the incident fields be stored everywhere in time and space on the Huygens' surface. These memory requirements can be prohibitive for three-dimensional sources that exist for long times on the Huygens' surface. In our case, for plane wave incidence, it is possible to reduce the source by one dimension as it is invariant in a transverse direction. Other approximations, such as interpolation schemes, are also feasible. If one were to attempt this type of excitation in the time domain, the memory costs would be traded for computational cost. For usual discretization sizes ($\lambda/30$ to $\lambda/20$), a reduction of the incident field dispersion error on the order of 30 dB (typically) is demonstrated for a 60^3 FDTD cell domain.

5.2 Maxwell's Equations in Discrete Space

This section will briefly review the notation for discrete calculus on a regular lattice, introduced in [116]. As will become clear, this notation is very convenient to treat the complex media considered here. Begin by defining the forward difference and the backward difference. If, in continuous space, the differentiations are:

$$E(t) = \partial_t H(t) \qquad H(t) = \partial_t E(t) \tag{5.1}$$

Then in discrete space:

$$H|^{n+\frac{1}{2}} = \tilde{\partial}_t E|^n = \frac{1}{\Delta_t}\left(E|^{n+1} - E|^n\right) \tag{5.2}$$

and

$$E|^n = \hat{\partial}_t H|^{n+\frac{1}{2}} = \frac{1}{\Delta_t}\left(H|^{n+\frac{1}{2}} - H|^{n-\frac{1}{2}}\right) \tag{5.3}$$

where $E|^n = E(n\Delta_t)$, Δ_t is the temporal discretization size, $\tilde{\partial}_t$ is the forward difference, and $\hat{\partial}_t$ is the backward difference. As an example, consider how discrete calculus

can derive the FDTD form of Ampere's Law, shown here for the E_x component:

$$\frac{\partial}{\partial t}E_x = \left(\frac{\partial}{\partial y}H_z - \frac{\partial}{\partial z}H_y\right) - \sigma E_x \tag{5.4}$$

The Yee FDTD formulation defines the electric and magnetic fields offset by half steps in time and space. Central differencing is used to differentiate the fields to second order accuracy. Due to the leapfrogging nature of the electric and magnetic fields, it is possible to relate them with respect to a single Yee cell using forward and backward differences. For example, the electric field on the left side of Equation 5.4 exists at time step n, and must be related to the magnetic fields on the right side which exist at time step $n + \frac{1}{2}$. Defining a forward difference as:

$$\tilde{\partial}_t E_x|^n = \frac{1}{\Delta_t}\left(E_x|^{n+1} - E_x|^n\right) \tag{5.5}$$

which is a central difference in time with respect to H. Relating the magnetic field to the electric field in Faraday's Law instead uses a backward difference:

$$\hat{\partial}_t H_x|^{n+\frac{1}{2}} = \frac{1}{\Delta_t}\left(H_x|^{n+\frac{1}{2}} - H_x|^{n-\frac{1}{2}}\right) \tag{5.6}$$

The same applies for the spatial derivatives. The $\hat{y}$ component of the magnetic field in Equation 5.4 exists at $(m+\frac{1}{2}, n, p+\frac{1}{2})$, and the $\hat{z}$ component exists at $(m+\frac{1}{2}, n+\frac{1}{2}, p)$, where m, n, and p are the discretized steps of the x, y, and z coordinates, respectively. The electric field E_x exists at $(m+\frac{1}{2}, n, p)$, hence to relate the magnetic fields one must take backward differences. For Equation 5.4,

$$\hat{\partial}_z H_y|_{(m+\frac{1}{2},n,p+\frac{1}{2})} = \frac{1}{\Delta_z}\left(H_y|_{(m+\frac{1}{2},n,p+\frac{1}{2})} - H_y|_{(m+\frac{1}{2},n,p-\frac{1}{2})}\right) \tag{5.7}$$

and

$$\hat{\partial}_y H_z|_{(m+\frac{1}{2},n+\frac{1}{2},p)} = \frac{1}{\Delta_y}\left(H_z|_{(m+\frac{1}{2},n+\frac{1}{2},p)} - H_z|_{(m+\frac{1}{2},n-\frac{1}{2},p)}\right) \tag{5.8}$$

which are central differences in space with respect to the location E_x. Substituting Equations 5.5, 5.7, and 5.8 into Equation 5.4 results in the usual FDTD update equation (also requiring the semi-implicit approximation for the current). A Fourier mode on the FDTD lattice is written as

$$\overline{E}^l_{m,n,p} = \overline{E}_o e^{ik_x m\Delta_x + ik_y n\Delta_y + ik_z p\Delta_z - i\omega l\Delta t} \tag{5.9}$$

where m, n, p are the spatial discrete coordinates, l is the discrete time coordinate, and Δt is the time step size. In the Fourier domain, the differential operators may be replaced as follows:

$$\tilde{\partial}_t \rightarrow \frac{-2i}{\Delta t} e^{-i\omega\Delta t/2} \sin\left(\frac{\omega\Delta t}{2}\right) = -i\Omega e^{-i\delta_t} \tag{5.10}$$

$$\hat{\partial}_t \rightarrow \frac{-2i}{\Delta t} e^{i\omega\Delta t/2} \sin\left(\frac{\omega\Delta t}{2}\right) = -i\Omega e^{i\delta_t} \tag{5.11}$$

$$\tilde{\partial}_t\hat{\partial}_t \rightarrow -\Omega^2 = -\frac{4}{(\Delta t)^2} \sin^2\left(\frac{\omega\Delta t}{2}\right) \tag{5.12}$$

where $\delta_t = \omega\Delta t/2$. One can see that the phase terms cancel when both a forward and backward differentiation is applied successively. In addition, $\Omega \rightarrow \omega$ when $\Delta t \rightarrow 0$, as expected. For the spatial differentiation,

$$\tilde{\partial}_x \rightarrow \frac{2i}{\Delta_x} e^{ik_x\Delta_x/2} \sin\left(\frac{k_x\Delta_x}{2}\right) = iK_x e^{i\delta_x} \tag{5.13}$$

$$\hat{\partial}_x \rightarrow \frac{2i}{\Delta_x} e^{-ik_x\Delta_x/2} \sin\left(\frac{k_x\Delta_x}{2}\right) = iK_x e^{-i\delta_x} \tag{5.14}$$

$$\tilde{\partial}_x\hat{\partial}_x \rightarrow -K_x^2 = -\frac{4}{(\Delta_x)^2} \sin^2\left(\frac{k_x\Delta_x}{2}\right) \tag{5.15}$$

where $\delta_x = k_x\Delta_x/2$ (and similarly for y and z). Again, $K_x \rightarrow k_x$ when $\Delta_x \rightarrow 0$, as expected. Using this notation, Maxwell's Equations in discrete space (on the Yee's

lattice) are given by:

$$\tilde{\nabla} \times \tilde{\overline{E}}^{l}_{\overline{m}} = -\tilde{\partial}_t \hat{\overline{B}}^{l-\frac{1}{2}}_{\overline{m}+\frac{1}{2}} \tag{5.16}$$

$$\hat{\nabla} \times \hat{\overline{H}}^{l-\frac{1}{2}}_{\overline{m}+\frac{1}{2}} = \hat{\partial}_t \tilde{\overline{D}}^{l}_{\overline{m}} + \tilde{\overline{J}}^{l-\frac{1}{2}}_{\overline{m}} \tag{5.17}$$

$$\tilde{\nabla} \cdot \hat{\overline{B}}^{l-\frac{1}{2}}_{\overline{m}+\frac{1}{2}} = 0 \tag{5.18}$$

$$\hat{\nabla} \cdot \tilde{\overline{D}}^{l}_{\overline{m}} = \rho^{l}_{\overline{m}} \tag{5.19}$$

where, for simplicity, $\overline{m}+\frac{1}{2}$ refers to $(m+\frac{1}{2}, n+\frac{1}{2}, p+\frac{1}{2})$. In addition, $\tilde{\nabla} = \hat{x}\tilde{\partial}_x + \hat{y}\tilde{\partial}_y + \hat{z}\tilde{\partial}_z$ and $\hat{\nabla} = \hat{x}\hat{\partial}_x + \hat{y}\hat{\partial}_y + \hat{z}\hat{\partial}_z$. The divergence equations are derived from the discrete charge continuity equation, $\hat{\nabla} \cdot \tilde{\overline{J}} + \hat{\partial}_t \rho = 0$. The constitutive relations are also defined in discrete space as:

$$\hat{\overline{B}}_{\overline{m}+\frac{1}{2}} = \overline{\overline{\mu}}_{\overline{m}+\frac{1}{2}} \cdot \hat{\overline{H}}_{\overline{m}+\frac{1}{2}} \tag{5.20}$$

$$\tilde{\overline{D}}_{\overline{m}} = \overline{\overline{\epsilon}}_{\overline{m}} \cdot \tilde{\overline{E}}_{\overline{m}} \tag{5.21}$$

The electric current is defined as:

$$\tilde{\overline{J}}^{l-\frac{1}{2}}_{\overline{m}} = \overline{\overline{\sigma}}_{\overline{m}} e^{i\delta_t} \cdot \tilde{\overline{E}}^{l}_{\overline{m}} \tag{5.22}$$

In these equations, $\overline{B}$ and $\overline{H}$ have been chosen as back-vectors while $\overline{D}$ and $\overline{E}$ have been chosen as fore-vectors. This choice is arbitrary, and follows the notation of [116]. Now that the discrete calculus notation has been reviewed, the next section derives the dispersion relation for discrete anisotropic media.

5.3 Numerical Dispersion Relation For Anisotropic Media

From the discrete Maxwell's Equations and the discrete constitutive relations, the vector wave equation in discrete space may be derived as:

$$\hat{\nabla} \times \overline{\overline{\mu}}^{-1}_{\overline{m}+\frac{1}{2}} \cdot \tilde{\nabla} \times \tilde{\overline{E}}_{\overline{m}} - \Omega^2 \overline{\overline{\epsilon}}_{\overline{m}} \cdot \tilde{\overline{E}}_{\overline{m}} = i\Omega \tilde{\overline{J}}_{\overline{m}} \tag{5.23}$$

The superscripts denoting the time coordinate have been dropped as all the terms exist at time l. For example, the current term on the right was originally at $l - \frac{1}{2}$, but in deriving the wave equation it became $\tilde{\partial}_t \tilde{\overline{J}}^{l-\frac{1}{2}}_{\overline{m}} = i\Omega \tilde{\overline{J}}^{l}_{\overline{m}}$. This derivation is limited to the biaxial anisotropic case, though it will be apparent that the formulation can be extended to the general anisotropic case in an obvious fashion. In this case, a real permittivity is defined as:

$$\overline{\overline{\epsilon}} = \begin{bmatrix} \epsilon_x & 0 & 0 \\ 0 & \epsilon_y & 0 \\ 0 & 0 & \epsilon_z \end{bmatrix} \tag{5.24}$$

and a biaxial conductivity as:

$$\overline{\overline{\sigma}} = \begin{bmatrix} \sigma_x & 0 & 0 \\ 0 & \sigma_y & 0 \\ 0 & 0 & \sigma_z \end{bmatrix} \tag{5.25}$$

For a medium with anisotropic permittivity, the vector wave equation in discrete space becomes:

$$\hat{\nabla} \times \tilde{\nabla} \times \tilde{\overline{E}}_{\overline{m}} - \Omega^2 \mu \overline{\overline{\epsilon}} \cdot \tilde{\overline{E}}_{\overline{m}} - i\Omega\mu \overline{\overline{\sigma}}_{\overline{m}} \cdot \tilde{\overline{E}}_{\overline{m}} = 0 \tag{5.26}$$

which can be written as:

$$\tilde{\nabla} \left(\hat{\nabla} \cdot \tilde{\overline{E}}_{\overline{m}} \right) - \tilde{\nabla}^2 \tilde{\overline{E}}_{\overline{m}} - \Omega^2 \mu \overline{\overline{\epsilon}} \cdot \tilde{\overline{E}}_{\overline{m}} - i\Omega\mu \overline{\overline{\sigma}}_{\overline{m}} \cdot \tilde{\overline{E}}_{\overline{m}} = 0 \tag{5.27}$$

where $\tilde{\nabla}^2 = \hat{\nabla} \cdot \tilde{\nabla}$. It follows that:

$$\begin{aligned}
\tilde{\nabla}\left(\hat{\nabla}\cdot\tilde{\overline{E}}_{\overline{m}}\right) &= \hat{x}\left[\tilde{\partial}_x\hat{\partial}_x\tilde{E}_{x,\overline{m}} + \tilde{\partial}_x\hat{\partial}_y\tilde{E}_{y,\overline{m}} + \tilde{\partial}_x\hat{\partial}_z\tilde{E}_{z,\overline{m}}\right] \\
&+ \hat{y}\left[\tilde{\partial}_y\hat{\partial}_x\tilde{E}_{x,\overline{m}} + \tilde{\partial}_y\hat{\partial}_y\tilde{E}_{y,\overline{m}} + \tilde{\partial}_y\hat{\partial}_z\tilde{E}_{z,\overline{m}}\right] \\
&+ \hat{z}\left[\tilde{\partial}_z\hat{\partial}_x\tilde{E}_{x,\overline{m}} + \tilde{\partial}_z\hat{\partial}_y\tilde{E}_{y,\overline{m}} + \tilde{\partial}_z\hat{\partial}_z\tilde{E}_{z,\overline{m}}\right] \qquad (5.28)
\end{aligned}$$

and

$$\begin{aligned}
\tilde{\nabla}^2\tilde{\overline{E}}_{\overline{m}} &= \hat{x}\left(\tilde{\partial}_x\hat{\partial}_x + \tilde{\partial}_y\hat{\partial}_y + \tilde{\partial}_z\hat{\partial}_z\right)\tilde{E}_{x,\overline{m}} \\
&+ \hat{y}\left(\tilde{\partial}_x\hat{\partial}_x + \tilde{\partial}_y\hat{\partial}_y + \tilde{\partial}_z\hat{\partial}_z\right)\tilde{E}_{y,\overline{m}} \\
&+ \hat{z}\left(\tilde{\partial}_x\hat{\partial}_x + \tilde{\partial}_y\hat{\partial}_y + \tilde{\partial}_z\hat{\partial}_z\right)\tilde{E}_{z,\overline{m}} \qquad (5.29)
\end{aligned}$$

The vector wave equation may be written in matrix form as:

$$\begin{bmatrix} C_1 & \tilde{\partial}_x\hat{\partial}_y & \tilde{\partial}_x\hat{\partial}_z \\ \tilde{\partial}_y\hat{\partial}_x & C_2 & \tilde{\partial}_y\hat{\partial}_z \\ \tilde{\partial}_z\hat{\partial}_x & \tilde{\partial}_z\hat{\partial}_y & C_3 \end{bmatrix} \begin{bmatrix} \tilde{E}_{x,\overline{m}} \\ \tilde{E}_{y,\overline{m}} \\ \tilde{E}_{z,\overline{m}} \end{bmatrix} = \begin{bmatrix} 0 \\ 0 \\ 0 \end{bmatrix} \qquad (5.30)$$

where

$$\begin{aligned}
C_1 &= -\tilde{\partial}_y\hat{\partial}_y - \tilde{\partial}_z\hat{\partial}_z + \mu\epsilon_x\tilde{\partial}_t\hat{\partial}_t + \mu\sigma_x e^{i\delta_t}\tilde{\partial}_t \\
C_2 &= -\tilde{\partial}_x\hat{\partial}_x - \tilde{\partial}_z\hat{\partial}_z + \mu\epsilon_y\tilde{\partial}_t\hat{\partial}_t + \mu\sigma_y e^{i\delta_t}\tilde{\partial}_t \\
C_3 &= -\tilde{\partial}_x\hat{\partial}_x - \tilde{\partial}_y\hat{\partial}_y + \mu\epsilon_z\tilde{\partial}_t\hat{\partial}_t + \mu\sigma_z e^{i\delta_t}\tilde{\partial}_t
\end{aligned}$$

In usual FDTD notation, coefficient C_1 for example would be:

$$\frac{4}{(\Delta_y)^2}\sin^2\left(\frac{k_y\Delta_y}{2}\right) + \frac{4}{(\Delta_z)^2}\sin^2\left(\frac{k_z\Delta_z}{2}\right) - \mu\epsilon_x\frac{4}{(\Delta_t)^2}\sin^2\left(\frac{\omega\Delta_t}{2}\right) - \mu\sigma_x\frac{2i}{\Delta_t}\sin\left(\frac{\omega\Delta_t}{2}\right) \qquad (5.31)$$

By substituting Equations 5.10 - 5.15 (and corresponding equations for y and z) in Equation 5.30 and by setting the determinant of the matrix in 5.30 to zero, a single algebraic equation for the discrete $\overline{k}$ is obtained, which can be solved by iterative means. In this study the Newton-Raphson method has been used, with the continuous $\overline{k}$ used as the initial guess. In the following sections, $\overline{k}$ will refer to the wave vector that has been already adjusted for numerical dispersion. Extending this formulation to the off-diagonal anisotropic case is straightforward, albeit cumbersome.

5.4 R and T Coefficients For Anisotropic, Layered Media in Discrete Space

For Huygens' sources to be implemented in anisotropic and *layered* media, the reflection (R) and transmission (T) coefficients for each interface must be known. As with the dispersion relation, these values must also be rigorously calculated for discrete space. The formulation here extends [117], which dealt with the PML reflection error in discrete space for TE incidence. Once both R and T are known for a single interface, they can be put into a recursive formulation for multiple layers [3]. For the sake of simplicity, the derivation will be restricted to the uniaxial case, where $\epsilon_x = \epsilon_y = \epsilon_t$ and $\sigma_x = \sigma_y = \sigma_t$ in each region. The fields are propagating in the $-\hat{z}$ direction, from region 1 to region 2.

5.4.1 TE Case

Given a plane wave incident on a halfspace, the $\tilde{\overline{E}}$ fields in regions 1 and 2 may be defined as:

$$\tilde{\overline{E}}_1 = \tilde{\overline{E}}_0 e^{i\overline{k}_i \cdot \overline{r}} + R^{TE} \tilde{\overline{E}}_0 e^{i\overline{k}_r \cdot \overline{r}} \tag{5.32}$$

$$\tilde{\overline{E}}_2 = T^{TE} \tilde{\overline{E}}_0 e^{i\overline{k}_t \cdot \overline{r}} \tag{5.33}$$

where $\tilde{\overline{E}}_0 = \hat{y}\tilde{E}_o$, $\overline{k}_i = \hat{x}k_{ix} + \hat{y}k_{iy} - \hat{z}k_{iz}$, $\overline{k}_r = \hat{x}k_{rx} + \hat{y}k_{ry} + \hat{z}k_{rz}$, $\overline{k}_t = \hat{x}k_{tx} + \hat{y}k_{ty} - \hat{z}k_{tz}$, and $\overline{r} = \hat{x}m\Delta_x + \hat{y}n\Delta_y + \hat{z}p\Delta_z$. On the FDTD lattice, the $\tilde{\overline{E}}$ fields exist at the dielectric interface boundaries. Phase matching of the tangential components at the boundary $z = 0$ may be used to find:

$$1 + R^{TE} = T^{TE} \tag{5.34}$$

From the discrete Maxwell's Equations, the $\hat{\overline{H}}$ fields are derived as:

$$\hat{\overline{H}}_1 = \frac{\tilde{\overline{K}}_i \times \tilde{\overline{E}}_0}{\tilde{\Omega}_t \mu_1} e^{i\overline{k}_i \cdot \overline{r}} + R^{TE} \frac{\tilde{\overline{K}}_r \times \tilde{\overline{E}}_0}{\tilde{\Omega}_t \mu_1} e^{i\overline{k}_r \cdot \overline{r}} \tag{5.35}$$

$$\hat{\overline{H}}_2 = T^{TE} \frac{\tilde{\overline{K}}_t \times \tilde{\overline{E}}_0}{\tilde{\Omega}_t \mu_2} e^{i\overline{k}_t \cdot \overline{r}} \tag{5.36}$$

where

$$\tilde{\overline{K}}_i = \hat{x}K_{x1}e^{i\delta_{1x}} + \hat{y}K_{y1}e^{i\delta_{y1}} - \hat{z}K_{z1}e^{-i\delta_{1z}} \tag{5.37}$$

$$\tilde{\overline{K}}_r = \hat{x}K_{x1}e^{i\delta_{1x}} + \hat{y}K_{y1}e^{i\delta_{y1}} + \hat{z}K_{z1}e^{i\delta_{1z}} \tag{5.38}$$

$$\tilde{\overline{K}}_t = \hat{x}K_{x2}e^{i\delta_{2x}} + \hat{y}K_{y2}e^{i\delta_{y2}} - \hat{z}K_{z2}e^{i\delta_{2z}} \tag{5.39}$$

and $K_{x1} = k_{x1} sinc(\delta_{x1})$, $\delta_{x1} = k_{x1}\Delta_x/2$ and $\tilde{\Omega}_t = \Omega e^{-i\omega\Delta t/2}$. The tangential $\hat{\overline{H}}$ fields exist $\Delta/2$ above and below the boundary, so phase matching may not be used directly. Going back to the discrete Maxwell's Equations,

$$\hat{\partial}_z \hat{z} \times \hat{\overline{H}}_{m+\frac{1}{2}} = \left(\frac{K_z^2 \tilde{\overline{E}}}{i\tilde{\Omega}_t \mu} \right)_{z=0} \tag{5.40}$$

Applying Equation 5.3,

$$\hat{z} \times \left(\hat{\overline{H}}_{z=\frac{1}{2}} - \hat{\overline{H}}_{z=-\frac{1}{2}} \right) = \left(\frac{K_z^2 \Delta_z \tilde{\overline{E}}}{i\tilde{\Omega}_t \mu} \right)_{z=0} \tag{5.41}$$

Note that when $\Delta_z \rightarrow 0$, Equation 5.41 reduces to the usual continuity of the $\hat{\overline{H}}$ fields at the interface. Using the tangential $\hat{\overline{H}}$ fields from Equations 5.35 and 5.36 in Equation 5.41,

$$-\frac{K_{z1}}{\mu_1}e^{-i\delta_{z1}} + R^{TE}\frac{K_{z1}}{\mu_1}e^{i\delta_{z1}} =$$

$$-T^{TE}\left[\frac{K_{z2}e^{i\delta_{z2}}}{\mu_2} - i\left(\frac{K_z^2\Delta_z}{\mu}\right)_{z=0}\right] \tag{5.42}$$

Solving for R^{TE} and T^{TE} in Equations 5.34 and 5.42,

$$R^{TE} = \frac{K_{z1}e^{-i\delta_{z1}} - K_{z2}e^{-i\delta_{z2}}\frac{\mu_1}{\mu_2} + \mu_1\left(\frac{iK_z^2\Delta_z}{\mu}\right)_{z=0}}{K_{z1}e^{i\delta_{z1}} + K_{z2}e^{-i\delta_{z2}}\frac{\mu_1}{\mu_2} - \mu_1\left(\frac{iK_z^2\Delta_z}{\mu}\right)_{z=0}} \tag{5.43}$$

$$T^{TE} = \frac{K_{z1}\left(e^{i\delta_{1z}} + e^{-i\delta_{1z}}\right)}{K_{z1}e^{i\delta_{z1}} + K_{z2}e^{-i\delta_{z2}}\frac{\mu_1}{\mu_2} - \mu_1\left(\frac{iK_z^2\Delta_z}{\mu}\right)_{z=0}} \tag{5.44}$$

5.4.2 TM Case

For the TM case, the $\hat{\overline{H}}$ fields in regions 1 and 2 may be defined as:

$$\hat{\overline{H}}_1 = \hat{\overline{H}}_0 e^{i\bar{k}_i\cdot\bar{r}_1} + R^{TM}\hat{\overline{H}}_0 e^{i\bar{k}_r\cdot\bar{r}} \tag{5.45}$$

$$\hat{\overline{H}}_2 = T^{TM}\hat{\overline{H}}_0 e^{i\bar{k}_t\cdot\bar{r}} \tag{5.46}$$

where $\tilde{\overline{H}}_0 = \hat{y}\tilde{H}_o$. Again, from the discrete Maxwell's Equations, the $\tilde{\overline{E}}$ fields may be derived:

$$\bar{\bar{\epsilon}}_1\cdot\tilde{\overline{E}}_1 = \frac{\hat{\overline{K}}_i\times\hat{\overline{H}}_0}{-\hat{\Omega}_t}e^{i\bar{k}_i\cdot\bar{r}} + R^{TM}\frac{\hat{\overline{K}}_r\times\hat{\overline{H}}_0}{-\hat{\Omega}_t}e^{i\bar{k}_r\cdot\bar{r}} \tag{5.47}$$

$$\bar{\bar{\epsilon}}_2\cdot\tilde{\overline{E}}_2 = T^{TM}\frac{\hat{\overline{K}}_t\times\hat{\overline{H}}_0}{-\hat{\Omega}_t}e^{i\bar{k}_i\cdot\bar{r}} \tag{5.48}$$

where

$$\hat{\overline{K}}_i = \hat{x}K_{x1}e^{-i\delta_{x1}} + \hat{y}K_{y1}e^{-i\delta_{y1}} - \hat{z}K_{z1}e^{i\delta_{z1}} \quad (5.49)$$

$$\hat{\overline{K}}_r = \hat{x}K_{x1}e^{-i\delta_{x1}} + \hat{y}K_{y1}e^{-i\delta_{y1}} + \hat{z}K_{z1}e^{-i\delta_{z1}} \quad (5.50)$$

$$\hat{\overline{K}}_t = \hat{x}K_{x2}e^{i\delta_{x2}} + \hat{y}K_{y2}e^{i\delta_{y2}} - \hat{z}K_{z2}e^{-i\delta_{z2}} \quad (5.51)$$

In a similar fashion as in the TE case, $\hat{\Omega}_t = \Omega e^{i\omega\Delta t/2}$. From the discrete definition of $\tilde{\overline{J}}$, complex permittivities can be defined as:

$$\epsilon_{\xi 1} \rightarrow \epsilon_{\xi 1} + \frac{i\sigma_{\xi 1}}{\Omega} \quad (5.52)$$

$$\epsilon_{\xi 2} \rightarrow \epsilon_{\xi 2} + \frac{i\sigma_{\xi 2}}{\Omega} \quad (5.53)$$

where ξ is t (transverse) or z (longitudinal). Note that these expressions for $\tilde{\overline{E}}$ hold at every point in space except $p = 0$ (the interface), where the tangential electric fields are defined through the magnetic fields in both regions 1 and 2.

Obtaining the TM reflection and transmission coefficients is more cumbersome than in the TE case, because the magnetic fields do not exist on the boundary. Whereas in the TE case one equation could be determined by matching the incident, transmitted, and reflected electric fields at the interface, this is not possible for the TM case. Some approximations can be made, such as assuming the magnetic fields do exist on the boundary, or naively applying Equations 5.47 and 5.48 at the boundary, but both cases offer only small improvements to the continuous formulation and are not effective over all angles and frequencies. Instead the coefficients may be solved exactly, by calculating the magnetic fields at different points directly above and below the interface. Consider the TM ($\hat{y}$) magnetic fields around the boundary, shown in Figure 5-1 (note the n dependence has been dropped):

$$\hat{H}_{y,(m+\frac{1}{2},p+\frac{1}{2})} = \frac{1}{i\tilde{\Omega}_t\mu_1}\left[\tilde{\partial}_z\tilde{E}_{x,(m+\frac{1}{2},p)} - \tilde{\partial}_x\tilde{E}_{z,(m,p+\frac{1}{2})}\right] \quad (5.54)$$

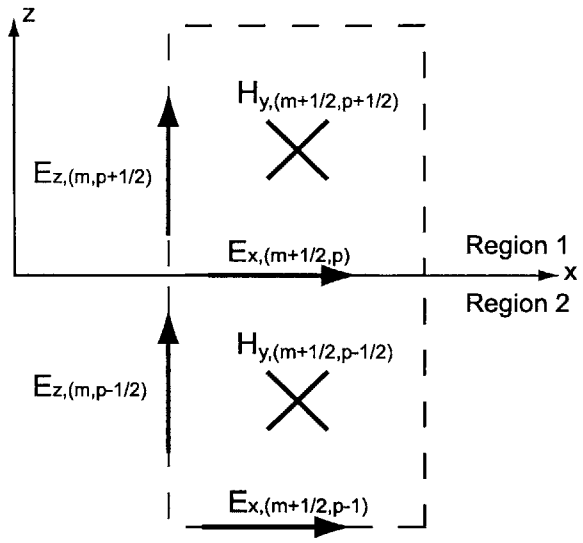

Figure 5-1: Magnetic and electric fields around the discrete FDTD boundary

$$\hat{H}_{y,(m+\frac{1}{2},p-\frac{1}{2})} = \frac{1}{i\tilde{\Omega}_t\mu_1}\left[\tilde{\partial}_z\tilde{E}_{x,(m+\frac{1}{2},p-1)} - \tilde{\partial}_x\tilde{E}_{z,(m,p-\frac{1}{2})}\right] \tag{5.55}$$

The electric fields around the boundary may be defined as:

$$\tilde{E}_{x,(m+\frac{1}{2},p)} = \frac{1}{i\Delta_z\hat{\Omega}\epsilon_{t,ave}}\left[a^{-1} + R^{TM}a - T^{TM}b\right] \tag{5.56}$$

$$\tilde{E}_{z,(m,p+\frac{1}{2})} = \frac{-K_x e^{-i\delta_{x1}}}{\hat{\Omega}_t\epsilon_{z1}}\left(a^{-1} + R^{TM}a\right) \tag{5.57}$$

$$\tilde{E}_{z,(m,p-\frac{1}{2})} = \frac{-K_x e^{-i\delta_{x2}}}{\hat{\Omega}_t\epsilon_{z2}}T^{TM}b \tag{5.58}$$

where:

$$a = \hat{H}_y e^{ik_{x1}\Delta_x(m+\frac{1}{2})+ik_{z1}\Delta_z(p+\frac{1}{2})} \tag{5.59}$$

$$b = \hat{H}_y e^{ik_{x2}\Delta_x(m+\frac{1}{2})-ik_{z2}\Delta_z(p-\frac{1}{2})} \tag{5.60}$$

$$\epsilon_{t,ave} = \frac{(\epsilon_{t1}+\epsilon_{t2})}{2} \tag{5.61}$$

Solving Equations 5.54 and 5.55 at $p = 0$,

$$\begin{aligned} T^{TM}e^{i\delta_{z2}} &= \frac{-e^{-i\delta_{z1}} - R^{TM}e^{i\delta_{z1}} + T^{TM}e^{i\delta_{z2}}}{\Delta_z^2\Omega_t^2\epsilon_{t,ave}\mu_2} \\ &- \frac{T^{TM}K_{z2}e^{i2\delta_{z2}}}{\Delta_z\Omega_t^2\epsilon_{t2}\mu_2} - \frac{T^{TM}K_{x2}^2e^{i\delta_{z2}}}{\Omega_t^2\epsilon_{z2}\mu_2} \end{aligned} \tag{5.62}$$

$$\begin{aligned} e^{-i\delta_{z1}} + R^{TM}e^{i\delta_{z1}} &= \frac{e^{-i\delta_{z1}} + R^{TM}e^{i\delta_{z1}} - T^{TM}e^{i\delta_{z2}}}{\Delta_z^2\Omega_t^2\epsilon_{t,ave}\mu_1} \\ &+ \frac{K_{z1}\left(e^{-i2\delta_{z1}} - R^{TM}e^{i2\delta_{z1}}\right)}{\Delta\Omega_t^2\epsilon_{t1}\mu_1} \\ &- \frac{K_{x1}^2\left(e^{-i\delta_{z1}} + R^{TM}e^{i\delta_{z1}}\right)}{\Omega_t^2\epsilon_{z1}\mu_1} \end{aligned} \tag{5.63}$$

These Equations are then solved for R^{TM} and T^{TM} using a computer algebra package. The resulting expressions for each are quite long, and are left to the Appendix at the end of this chapter. Again, as for the TE case, the reflection and transmission coefficients may now be substituted into a recursive formula or propagation matrices to obtain the transmission and reflection coefficients for a multi-layered medium.

5.5 Discrete Space Field Coefficients

It is important to note that given a TE or TM incident plane wave, the corresponding magnetic or electric fields (implemented on the Huygens' surface) must be found using the discrete Maxwell's Equations. This defines a discrete-space impedance which is distinct from the continuous case and also depends on the discretization sizes.

5.5.1 TE Case Field Coefficients

For the TE case, begin by defining a transverse $\overline{E}$ field propagating in the $\phi = 0$ (xz) plane:

$$\tilde{E}_y = E_o e^{i\overline{k}\cdot\overline{r} - i\omega l\Delta t} \tag{5.64}$$

where $\overline{k} = \hat{x}k_x - \hat{z}k_z$. The $\overline{H}$ fields are then:

$$\hat{H}_x = \frac{\Delta t \sin\left(\frac{k_z \Delta_z}{2}\right) e^{-i\delta_z/2}}{\Delta_z \sin\left(\frac{\omega \Delta t}{2}\right) e^{-i\delta_t/2} \mu} \tilde{E}_y \tag{5.65}$$

$$\hat{H}_z = \frac{\Delta t \sin\left(\frac{k_x \Delta_x}{2}\right) e^{i\delta_x/2}}{\Delta_x \sin\left(\frac{\omega \Delta t}{2}\right) e^{-i\delta_t/2} \mu} \tilde{E}_y \tag{5.66}$$

The phase terms above reflect the staggering of the fields in space and time. When using these field values as Huygens' sources, the phase terms must be dropped. This is because the incident sources for the $\hat{\overline{H}}$ field components is already spatially and temporally offset on the FDTD lattice with respect to the $\tilde{\overline{E}}$ field components.

5.5.2 TM Case Field Coefficients

The TM case begins with a transverse magnetic field, propagating in the $\phi = 0$ plane, defined here as:

$$\hat{H}_y = H_o e^{i\overline{k}\cdot\overline{r} - i\omega l \Delta t} \tag{5.67}$$

from which the $\tilde{\overline{E}}$ fields are:

$$\tilde{E}_x = \frac{\Delta t \sin\left(\frac{k_z \Delta_z}{2}\right) e^{i\delta_z/2}}{\Delta_x \sin\left(\frac{\omega \Delta t}{2}\right) \epsilon_t e^{i\delta_t/2}} \hat{H}_y \tag{5.68}$$

$$\tilde{E}_z = \frac{\Delta t \sin\left(\frac{k_x \Delta_x}{2}\right) e^{-i\delta_x/2}}{\Delta_x \sin\left(\frac{\omega \Delta t}{2}\right) \epsilon_z e^{i\delta_t/2}} \hat{H}_y \tag{5.69}$$

5.6 Numerical Experiments

For the numerical experiments, consider a three-region medium as shown in Figure 5-2. The total field region is empty, so the scattered fields should be zero. Dispersion error can then be measured by examining the fields that escape into the scattered field domain. The results will be presented as surface plots of the xz plane at $y = 0$ for visualization purposes, as well as dB graphs of the maximum field error (scattered field divided by incident field) for exact quantitative evaluation. TE and TM waves

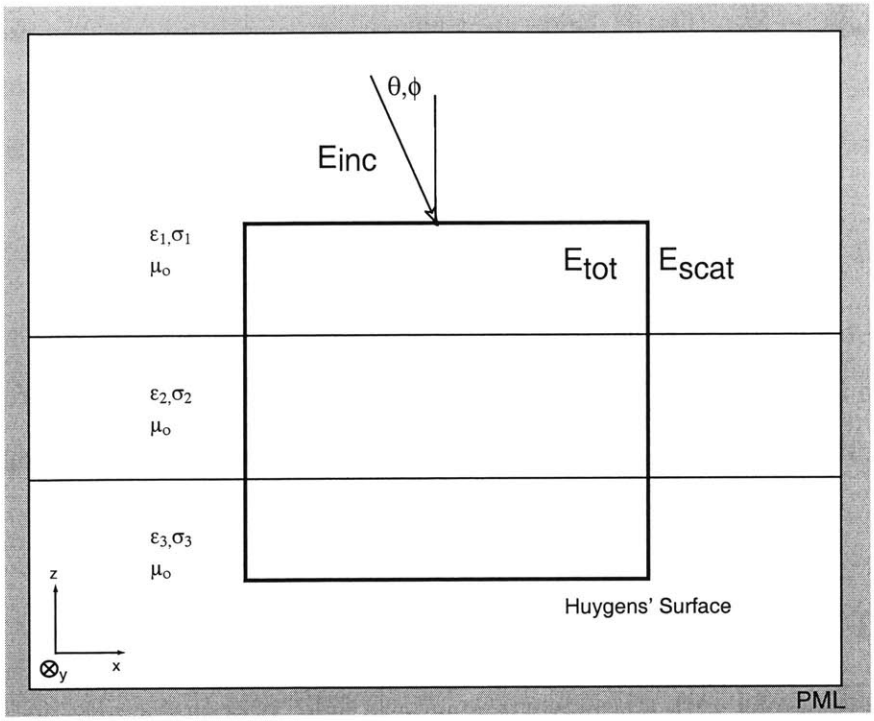

Figure 5-2: Computational domain for discrete formulation testing

will be tested for $\theta = 0^o$ incidence and $\theta = 45^o$ incidence ($\phi = 0^o$), which correspond to worst case and best case dispersion, respectively. The uniaxial medium and the incident field are chosen to examine the dispersion for typical spatial discretization sizes, to allow for fair comparison between the standard FDTD technique and the compensated technique. Note, however, that the dispersion compensation is effective up to a discretization size of $\lambda/5$, though obviously FDTD results would be poor at that frequency. Region 1 of the computational domain is air ($\epsilon_{t1} = \epsilon_{z1} = 1.0\epsilon_o$, $\sigma_{t1} = \sigma_{z1} = 0.0$), region 2 is an anisotropic slab with $\epsilon_{t2} = 1.25\epsilon_o$, $\epsilon_{z2} = 1.5\epsilon_o$, $\sigma_{t2} = 1.0 \times 10^{-4}$, and $\sigma_{z2} = 1.5 \times 10^{-4}$. region 3 is also anisotropic with $\epsilon_{t3} = 1.75\epsilon_o$, $\epsilon_{z3} = 2.0\epsilon_o$, $\sigma_{t3} = 2.0 \times 10^{-4}$, and $\sigma_{z3} = 2.5 \times 10^{-4}$. The total field region is $60\Delta_x \times 60\Delta_y \times 60\Delta_z$ in size, and the scattered field domain extends 10Δ beyond the total field region to to the PML. The boundaries are located at $15\Delta_z$ and $-15\Delta_z$, with respect to the axes origin at the center of the domain. For most cases, the incident

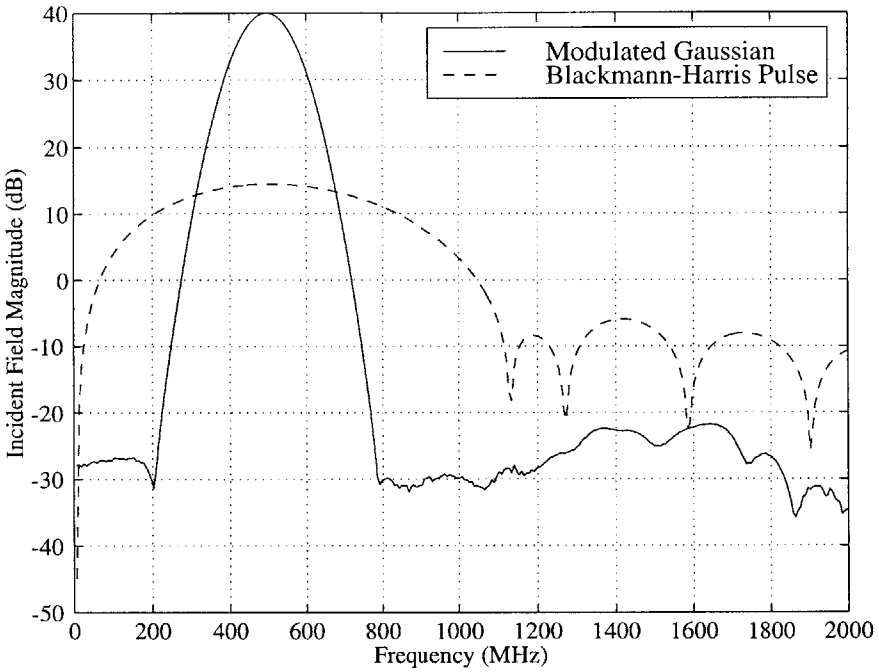

Figure 5-3: Bandwidth of narrowband and wideband pulses

field used to measure numerical dispersion will be a narrowband Gaussian pulse, with a center frequency of 500 MHz ($\Delta = \lambda/30$ in region 1, $\Delta = \lambda/21.2$ in region 3). The bandwidth of the incident pulse is such that the signal is 40 dB down at 700 MHz. In addition, the case of a very wide bandwidth Blackmann-Harris pulse is also examined. The bandwidth of both pulses is shown in Figure 5-3. The Blackmann-Harris pulse has a useable bandwidth of at least 100 MHz to 1 GHz, with higher frequency components being no more than 20 dB down from the center frequency. In Figure 5-4, as with all surface plots presented in this section, the total field is removed for visualization purposes. The field is traveling along the z axis (at $\theta = 0$) in the $-\hat{z}$ direction. Note that each facet of the surface plot corresponds to 4 FDTD cells (2 x 2 averaged). The maximum amplitude of the incident Gaussian pulse is 100 V/m, and the time step of this plot corresponds approximately to the maximum field value leaving the total field domain. The numerical dispersion (uncompensated) of the FDTD domain results in

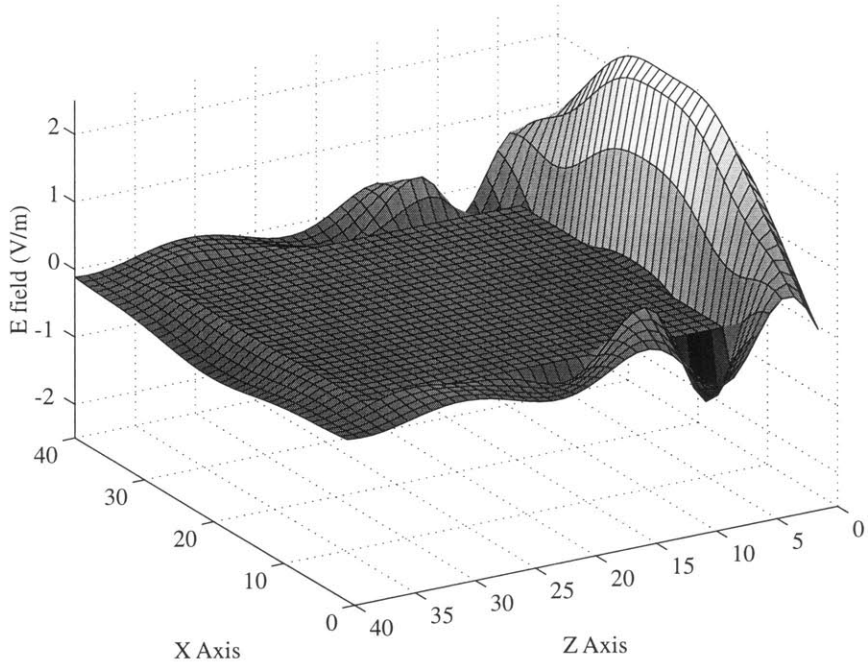

Figure 5-4: TE and TM numerical dispersion error, $\theta = 0^o$ incidence, continuous formulation

a scattered field error which is 14.8 dB less than the incident field, at the maximum field error point directly below the total/scattered field box. Figure 5-5 is a surface plot similar to Figure 5-4, after the discrete formulation has been applied to $\overline{k}$, the field coefficients, R^{TE}, and T^{TE}. In this optimized case, the scattered field error is much smaller, 43.3 dB down from the incident field. Next, Figure 5-6 compares the value of the scattered field error at the point on the z axis below the area where the incident field is removed on the Huygens' surface. The error is defined as the scattered field normalized by the total (incident) field just within the Huygens' surface. Taking a measurement at a single point is a reasonable indication of error, as will be shown later when the total error is summed over a second Huygens' surface. The benefits of the discrete formulation are quite obvious here, with a noise floor for the optimized case that is 28.5 dB lower than the uncompensated case (measured at the maximum error in time). The average field error improvement (taken over the time that the

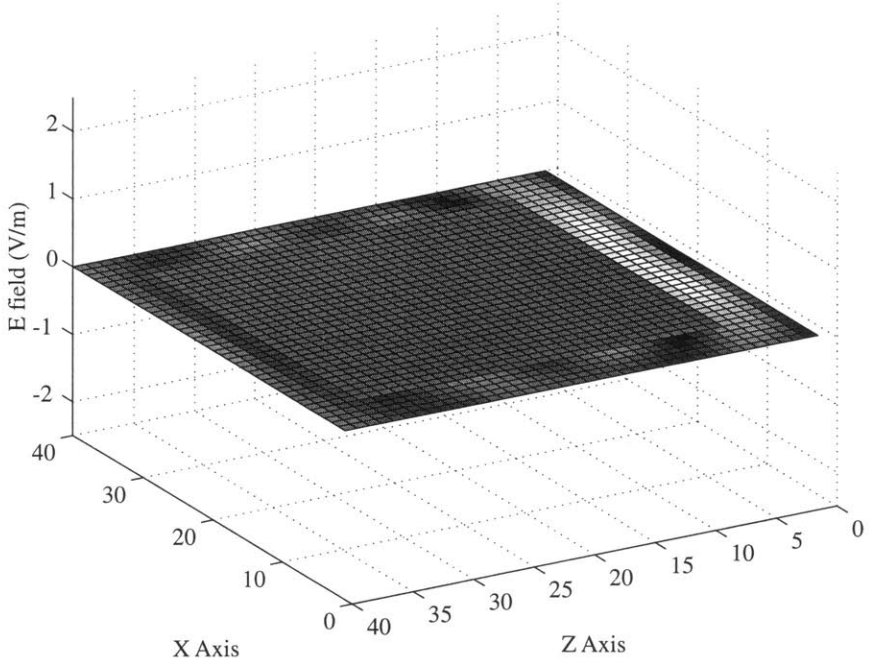

Figure 5-5: TE and TM numerical dispersion error, $\theta = 0^o$ incidence, optimized formulation

incident pulse is in the computational domain) is 28.4 dB. For $\theta = 0^o$ incidence, this dispersion compensated total/scattered field formulation has nearly doubled the dynamic range of the scattered field measurements. Figure 5-7 shows the maximum error of a TM field (the H_y component) at $\theta = 0^o$ incidence. As expected, this is very similar to the TE field at normal incidence, because the TM and TE cases are both ordinary waves when propagating along the optical axis. Figures 5-8 and 5-9 show the scattered field error for a TE wave at $\theta = 45^o$ incidence, for the continuous and discrete formulations. For the continuous formulation, the error is 19.1 dB down from the incident field, which is better than the $\theta = 0^o$ incidence case as expected. In the optimized case, the scattered field error drops to -42.7 dB. Figure 5-10 shows the TE scattered field for $\theta = 45^o$ incidence at the point of maximum error. The improvement here is 23.6 dB (at the pulse maximum in time), which is less than the gains achieved in the $\theta = 0^o$ case. This is expected due to the fact that at this incident

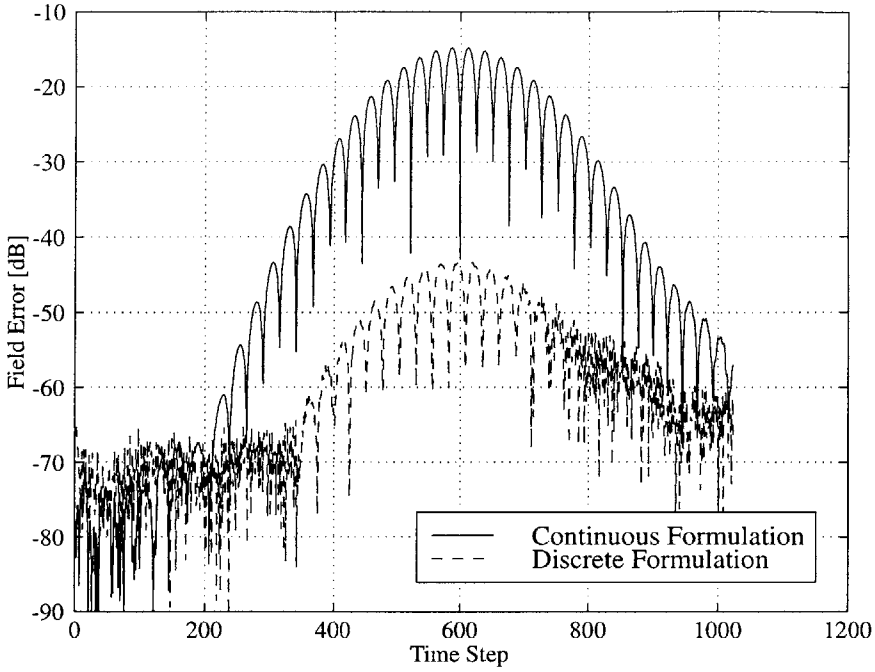

Figure 5-6: TE numerical dispersion error, $\theta = 0^o$ incidence, maximum error (measured at $(0, 0, -35)$)

angle there is less dispersion error in the continuous $\overline{k}$ formulation, so the discrete $\overline{k}$ formulation yields less improvement. The average scattered field error improvement is 23.9 dB. In Figure 5-11, the error of the total/scattered field formulation for a TM wave at $\theta = 45^o$ incidence is shown. The maximum error is 17.9 dB down from the incident field. The TM field error is worse than the TE field error at this propagation angle because the TM field is an extraordinary wave. The TE wave, however, does not see the anisotropy at any angle of incidence, and is always an ordinary wave (as is the TM wave at $\theta = 0^o$ incidence). In these experiments, the vertical permittivity is greater than the transverse permittivity, hence the extraordinary wave experiences greater error (smaller wavelength means poorer discretization). Figure 5-12 shows the error after optimization, and the improvement is evident. The maximum error is 44 dB down from the incident field. Figure 5-13 shows the error of the H_y field. The optimization has reduced the maximum field error by 26.1 dB, and the average field

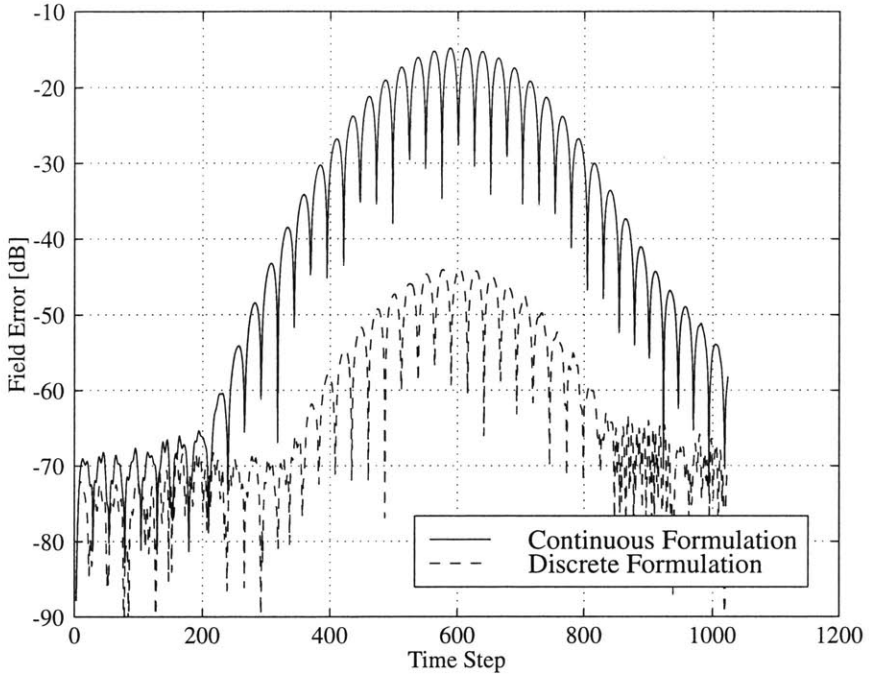

Figure 5-7: TM numerical dispersion error, $\theta = 0^o$ incidence, maximum error (measured at $(0, 0, -35)$)

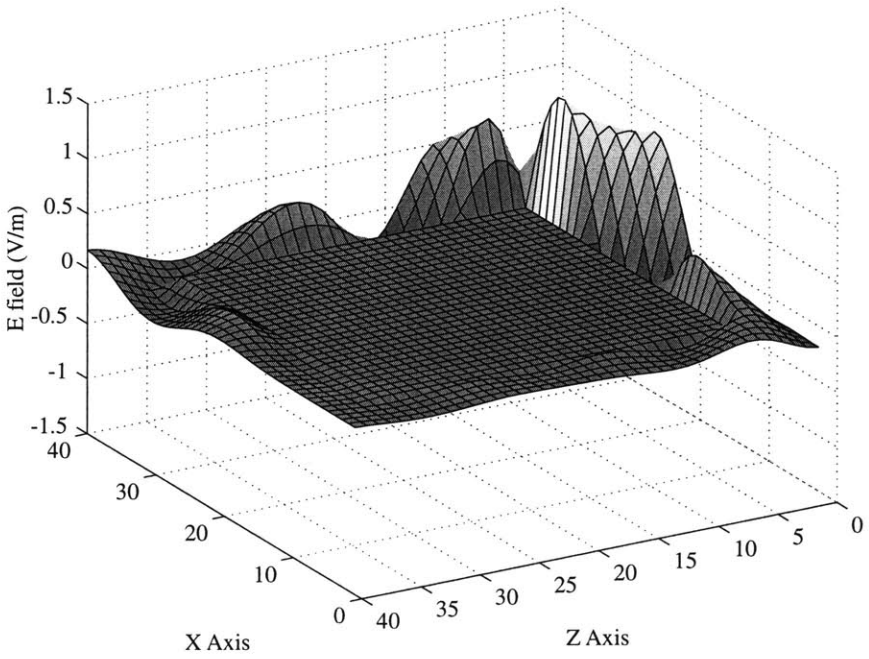

Figure 5-8: TE numerical dispersion error, $\theta = 45^o$ incidence, continuous formulation

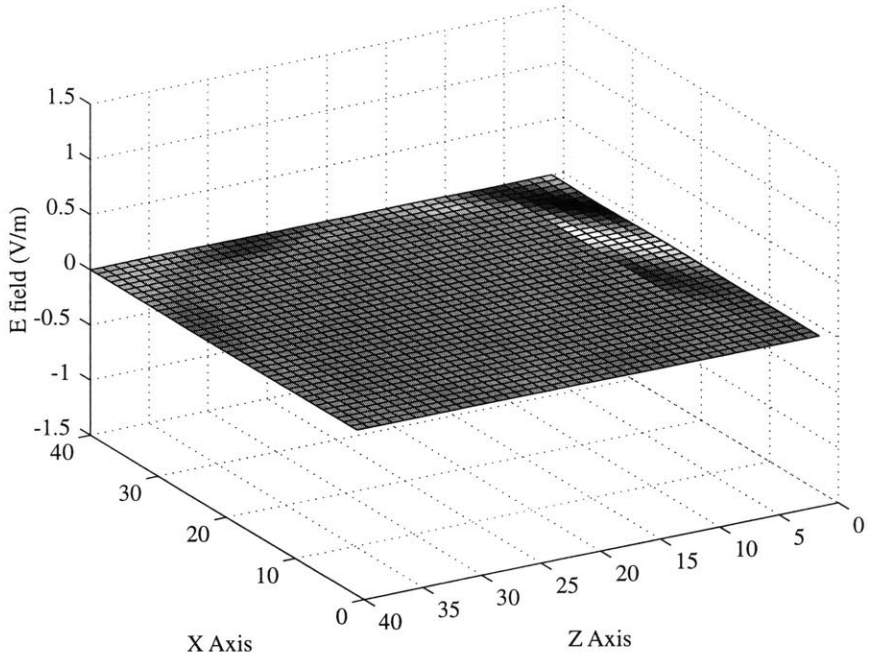

Figure 5-9: TE numerical dispersion error, $\theta = 45^o$ incidence, optimized formulation

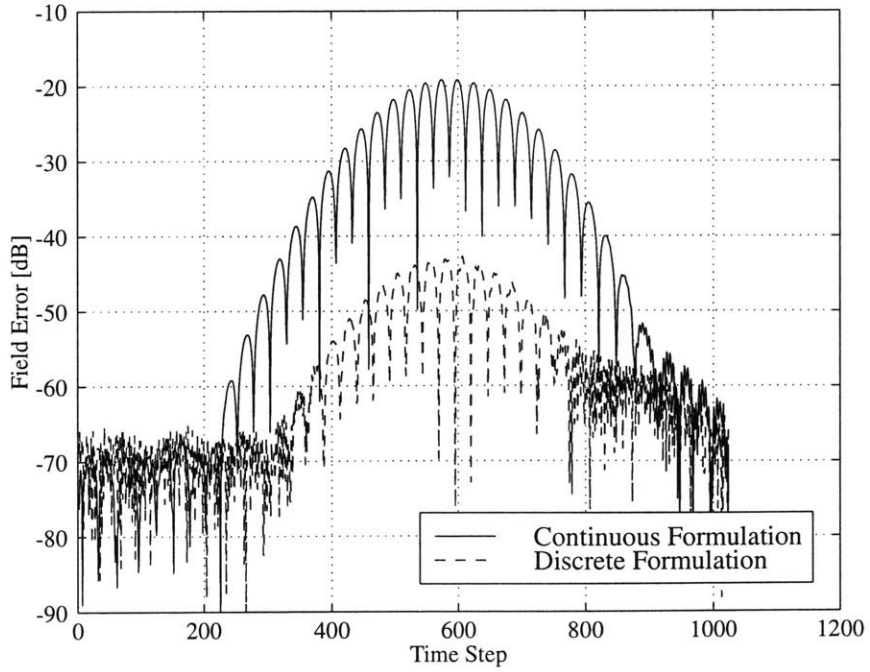

Figure 5-10: TE numerical dispersion error, $\theta = 45^o$ incidence, maximum error (measured at $(0, 0, -35)$)

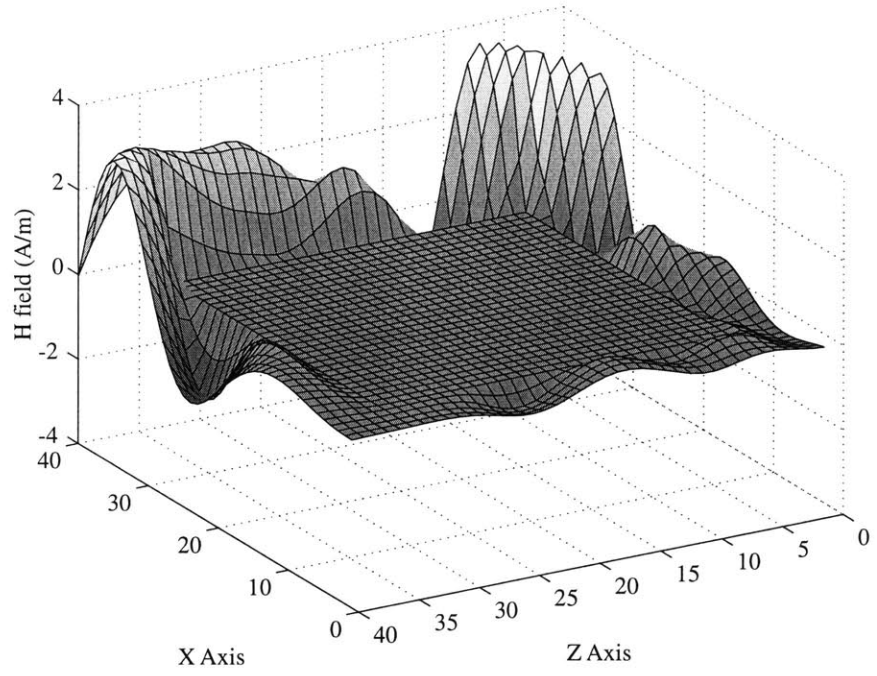

Figure 5-11: TM numerical dispersion error, $\theta = 45^o$ incidence, continuous formulation

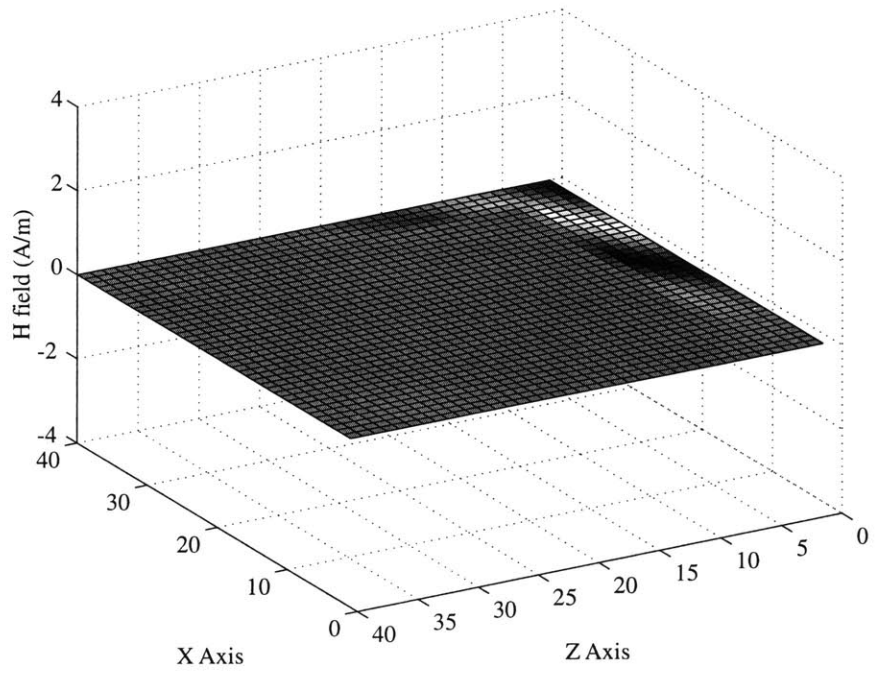

Figure 5-12: TM numerical dispersion error, $\theta = 45^o$ incidence, optimized formulation

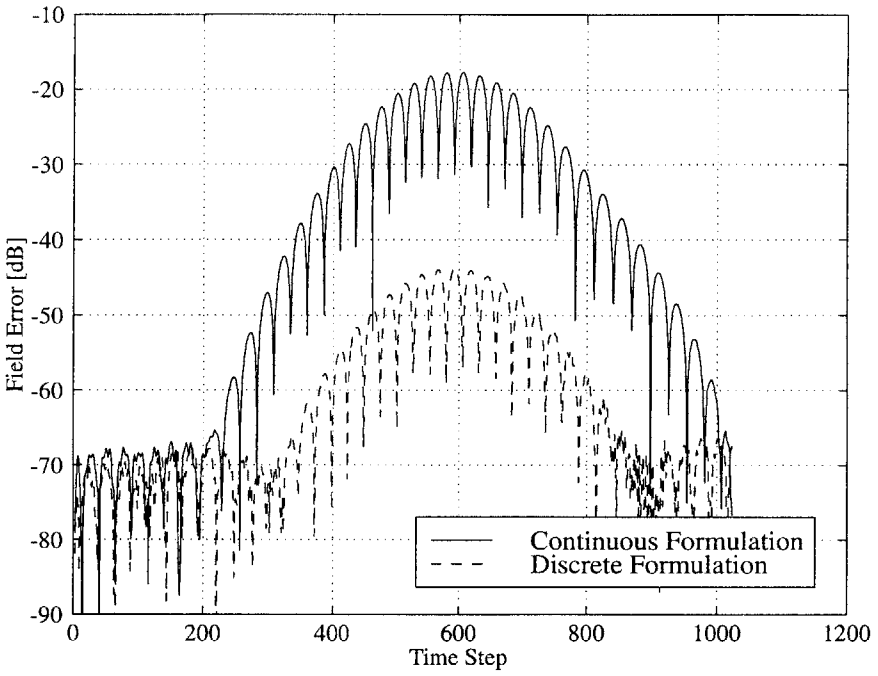

Figure 5-13: TM numerical dispersion error, $\theta = 45^o$ incidence, maximum error (measured at $(0, 0, -35)$)

error has been reduced by 26 dB. Figure 5-14 shows the scattered field error for the TE and TM fields over angles from normal incidence to 70 degrees. As expected both the continuous formulation TE and TM field errors decrease with oblique incidence due to the lower dispersion error at 45 degrees. However, the TE field error does not increase again as grazing incidence is approached, and the TM field error increases in an asymmetric fashion. This behavior is due to the additional error incurred in the reflection and transmission coefficients. For the discrete formulation, the error in all cases is reduced by at least 25 dB, and is fairly independent of angle as expected. Figure 5-15 shows the individual effects of the numerical dispersion correction and the discrete Fresnel coefficients. Note that these results depend on the number of interfaces in the simulation as well as the contrast between regions. Obviously in the limit of homogeneous regions, the numerical dispersion compensation would fully account for all error correction. For the three-region simulation performed here, the

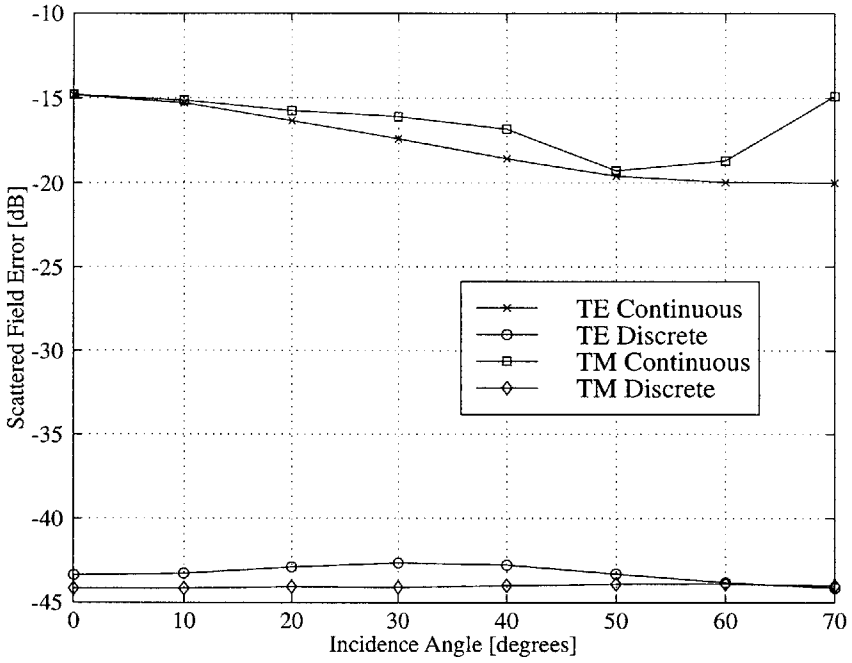

Figure 5-14: TE and TM numerical dispersion error, measured over angle at $(0, 0, -35)$.

additional correction of the Fresnel coefficients provides 18 dB greater accuracy at normal incidence and 30 dB more accuracy at near grazing incidence. At larger incidence angle, the solution error when only considering discrete $\mathbf{k}$ approaches the continuous formulation. For grazing incident angles, it is obviously very important to consider the effects of the Fresnel coefficients as well as the numerical dispersion relation. The dispersion compensation of the wideband pulse is shown in Figure 5-16. The maximum error in the continuous formulation is -10.23 dB, whereas the maximum error for the discrete formulation is -30.1 dB, and improvement of approximately 20 dB. Note that this is likely close to the maximum error correction possible, as the Blackmann-Harris pulse has very high frequency components that are only 20 - 25 dB down from the center frequency. This bandwidth includes frequencies up to and including those that cannot be propagated on the FDTD grid ($\Delta = \lambda/3$), and as such cannot be fully compensated with our formulation. Finally, consider the effects the dispersion error could have on radar cross section (RCS) measurements

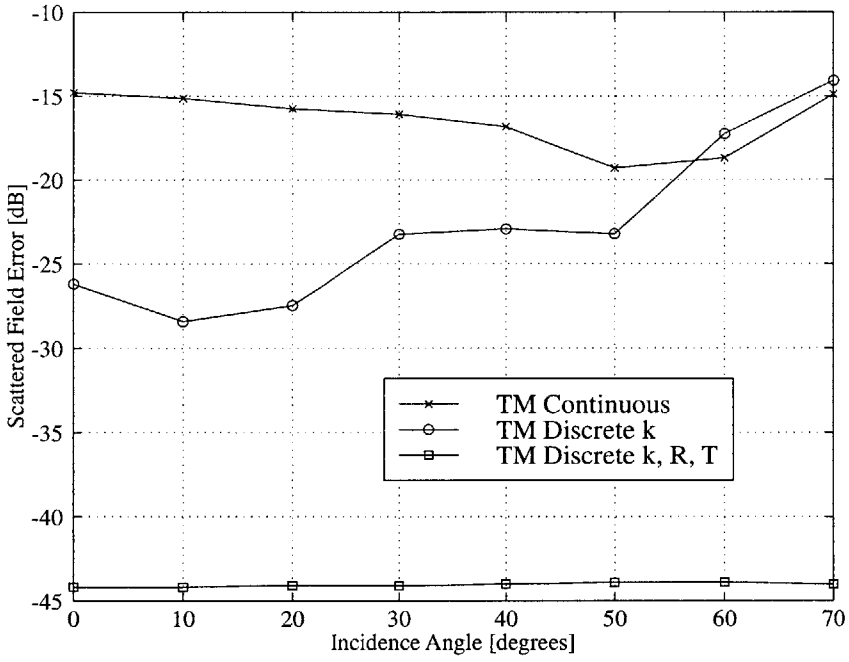

Figure 5-15: TM numerical dispersion error, measured over angle comparing the effects of the numerical dispersion relation compensation and the Fresnel coefficients correction (measured at $(0, 0, -35)$).

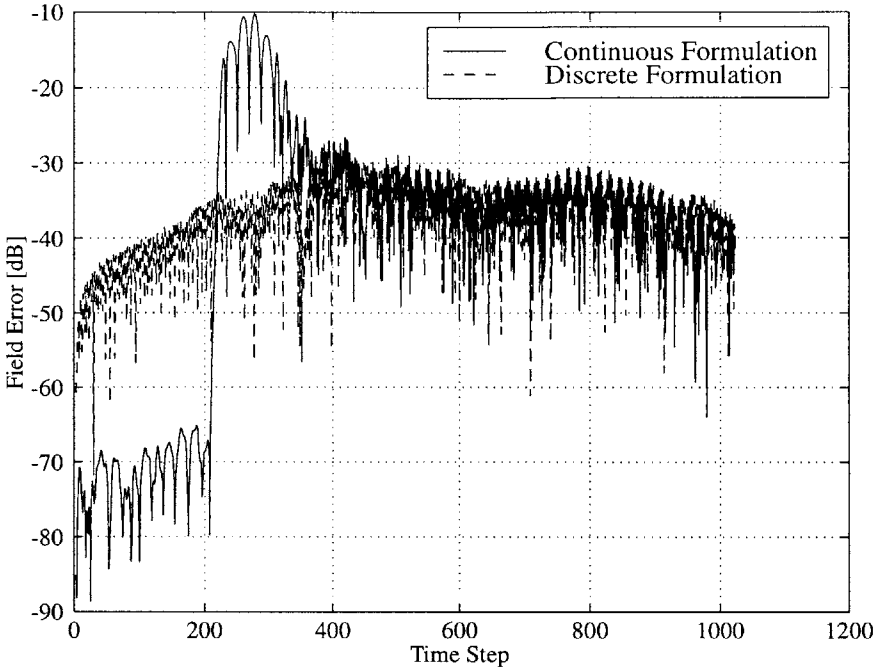

Figure 5-16: TE and TM numerical dispersion error, $\theta = 0^o$ incidence, maximum error (measured at $(0, 0, -35)$), wideband pulse

(chapter 8, [18]). A second Huygens' surface enclosing the total field domain was used to measure the scattered field error everywhere for the duration of the simulation. These measurements were then used to calculate the far field RCS error. Figure 5-17 shows the RCS error for 500 MHz and 700 MHz frequencies, using the discrete and continuous formulations. At 700 MHz, the discretization in region 1 is $\lambda/21$ and in region 3 is $\lambda/15$. In the continuous formulation, the maximum RCS errors for the two frequencies are-28.8 dB and -20.6 dB, whereas the errors for the discrete formulation are -76.6 dB and -61.1 dB. The RCS error for the continuous case is similar in magnitude to the error measured at a single point in previous Figures, whereas the discrete case error is much lower for this type of measurement. The reductions in error are 47.8 dB and 40.5 dB for the 500 MHz and 700 MHz frequencies, respectively. Note that the discrete formulation is still sensitive to discretization sizes, due to the averaging required of certain terms as well as the semi-implicit

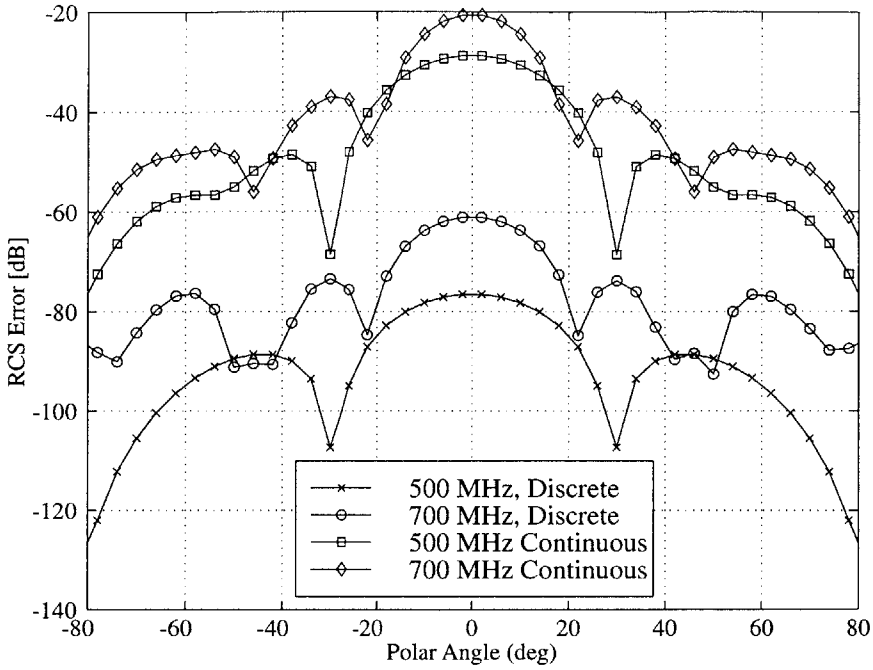

Figure 5-17: Radar cross section error for two frequencies, $\theta = 0^o$ incidence.

approximation of the FDTD formulation. The discrete formulation can sometimes even exhibit a larger relative increase in error over frequency than the continuous formulation (as in Figure 5-17), however this is not always the case. Ultimately, the compensation method still provides broadband error reduction, with a minimum of 40 dB improvement demonstrated here. Note that this method could also be used to correct the numerical dispersion in the scattered field region when using a Huygens' surface for far-field calculations, where the source locations are known (radiation problems).

5.7 Conclusions

In this chapter, the numerical dispersion effects for the FDTD method in anisotropic and layered media have been studied. This result can be used for many applications, and as an example a dispersion compensated Huygens' source in layered, uniaxial

media was presented. The new technique achieved a typical wideband improvement on the order of 30 dB over the conventional implementation for modest discretization sizes of ($\lambda/30$ - $\lambda/20$) in a 60^3 cell domain.

5.8 Appendix

The transmission and reflection coefficients for the TM case are:

$$T^{TM} = \frac{2i\sin(\delta_{z1})\epsilon_{z1}\,\epsilon_{t2}\,\epsilon_{z2}\,\left(1+e^{-2i\delta_{z1}}\right)e^{-i\delta_{z1}-i\delta_{z2}}}{D^{TM}} \tag{5.70}$$

$$\begin{aligned}
R^{TM} &= e^{-3i\delta_{z1}}[-2\,i\sin(\delta_{z1})\epsilon_{t,ave}\,\epsilon_{z1}\,\Omega^2\Delta^2\epsilon_{t2}\,\epsilon_{z2}\,e^{-i\delta_{z1}} \\
&+ \Omega^4\Delta^4\epsilon_{t,ave}\,\epsilon_{t1}\,\epsilon_{z1}\,\epsilon_{t2}\,\epsilon_{z2} \\
&- 2\,\Omega^2\Delta^2\epsilon_{t1}\,\epsilon_{z1}\,\epsilon_{t2}\,\epsilon_{z2} \\
&+ 2\,i\Omega^2\Delta^2\epsilon_{t,ave}\,\epsilon_{t1}\,\epsilon_{z1}\,\sin(\delta_{z2})e^{i\delta_{z2}}\epsilon_{z2} \\
&- 4\,\Omega^2\Delta^2\epsilon_{t,ave}\,\epsilon_{t1}\,\epsilon_{z1}\,\sin^2(\delta_{x1})\epsilon_{t2} \\
&- 2\,i\epsilon_{t1}\,\epsilon_{z1}\,\sin(\delta_{z2})e^{i\delta_{z2}}\epsilon_{z2} \\
&+ 4\,\epsilon_{t1}\,\epsilon_{z1}\,\sin^2(\delta_{x1})\epsilon_{t2} \\
&- 4\,\sin^2(\delta_{x1})\epsilon_{t,ave}\,\epsilon_{t1}\,\Omega^2\Delta^2\epsilon_{t2}\,\epsilon_{z2} \\
&+ 4\,\sin^2(\delta_{x1})\epsilon_{t1}\,\epsilon_{t2}\,\epsilon_{z2} \\
&- 8\,i\sin^2(\delta_{x1})\epsilon_{t,ave}\,\epsilon_{t1}\,\sin(\delta_{z2})e^{i\delta_{z2}}\epsilon_{z2} \\
&+ 16\,\sin^4(\delta_{x1})\epsilon_{t,ave}\,\epsilon_{t1}\,\epsilon_{t2} \\
&+ 2\,i\sin(\delta_{z1})\epsilon_{z1}\,e^{-i\delta_{z1}}\epsilon_{t2}\,\epsilon_{z2} \\
&+ 4\,\sin(\delta_{z1})\epsilon_{t,ave}\,\epsilon_{z1}\,\sin(\delta_{z2})\epsilon_{z2}\,e^{-i\delta_{z1}+i\delta_{z2}} \\
&+ 8\,i\sin(\delta_{z1})\epsilon_{t,ave}\,\epsilon_{z1}\,\sin^2(\delta_{x1})\epsilon_{t2}\,e^{-i\delta_{z1}}) \\
&\times (D^{TM})^{-1}
\end{aligned} \tag{5.71}$$

$$
\begin{aligned}
D^{TM} &= [-\Omega^4\Delta^4\epsilon_{t,ave}\,\epsilon_{t1}\,\epsilon_{z1}\,e^{-i\delta_{z1}}\epsilon_{t2}\,\epsilon_{z2} \\
&+ 2\,\Omega^2\Delta^2\epsilon_{t1}\,\epsilon_{z1}\,e^{-i\delta_{z1}}\epsilon_{t2}\,\epsilon_{z2} \\
&- 2\,i\Omega^2\Delta^2\epsilon_{t,ave}\,\epsilon_{t1}\,\epsilon_{z1}\,\sin(\delta_{z2})\epsilon_{z2}\,e^{-i\delta_{z1}+i\delta_{z2}} \\
&+ 4\,\Omega^2\Delta^2\epsilon_{t,ave}\,\epsilon_{t1}\,\epsilon_{z1}\,e^{-i\delta_{z1}}\sin^2(\delta_{x1})\epsilon_{t2} \\
&- 2\,i\sin(\delta_{z1})\epsilon_{t,ave}\,\epsilon_{z1}\,\Omega^2\Delta^2\epsilon_{t2}\,\epsilon_{z2} \\
&+ 2\,i\sin(\delta_{z1})\epsilon_{z1}\,\epsilon_{t2}\,\epsilon_{z2} \\
&+ 4\,\sin(\delta_{z1})\epsilon_{t,ave}\,\epsilon_{z1}\,\sin(\delta_{z2})e^{i\delta_{z2}}\epsilon_{z2} \\
&+ 8\,i\sin(\delta_{z1})\epsilon_{t,ave}\,\epsilon_{z1}\,(\sin^2(\delta_{x1})\epsilon_{t2} \\
&+ 2\,i\epsilon_{t1}\,\epsilon_{z1}\,\sin(\delta_{z2})\epsilon_{z2}\,e^{-i\delta_{z1}+i\delta_{z2}} \\
&- 4\,\epsilon_{t1}\,\epsilon_{z1}\,e^{-i\delta_{z1}}\sin^2(\delta_{x1})\epsilon_{t2} \\
&+ 4\,\sin^2(\delta_{x1})\epsilon_{t,ave}\,\epsilon_{t1}\,e^{-i\delta_{z1}}\Omega^2\Delta^2\epsilon_{t2}\,\epsilon_{z2} \\
&- 4\,\sin^2(\delta_{x1})\epsilon_{t1}\,e^{-i\delta_{z1}}\epsilon_{t2}\,\epsilon_{z2} \\
&+ 8\,i\sin^2(\delta_{x1})\epsilon_{t,ave}\,\epsilon_{t1}\,\sin(\delta_{z2})\epsilon_{z2}\,e^{-i\delta_{z1}+i\delta_{z2}} \\
&- 16\,\sin^4(\delta_{x1})\epsilon_{t,ave}\,\epsilon_{t1}\,e^{-i\delta_{z1}}\epsilon_{t2}]
\end{aligned}
\tag{5.72}
$$

Chapter 6

Detection of Targets in Continuous Random Media Using the Angular Correlation Function

6.1 Introduction

Electromagnetic wave propagation in random media is a topic of importance in fields such as remote sensing [67] and communications [118]. This is because many natural media such as foliage or soil cannot be described in a purely deterministic manner [119]. For example, predictions of radar return from objects obscured by foliage [120] or buried under the soil [121] are clearly dependent on the knowledge of the effects of such media on the total scattered field response. Random media have constitutive parameters that are random variables in space or time. Statistical models can be used to characterize a random medium in terms of effective (mean) constitutive parameters and fluctuations described by some correlation function. The study of statistical properties of electromagnetic wave scattering in such media can be carried out by Monte Carlo simulations on an ensemble of random media. In some very particular cases, a single realization may be sufficient by assuming spatial ergodicity, but in gen-

eral, the Monte Carlo ensemble should be large enough to ensure statistical meaningful results. The statistical description of random volumetric material inhomogeneities in this way is similar to the statistical description of random rough surfaces [122]. In this work, soil will be characterized as an inhomogeneous, continuous random media with subsurface detection applications in mind [123, 115, 124, 125, 126]. A number of studies have demonstrated that the soil constitutive parameters are highly sensitive to both moisture [127] and material content [128], so it is important to characterize such effects in terms of random permittivity fluctuations.

The bistatic scattered fields from targets buried in random media, using both ensemble and frequency averaging techniques have previously been studied [129]. In this chapter, the 3-D FDTD method presented in Chapter 5 is employed to characterize the angular correlation function (ACF) [130] of the scattered fields of targets in continuous random media. These results will serve to verify the effectiveness of the ACF for object detection in situations where the clutter from the surrounding volumetric scattering is important. The motivation for using the ACF is that scattered fields from buried objects should exhibit greater correlation than the random medium clutter, especially away from the memory line (or dot). This has been shown for rough surfaces and discrete random media in [131]. The angular correlation should be particularly large when the object has some kind of symmetry (such as spherical or cylindrical). The goal then is to compare the ACF of a random medium for cases with and without an buried object present, with the hope that the ACF will exhibit significant differences.

6.2 Angular Correlation Function (ACF)

Consider two plane waves impinging on a random medium, with incident angles θ_{i1} and θ_{i2}. The ACF [130] is defined as the correlation between the two scattered waves in directions θ_{s1} and θ_{s2}. Generally, the angles can be a function of ϕ or θ in a three-

dimensional geometry, but in this work is limited to $\phi_{i1} = \phi_{i2} = 0$. The random medium is a halfspace with permittivity:

$$\epsilon(\overline{r}) = \epsilon_m + \epsilon_f(\overline{r}) \tag{6.1}$$

where $\overline{r} = x\hat{x} + y\hat{y} + z\hat{z}$ and $\epsilon_f(\overline{r})$ is a function of position $\overline{r}$ characterizing the random fluctuation, and is such that $\langle \epsilon_f(\overline{r}) \rangle = 0$. The fluctuation at each position is a Gaussian random variable, with correlation function $C(\overline{r}_1 - \overline{r}_2)$. The generation of $\epsilon_f(\overline{r})$ is implemented in the Fourier domain by passing a three-dimensional array of random numbers (with Gaussian distribution and zero mean) through a digital filter whose response corresponds to $W(\overline{k})$, the Fourier transform of $C(\overline{r}_1 - \overline{r}_2)$. $W(\overline{k})$ is then the spectral density function of the dielectric fluctuation. This work will consider the following correlation function [132, 133]:

$$\left\langle \epsilon_f(\overline{r}_1)\epsilon_f^*(\overline{r}_1) \right\rangle = C(\overline{r}_1 - \overline{r}_2) = \delta\epsilon_{1m}^2 e^{-\frac{\left(|x_1-x_2|^2+|y_1-y_2|^2\right)}{l_\rho^2}} e^{\frac{|z_1-z_2|^2}{l_z}} \tag{6.2}$$

where l_ρ and l_z are the transverse and vertical correlation lengths, respectively, ϵ_{1m} is the mean permittivity, and δ is the variance. The correlation function in Equation 6.2 has a Gaussian profile in both the transverse and vertical directions. A typical $x - y$ plane cross section of one realization is depicted in Figure 6-1. Note that other correlation functions could be used as well. A Gaussian correlation is employed for its generality and because it can be fully described with a minimal number of parameters l_ρ, l_z, ϵ_{1m}, and δ (low order statistics). The ACF, Γ, is written as

$$\Gamma\left(\theta_{s1}, \theta_{i1}; \theta_{s2}, \theta_{i2}\right) = < E_s\left(\theta_{s1}, \theta_{i1}\right) E_s^*\left(\theta_{s2}, \theta_{i2}\right) > \tag{6.3}$$

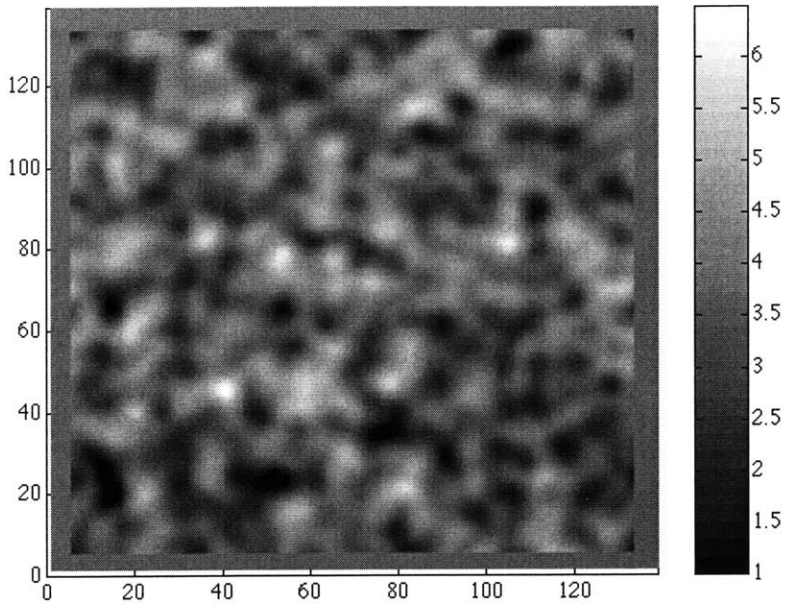

Figure 6-1: Cross-section of the random medium permittivity in the x-y plane. $\epsilon_{1m} = 3.5$.

where E_s is the scattered field and the angular brackets denote averaging. The averaging can be performed in many ways, the most common being realization averaging:

$$\begin{aligned} \Gamma_r\left(\theta_{s1}, \theta_{i1}; \theta_{s2}, \theta_{i2}\right) &= \frac{1}{N_r} \sum_{n=1}^{N_r} \psi_s^N\left(\theta_{s1}, \theta_{i1}, n\right) \\ &\times \psi_s^{N*}\left(\theta_{s2}, \theta_{i2}, n\right) / \sqrt{P_1 P_2} \end{aligned} \tag{6.4}$$

and frequency averaging [131]:

$$\begin{aligned} \Gamma_f\left(\theta_{s1}, \theta_{i1}; \theta_{s2}, \theta_{i2}\right) &= \frac{1}{N_f} \sum_{n=1}^{N_f} \psi_s^N\left(\theta_{s1}, \theta_{i1}, f_n\right) \\ &\times \psi_s^{N*}\left(\theta_{s2}, \theta_{i2}, f_n\right) / \sqrt{P_1 P_2} \end{aligned} \tag{6.5}$$

where the bandwidth can be defined as $2\Delta f$, $f_o - \Delta f < f_n < f_o + \Delta f$, N_r and N_f are the number of medium realizations and frequencies, respectively, and P_1, P_2 describe

the power of the incident fields. Equation 6.3 has a correlation that is described by what is known as the memory effect, which is a function of the incident and scattered wave angles. The memory effect is a result of the *statistical* translational invariance of the random volume, and reduces to phase matching for the deterministic (zero variance) case. In the case of a random rough *surface* scattering, the strongest correlation occurs along the memory *line*, described by $\sin\theta_{s2} - \sin\theta_{s1} = \sin\theta_{i2} - \sin\theta_{i1}$. When considering *volumetric* scattering from a random medium, another phase matching condition exists in the vertical direction, described by $\cos\theta_{i1} + \cos\theta_{s1} = \cos\theta_{i2} + \cos\theta_{s2}$. This latter phase matching condition makes the memory line shorter [131], creating what is called a *memory dot*. Note that random medium scattering is not statistically invariant in the vertical direction, due to loss (finite conductivity), so this memory effect is not exact. Realization averaging is akin to Monte-Carlo averaging, and is very useful to describe the statistical properties of scattered fields. However, while realization averaging is useful in demonstrating the memory effects theoretically, it cannot be applied to real subsurface detection problems because only one realization is available in practice. Frequency averaging is an alternative technique that can be used in practical detection problems. FDTD is suited for simulations involving frequency averaging, with proper care taken to avoid numerical dispersion effects at higher frequencies. Moreover, the objects must be relatively shallow, due to the frequency dependence of penetration depth. A weighting function, $W_e(f)$, must then be used to compensate for the frequency dependent response of the system (penetration depth, object size) [131]. This work will examine both realization and frequency averaging techniques. The motivation for using the ACF is that scattered fields from buried objects should exhibit greater correlation than the random medium clutter, especially away from the memory line (or dot). This is particularly true when the object has some kind of symmetry (such as spherical or cylindrical). The goal then is to compare the ACF of a random medium for cases with and without an buried object present, with the hope that the ACF will exhibit significant differences.

The Born approximation can be used to gain insight into the ACF. Given a plane wave incident on the half-space random medium defined in Section 2, the fields in regions 0 (upper) and 1 (lower) can be calculated using dyadic layered Green's functions, $\overline{\overline{G}}_{01}^{(0)}(\overline{r},\overline{r}')$ and $\overline{\overline{G}}_{11}^{(0)}(\overline{r},\overline{r}')$, as [66]:

$$\overline{E} = \overline{E}^{(0)} + \omega^2\mu \int_{V_1} dr' \ \overline{\overline{G}}_{01}^{(0)}(\overline{r},\overline{r}')\epsilon_{1f}(\overline{r}') \cdot \overline{E}_1(\overline{r}') \tag{6.6}$$

$$\overline{E}_1 = \overline{E}_1^{(0)} + \omega^2\mu \int_{V_1} dr' \ \overline{\overline{G}}_{11}^{(0)}(\overline{r},\overline{r}')\epsilon_{1f}(\overline{r}') \cdot \overline{E}_1(\overline{r}') \tag{6.7}$$

where V_1 is the random medium volume. Using the Born approximation [66] to obtain the first order solution, we replace the total field $\overline{E}_1$ in the integral by the incident field $\overline{E}_1^{(0)}$. The approximation is applicable when $\epsilon_1(\overline{r}') \simeq \epsilon_{1m}$ (low contrast). The perturbed part of the scattered field in region 0 is then:

$$\overline{E}_s^{(1)}(\overline{r}) = \omega^2\mu \int_{V_1} dr' \ \overline{\overline{G}}_{01}^{(0)}(\overline{r},\overline{r}')\epsilon_{1f}(\overline{r}') \cdot \overline{E}_1^{(0)}(\overline{r}') \tag{6.8}$$

The half-space Green's function in the far field is:

$$\overline{\overline{G}}_{01}^{(0)}(\overline{r},\overline{r}') = \frac{e^{ikr}}{4\pi r}[X_{01s}\hat{h}(\theta_s,\phi_s)\hat{h}(\theta_{s1},\phi_{s1}) + \frac{k}{k_{1m}}Y_{01s}\hat{v}(\theta_s,\phi_s)\hat{v}(\theta_{s1},\phi_{s1})]e^{-i\overline{k}_{1s}\cdot\overline{r}'} \tag{6.9}$$

where X_{01s} and Y_{01s} are the transmission coefficients of the half-space interface, with the subscript s indicating they are evaluated in the direction of the scattered fields, and $\hat{h}$ and $\hat{v}$ are the standard polarization vectors [66]. Given two incident fields in region 0, $\overline{E}_{ia}$ and $\overline{E}_{ib}$, the unperturbed fields in region 1 are:

$$\overline{E}_{1a}^{(0)}(\overline{r}) = X_{01ia}\hat{h}_{1ia}e^{i\overline{k}_{1ia}\cdot\overline{r}}$$

$$\overline{E}_{1b}^{(0)}(\overline{r}) = X_{01ib}\hat{h}_{1ib}e^{i\overline{k}_{1ib}\cdot\overline{r}}$$

where the transmission coefficients, polarization vectors, and k vectors are denoted

with a or b subscripts to correspond to the respective incident fields. The co-polarized ACF using ensemble averaging and the Born approximation may be written as:

$$\Gamma_{ab} = \frac{k_m^4 \delta}{16\pi^2 r^2} X_{01sb} X_{01ib} X_{01sa} X_{01ia} A \tag{6.10}$$

where A is:

$$A = \int_{V_1} d\overline{r}' \int_{V_1} d\overline{r}'' e^{i(\overline{k}_{d1a}\cdot\overline{r}' - \overline{k}_{d1b}\cdot\overline{r}'')} C\left(\overline{r}' - \overline{r}''\right) \tag{6.11}$$

and k_{d1a} is $k_{1ia} - k_{1sa}$ (similarly for k_{d1b}). Changing to average and difference coordinates, $\hat{r}_{av} = (\hat{r}' + \hat{r}'')/2$ and $\hat{r}_d = \hat{r}' - \hat{r}''$, we obtain:

$$A = \int_{V_1} d\overline{r}_{av} \int_{V_1} d\overline{r}_d e^{i((\overline{k}_{d1a} - \overline{k}_{d1b})\cdot\overline{r}_a + (\overline{k}_{d1a} + \overline{k}_{d1b})\cdot\overline{r}_d/2)} C\left(\overline{r}_d\right) \tag{6.12}$$

Evaluating the A factor results in:

$$A = \frac{4i\left(e^{-ik_{z1d}^{d-}d} - 1\right)}{k_{z1d}^{d-}} \frac{\sin k_{x1d}^{d-} L_x/2}{k_{x1d}^{d-}} \frac{\sin k_{y1d}^{d-} L_y/2}{k_{y1d}^{d-}}$$

$$\frac{\pi^{\frac{3}{2}} l_\rho^2 l_z}{4} e^{-\frac{l_\rho^2}{16}\left(k_{x1d}^{d\ 2} + k_{y1d}^{d\ 2}\right) - \frac{l_z^2}{16} k_{z1d}^{d\ 2}} \left[erf\left(\frac{L_x}{l_\rho} + \frac{ik_{x1d}^d l_\rho}{4}\right) + erf\left(\frac{L_x}{l_\rho} - \frac{ik_{x1d}^d l_\rho}{4}\right)\right]$$

$$\left[erf\left(\frac{L_y}{l_\rho} + \frac{ik_{y1d}^d l_\rho}{4}\right) + erf\left(\frac{L_y}{l_\rho} - \frac{ik_{y1d}^d l_\rho}{4}\right)\right]$$

$$\left[erf\left(\frac{d}{l_z} + \frac{ik_{z1d}^d l_z}{4}\right) + erf\left(\frac{d}{l_z} - \frac{ik_{z1d}^d l_z}{4}\right)\right] \tag{6.13}$$

where $k_{x1d}^{d-} = k_{x1da} - k_{x1db}$ and $k_{x1d}^{d} = k_{x1da} + k_{x1db}$.

The dominant factors in the ACF are the first three factors of A, which are sinc functions in terms of k_x, k_y, and k_z. These results show that the width of the memory

line (or dot) is on the order of λ/L_x and λ/L_y, where L_x and L_y are the transverse linear dimensions of the random medium volume considered (illuminated area). The depth of the random medium is indicated by d, hence the random permittivity fluctuations exist over a total volume defined by $L_x \times L_y \times d$ in the halfspace. As shown in [129], larger correlation lengths result in larger scattered fields, and hence the total ACF increases in magnitude as the correlation lengths increase (the shape remains similar). However, as the correlation length approaches the dimensions of the volume, the ACF rapidly decreases to zero, as the random medium becomes homogeneous. The ACF is determined by averaging over angles to obtain different wave vectors. However it is also possible to obtain the frequency correlation function (FCF) by averaging over frequency (the sinc functions depend only on k), although it is not as likely that the scattered fields of the object will be well correlated over frequency as they are over angles. Hence, one cannot expect that the FCF will have a significantly greater correlation when the object is placed in the random medium.

6.3 FDTD Model

Our FDTD computational domain is show in Figure 6-2, containing a perfect electrically conducting (PEC) cylinder embedded in a random medium half-space. The incident field is introduced on the Huygens' surface A enclosing the target as well as the random medium half-space, using the total/scattered (T/S) field formulation [18]. Using a plane wave incidence, the half-space Green's function [115] is used to calculate the incident field everywhere on the Huygens' surface A. When calculating the incident field, the permittivity of the half-space is taken to be the effective permittivity of the random medium. The numerical dispersion compensation scheme introduced in Chapter 5 is used here. The scattered far field is calculated on the Huygens' surface B in the scattered field domain [134], again using the layered Green's function. A perfectly matched layer (PML) formulated via stretched coordinates [22] is

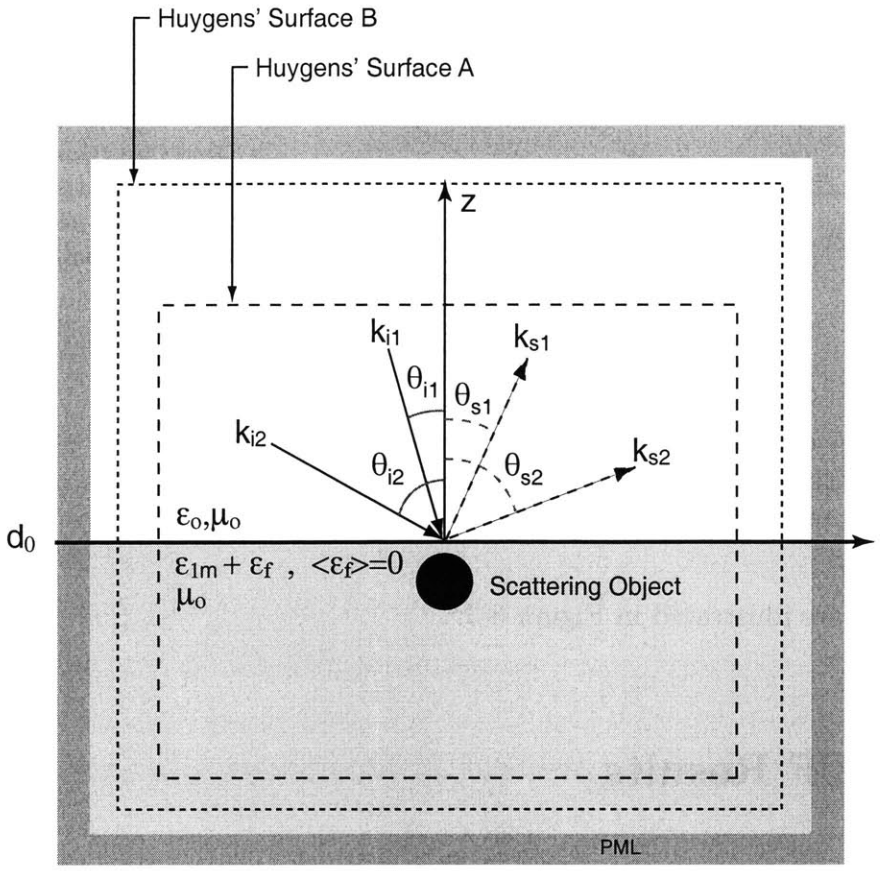

Figure 6-2: Object is a cylinder, buried in the random medium halfspace with $\epsilon_{1m} = 3.5$.

used to match the interior medium and truncate the computational domain. The results presented here do not include the direct reflection from the half-space interface (free-space/mean permittivity). The interface return (surface scattering) is removed because only the perturbations to the RCS response caused by the buried object and the random medium are of interest. Therefore, the scattered field results shown can be considered as perturbations in the steady-state average return with no object present. If necessary, direct returns from the interface layer can be easily obtained (even analytically). Moreover, given a planar interface is considered here, the simulations presented here do not include any surface roughness (and the associated surface-scattering clutter) effects in the scattering results. This is purposely done in order to isolate and better analyze the volumetric scattering effects. The possible

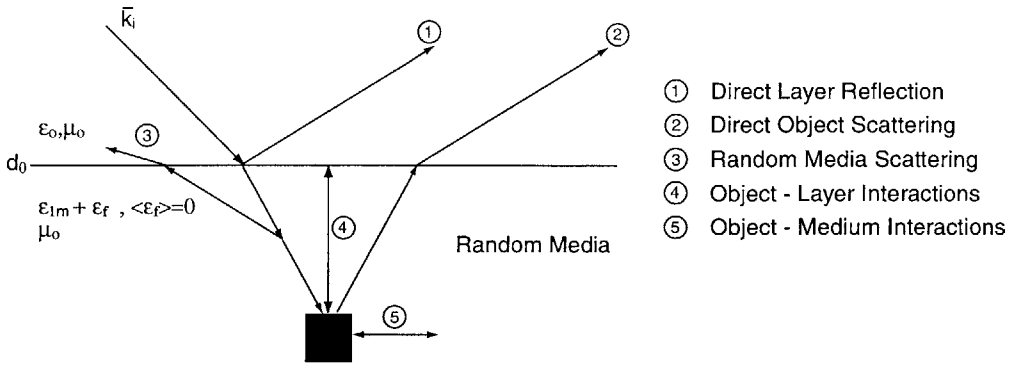

Figure 6-3: The possible interactions between the incident field, surface, random medium, and target. Interaction 1 is not included in the results of this Chapter.

interactions are illustrated in Figure 6-3.

6.4 ACF Results

The FDTD computational domain is created by discretizing the half-space into a $140 \times 140 \times 74$ lattice (composed of the standard Yee cells [17]), where the random soil comprises $128 \times 128 \times 64$ cells. This results in a system with 12.85 million unknowns, solved at 1000 time steps, taking 683 seconds per realization on an AlphaServer DS20E (667 MHz with 4 GB RAM). The actual physical size of the random medium corresponds to 1.71 m $\times$ 1.71 m $\times$ 0.855 m. The discretization size is chosen to be 1.2 cm, which corresponds to $\lambda/84$ in free-space and approximately $\lambda/45$ within the soil (mean permittivity) for a 300 MHz pulse (center frequency). In terms of the central frequency and the corresponding soil wavelength, the electrical size of the random medium is $3.2\lambda \times 3.2\lambda \times 1.9\lambda$.

The soil model has an average relative permittivity of $\epsilon_{1m} = 3.5$ and conductivity $\sigma = 3.37 \times 10^{-3}$ [S/m], which have been experimentally determined [135] for a Puerto Rico type of clay loam [136]. The standard deviation of the soil permittivity is chosen to be between 15% and 25% of the mean value. These values roughly corresponds to

moisture content (water volume) fluctuations of a few percent, with a mean moisture content approximately 5%. The random medium has correlation lengths (l_ρ and l_z) corresponding to approximately 5 to 7 FDTD cells (0.4 m).

The FDTD results may be compared against the Born approximation. The incident field angles are $\theta_{s1} = 20^o$, $\theta_{s2} = -10^o$. Figure 6-4 shows the FDTD simulated ACF magnitude with no object *vs.* the scattered field angle, averaged over 75 realizations. The strong correlation along the memory line, described by $\sin\theta_{s2} - \sin\theta_{s1} = -0.515$, is clearly visible. A peak occurs at the intersection with the vertical phase matching condition $\cos\theta_{s2} - \cos\theta_{s1} = -0.0451$. The correlation away from the memory line is relatively weak. Figure 6-5 shows the comparison of the ACF obtained with both the FDTD results and the Born approximation. The agreement is generally good, especially at the memory line. Generally, the Born approximation results overestimate the scattered fields, although it is not noticeable given these parameters. In this figure, the agreement is poorest away from the memory line, although that is not always the case. To study the effectiveness of the ACF for object detection, a PEC cylinder (discretized using a conformal FDTD [18]) is placed inside the random medium. The cylinder is approximately 10 cm in length and 9 cm in diameter, and it is buried 7 cm below the surface. The ACF and bistatic RCS of the scattered fields can then be compared (in dB), with and without the target present, using:

$$\Lambda_{ACF} = \frac{|\Gamma_f(\text{object})|}{|\Gamma_f(\text{no object})|} \qquad (6.14) \qquad \Lambda_{RCS} = \frac{|RCS_f(\text{object})|}{|RCS_f(\text{noobject})|} \qquad (6.15)$$

The f subscript above denotes frequency averaging, which will be the focus in this case. The ACF and RCS are averaged from 150 MHz to 450 MHz in 10 MHz steps. The angles chosen for this case are $\theta_{s1} = 30^o$ and $\theta_{s2} = -15^o$. Examining the RCS alone at any single frequency is not useful in determining the presence of the target object because the response over angle shows only small fluctuations. The results are depicted in Figure 6-6(a), which compares Λ_{RCS} against Λ_{ACF}, where Λ_{ACF} is

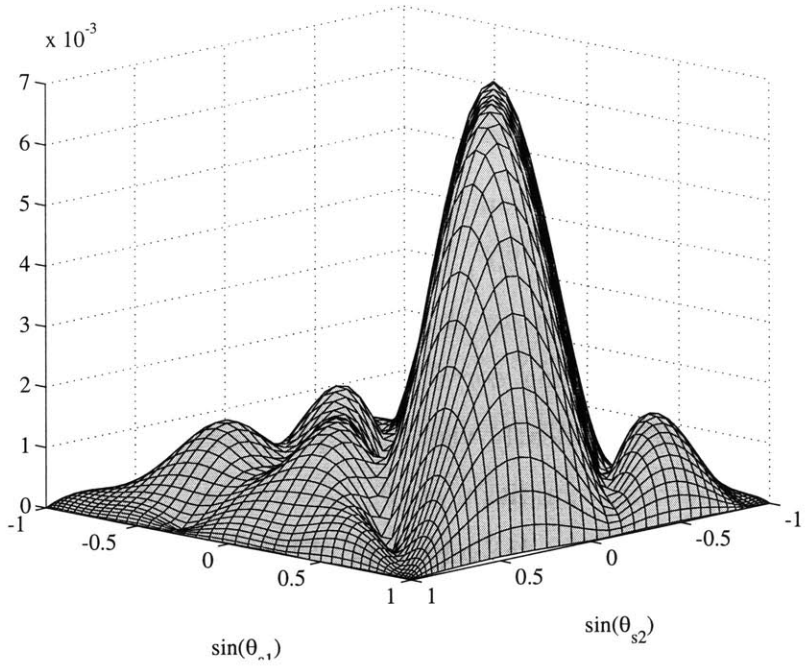

Figure 6-4: ACF magnitude for the random medium without and object, using random medium averaging.

measured along and perpendicular to the memory line (intersecting at the peak). In this case, the presence of the object is difficult to determine solely with frequency averaging on the RCS because the difference does not fluctuates more that 1 dB. On the other hand, the ACF away from the memory line shows a correlation that is 16 dB greater when the object is present, and peaks at 3 dB elsewhere. The ACF along the memory line in this case is less effective, showing less change than the Λ_{RCS}. Note that the peak of the memory line occurs here in both cases at $\theta_{s2} = -20^o$, and at this point the ACF is least effective for target detection. The effectiveness of examining the ACF variations away from the memory line is again demonstrated in Figure 6-6(b), where one of the scattered field directions is held constant at either $\theta_{s1} = -30^o$ (specular direction) or $\theta_{s1} = 30^o$ (back scattering). The ACF in the specular direction does little better than the RCS, but for $\theta_{s1} = 30^o$, two strong peak fluctuations of 9 dB and 10 dB are observed, as well as a third smaller peak of -4 dB. These results

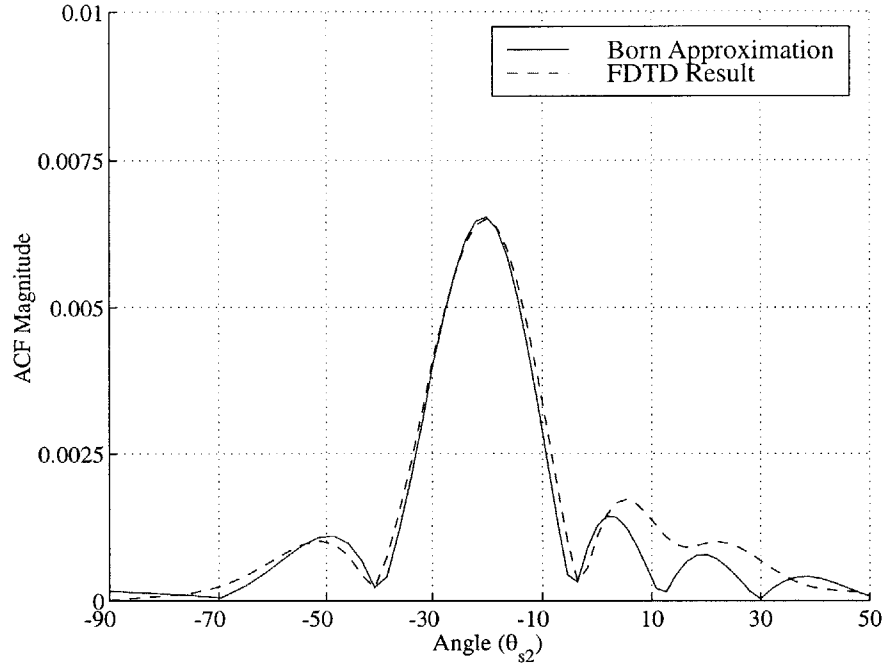

Figure 6-5: Comparisons of the ACF obtained from FDTD and the Born approximation, plotted perpendicular to the memory line.

suggest that a ground penetrating radar setup could be designed to explore this effects by, for instance, employing two transmitting antennas at fixed angles (with one acting also as a receiver), and a third antenna acting only as a receiver that would scan over discrete angles or bands of angles. Finally, consider a larger domain simulation (larger illuminated volume). In this case, higher fluctuations in the ACF may cause larger fluctuations on Λ_{ACF} (because of the sinc like behavior of the ACF). Figure 6-7(a) shows the Λ_{RCS} and Λ_{ACF} results for a random medium that is $6.4\lambda \times 6.4\lambda \times 1.6\lambda$. Λ_{RCS} in this case fluctuates between plus and minus 2 dB, as does Λ_{ACF} along the memory line. Perpendicular to the memory line, note the more interesting results for Λ_{ACF}, with larger fluctuations of 3 dB and -7 dB. Moreover, in Figure 6-7(b), the Λ_{ACF} in the specular, $\theta_{s1} = -30^o$, and backscattering, $\theta_{s1} = 30^o$, directions fluctuates many times from 4 dB to 10 dB. Either scattering angle choice produces three or four large fluctuations, which would result in a useful criteria and better

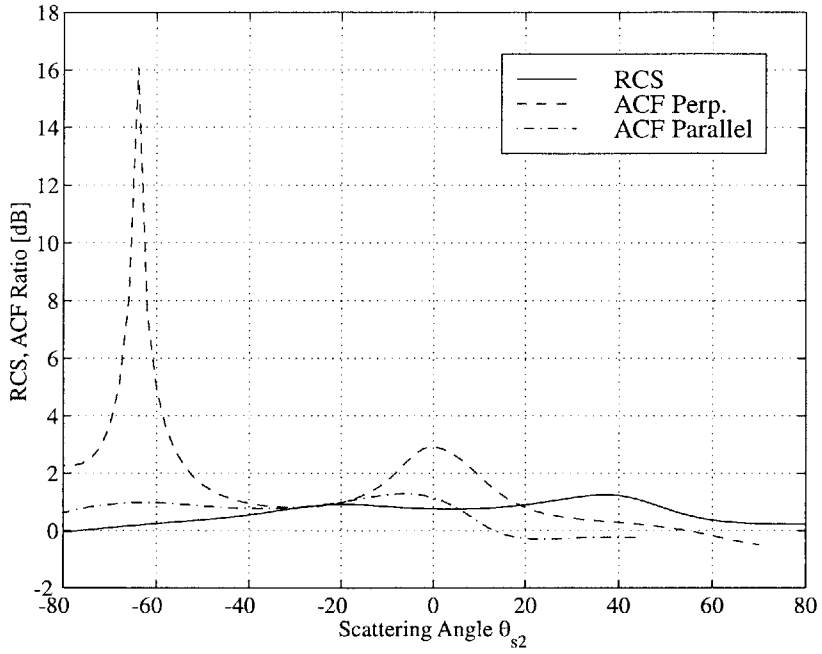

(a) Along and perpendicular to the memory line.

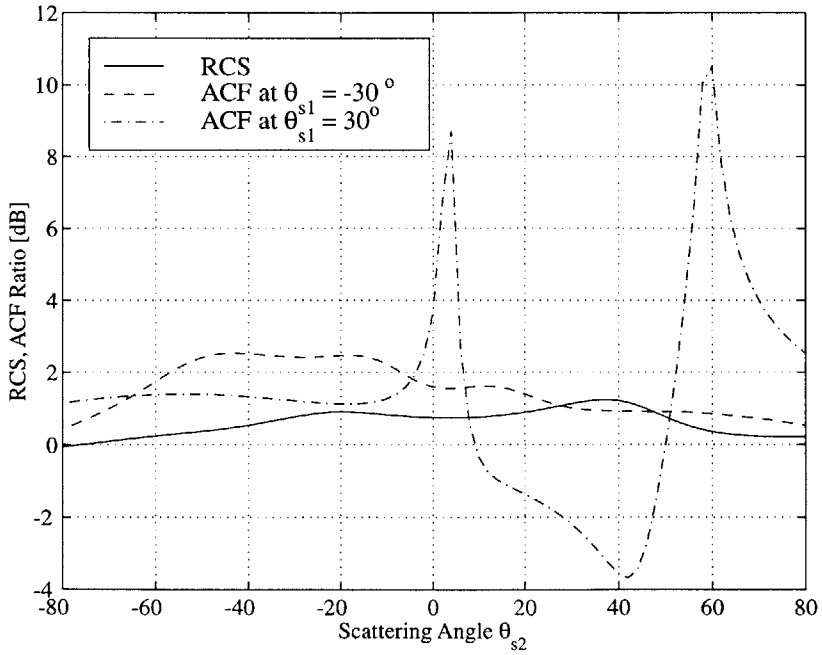

(b) Away from the memory line (specular and back scattering).

Figure 6-6: Frequency averaged RCS and ACF results. The domain is $3.2\lambda \times 3.2\lambda \times 1.6\lambda$

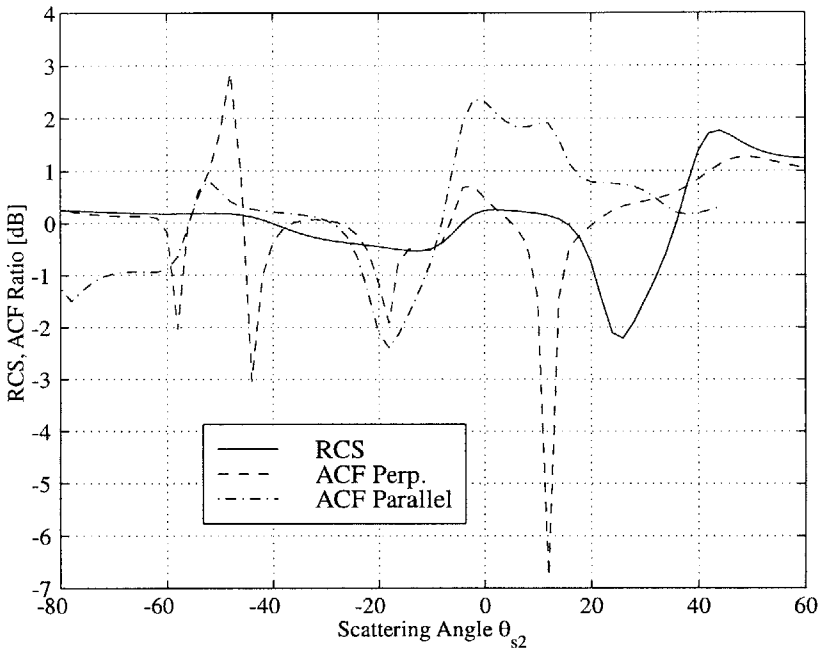

(a) Along and perpendicular to the memory line.

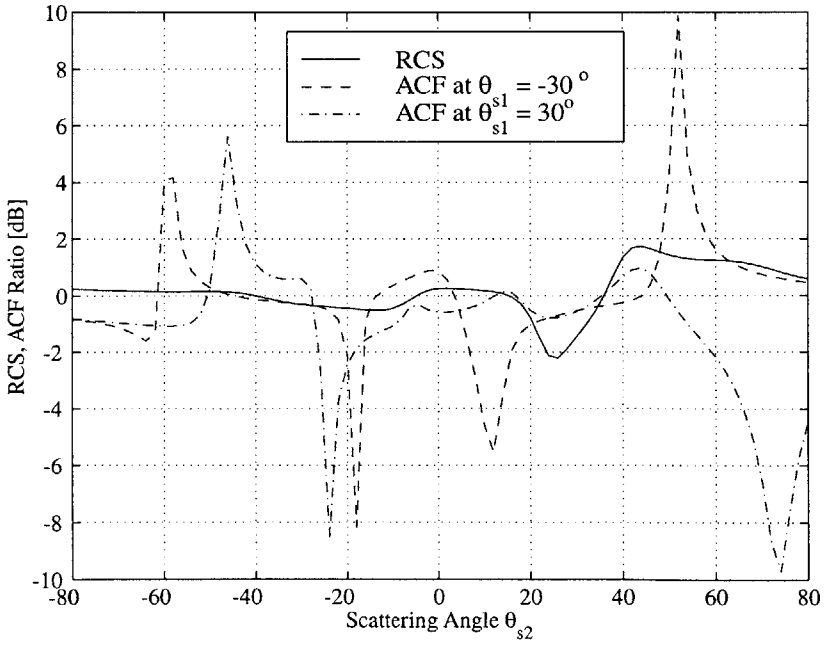

(b) Away from the memory line (specular and back scattering).

Figure 6-7: Frequency averaged RCS and ACF results. The domain size is $6.4\lambda \times 6.4\lambda \times 1.6\lambda$

chance of object detection for a finite number of θ_{s2} measurements. Note that this frequency averaged results are obtained by considering a single particular realization of the random medium. May tests have been performed on different realizations and, although the details may vary, the same general behavior was observed.

6.5 Conclusions

FDTD simulations have been employed to characterize the ACF of the scattering from targets in continuous random media. The new FDTD scheme developed in Chapter 5 was employed to examine the effectiveness of ACF for object detection in the presence of volumetric clutter. The ACF generated from FDTD simulations is also compared against ACF obtained from the Born approximation (when the latter is applicable). The memory effect of the ACF was clearly demonstrated through an average over random medium realizations. The effectiveness of the ACF in detecting a buried cylinder under frequency averaging was also demonstrated. When the cylinder was placed in the medium, the ACF exhibited as much as a 10 dB greater variation than the bistatic RCS, especially away from the memory line.

Chapter 7

Summary

This thesis has studied various problems of electromagnetic propagation and scattering in complex media, and has developed a range of new numerical methods to obtain solutions with improved accuracy and speed. For each topic, this summary will focus on the original contributions, and discuss possible future directions for the research.

Chapter 2 presented a hybrid time domain numerical method that can calculate the Electromagnetic Induction (EMI) response from a conducting, permeable body-of-revolution (BOR) in early time (or high frequencies). The first step of the work was to implement a standard numerical technique. An FEM was used to model the interior of the target, and was chosen for its ability to model inhomogeneous objects of arbitrary shape. The FEM was developed using various existing techniques in the literature, so its implementation was an incremental development based on a combination of previously published work. The unbounded exterior domain was accounted for using an MoM technique, adapted from mechanical engineering applications (that refer to it as the boundary element method), and was coupled to the FEM through the boundary conditions, resulting in the Finite Element - Boundary Integral (FE-BI) method. The main contribution of the FE-BI method in Chapter 2 is the implementation for transverse excitation. No publications could be found that developed the appropriate Green's functions or dealt with the additional complexities in the FEM.

As expected, the FE-BI method was inaccurate due to the small skin depths that occur early in time after the primary field transient. This is a problem that has plagued many engineers in the past, in unexploded ordnance (UXO) applications and in transformer (or electric motor) eddy current analysis (all treating axial excitation only). The problem is often ignored, as the FE-BI solutions do eventually converge to the correct solution later in time. However, as shown in the experimental comparisons of Chapter 2, the new generation of sensors take measurements in early time, where important EMI characteristics exist. Hence, there is a significant need for an accurate model of the EMI early time response. The Thin Skin Approximation (TSA) method had been previously developed for the frequency domain three dimensional case, and in Chapter 2 it is first adapted to the BOR case, then implemented in the time domain. The resulting formulation was significantly different from the previous TSA implementation, requiring a recursive solution that utilized the complementary error function, the analytical time domain solution of the diffusion equation in a half space. The TSA was then coupled to the MoM, resulting in the TSA - Boundary Integral (TSA-BI) method that is accurate in early time. For steel UXO, the TSA-BI method was accurate throughout the entire time of interest. Finally, the FE-BI and TSA-BI methods were combined in a simple fashion by running each separately and matching the point where the responses overlap in intermediate time. It turned out that for a given mesh and for materials with larger skin depths, the TSA was accurate for a shorter period of time while the FEM converged quickly to the exact solution. For materials with smaller skin depths, the TSA was accurate for a longer period of time while the FEM took longer to converge. In general, while both methods had different regions of accuracy, their combined region of accuracy covered the entire EMI response time. Furthermore, the TSA-BI method was very fast, and the FE-BI method can be quickly solved on a relatively coarse mesh, resulting in a new solution method that was both faster and more accurate than the original FE-BI alone. Further work on this subject could include a mathematical demonstration that both

methods combined will (or will not) always produce an accurate and complete time domain response with a given mesh discretization. Likely there is some minimum mesh discretization necessary for both methods to converge. Another topic of study could be the way in which both methods are combined; instead of running each separately, a better solution would be to map the TSA-BI result into the FEM mesh when the skin depth reaches a certain value. This is not possible with the current formulation, where the TSA uses the magnetic field and the FEM uses the magnetic vector potential, so the combined method would require a new approach for one or the other. It is possible that such a new approach would introduce disadvantages that outweigh any possible accuracy or speed gains, but it is worth investigating. At the end of Chapter 2, the results were compared with experimental data of the EMI response from a chrome steel sphere, and the agreement was excellent. In summary, the contribution of Chapter 2 was both a new numerical method to calculate the EMI scattered fields, as well as a demonstrated application of time domain UXO detection and discrimination. The method is well-suited to use in inversion routines for experimental systems like the one shown in Chapter 2.

Chapter 3 presented an MoM formulation for scattering from 1-D layered rough surfaces. The MoM formulation for scattering from a single 1-D penetrable rough surface is well-established, and the formulation presented in Chapter 3 was based on this formulation and extended it to layered rough surfaces. A number of approximations were necessary to do this, such as the assumption that the fields are zero at the ends of the surfaces. The method was partially validated through comparison with analytical solutions for flat surfaces. Given the linear increase in the number of unknowns (N) for each layer, the Forward Backward Spectral Acceleration (FBSA) method was adapted and $\mathcal{O}(N)$ efficiency was demonstrated. As mentioned in Chapter 3, the FBSA method has only recently been developed for a single penetrable rough surface, and several new ideas were introduced to allow its implementation for layered rough surfaces. The standard MoM and FBSA formulations were compared

for scattering from a three-region medium, and excellent agreement was obtained. Finally, numerical experiments were performed to establish the applicability of the method. Although the new method can solve many cases, the convergence time increases as the surface roughness increases, the surface separation decreases, and the dielectric contrast between the layers increases, to the point where the method actually diverges. Physics based reasons for the method's failure in certain cases were described in Chapter 3, and similar problems are also present for the single-surface case. This new numerical tool enables more accurate solutions for applications including remote sensing, radar system modeling, and microwave communication link studies. However, the applications were not investigated in detail. Such studies are more of interest to systems engineers interested in specific applications, for which they may obtain more accurate results with the new method. Hence, the contribution of Chapter 3 is the new numerical method that will allow engineers to solve a standard problem of rough surface scattering with greater accuracy. A future extension of this method would be to adapt it to two dimensional (2D) surfaces. However, given that single 2D surface scattering simulations are computationally limited to very small domains, layered 2D scattering simulations are probably not possible with current computational resources.

Chapter 4 examined three techniques to demonstrate the Left Handed (LH) behavior of a metamaterial. This work was motivated by the controversy surrounding such metamaterials, resulting from the difficulty in experimental demonstrations. Although experimental results are the only way to prove the existence of any physical phenomena, numerical methods like the FDTD can provide rigorous and convincing arguments. Hence, the goal of this work was to isolate and identify unique properties, using the FDTD, that unambiguously verified the LH behavior of metamaterials. First, the possible frequency band of LH behavior was determined by calculating the transmitted power of a wideband pulse through a slab of metamaterial. In that frequency band, the backward phase velocity in a slab was then verified, and the index

of refraction was calculated. At the same frequencies, a negative index of refraction was demonstrated by calculating the direction of power leaving a metamaterial prism. Both methods of calculating the index of refraction of the metamaterials (using the prism or phase velocity) gave consistent results. The FDTD model in this work used two similar Split-Ring Resonator (SRR) geometries, one that has dimensions scaled and optimized for the uniform Cartesian grid, and the other that is a model of geometries used in previous experiments [30]. The scaled SRR geometry is useful in that it allows LH metamaterials to be simulated quickly using an efficient FDTD grid. A new SRR design was studied and shown to be less lossy than the original design. The numerical study enables a greater understanding of the phenomena that leads to LH behavior in metamaterials, and can be easily changed to examine new metamaterial geometries in the future. Furthermore, the numerical study could be extended to include lossy metals and dielectrics, metamaterials without waveguides, and larger prisms. In terms of original contributions, the focus of Chapter 4 was the demonstration of the LH behavior of metamaterials, rather than the numerical methods that were used. Indeed, the results presented in Chapter 4 are the first to rigorously demonstrate the LH behavior of metamaterials using a complete numerical simulation.

In Chapter 5, the numerical dispersion effects were studied in the FDTD method for anisotropic and layered media. Discrete versions of Maxwell's Equations were derived, based on previous work, and were used to derive the discrete wave equation and numerical dispersion equation for uniaxial media. The reflection and transmission coefficients were then derived for planar surfaces in an FDTD grid. This information can be used for many applications, and as an example a numerical dispersion compensated Huygens' source in layered, uniaxial media was presented. The new technique achieved a typical wideband improvement on the order of 30 dB over the conventional implementation for modest discretization sizes of ($\lambda/30$ - $\lambda/20$) in a 60^3 cell domain. Note that numerical dispersion was not eliminated from the FDTD method; rather,

the scattered field noise from the Huygens' sources was eliminated. For example, when calculating the radar cross section of a target, the incident field created by the compensated Huygens' sources still accumulates numerical dispersion error. The scattered field also accumulates error as it propagates away from the target. However, the noise floor in the scattered field region is reduced (on the order of 30 dB) when using the compensated Huygens' sources. This method has application in any study of wave propagation through layered media. In particular, ground penetrating radar, microstrip, and antenna applications benefit from this method, particularly when the scattered field is weak or accurate results are required. Specific applications were not studied in Chapter 5, and the contribution lies in the new numerical method. The discrete Maxwell's Equations could be used to derive other numerical parameters, such as dispersions relations for any type of media, that could also be included in an FDTD simulation.

As the thesis began with a problem of buried object detection, it also ends with such a problem, albeit one solved with a different method. The new FDTD method of Chapter 5 was employed in Chapter 6 to characterize the Angular Correlation Function (ACF) of the scattered fields from targets in random media. The effectiveness of the ACF for object detection in the presence of volumetric clutter was investigated. The ACF generated from FDTD simulations was also compared against ACF obtained from the Born approximation (when the latter is applicable), and good agreement was obtained. The memory effect of the ACF was clearly demonstrated through an average over random medium realizations. The effectiveness of the ACF in detecting a buried cylinder under frequency averaging was also demonstrated. When the cylinder was placed in the medium, the ACF exhibited as much as a 10 dB greater variation than the bistatic radar cross section, especially away from the memory line. Future work on this topic could involve modeling a new source which, instead of a plane wave, is likely to be a horn antenna of a ground penetrating radar (GPR) system. In addition, the random media model for soil could be improved, perhaps by quantifying

the actual variations in soil material and moisture (a Gaussian correlation function was used for mathematical simplicity). Finally, a numerical study could investigate the utility of combining GPR results with EMI results, using the methods developed in Chapter 6 along with the method of Chapter 2. In summary, Chapter 6 demonstrated the utility of a new post-processing technique for remote sensing applications when the target is in a continuous random medium. The contribution of the chapter lies in the application, not in the method itself.

As shown in Table 7.1, each chapter of this thesis makes a contribution to applications of electromagnetic wave theory, or outlines a new method that others may used to model propagation and scattering with improved accuracy and efficiency, or both. It is hoped that these new methods will be useful to scientists and engineers who routinely require solutions of Maxwell's Equations for fields in complex media.

	Method	Application
Chapter 2	√	√
Chapter 3	√	
Chapter 4		√
Chapter 5	√	
Chapter 6		√

Table 7.1: Each chapter in this thesis focused on numerical methods in electromagnetic wave propagation and scattering, but some only develop improved numerical methods while others only study new applications.

Bibliography

[1] C. Elachi. *Introduction to the Physics and Techniques of Remote Sensing.* Wiley, New York, 1987.

[2] F. F. Sabins. *Remote Sensing: Principles and Interpretation.* Freeman, New York, 1987.

[3] J. A. Kong. *Electromagnetic Wave Theory.* John Wiley & Sons, Inc., New York, second edition, 1990.

[4] D. S. Burnett. *Finite Elements Analysis.* Addison-Wesley, first edition, 1987.

[5] O. C. Zienkiewicz and R. L. Taylor. *The Finite Element Method. Vol 1: Basic Formulation and Linear Problems.* McGraw Hill, New York, fourth edition, 1989.

[6] N. Gershenfeld. *The Nature of Mathematical Modeling.* Cambridge University Press, first edition, 1999.

[7] P. P. Silvester and R. L. Ferrari. *Finite Elements for Electrical Engineers.* Cambridge University Press, third edition, 1996.

[8] J. Wu, D. M. Kingsland, J. F. Lee, and R. Lee. A comparison of anisotropic PML to Berenger's PML and its application to the finite-element method for EM scattering. *IEEE Trans. Antennas and Propagation*, 45(1):40–50, 1997.

[9] Y. Chung, T. K. Sarkar, S. Llorento-Romano, and M. Salarzar-Palma. Finite element time domain method using Laguerre polynomials. In *MTT-S International Microwave Symposium Digest*, pages 981–984, 2003.

[10] A. Bossavit. Whitney forms: a class of finite elements for three-dimensional computations in electromagnetism. *IEE Proceedings A*, 135(8):493–500, Nov. 1988.

[11] T. A. Davis and I. S. Duff. A combined unifrontal/multifrontal method for unsymmetric sparse matrices. *ACM Transactions on Mathematical Software*, 25(1):1–19, 1999.

[12] R. F. Harrington. *Field Computation by Moment Methods.* Macmillan, New York, 1968.

[13] A. A. Ergin, B. Shanker, K. Ayglin, and E. Michielssen. Computational complexity and implementation of two-level plane wave time domain algorithm for scalar wave equation. In *Antennas and Propagation Society International Symposium*, volume 2, pages 944–947, 1998.

[14] B. Barrowes. *Electromagnetic Scattering and Induction Models for Spheroidal Geometries.* PhD thesis, Massachusetts Institute of Technology, January 2004.

[15] D. Torrungrueng, J. T. Johnson, and H.-T. Chou. Some issues related to the novel spectral acceleration (NSA) method for the fast computation of radiation/scattering from one-dimensional extremely large-scale quasi-planar structures. *Radio Science*, 37(2), Mar. 2002.

[16] F. L. Teixeira and J. R. Bergmann. Spatial-frequency localized representations for integral equation reflector analysis. In *Antennas and Propagation Society International Symposium Digest*, volume 2, pages 890–893, July 21-26, 1996.

[17] K. S. Yee. Numerical solution of initial boundary value problems involving Maxwell's equations in isotropic media. *IEEE Trans. Antennas and Propagation*, 14(3):302–307, Mar. 1966.

[18] A. Taflove. *Computational electrodynamics: the finite-difference time-domain method.* Artech House, Boston, 1995.

[19] K. S. Kunz and R. J. Luebbers. *The finite difference time domain method for electromagnetics.* Boca Raton: CRC Press, first edition, 1993.

[20] J. P. Berenger. A perfectly matched layer for the absorption of electromagnetic waves. *J. Comp. Phys.*, 114:185–200, 1994.

[21] J. Fang and Z. Wu. Generalized perfectly matched layer for the absorption of propagating and evanescent waves in lossless and lossy media. *IEEE Trans. Microwave Theory and Techniques*, 44(12):2216–2222, Dec. 1996.

[22] W. C. Chew and W. H. Weedon. A 3D perfectly matched medium from modified Maxwell's equations with stretched coordinates. *Microwave Opt. Technol. Lett.*, 7(13):599–604, Sep. 1994.

[23] F.L. Teixeira and W.C. Chew. A general approach to extend Berenger's absorbing boundary condition to anisotropic and dispersive media. *IEEE Trans. Antennas and Propagation*, 46(9):1386–1387, 1998.

[24] S. V. Georgakopoulos, C. R. Birtcher, C. A. Balanis, and R. A. Renaut. Higher-order finite-difference schemes for electromagnetic radiation, scattering, and penetration - 1. Theory. *IEEE Antennas and Propagation Magazine*, 44(1):134–142, Feb. 2002.

[25] S. V. Georgakopoulos, C. R. Birtcher, C. A. Balanis, and R. A. Renaut. Higher-order finite-difference schemes for electromagnetic radiation, scattering, and

penetration - 2. Applications. *IEEE Antennas and Propagation Magazine*, 44(2):92–101, Apr. 2002.

[26] T. Namiki. Unconditionally stable FDTD algorithm for solving three-dimensional Maxwell's equations. In *Microwave Symposium Digest*, volume 1, pages 231–234, June 11-16, 2000.

[27] F. Zheng, Z. Chen, and J. Zhang. A finite-difference time-domain method without the courant stability conditions. *IEEE Microwave and Guided Wave Letters*, 9(11):441–443, Nov. 1999.

[28] M. Krumpholz and L. P. B. Katehi. MRTD : new time-domain schemes based on multiresolution analysis. *IEEE Trans. Microwave Theory and Techniques*, 44(4):555–571, Apr. 1996.

[29] J.D. McNeill and M. Bosnar. Application of time domain electromagnetic techniques to UXO detection. In *Proceedings of UXO Forum, Williamsburg, VA*, pages 34–42, March 26-28, 1996.

[30] R. A. Shelby, D. R. Smith, and S. Schultz. Experimental verification of a negative index of refraction. *Science*, 292, April 2001.

[31] C. D. Moss, T. M. Grzegorczyk, Y. Zhang, and J. A. Kong. Numerical studies of left handed metamaterials. *Progress in Electromagnetics Research*, (35):315–334, 2002.

[32] C. D. Moss, T. M. Grzegorczyk, K. O'Neill, and J. A. Kong. A hybrid time domain model of electromagnetic scattering from conducting, permeable targets. *submitted to IEEE Trans. Geoscience and Remote Sensing.*

[33] C. D. Moss, K. O'Neill, T. M. Grzegorczyk, and J. A. Kong. A hybrid time domain method to calculate electromagnetic induction scattering from targets

with arbitrary skin depths. In *Applied Computational Electromagnetics Symposium*, Mar. 2003.

[34] C. D. Moss, T. M. Grzegorczyk, H. C. Han, and J. A. Kong. Forward backward method with spectral acceleration for scattering from layered rough surfaces. *submitted to IEEE Trans. Antennas and Propagation.*

[35] C. D. Moss, F. L. Teixeira, and J. A. Kong. Analysis and compensation of numerical dispersion in the FDTD method for layered, anisotropic media. *IEEE Trans. Antennas and Propagation*, 50(9):1174–1184, Sep. 2002.

[36] C. D. Moss, F. L. Teixeira, and J.A Kong. Detection of targets in continuous random media: A numerical study using the angular correlation function. *Microwave Opt. Technol. Lett.*, 33(4):242–247, May 2002.

[37] B. Johnson, T. G. Moore, B. J. Blejer, C. F. Lee, T. P. Opar, S. Ayasli, and C. A. Primmerman. A research and development strategy for unexploded ordnance sensing. *Lincoln Laboratory Project Report, EMP-1*, Apr. 1996.

[38] H. Nelson. *ESTCP Ongoing Project Review.* 1998.

[39] C. D. Moss. Finite-difference time-domain simulation of electromagnetic scattering from objects under random media. Master's thesis, Massachusetts Institute of Technology, 2000.

[40] D. K. Keiswetter, I. J. Won, B. Barrow, and T. Bell. Object identification using multi-frequency EMI data. In *Proc. UXO Forum*, 1999.

[41] J. R. Wait and K. P. Spies. Quasi-static transient response of a conducting permeable sphere. *Geophysics*, 34(5):789–792, Oct. 1969.

[42] H. Braunisch, C. O. Ao, K. O'Neill, and J.A Kong. Magnetoquasistatic response of conducting and permeable prolate spheroid under axial excitation. *IEEE Trans. Geoscience and Remote Sensing*, 39(12):2689–2701, Dec. 2001.

[43] Y. Zhang, L. Collins, H. Yu, C.E. Baum, and L. Carin. Sensing of unexploded ordnance with magnetometer and induction data: theory and signal processing. *IEEE Trans. Geoscience and Remote Sensing*, 41(5):1005–1015, May 2003.

[44] N. Geng, C. E. Baum, and L. Carin. On the low frequency natural response of conducting and permeable targets. *IEEE Trans. Geoscience and Remote Sensing*, 37(1):347–359, 1999.

[45] L. Carin, H. Yu, Y. Dalichaouch, A. R. Perry, P. V. Czipott, and C. E. Baum. On the wideband EMI response of a rotationally symmetric permeable and conducting target. *IEEE Trans. Geoscience and Remote Sensing*, 39(6):1206–1213, 2001.

[46] F. Shubitidze, K. O'Neill, S. A. Haider, K. Sun, and K. D. Paulsen. Application of the method of auxiliary sources to the wide band electromagnetic induction problem. *IEEE Trans. Geoscience and Remote Sensing*, 40(4):928–942, Apr. 2002.

[47] V. Kupradze. About approximate solutions in mathematical physics problems. *Success of Mathematical Sciences*, 22:59–107, 1967.

[48] D. Rodger, P. J. Leonard, H. C. Lai, and P. C. Coles. Finite element modelling of thin skin depth problems using magnetic vector potential. *IEEE Trans. Magnetics*, 33(2):1299–1301, Mar. 1997.

[49] A. Sebak, L. Shafai, and Y. Das. Near-zone fields scattered by three-dimensional highly conducting permeable objects in the field of an arbitrary loop. *IEEE Trans. Geoscience and Remote Sensing*, 29:9–15, 1991.

[50] K. R. Shao and J. D. Lavers. On the application of hinged finite elements to eddy current problems. *IEEE Trans. Magnetics*, 23(5):3059–3061, Sep. 1987.

[51] K. R. Shao and J. D. Lavers. A new hybrid method using hinged finite element formulations for the skin effect eddy current problems. *IEEE Trans. Magnetics*, 26(5):2765–2767, Sep. 1990.

[52] C.O. Ao, H. Braunisch, K. O'Neill, and J.A Kong. Quasi-magnetostatic solution for a conducting and permeable spheroid with arbitrary excitation. *IEEE Trans. Geoscience and Remote Sensing*, 40(4):887–897, Apr. 2002.

[53] K. Sun, K. O'Neill, F. Shubitidze, S. A. Haider, and K. D. Paulsen. Simulation of electromagnetic induction scattering from targets with negligible to moderate penetration by primary fields. *IEEE Trans. Geoscience and Remote Sensing*, 40(4):910–327, Apr. 2002.

[54] C. A. Brebbia, J. C. F. Telles, and L. C. Wrobel. *Boundary Element Techniques.* Springer-Verlag, first edition, 1984.

[55] Q. Chen, A. Konrad, and P. P. Biringer. A finite element - Green's function method for the solution of unbounded three-dimensional eddy current problems. *IEEE Trans. Magnetics*, 30(5):3048–3051, Sep. 1994.

[56] M. Ayoub, F. Roy, F. Bouillault, and A. Razek. Numerical modelling of 3D magnetostatic saturated structures with a hybrid FEM-BEM technique. *IEEE Trans. Magnetics*, 28(2):1052–1055, Mar. 1992.

[57] W. H. Press, S. A. Teukolsky, W. T. Vetterling, and B. T. Flannery. *Numerical Recipes in Fortran 77.* Cambridge University Press, New York, 1986-1992.

[58] F. J. Rizzo and D. J. Shippy. A boundary integral approach to potential and elasticity problems for axisymmetric bodies with arbitrary boundary conditions. *Mechanics Research Communications*, 6(2):99–103, 1979.

[59] Milton Abramowitz and Irene A. Stegun. *Handbook of Mathematical Functions.* Dover, New York, 1965.

[60] J. Crank. *The Mathematics of Diffusion.* Clarendon Press, second edition, 1975.

[61] C. Pozrikidis. *Numerical Computation in Science and Engineering.* Oxford University Press, first edition, 1998.

[62] H. Braunisch. *Methods in Wave Propagation and Scattering.* PhD thesis, Massachusetts Institute of Technology, February 2001.

[63] C. O. Ao. *Electromagnetic Wave Scattering by Discrete Random Media with Remote Sensing Applications.* PhD thesis, Massachusetts Institute of Technology, June 2001.

[64] K. O'Neill. *Forthcoming publication.* 2003.

[65] L. Tsang, J. A. Kong, and R. T. Shin. *Theory of Microwave Remote Sensing.* John Wiley, New York, 1985.

[66] L. Tsang, J. A. Kong, and K. H. Ding. *Scattering of Electromagnetic Waves: Theories and Applications.* John Wiley & Sons, Inc., New York, first edition, 2000.

[67] F. T. Ulaby, R. K. Moore, and A. K. Fung. *Microwave Remote Sensing: Active and Passive.* Artech House, Boston, 1981.

[68] J. T. Hviid, J. B. Andersen, J. Toftgard, and J. Bøjer. Terrain-based propagation model for rural area - an integral equation approach. *IEEE Trans. Antennas and Propagation*, 43(1):41–46, Jan. 1995.

[69] L. Tsang, J. A. Kong, and K.H. Ding. *Scattering of Electromagnetic Waves: Numerical Simulations.* John Wiley & Sons, Inc., New York, first edition, 2001.

[70] D. Torrungrueng and J. T. Johnson. An improved FB/NSA algorithm for the computation of scattering from two-dimensional large-scale rough surfaces. *J. Electromagnetic Waves and Applications*, 15(10):1337–1362, 2001.

[71] M. Y. Xia, C. H. Chan, S. Q. Li, B. Zhang, and L. Tsang. An efficient algorithm for electromagnetic scattering from rough surfaces using a single integral equation and multilevel sparse-matrix canonical-grid method. *IEEE Trans. Antennas and Propagation*, 51(6):1142–1149, June 2003.

[72] K. F. Warnick and W. C. Chew. Numerical simulation methods for rough surface scattering. *Waves in Random Media*, 11:1–30, 2001.

[73] D. Chen, L. Tsang, L. Zhou, S.C. Reising, W.E. Asher, L.A. Rose, K.-H. Ding, and C.-T. Chen. Microwave emission and scattering of foam based on Monte Carlo simulations of dense media. *IEEE Trans. Geoscience and Remote Sensing*, 41(4):782–790, Apr. 2003.

[74] K. Sarabandi and I.-S. Koh. Effect of canopy-air interface roughness on HF-VHF wave propagation in forest. *IEEE Trans. Antennas and Propagation*, 50(2):111–121, Feb. 2002.

[75] K. M. Golden, M. Cheney, K.-H. Ding, A. K. Fung, T. C. Grenfell, D. Issacson, J. A. Kong, S. V. Nghiem, J. Sylvester, and D. P. Winebrenner. Forward electromagentic scattering models for sea ice. *IEEE Trans. Geoscience and Remote Sensing*, 36(5):1655–1674, Sep. 1998.

[76] Y. Zhang. High-frequency mode-expansion method for electromagnetic wave scattering by objects on rough ocean surface. In *Progress in Electromagnetics Research Symposium*, 2002.

[77] D. A. Kapp and G. S. Brown. A new numerical method for rough-surface scattering calculations. *IEEE Trans. Antennas and Propagation*, 44(5):711–721, May 1998.

[78] D. Holliday, L. L. DeRaad, and G. J. St-Cyr. Forward-backward: A new method for computing low-grazing angle scattering. *IEEE Trans. Antennas and Propagation*, 44(5):722–729, May 1998.

[79] H.-T. Chou and J. T. Johnson. A novel acceleration algorithm for the computation of scattering from rough surfaces with a forward-backward method. *Radio Science*, 33(5):1277–1287, Sep. 1998.

[80] H.-T. Chou and J. T. Johnson. Formulation of forward-backward method using novel spectral acceleration for the modeling of scattering from impedance rough surfaces. *IEEE Trans. Geoscience and Remote Sensing*, 38(1):605–607, Jan. 2000.

[81] C. H. Chan, L. Tsang, and Q. Li. Monte Carlo simulations of large-scale one-dimensional random rough-surface scattering at near-grazing incidence: Penetrable case. *IEEE Trans. Antennas and Propagation*, 46(1):142–149, Jan. 1998.

[82] Q. Li, L. Tsang, J. Shi, and C. H. Chan. Application of physics-based two-grid method and sparse matrix canonical grid method for numerical simulations of emissivities of soils with rough surfaces at microwave frequencies. *IEEE Trans. Geoscience and Remote Sensing*, 38(4):1635–1643, July 2000.

[83] A. Iodice. Forward-backward method for scattering from dielectric rough surfaces. *IEEE Trans. Antennas and Propagation*, 50(7):901–911, 2002.

[84] J. A. DeSanto and P. A. Martin. On the derivation of boundary integral equations for scattering by an infinite one-dimensional rough surface. *Journal of the Acoustical Society of America*, 102(1):67–77, July 1997.

[85] M. R. Pino, L. Landesa, J. L. Rodriguez, F. Obelleiro, and R. J. Burkholder. The generalized forward-backward method for analyzing the scattering from targets on ocean-like rough surfaces. *IEEE Trans. Antennas and Propagation*, 47(6):961–969, June 1999.

[86] M. R. Pino, L. Landesa, J. L. Rodriguez, F. Obelleiro, and R. J. Burkholder. The generalized forward-backward method for analyzing the scattering from

targets on ocean-like rough surfaces. *IEEE Trans. Antennas and Propagation*, 47(6):961–969, June 1999.

[87] D. R. Smith, W. J. Padilla, D. C. Vier, S. C. Nemal-Nasser, and S. Schultz. Composite medium with simultaneously negative permeability and permittivity. *Phys. Rev. Lett.*, 84(18), May 2000.

[88] J. A. Kong. Electromagnetic wave interaction with stratified negative isotropic media. *J. Electromagnetic Waves and Applications*, 15(10), 2001.

[89] J. B. Pendry, A. J. Holden, W. J. Stewart, and I. Youngs. Extremely low frequency plasmons in metallic mesostructures. *Phys. Rev. Lett.*, 76(25):4773–4776, June 1996.

[90] J. B. Pendry, A. J. Holden, D. J. Robbins, and W. J. Stewart. Low frequency plasmons in thin wire structures. *J. Phys. Condens. Matter*, 10(22):4785–4809, June 1998.

[91] R. W. Ziolkowski and E. Heyman. Wave propagation in media having negative permittivity and permeability. *Physical Review E*, 64(056625), 2001.

[92] J. B. Pendry, A. J. Holden, D. J. Robbins, and W. J. Stewart. Magnetism from conductors and enhanced nonlinear phenomena. *IEEE Trans. Microwave Theory and Techniques*, 47(11), November 1999.

[93] V. G. Veselago. The electrodynamics of substances with simultaneously negative values of ϵ and μ. *Soviet Physics Uspekhi*, 10(4), January 1968.

[94] J. B. Pendry. Negative refraction makes a perfect lens. *Phys. Rev. Lett.*, 85(18), October 2000.

[95] J. A. Kong, B.-I. Wu, and Y. Zhang. Lateral displacement of a Gaussian beam reflected from a grounded slab with negative permittivity and permeability. *Appl. Phys. Lett.*, 80(12), March 2001.

[96] C. Caloz, C.-C. Chang, and T. Itoh. Full-wave verification of the fundamental properties of left-handed materials in waveguide configurations. *Journal of Applied Physics*, 90(11):5483–5486, December 2001.

[97] P. Markos and C. M. Soukoulis. Transmission studies of left-handed materials. *Physical Review B*, 65, December 2001.

[98] T. Weiland, R. Schuhmann, R. B. Greegor, C. G. Parazzoli, A. M. Vetter, D. R. Smith, D. C. Vier, and S. Schultz. *Ab initio* numerical simulation of left-handed metamaterials: Comparison of calculations and experiments. *Journal of Applied Physics*, 90(10):5419–5424, November 2001.

[99] S. O'Brien and J.B. Pendry. Magnetic activity at infrared frequencies in structured metallic photonic crystals. *J. Phys. Cond. Matter*, 14:6383–6394, 2002.

[100] F. J. Harris. On the use of windows for harmonic analysis with discrete Fourier Transform. *Proc. IEEE*, 66, 51-83 1978.

[101] J. Pacheco Jr. *Theory and application of left-handed metamaterials.* PhD thesis, Massachusetts Institute of Technology, 2004.

[102] G. V. Eleftheriades, A. K Iyer, and P. C. Kremer. Planar negative refractive index media using periodically l-c loaded transmission lines. *IEEE Trans. Microwave Theory and Techniques*, 50(12):2702–2712, 2002.

[103] A. Grbic and G. V. Eleftheriades. Experimental verification of backward-wave radiation from a negative refractive index metamaterial. *Journal of Applied Physics*, 92(10):5930–5935, 2002.

[104] G. Gay-Balmaz and O. J. F. Martin. Electromagnetic resonances in individual and coupled split-ring resonators. *Journal of Applied Physics*, 95(5):2929–2936, 2002.

[105] G. Gay-Balmaz and O. J. F. Martin. Efficient isotropic magnetic resonators. *Appl. Phys. Lett.*, 81(5):939–941, 2002.

[106] R. Marques, F. Medina, and R. Rafii-El-Idrissi. Role of bianisotropy in negative permeability and left-handed metamaterials. *Phys. Rev. B*, 65(144440), 2002.

[107] R. Marques, F. Medina, and R. Rafii-El-Idrissi. Comparative analysis of edge- and broadside- coupled split ring resonators for metamaterial design - theory and experiments. *IEEE Trans. Antennas and Propagation*, 51(10):2572–2581, 2003.

[108] C. R. Simovski and S. L. He. Frequency range and explicit expressions for negative permittivity and permeability for an isotropic medium formed by a lattice of perfectly conducting omega particles. *Phys. Lett. A*, 311(1-2):254–263, 2003.

[109] M. M. I. Saadoun and N. Engheta. A reciprocal phase shifter using novel psuedochiral or omega medium. *Microwave Opt. Technol. Lett.*, 5(4):184–188, 1992.

[110] E. A. Forgy and W. C. Chew. A new FDTD formulation with reduced dispersion for the simulation of wave propagation through inhomogeneous media. In *AP IEEE International Symposium*, volume 2, pages 1316–1319, 1999.

[111] T. Materday et al. A new vision of numerical methods for the solution of Maxwell's equations related to the FDTD method; application to general anisotropic media. In *IEE Second International Conference on Computation in Electromagnetics*, pages 138–141, 1994.

[112] C. Huber et al. Dispersion in anisotropic media modeled by three-dimensional TLM. *IEEE Transactions on Microwave Theory and Techniques*, 43(8):1923–1934, Aug 1995.

[113] F. Xiao and H. Yabe. Numerical dispersion relation for FDTD method in general curvilinear coordinates. *IEEE Microwave and Guided Wave Letters*, 7(2):48–50, Feb 1997.

[114] T. Martin and L. Pettersson. Dispersion compensation for Huygens' sources and far-zone transformation in FDTD. *IEEE Trans. Antennas and Propagation*, 48(4):494–501, April 2000.

[115] K. Demarest, R. Plumb, and Z. Huang. FDTD modeling of scatterers in stratified media. *IEEE Trans. Antennas and Propagation*, 43(10):1164–1168, Oct. 1995.

[116] W. C. Chew. Electromagnetic theory on a lattice. *Journal of Applied Physics*, 75(10):4843–4850, May 1994.

[117] W. C. Chew and J. M. Jin. Perfectly matched layers in the discretized space: An analysis and optimization. *Electromagnetics*, 16:325–340, 1996.

[118] M. Z. M. Jenu and D. H. O. Bebbington. Two-dimensional modelling of optical propagation in turbulent atmosphere. *Electronics Letters*, 29(9):769–771, Apr. 1993.

[119] A. K. Fung. Scattering from a vegetation layer. *IEEE Trans. Geosci. Elec.*, 17(1):1–6, Jan. 1979.

[120] R. G. Atkins. *Microwave Scattering and Synthetic Aperture Radar Imaging of Targets Buried in Random Media.* PhD thesis, Massachusetts Institute of Technology, 1993.

[121] J. Bourgeois. *A Complete Three-Dimensional Electromagnetic Simulation of Ground-Penetrating Radars Using the Finite-Difference Time-Domain Method.* PhD thesis, Georgia Institute of Technology, 1997.

[122] K. O'Neill, R. F. Jr. Lussky, and K. D. Paulsen. Scattering from a metallic object embedded near the randomly rough surface of a lossy dielectric. *IEEE Trans. Geosci. Remote Sensing*, 34(2):367–376, Mar. 1996.

[123] T. J. Cui and W. C. Chew. Fast evaluation of Sommerfeld integrals for EM scattering and radiation by three-dimensional buried objects. *IEEE Trans. Geosci. Remote Sensing*, 37(2):887–900, Mar. 1999.

[124] D. A. Hill. Electromagnetic scattering by buried objects of low contrast. *IEEE Trans. Geosci. Remote Sensing*, 26(2):195–203, Mar. 1988.

[125] S. Vitebskiy, L. Carin, M. A. Ressler, and F. H. Le. Ultra-wideband, short-pulse ground-penetrating radar: Simulation and measurement. *IEEE Trans. Geosci. Remote Sensing*, 35(3):762–772, May 1997.

[126] T. Dogaru and L Carin. Time-domain sensing of targets buried under a rough air-ground interface. *IEEE Trans. Antennas and Propagation*, 46(3):360–372, Mar. 1998.

[127] W. R. Scott and G. S. Smith. Measured electrical constitutive parameters of soil as functions of frequency and moisture content. *IEEE Trans. Geosci. Remote Sensing*, 30(3):621–623, May 1992.

[128] Y. Miyazaki, J. Sonoda, and Y. Jonori. Statistical analysis of electromagnetic scattering of buried objects in random media using FDTD method. *Transactions of the Institute of Electrical Engineers of Japan, Part C*, 117-C(1):35–41, January 1997.

[129] C. D. Moss, F. L. Teixeira, and J. A. Kong. Finite difference time domain simulation of scattering from objects in continuous random media. *IEEE Trans. Geosci. Remote Sensing*, 40(1):178–186, Jan. 2002.

[130] S. Feng, C. Kane, P. A. Lee, and A. D. Stone. Correlations and fluctuations of coherent wave transmission through disordered media. *Phys. Rev. Lett.*, 61:834–837, 1988.

[131] G. Zhang and L. Tsang. Angular correlation function of wave scattering by a random rough surface and discrete scatterers and its application in the detection of a buried object. *Waves in Random Media*, 7:467–479, 1997.

[132] M. Borgeaud, R. T. Shin, and J. A. Kong. Theoretical models for polarimetric radar clutter. *J. Electromagnetic Waves and Applications*, 1(1):73–89, 1987.

[133] A. K. Fung and F. T. Ulaby. A scatter model for leafy vegetation. *IEEE Trans. Geosci. Elec.*, 16(4):281–286, Oct. 1978.

[134] K. Demarest, Z. Huang, and R. Plumb. An FDTD near- to far-zone transformation for scatterers buried in stratified grounds. *IEEE Trans. Antennas and Propagation*, 44(8):1150–1157, Aug. 1996.

[135] J. E. Hipp. Soil electromagnetic parameters as functions of frequency, soil density, and soil moisture. *Proc. IEEE*, 62:98–103, Jan 1974.

[136] F.L. Teixeira, W.C. Chew, M. Straka, M.L. Oristaglio, and T. Wang. Finite-difference time-domain simulation of ground penetrating radar on dispersive, inhomogeneous, and conductive soils. *IEEE Trans. Geosci. Remote Sensing*, 36(6):1928–1937, Nov 1998.

List of Acronyms

ABC	:	Absorbing Boundary Condition
ACF	:	Angular Correlation Function
BOR	:	Body of Revolution
EMI	:	Electromagnetic Induction
FB	:	Forward Backward
FCF	:	Frequency Correlation Function
FDTD	:	Finite Difference Time Domain
FEM	:	Finite Element Method
FE-BI	:	Finite Element - Boundary Integral
GPR	:	Ground Penetrating Radar
IE	:	Integral Equation
LH	:	Left Handed
MoM	:	Method of Moments
MQS	:	Magnetoquasistatic
MRTD	:	Multi-Resolution Time Domain
NC	:	No Convergence
ODE	:	Ordinary Differential Equation
PDE	:	Partial Differential Equation
PEC	:	Perfect Electric Conductor

PML	:	Perfectly Matched Layer
RCS	:	Radar Cross Section
SA	:	Spectral Acceleration
SDP	:	Steepest Descent Path
SP	:	Saddle Point
SPA	:	Small Penetration Approximation
SRR	:	Split-Ring Resonator
TE	:	Transverse Electric
TM	:	Transverse Magnetic
TSA	:	Thin Skin Approximation
TSA-BI	:	Thin Skin Approximation - Boundary Integral
UXO	:	Unexploded Ordnance

Biographical Note

C. D. Moss received the B.S. degree from the University of Alberta in 1997, and the M.S. degree in electrical engineering from the Massachusetts Institute of Technology in 2000. He worked as an Engineer at Raytheon Company in the Microwave Systems Department from 1997 to 1998, where he was mainly involved in MMIC design. In addition, he has held internships at Philips Semiconductors, Nortel Networks, The Canadian Department of National Defense, and ATCO Power. Since 1998, he has been a Research Assistant at MIT in the Center for Electromagnetic Theory and Applications, and in Lincoln Laboratory. In 2002 he received an IEEE MTT-S Graduate Fellowship Award. His research interests include both analytical and numerical methods for electromagnetics.